THÈSE PRÉSENTÉE
POUR OBTENIR LE GRADE DE

DOCTEUR DE L'UNIVERSITÉ DE BORDEAUX

ECOLE DOCTORALE SCIENCES PHYSIQUES ET DE L'INGENIEUR

Laser, Matière et Nanoscience

Par **Théo GUILBERTEAU**

Traitement et fonctionnalisation de surface par rayonnement laser femtoseconde en régime rafale GHz

Sous la direction de : **Inka MANEK-HÖNNINGER**
Co-encadrant : **John LOPEZ** Co-encadrante : **Laura GEMINI**

Soutenue le 25 juin 2026

Membres du jury :

Mme. Inka MANEK-HÖNNINGER	Professeure	CELIA	Directrice
M. Ilday ÖMER	Professeur	Ruhr Universität Bochum	Rapporteur
M. Jean-Phillipe COLOMBIER	Professeur	Laboratoire Hubert Curien	Rapporteur
M. François COURVOISIER	Directeur de recherche	Institut FEMTO-ST	Examinateur
M. Emmanuel D'HUMIERES	Professeur	CELIA	Président
M. John LOPEZ	Ingénieur de Recherche	CELIA	Invité
Mme. Laura GEMINI	Ingénieure	ALPhANOV	Invitée

Traitement et fonctionnalisation de surface par rayonnement laser femtoseconde en régime rafale GHz

Résumé : Les lasers femtosecondes sont aujourd'hui largement reconnus pour leur capacité à réaliser des traitements et une fonctionnalisation de surface de haute précision grâce à un dépôt d'énergie fortement localisé et à une réduction significative de la zone affectée thermiquement. Malgré ces avantages, leur adoption sur le plan industriel reste limitée, principalement en raison de leur coût élevé et d'une productivité des procédés associés encore insuffisante. En effet, les régimes de fonctionnement conventionnels de ces sources laser opérant à faible cadence de répétition ne permettent pas toujours d'exploiter pleinement la puissance moyenne disponible ; le bénéfice en précision et en qualité d'usinage est alors obtenu au détriment du temps de traitement. Dans ce contexte, cette thèse explore des stratégies visant à améliorer l'efficacité et la contrôlabilité du traitement et de la fonctionnalisation de surface par laser femtoseconde en s'appuyant sur une mise en forme spatiale et temporelle du faisceau. Une attention particulière est portée au régime rafale GHz, dans lequel une impulsion laser est divisée en trains d'impulsions de plus faible énergie séparées par des délais très courts, favorisant ainsi les effets coopératifs entre impulsions successives et un dépôt d'énergie plus efficace. Les travaux adressés dans le cadre de cette thèse portent à la fois sur des matériaux métalliques et diélectriques. La fonctionnalisation de surface de l'acier inoxydable AISI 316L est étudiée à travers des procédés de polissage laser en régime rafales GHz, en analysant l'influence de la configuration des rafales, de la mise en forme spatiale du faisceau (gaussien et vortex), des recouvrements spatiaux et de l'état de surface initial sur l'efficacité du procédé et la qualité de surface obtenue. En parallèle, la structuration sub-surface de matériaux diélectriques transparents à l'aide de faisceaux de Bessel en régimes mono-impulsion, rafales MHz et rafales GHz, est étudiée dans le but de générer des modifications à fort rapport d'aspect. Afin de mieux comprendre les mécanismes d'interaction laser-matière en régime rafale GHz, des diagnostics résolus en temps, combinant l'ombroscopie pompe-sonde et interférométrie de Mach–Zehnder, sont mis en œuvre. Ces techniques permettent de caractériser la dynamique du plasma et le dépôt d'énergie en volume, et de comparer les comportements observés entre les régimes MHz et GHz dans les matériaux diélectriques. L'ensemble des résultats met en évidence le potentiel du régime rafale GHz, associé à une mise en forme adaptée du faisceau, pour concilier haute précision, fonctionnalisation de surface et amélioration de la productivité dans le traitement ultrarapide des matériaux.
Mots-clés : Laser femtoseconde, Fonctionnalisation de surface, Rafales GHz, Interaction laser-matière.

Treatment and surface functionalization by laser irradiation in femtosecond GHz-burst mode.

Abstract: Femtosecond lasers are widely recognized for their ability to perform high-precision surface treatment and functionalization thanks to strongly localized energy deposition and reduced heat affected zones. Despite these advantages, their industrial adoption remains limited due to high system costs and insufficient throughput of the associated processes. In conventional low-repetition-rate regimes, the available average power is not always fully exploited; the high accuracy and machining quality of femtosecond processing is obtained through an increase of processing times. In this context, this thesis investigates strategies to improve the efficiency and controllability of femtosecond laser surface treatment and functionalization through spatial and temporal beam shaping. Emphasis is placed on the GHz-burst regime, in which a single laser pulse is divided into a train of lower-energy sub-pulses separated by very short time delays, promoting cooperative pulse-to-pulse effects and more efficient energy deposition. The work deals with both metallic and dielectric materials. Surface functionalization of AISI 316L stainless steel is investigated through GHz-burst laser polishing, with a detailed analysis of the influence of burst configuration, spatial beam shaping (Gaussian and vortex beams), spatial overlap, and initial surface condition on process efficiency and final surface quality. In parallel, structuring of transparent dielectric materials is explored using Bessel beams operated in single-pulse, MHz-burst, and GHz-burst regimes, enabling the generation of high-aspect-ratio modifications. To gain deeper insight into the laser–matter interaction mechanisms specific to the GHz-burst regime, time-resolved diagnostics combining pump–probe shadowgraphy and Mach–Zehnder interferometry are employed. These measurements provide access to plasma dynamics and in-volume energy deposition, allowing direct comparison between MHz- and GHz-burst regimes. Overall, the results demonstrate the potential of GHz-burst irradiation combined with tailored beam shaping to reconcile high-precision surface functionalization with improved throughput in ultrafast laser material processing.
Keywords: Femtosecond laser, Surface functionalization, GHz bursts, Laser–matter interaction.

Centre Lasers Intenses et Applications
UMR 5107 Université de Bordeaux, 33000 Bordeaux, France.

French summary

Contexte scientifique

Les lasers avec impulsions ultrabrèves constitue aujourd'hui un outil extrêmement polyvalent pour le micro-usinage des matériaux, qu'il s'agisse de modifications en surface ou en volume. Grâce à la très faible durée des impulsions femtosecondes ($10^{-15}s$, le dépôt d'énergie se produit sur des échelles de temps plus courtes que le temps caractéristique pour la diffusion thermique dans les matériaux. Il en résulte des modifications très précices, des zones affectées thermiquement réduites et une qualité d'usinage amélioré. De plus, ces procédés sont sans contact et ne nécessitent ni d'opération de masquage, ni produits chimiques, et sont compatibles avec les exigences technico-économiques des procédés de fabrication moderne la plupart du temps. Ces différents avantages confère aux lasers femtosecondes un rôle central dans les procédés de fabrication pour l'optoélectronique, la micro-électronique, la photonique et de nombreuses applications industrielles exigeant une grande précision comme l'aéronautique ou les dispositifs médicaux.

Comme énoncé précedement ses procédés couvrent un large spectre de domaine d'applications allant de l'ablation directe (nettoyage, gravure, texturation) jusqu'à la micro- et nano-structuration avancée, par exemple via la formation de structures périodiques induites par laser (LIPSS) ou par interférométrie laser (DLIP). Ces approches permettent d'obtenir des fonctionnalités spécifiques : anti-réflectivité, super hydrophobicité, super hydrophilicité, anti-bactérienne, ou résistance à la formation du givre. D'autres applications incluent la micro-perforation pour ajuster la perméabilité ou l'acoustique, ainsi que la fusion de surface contrôlée pour le polissage.

Cependant, l'atteinte des objectifs en termes de productivité, extrême précision et de qualité demeure un défi pour de nombreuses applications industrielles. Deux approches sont généralement envisagées :

(1) l'optimisation des paramètres lasers (longueur d'onde, durée d'impulsion, fluence, polarisation) pour maximiser le dépôt d'énergie de chaque impulsion laser en évitant les effets indésirables ;

(2) la mise en forme spatial ou temporel du faisceau, ouvre de nouveaux degrés de liberté pour l'interaction laser-matière tel que le multi-spot pour la parrallelisation des procédés.

Dans ce contexte, l'exploration de nouveaux régimes d'interaction représente un axe de recherche majeur, en particulier pour étendre les capacités de fonctionnalisation de surface et d'usinage en volume des matériaux à gap. Un intérêt croissant se porte notamment sur le régime rafale (burst), qui permet d'améliorer la dynamique d'absorption et les mécanismes d'ablation. Dans un régime rafale, une série d'impulsions ultrabrèves est délivrée avec un délai intra-rafale plus court que le

régime mono-impulsion classique, de sorte que les impulsions successives au sein de chaque rafale interagissent avec une surface encore excitée ou partiellement fondue. Ce dépôt d'énergie, mis en forme temporellement permet d'amplifier les effets cumulatifs, d'augmenter l'absorption, et d'influencer la morphologie de surface finale.

Plus récemment, l'émergence du régime rafale GHz a ouvert un nouveau domaine de recherche dans l'interaction laser-matière. Dans cette configuration, chaque impulsion de forte énergie est remplacée par un train d'impulsions beaucoup plus faibles, mais séparées par des délais de l'ordre de quelques centaines de picosecondes à quelques nanosecondes. Ce délai est plus court que le temps de relaxation thermique du matériau : la zone irradiée ne peut donc pas se refroidir complètement entre deux impulsions, ce qui génère un échauffement cumulatif extrêmement efficace sur la durée de la rafale. Ce mécanisme permet de modifier, voire d'ablater, les matériaux à gap pour des fluences inférieures au seuil d'ablation par régime impulsionnelle classique, tout en limitant les effets non linéaires indésirables en amont de point focal dans les matériaux diélectriques et en favorisant ainsi un dépôt d'énergie optimal au voisinage du foyer.

Démarches utilisées

Station d'usinage

Ces travaux de thèse ont été réalisés dans le cadre d'un laboratoire commun nommé TRICORN, incluant deux partenaires industriels: le centre technologique ALPhANOV et l'entreprise Amplitude . Dans le cadre de ce partenariat, Amplitude a mis à disposition du laboratoire CELIA une source laser femtoseconde prototype, développée à partir de l'architecture Tangor 100, capable d'opérer en trois régimes distincts : mono-impulsion répétitif, rafale MHz et rafale GHz.

Dans le premier cas, le laser délivre des impulsions très énergétiques à une cadence pouvant atteindre quelques mégahertz. En mode rafale MHz, l'énergie d'une impulsion est répartie en une série de sous-impulsions de plus faible intensité séparées par un delai de 25 ns (40 MHz), ses rafales peuvent être délivrées avec une fréquence pouvant atteindre le mégahertz. Le mode rafale GHz adopte le même principe, mais avec des délais intra-rafale encore plus courts, d'une valeur de 0,8 ns (1,28 GHz), permettant d'exploiter des effets cumulatifs avec plus d'efficatité.

Dans le cadre de ces travaux, l'ensemble des expériences d'usinage laser et de diagnostic a été réalisé sur la station de micro-usinage FemtoWeld, spécialement conçue pour offrir un haut niveau de flexibilité expérimentale et une stabilité mécanique optimale. Développée par ALPhANOV sur la base d'un cahier des charges établi par le CELIA et construite autour d'un portique monolithique en granite, cette plateforme assure une excellente rigidité ainsi qu'un amortissement des vibrations efficace, deux éléments indispensables pour un procédé laser de précision et des diagnostics résolus tant spatialement que temporellement.

Le faisceau laser est injecté à l'arrière de la station et guidé vers la zone d'usinage grâce à un ensemble de miroirs fixé a la structure en granite. La station permet d'accueillir différents modules optiques selon la configuration expérimentale souhaitée, notamment une tête de focalisation Gaussienne classique ou un module de génération de faisceau de Bessel comme illustré dans Figure 1.

Dans ce cas, le faisceau Gaussien est d'abord agrandi afin d'ajuster précisément

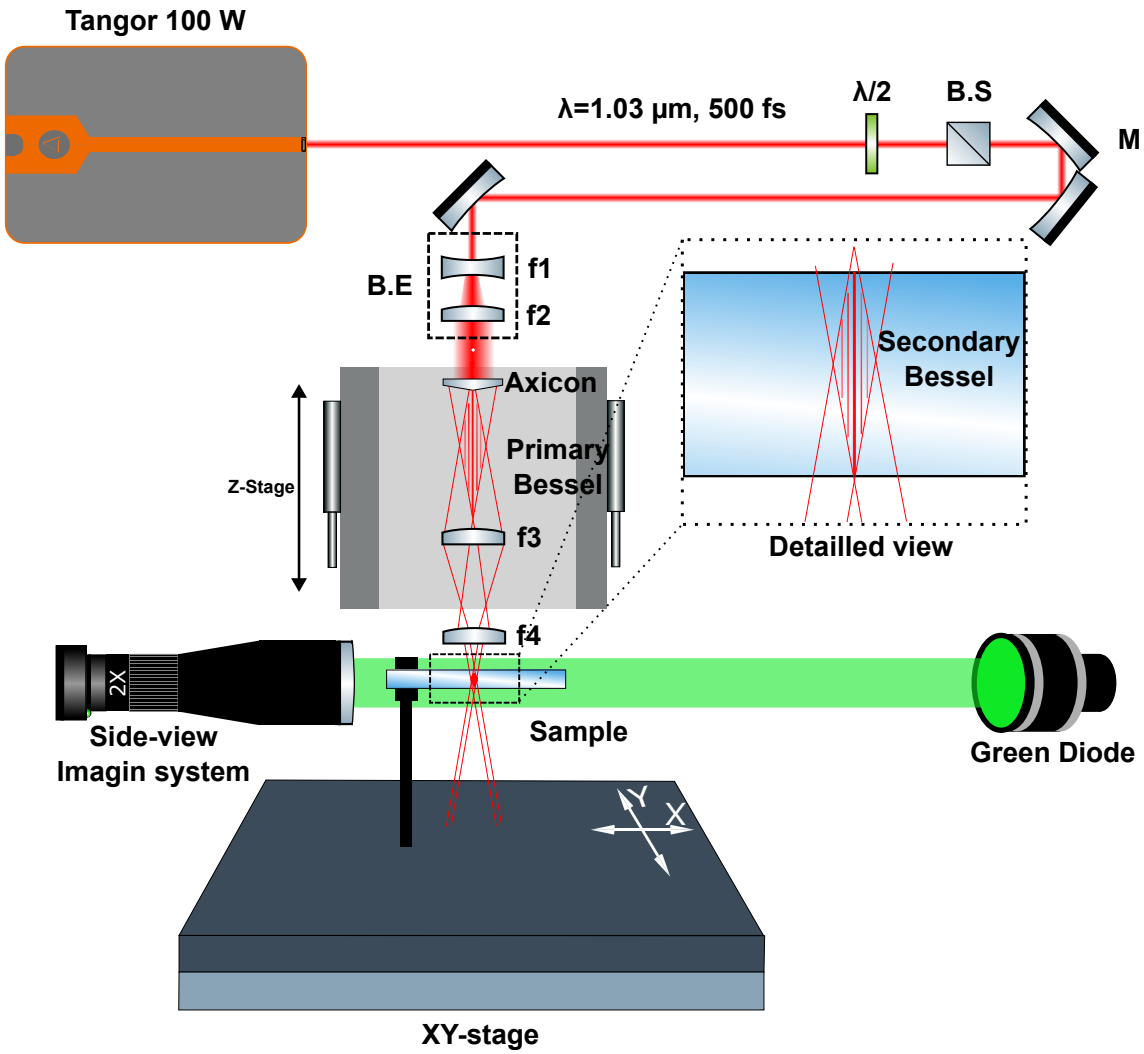

Figure 1: Representation schématique du set-up expérimental utilisé pour le faisceau de Bessel.

son diamètre pour exploiter au maximum la pupille d'entrée permise par les optiques. Ensuite, le faiceau est transmis à travers un axicon de 170° (demi-angle de 5°), qui génère un faisceau de Bessel dit "primaire". Étant donné que ce faisceau présente des dimensions trop importantes pour atteindres les intensitées necéssaire à la génération de modification dans les diélectriques, il est ensuite réduit par un système optique 4f d'un facteur de 12,5. On obtient ainsi un faisceau de Bessel dit "secondaire" avec des dimensions caracteristiques réduites et plus intense. Le faisceau ainsi obtenu presente un diamètre du lobe central d'environ 3 µm sur plusieurs centaines de micromètres de longueur (800-1000 µm), parfaitement adapté aux processus d'absorption non-linéaire et aux modifications en volume.

La station FemtoWeld est également équipée d'un système de visualisation latéral permettant l'observation directe de la zone d'interaction durant l'usinage. Celui-ci repose sur une diode verte émettant à 520 nm, un microscope à longue distance de travail InfiniMax (avec option ×2), ainsi qu'un filtre passe-bande centré autour de 520 nm pour éviter toute lumière issue de l'usinage du laser opérant à 1030 nm. Selon le type d'échantillon utilisé, différents supports dédiés peuvent être installés

sur la platine XY monolithique motorisée de la station. Une platine additionelle en Z, manuelle, ou un module d'inclinaison peuvent être ajoutés afin d'assurer un réglage précis en hauteur et en planéité de l'échantillon.

L'ensemble de cette architecture en granite intégrant guidage optique, modules Gaussien et Bessel et visualisation latérale haute résolution, confère à FemtoWeld une grande flexibilité expérimentale, notamment avec la capacité à intégrer de nombreux diagnostics autour de la zone usinée. Ainsi, elle permet d'explorer de manière approfondie les mécanismes d'interaction laser-matière en régime rafale et de travailler dans des conditions parfaitement maîtrisées, essentielles pour l'étude des processus physiques mis en jeu dans ces travaux de thèse.

Expérience pompe-sonde

Dans cette thèse, un dispositif d'ombroscopie pompe–sonde particulier a été développé afin d'étudier les phénomènes transitoires induits par le laser en régime rafale. Ce diagnostic s'appuie sur l'utilisation de deux impulsions laser synchronisées, une pompe et une sonde, séparées par un délai temporel précisément contrôlé, permettant l'imagerie active de la zone d'interaction. Cette technique offre une visualisation résolue dans le temps de la réponse du matériau et de la dynamique du plasma, avec une incertitude absolue inférieure à la nanoseconde et une incertitude relative d'environ 500 fs.

La complexité de ce dispositif est majoritairement due au fait que la pompe soit en régime rafale alors que la sonde doit etre en régime impulsionnelle classique afin d'obtenir une meilleure resolution temporelle. Ainsi, le dispositif complet est organisé en quatre parties. La première décrit la stratégie de synchronisation entre les lasers pompe et sonde. La seconde présente les éléments optiques communs aux différentes configurations, incluant notamment la ligne de retard optique. Enfin, une configuration d'imagerie sera détaillée : la technique de ombroscopie classique. Cependant, une deuxieme technique a été développé pendant cette thèse consitant d'une technique de ombroscopie couplée à un interféromètre de Mach–Zehnder mais ne sera pas abordé dans ce résumé du fait de sa complexité.

Module de synchronisation

Cette partie décrit le principe de fonctionnement du module électronique de synchronisation utilisé pour les expériences pompe–sonde. Des stratégies similaires ont été rapportées dans la littérature [1]. Un schéma de la logique de synchronisation est présenté en Figure 2. Deux lasers sont impliqués : un Tangor 100, utilisé comme source pompe et un YUJA, servant de source sonde.

Le Tangor délivre jusqu'à 100 W de puissance moyenne, tandis que le YUJA opère à 10 W. Une fuite optique provenant de l'oscillateur du Tangor est injectée dans une fibre et utilisée pour amorcer le pré-amplificateur et l'amplificateur de l'impulsion dans le YUJA. À ce stade, aucune structure de rafale n'est encore générée et le YUJA est injecté en régime impulsionelle classique. Cette architecture garantit que les deux lasers partagent le même oscillateur maître et la même fréquence d'horloge, indépendamment du régime rafale sélectionné sur le Tangor. Les deux sources restent ainsi parfaitement synchronisées dans le temps. L'oscillateur maître fonctionne à 40 MHz, correspondant à un intervalle de 25 ns entre deux impulsions successives. Les impulsions du Tangor sont ensuite amplifiées et mises en forme

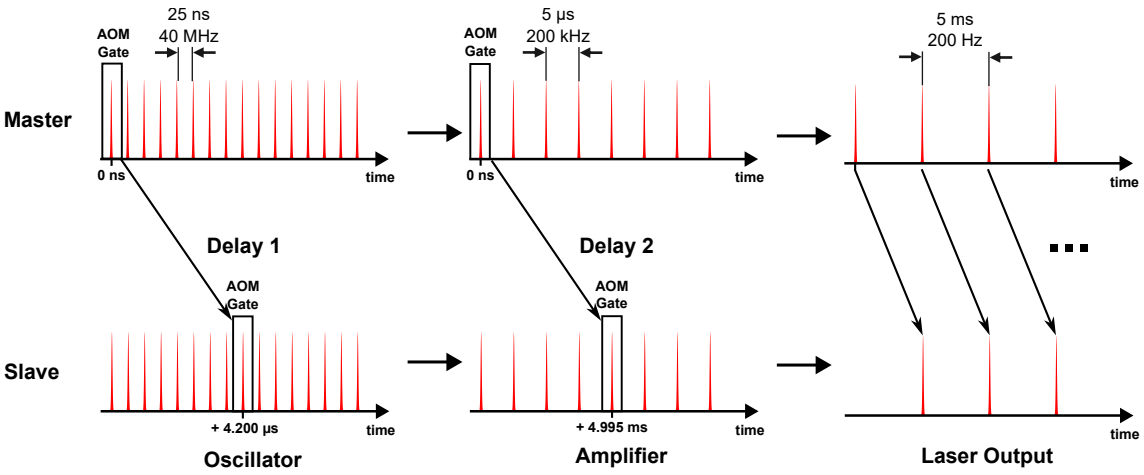

Figure 2: Representation schématique de la procédure de synchronisation.

temporellement pour produire une impulsion unique, une rafale d'impulsion MHz ou une rafale d'impulsion GHz. Le YUJA fournit quant à lui des impulsions classiques jouant le rôle de sonde. Les deux faisceaux ont une durée d'environ 500 fs, une longueur d'onde centrale de 1030 nm et une polarisation linéaire. Comme le YUJA ne peut pas être déclenché de manière externe, il fonctionne en tant que système maître tandis que le Tangor joue le rôle d'esclave. La procédure de synchronisation vise à aligner temporellement les impulsions pompe et sonde afin qu'elles se superposent avec un délai initial nul. Elle repose sur les étapes suivantes :

- **Etape 0**: les deux lasers partagent la même horloge maître.
- **Etape 1** : sélection manuelle de l'impulsion injectée dans l'amplificateur esclave via le premier sélectionneur d'impulsion (délai 1 = +4,2 µs).
- **Etape 2** : sélection manuelle de l'impulsion extraite du même amplificateur via le second sélectionneur d'impulsion (délai 2 = +4,995 ms).
- **Etape 3** : ajustement fin du délai : la N impulsion du maître déclenche la (N+1) impulsion de l'esclave. Les deux délais peuvent être ajustés par pas de 25 ns ou de 5 µs, permettant une exploration temporelle étendue.

Lignes de retard optiques

Cette section décrit la ligne de retard optique utilisée pour contrôler précisément le délai temporel (inférieur à 25 ns) entre les impulsions pompe et sonde, la synchronisation électronique étant limitée par la fréquence de 40 MHz de l'oscillateur maître. Un schéma de la ligne de retard est présenté en Figure 3.

Le faisceau sonde est injecté dans la ligne à retard et guidé par une succession de miroirs. Après les deux premières réflexions, il traverse un cube séparateur de polarisation (PBS dans le schéma). La polarisation est ajustée pour garantir une transmission totale. Le faisceau atteint ensuite une platine de translation motorisée (DDS300, Thorlabs) offrant 300 mm de course. Sur cette platine, quatre miroirs forment un trajet optique replié. Après avoir suivi ce parcours aller-retour et traversé une lame quart-d'onde deux fois, la polarisation est modifiée de sorte que le faisceau

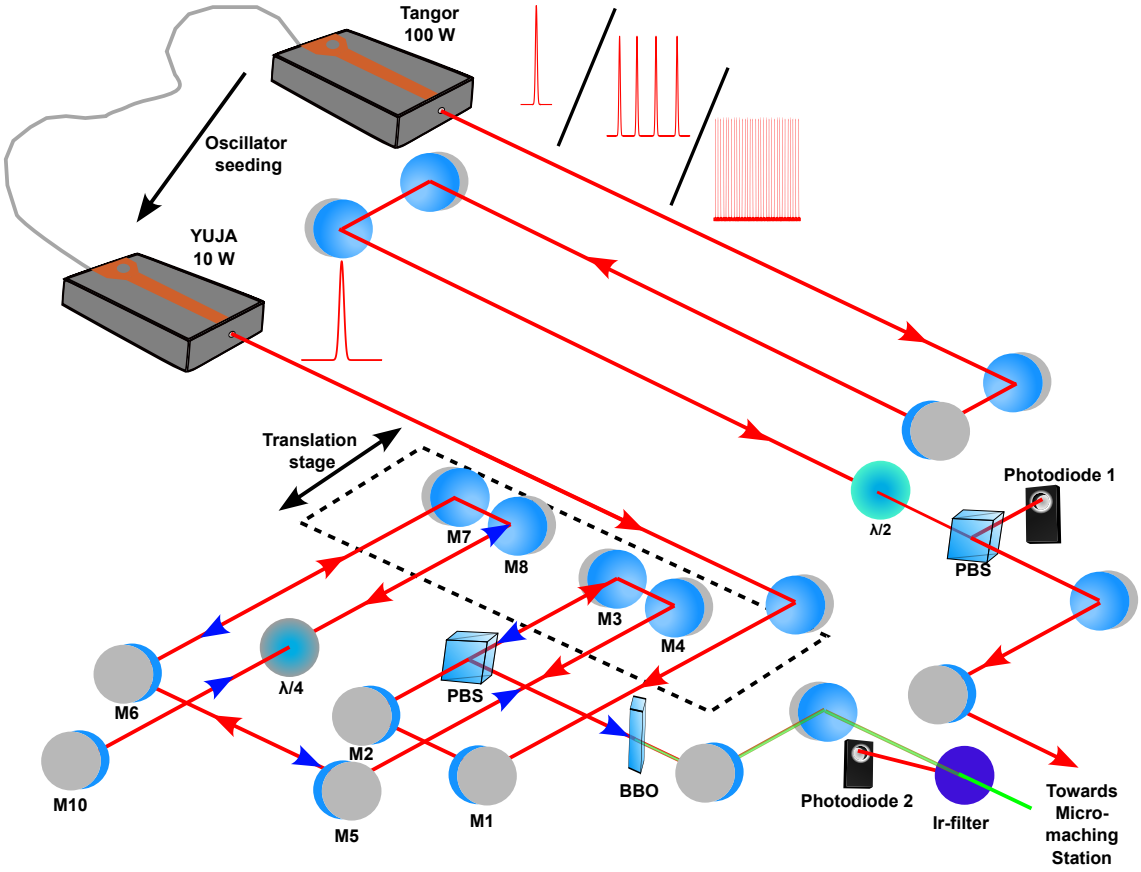

Figure 3: Representation schématique de la ligne à retard du montage experimental pompe-sonde. BBO : barium borate crystal.

soit réfléchi par le cube séparateur de polarisation, puis envoyé vers un cristal de barium borate (BBO dans le schéma) où une génération de seconde harmonique (515 nm) est produite (taux de conversion $\approx$ 30 %). Le reste du faisceau (1030 nm) est filtré et envoyé vers une photodiode rapide, permettant le suivi temporel du retard introduit. Ce système permet un réglage continu jusqu'à environ 8 ns, correspondant à un trajet optique d'environ 2,4 m. Un soin particulier est apporté à l'alignement afin d'éviter que le faisceau soit tronqué par les mirroirs ou évité une dérive spatiale après propagation. Le faisceau pompe est quant à lui injecté dans un trajet optique plus long afin de compenser le retard introduit par la fibre d'injection provenant du YUJA. Trois configurations de trajet optique (0, –8 m, –16 m) permettent de couvrir de manière continue une fenêtre temporelle de 0 à 25 ns. À l'entrée de la station, une fraction du faisceau pompe est envoyée vers une photodiode rapide afin d'assurer une référence temporelle commune avec la sonde.

ombroscopie

Cette partie décrit le dispositif classique de ombroscopie pompe–sonde utilisé pour imager les phénomènes induits par la pompe. Le schéma du montage est présenté en Figure 4.

Le faisceau pompe est guidé dans la station via une série de miroirs avant d'entrer

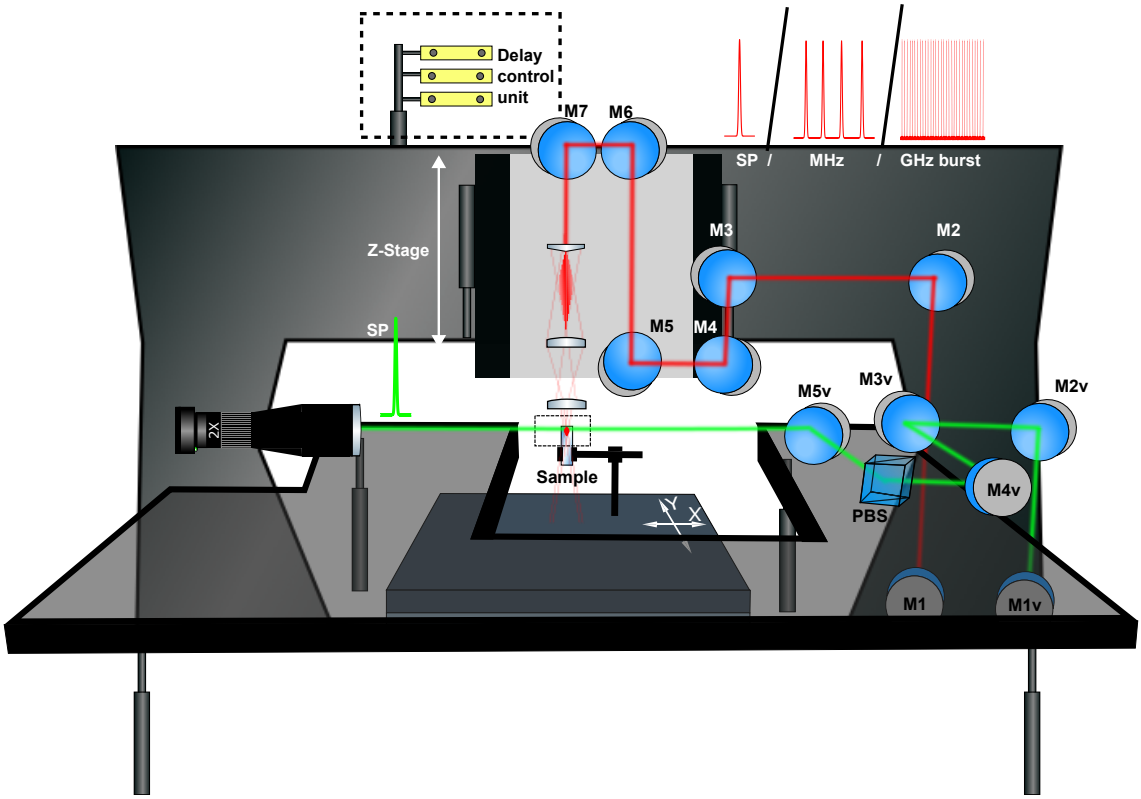

Figure 4: Representation schématique du montage experimental pompe-sonde combiné au faisceau de Bessel.

dans le module Bessel décrit précédemment. Le faisceau sonde suit un chemin optique latéral, adapté grâce à une plaque en U usinée sur mesure afin de réaliser une observation latérale. Après réflexion sur plusieurs miroirs et traversée d'un cube séparateur de polarisation utilisé ici comme miroir, la sonde se superpose au faisceau pompe et traverse la zone d'interaction. L'imagerie est assurée par un microscope à longue distance (InfiniMax, avec anneau $\times 2$) équipé de trois filtres passe-bande centrés sur 515 nm pour atténuer la lumière du plasma. Les images sont enregistrées par une caméra Basler à haute fréquence d'acquisition (220 Hz). La synchronisation de l'imagerie repose sur trois générateurs de retard (Aerodiode Tombak) contrôlant respectivement les étapes 1 et 2 de la synchronisation entre les deux sources laser (maître et esclave), puis le déclenchement de la caméra. Les images sont ensuite traitées en divisant l'image obtenue avec l'interaction issues de la pompe par l'image obtenue sans interaction de la pompe afin de ne garder que l'image issue de l'interaction.

Résultats expérimentaux

Etude pompe-sonde dans le Soda-lime

La Figure 5 présente les images d'ombroscopies obtenues dans du verre Soda-lime en régime rafale MHz (4 impulsions par rafale) en fonction du délai pompe–sonde. Chaque délai a été répété cinq fois sur le même échantillon, avec un pas latéral de

50 µm pour garantir la répétabilité. Les délais ont d'abord été explorés de 0 à 8 ns avec un pas de 1 ns via la ligne de retard mécanique. Le zéro temporel a ensuite été décalé à 25 ns à l'aide du premier pulse-picker, puis une nouvelle fenêtre de 8 ns a été balayée. Cette procédure a été répétée jusqu'à couvrir l'intervalle complet de 0 à 100 ns. Enfin, une dernière série de mesures a été réalisée en positionnant le zéro temporel à 9 ns afin d'obtenir une cartographie complète des délais. La partie supérieure de la figure illustre l'axe temporel de 0 à 100 ns, avec un schéma de la mise en forme temporelle de la rafale MHz (4 ppb), dont les sous-impulsions sont situées à 0, 25, 50 et 75 ns. Les images de d'ombroscopies sont regroupées en différentes phases : des phases d'absorption (Abs. i), caractérisées par une diminution de transmission, et des phases de relaxation (Rlx. i), marquées par une augmentation de transmission. À 0 ns, l'arrivée de la première impulsion ne montre pas de modification visible, et

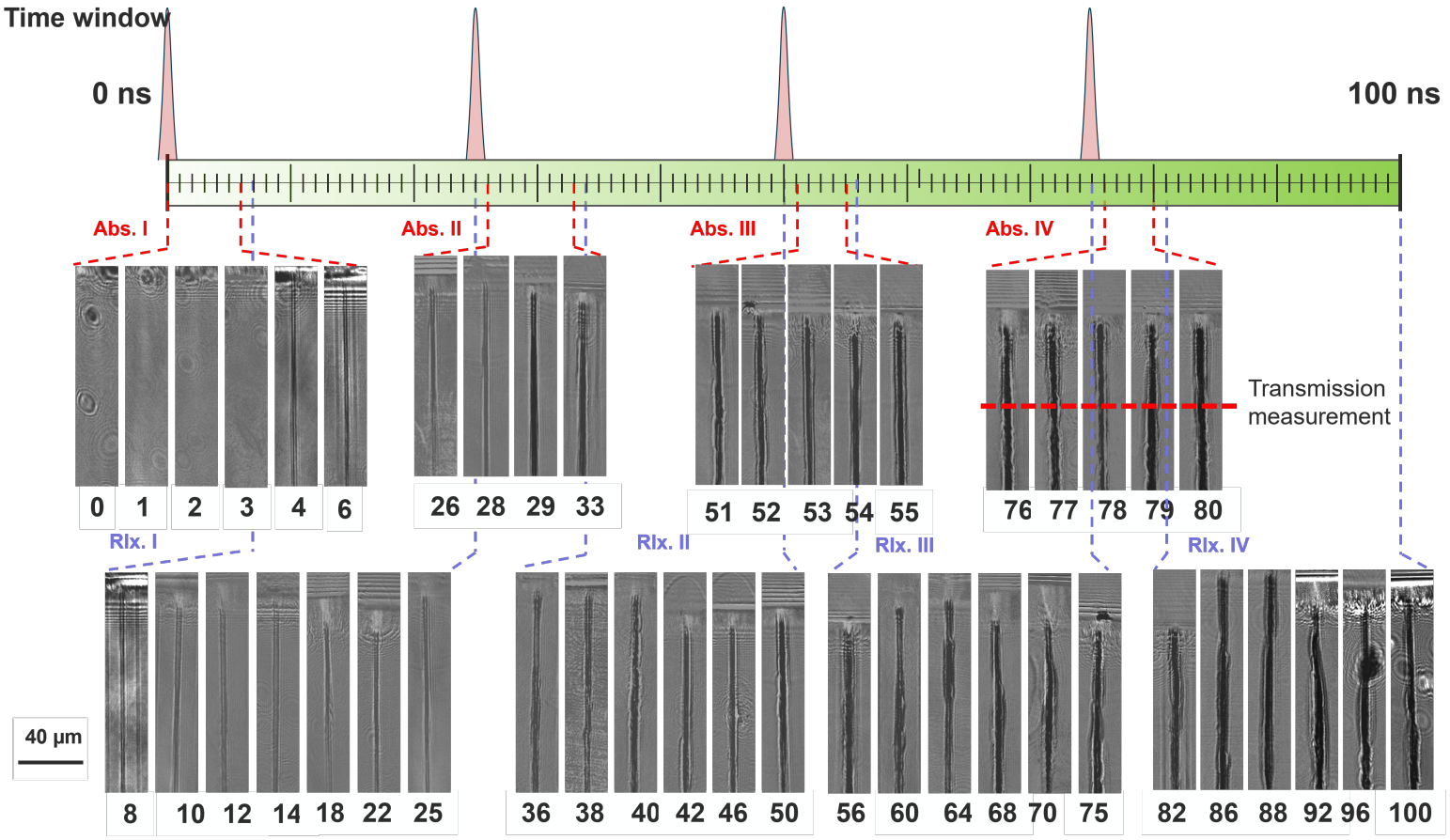

Figure 5: Imagerie pompe–sonde dans du verre Soda-lime en régime rafale MHz, avec 4 impulsions par rafale et une énergie de 270 µJ par rafale. Les délais étudiés s'étendent de 0 ns à 100 ns pour une seule rafale appliquée, avec un pas minimal d'acquisition de 1 ns

cela reste le cas de 1 à 3 ns. Avec un grossissement de 5.8× et une ouverture numérique (O.N.) estimée à 0.1 (résolution latérale ≈ 2,2 µm), il est probable que l'interaction soit présente mais en-deçà de notre seuil de détection. À 4 ns, un assombrissement de la region central apparaît, attribué à une densification de la matière induite par la première impulsion. À 6 ns, une onde de compression devient visible, marquant la transition vers la première phase de relaxation. À 8 ns, l'onde

de compression est encore observable, confirmant un fort gradient de pression dans le volume [**?**]. Son suivi donne une vitesse acoustique de 5,72 µm/ns (5,72 km/s), cohérente avec les valeurs rapportées dans la littérature scientifique pour la vitesse du sonde dans le verre Soda-lime[2, **?**], et indiquant que la pression reste inférieure au seuil inélastique d'environ 5 GPa [**?**]. La relaxation (Rlx. I) se poursuit jusqu'à 25 ns. À 25 ns, la deuxième impulsion déclenche une nouvelle phase d'absorption (Abs. II), avec un assombrissement maximal vers 29 ns. La relaxation suivante (Rlx. II), à partir de 35 ns, montre une nouvelle onde acoustique ($\approx$ 5,69 km/s), mais la transmission ne retrouve pas celle de Rlx. I. À 50 ns, la troisième impulsion initie Abs. III, caractérisée par un assombrissement plus homogène de la partie centrale, maximal à 55 ns. Une troisième relaxation (Rlx. III) commence à 56 ns, avec une onde acoustique à 5,75 km/s. La partie centrale s'éclaircit progressivement jusqu'à 75 ns. À 75 ns, la quatrième impulsion génère une structure blanche ondulée à la périphérie de la partie centrale, suggérant le début d'une fissuration en volume. La phase Abs. IV ($\approx$76–80 ns) entraîne un assombrissement supplémentaire qui sature rapidement. L'onde acoustique associée apparaît à 82 ns à 5,85 km/s. En phase Rlx. IV, la structure évolue jusqu'à 100 ns sans relaxation complète. Une image représentative de la modification finale est donnée en Figure 4.9b.

La section suivante présente les résultats obtenus par ombroscopie pompe-sonde dans du verre Soda-lime en régime rafale GHz. Les images sont acquises en fonction du délai pompe–sonde selon la même méthodologie que précédemment. Une vue d'ensemble de la configuration 50 ppb est donnée dans Figure 4.11. La partie supérieure de la figure montre l'axe temporel de 0 à 100 ns, accompagné d'une représentation schématique de la mise en forme temporelle de la rafale GHz. Bien que l'amplitude soit arbitraire, la forme temporelle reproduit fidèlement la distribution d'énergie mesurée à l'oscilloscope [**?**]. Les sous-impulsions sont situées entre 0 et 40 ns, séparées de 0,8 ns (1,25 GHz). Sous cet axe, les images de ombroscopie sont regroupées en phases d'absorption (Abs. i, transmission réduite) et de relaxation (Rlx. i, transmission accrue).

Contrairement au régime MHz, seules deux phases principales sont distinguées visuellement en régime GHz. D'après l'inspection directe, la première sous-impulsion arrive à 0 ns. Aucune modification n'est visible jusqu'à 13 ns, ce qui est cohérent avec la résolution latérale de notre système (2,2 µm avec un grossissement de 5,8× et une NA estimée à 0,1). L'interaction est possiblement en cours mais reste sous le seuil de détection. En comparant avec le régime MHz, un décalage autours de 10 ns est observé ; en effet, la première interaction détectable apparaît vers 10–14 ns. À 14 ns, un assombrissement de la region central apparaît, probablement associé à la densification induite par la 8 ou 9 sous-impulsion, en tenant compte du délai de détection. À 16 ns, une onde de compression devient visible ; son amplitude est plus faible que dans le cas MHz. À plus long délai, cette onde acquiert une forme périodique, composée de petites oscillations séparées d'environ 4,5 µm. La vitesse acoustique mesurée ($\approx$ 5,6 km/s) indique un régime élastique. Le rapport entre la période spatiale et la vitesse acoustique correspond à un intervalle temporel $\approx$ 0,8 ns, montrant que l'émission acoustique est synchronisée avec les sous-impulsions du burst GHz. En d'autres termes, le matériau génère une onde acoustique à chaque sous-impulsion, même sous pression induite par le laser très court. Entre 14 et 26 ns, la transmission décroît presque linéairement, correspondant à la séquence où les impulsions les plus énergétiques de la rafale (environ de la 17 à la 33) sont délivrées.

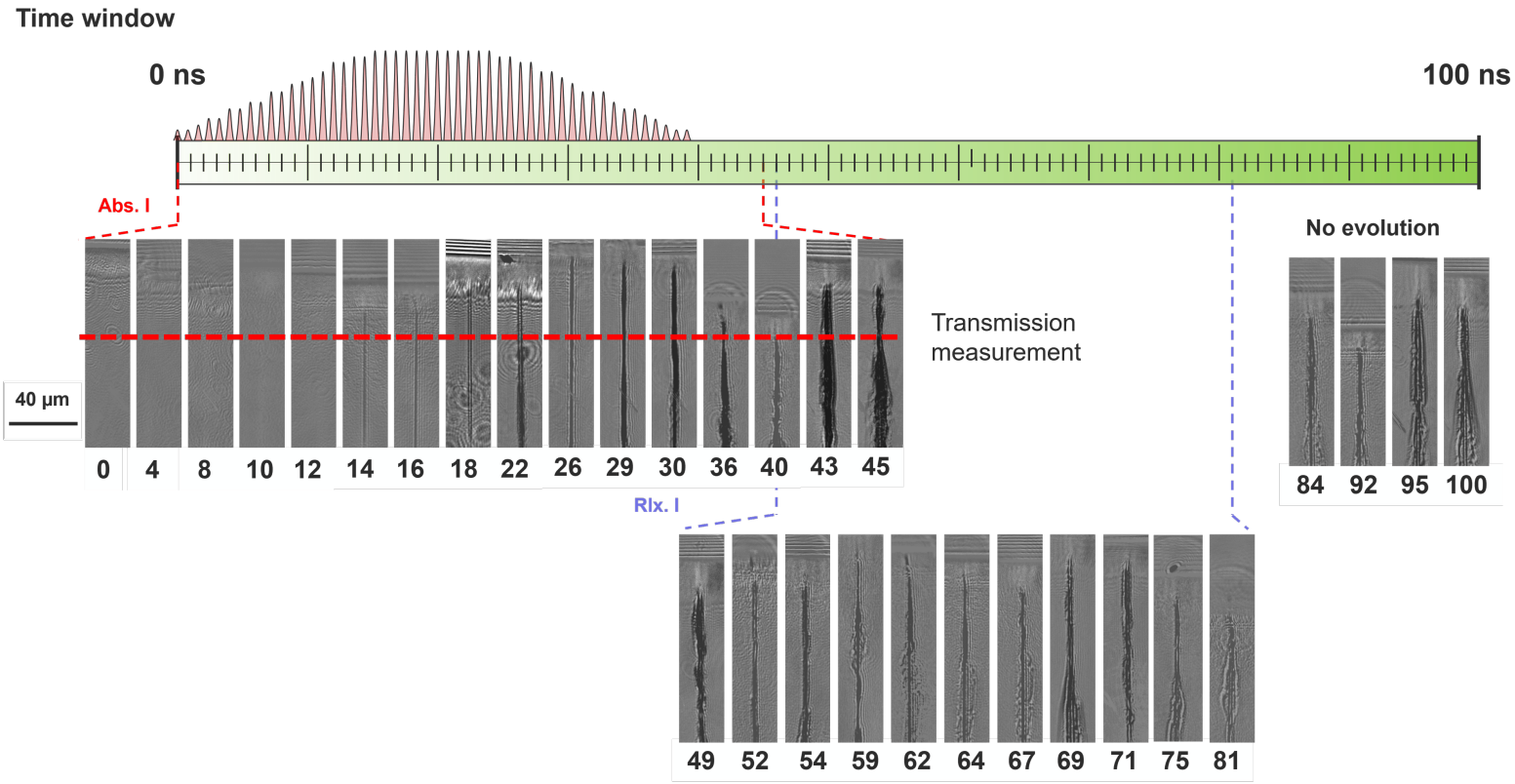

Figure 6: Imagerie pompe–sonde dans du verre Soda-lime en régime rafale GHz, avec 50 impulsions par rafale et une énergie de 270 µJ par rafale. Les délais étudiés s'étendent de 0 ns à 100 ns pour une seule rafale appliquée, avec un pas minimal d'acquisition de 1 ns

À 29 ns, une nouvelle diminution marquée de la transmission est observée. Au-delà, la transmission se stabilise à une valeur faible, tandis que le diamètre de la zone affectée continue de croître jusqu'à 44–45 ns. La rafale se termine temporellement vers 40 ns ; l'image à 45 ns marque la fin de la seule phase d'absorption observée. La phase de relaxation (Rlx. I) débute après 45 ns. À 49 ns, la region centrale commence à se contracter. À 52 ns, la région de très faible transmission disparaît, indiquant une relaxation progressive en l'absence de pression induite par laser. À 59 ns, des fissures apparaissent sur les flancs de la zone modifiée. Entre 59 et 81 ns, de nouvelles fissures se forment, avec toutefois une géométrie globale relativement stable. À noter : ces fissures sont morphologiquement différentes de celles observées en régime MHz. Après 82 ns, aucune évolution notable n'est observée d'une image à l'autre, indiquant que le processus d'interaction est achevé et que les images correspondent à la modification finale. Cette première analyse visuelle met en évidence une différence nette de dynamique de réponse du verre entre les régimes MHz et GHz, soulignant le caractère déterminant de la mise en forme temporelle de la rafale dans les mécanismes d'interaction laser-matière.

Conclusion

L'étude met clairement en évidence l'impact majeur de la mise en forme temporelle des rafales sur la dynamique d'interaction laser–matière dans le verre Soda-lime. En régime MHz, la réponse du matériau s'organise en phases successives d'absorption et de relaxation, tandis qu'en régime GHz, l'accumulation d'énergie est quasi-continue et conduit à une unique phase d'absorption prolongée suivie d'une relaxation. Ces différences soulignent l'importance du régime temporel utilisé et montrent que l'imagerie pompe–sonde constitue un outil très efficace pour analyser et optimiser l'usinage laser ultrarapide.

Acknowledgements

During these three years of PhD work (or 3.5 if we include my M2 internship beforehand), I had the chance to be surrounded by a handful of people who helped me throughout this journey, but more importantly, with whom I shared a lot of great moments.

In this section, I'll try to thank everyone.

But first, before going chronologically, I want to start with my supervisor and advisors, as they were the ones who were there all along. For three years, I had the chance to work alongside three exceptional people.

Inka, thank you for making this PhD possible and for making sure we were all well fed during those three years thanks to your Ferrero giveaways. Thank you as well for our numerous discussions and "disagreements" on various subjects, which really taught me how to better organize my ideas and express them more clearly. A special thanks as well for your German network, which helped us enjoy many free beers at the Munich conference.

John, you were the person with whom I probably spent the most time discussing both science and non-science topics. Beyond the countless anecdotes and jokes, you really helped me through your CLP hat, thanks to your enormous network and your willingness to help others across a wide range of subjects. Thank you for being the second most dedicated reader of this manuscript and for our many discussions, especially about the pump-probe part. I hope you'll manage to break free from work during lunch breaks for the Lunch Run from time to time. I'll definitely remember your endless supply of jokes and all the fun we had at conferences.

And Laura, I really enjoyed our battles over performance reviews and grade scaling. I'm sure I'll have plenty of opportunities to keep bothering you now that I'll be working full-time at ALPhANOV. Even though you were only there during my first and third years, we shared one conference together—my last one—in Strasbourg with John, and it was a really fun trip filled with great food, drinks, and countless anecdotes.

A quick thanks to Marc as well, as you stepped in during my second year on the ALPhANOV side. I really enjoyed our discussions and "disagreements" too, and they helped me grow as a person.

Another special thanks to Michael Jarwitz. Even though you joined the lab late in my PhD, you were, I think, the number one reader of this manuscript. I'm truly grateful because your late arrival meant you could read it with fresh eyes, and your help was invaluable.

Now, starting from the beginning, I'd like to thank my parents, Cyril and Christelle Guilberteau. My father played a particularly important role in my education because, as far back as I can remember, he was always trying new things and adapting to solve problems, as an engineer is supposed to do, I guess. More importantly,

he truly sparked in me this desire to fix things and find solutions where none seem obvious.

Now, thank you, Mom, for always being there, even though the task wasn't always an easy one. Your strength and resilience have taught me a lot in life, and I think I can honestly say they made me stronger. You always took care of me, even when I was far away. Thank you for all the little treats you brought every time you came to visit me during my studies. And above all, thank you for being such a supportive mother.

I'd also like to thank my two younger brothers, Paul and Enzo, for all the fights we had growing up.

Continuing with my family, I'd like to thank my aunts, Pascal and Sylvie, and my uncle Etienne, for always being there and supporting me throughout my life and education.

Thank you as well Alba, you been supporting me since almost 3 years now and can't wait to take my next step with you. (Special S/o to the Kaloo)
Now let's thank all the friends I made who helped me throughout my education. Starting with Lou, my former neighbor. It's now been 16 years since we first met, and we've really grown up and partied together. I hope we'll keep doing so for many years to come.

Next comes Florent, whom I've known for about 13 years, if I'm not mistaken. Back then, you really were a model of excellence and helped me a lot during middle school and high school. Thanks for the occasional bike rides and all the parties we shared over the years.

Now let's move on to high school and thank Valentin, aka Geule d'Or, for growing up alongside me. We've known each other for almost 10 years now. Just like Lou and Florent, all the parties we shared were memorable, and I can't wait to see where life takes us in the future.
Overall, throughout those years, you were also my partners for countless hours spent playing video games. I'm skipping many other gaming partners here, but you were definitely the highlights.
Time to thank my university buddies, starting with my bachelor's classmates. Thanks to Léa, Amélie, Arno, and Baptiste for all the memories we've made together, and for the many more to come. A special thanks to Baptiste for the numerous weekend runs over the last three years.

Moving on to my master's degree, I'd like to thank Gary and Lucas, who made those two years truly enjoyable in so many ways.

Almost at the end, I'll try not to forget all the people who accompanied me throughout these three years of PhD. I'll try to do it in chronological order.

First, thanks to Lou (during my M2 internship that eventually led to this PhD). We had a great time together and collected some fun memories.

Then comes my mentor, the dude who taught me everything he knew about the experimental room. I'm obviously talking about Pierre Balage. Thanks as well for all the squash games, the countless Decathlon training programs we've followed over the years, and all the fun we had in the experimental room.

Thank you, Manon Lafargue, as well. You were my desk neighbor throughout those three years and played a crucial role in the success of the pump-probe experiment thanks to your fiber-splicing skills. Thanks also for all the squash games and the occasional runs together.

I'd also like to thank Maxime Quirke, the medicine guy, who gave me back my passion for cycling and inspired me to start running through his own example. You were a quick learner, and it was always a pleasure discussing with you.

Moving on to the second year of this PhD, I'd like to thank Akhil Kuriakose for all the insane stories and adventures we went through together (the great quest of the Holy Gratings being one of them).

Next comes another legend of this PhD, if I may say so: Guilhem Vidor, who joined us for a six-month engineering internship. The fun and randomness were limitless, to the point where we ended up climbing the Tourmalet by bike simply because of a bold statement and a bit of pride. That was also the beginning of the biking era, followed by far too much money invested in bikes and equipment for both of us. I can't wait to organize another great cycling adventure once you're back from Japan.

Continuing on the biking path, I'd like to thank my apprentice—the one I taught almost everything I know about the experimental room, along with all the knowledge I gained during these three years: Alexandre Urruty (aka Ice Tigre), who joined the lab as both an M1 and M2 internship student. You also fell into the cycling trap alongside Guilhem and me. You missed the very first edition of the great Tourmalet climb, but we made up for it this year by warming up on Hautacam before climbing the Tourmalet the next day and watching the Tour de France pass from the top. Before that, we also went to the Basque Country to take on Jaizkibel and Artzamendi... A memory that will be anchored deep in the pain section of my brain thanks to those endless 18% gradients. Thanks as well for joining the Lunch Run and for sharing the Semi-Marathon de Bordeaux adventure with me. I wish you all the best for the PhD you're about to start, and I can't wait for our next 10 km training block and many more cycling adventures in the future.

I'd also like to thank Théo Fillez, M1 and M2 internship student (aka the Sorcerer's Apprentice and McWaltigre). It was a pleasure helping you with the polarimeter project, and I hope you'll join the bike training next year and be there for the next ascent of the Tourmalet. I'm also wishing you all the best for the PhD to come!

A special mention goes to Gabriel Perruchon-Bougès, who helped me tremendously during the pump-probe campaign by carrying out a large part of the image acquisition. Thank you so much—I would probably have gone crazy doing it alone. It was also a pleasure playing Clash Royale in between experiments for a bit of mental stimulation.

Lastly, I'd like to thank all the interns and PhD students from my third year. Thanks to Maxime Fenech—I wish you all the best for your PhD and your everlasting love for beam expanders and Airy beams. I'd also like to thank Doriane Mazuranok, M1 internship student, one of the most random people I've ever met. We had a lot of fun both in the experimental room and during lunch breaks. Finally, thanks to Pierrick Luez, also an M1 internship student. I guess you're the second most random person I've ever met. Thank you for your beer-tasting expertise. I'm expecting both of you at next year's Lunch Run, which you've both consistently managed to dodge so far.

Foreword

This doctoral work was financially supported by ALPhANOV and the French National Association of Technological Research (ANRT). The research was carried out within the CELIA laboratory and at ALPhANOV, in close collaboration with the industrial partner Amplitude. Since August 2023, this collaboration has been formalized within the framework of a tripartite joint laboratory (LabCom) named TRICORN, bringing together CELIA, Amplitude, and ALPhANOV.

The CELIA laboratory is a joint research unit located in Talence, under the joint supervision of the University of Bordeaux, the French Alternative Energies and Atomic Energy Commission (CEA), and the National Centre for Scientific Research (CNRS). Its scientific activities cover a wide range of topics, including: (i) high-repetition-rate and high-intensity femtosecond lasers and intense laser optics; (ii) ultra-intense laser fields, ionic collisions, and plasma-based X-ray sources; (iii) extreme ultraviolet (XUV) harmonics and their applications to ultrafast and attosecond-scale processes; (iv) laser–plasma interactions, hot and dense plasma physics, inertial confinement fusion, and laboratory astrophysics; and (v) laser–material interactions, including direct femtosecond laser writing, multiscale laser processing in the nanosecond, picosecond, and femtosecond regimes, as well as laser and plasma spectroscopy.

Contents

French summary . . . 2
Acknowledgements . . . 13
Foreword . . . 16
Introduction . . . 26

1 Theoretical background **29**
1.1 Metals . . . 29
1.1.1 Free electron gas . . . 30
1.1.2 Two-temperature model . . . 30
1.1.3 Thermal properties . . . 31
1.2 Dielectrics . . . 33
1.2.1 Band structure . . . 33
1.2.2 Ultrafast Laser & Matter Interaction Regimes . . . 34
1.2.2.1 Multiphoton ionization . . . 35
1.2.2.2 Avalanche ionization . . . 35
1.2.2.3 Carrier relaxation . . . 36
1.3 Optical properties under extreme conditions . . . 36
1.3.1 Drude model . . . 36
1.3.2 Critical plasma density . . . 38
1.3.3 Refractive index modification . . . 38
1.3.4 Relation between refractive index variation and pressure (Lorentz–Lorenz) . . . 39
1.4 Temporal and spatial control of energy deposition . . . 40
1.4.1 Temporal beam shaping . . . 41
1.4.1.1 MHz-burst . . . 41
1.4.1.2 GHz-burst . . . 42
1.4.2 Spatial beam shaping . . . 42
1.4.2.1 Gaussian beam . . . 43
1.4.2.2 Quasi-Bessel-Gauss beams . . . 43
1.4.2.3 Vortex phase plate . . . 44
1.5 Applications and surface functionalization . . . 45
1.5.1 Thesis context: Burst approaches for ultrafast laser-based material processing . . . 46

2 Materials & methods **48**
2.1 Laser system . . . 48
2.2 Micromachining workstation . . . 50
2.2.1 Automated laser power control . . . 50
2.2.2 Set-up with Gaussian beam . . . 52

2.2.3 Set-up with Quasi Bessel-Gauss beam . . . 53
2.2.4 Pump-probe shadowgraphy . . . 55
2.2.4.1 Synchronization module . . . 55
2.2.4.2 Delay lines . . . 56
2.2.4.3 Shadowgraphy . . . 58
2.2.4.4 Data processing for shadowgraphy . . . 59
2.2.4.5 Mach-Zehnder interferometer . . . 61
2.2.4.6 Data Processing for Mach-Zehnder Interferometry . . . 62
2.3 Measuring equipments, sample preparation & methods . . . 64
2.3.1 Laser beam characterization tools . . . 64
2.3.2 Etching set-up . . . 65
2.3.3 Sample characterization . . . 66
2.3.4 Methods . . . 67
Surface roughness and ISO standards: . . . 67
Overlap Computation: . . . 67
2.4 Materials of interest . . . 68
2.4.1 Metals . . . 68
2.4.2 Dielectrics . . . 69

3 Surface processing of metallic materials 70
3.1 Investigation of different beam shapes . . . 70
3.1.1 Vortex beam . . . 73
3.1.1.1 Single burst study . . . 73
3.1.1.2 Influence of overlap . . . 76
Spot-to-spot overlap . . . 76
Line-to-line overlap . . . 77
3.1.2 Gaussian beam . . . 79
3.1.2.1 Single-burst study . . . 79
3.1.2.2 Impact of overlap . . . 82
Spot-to-spot overlap . . . 82
Line-to-line overlap . . . 82
3.2 Investigation of the potential of long GHz-burst . . . 84
3.2.1 Combined laser milling-polishing approach . . . 84
3.2.1.1 Laser milling step . . . 85
3.2.1.2 Laser polishing step . . . 86
3.2.2 Influence of the spot-to-spot overlap . . . 88
3.2.3 Influence of the number of passes . . . 90
3.2.4 Scalability . . . 91

4 Dielectric materials functionalization 95
4.1 Bessel beam intensity profile: influencing parameters . . . 95
4.2 Bessel beam induced in-bulk modifications . . . 98
4.2.1 Single Pulse / MHz-burst / GHz-burst . . . 99
4.2.2 Etching study . . . 102
4.2.3 Towards direct TGV-drilling with single GHz-burst . . . 105
4.3 Pump probe shadowgraphy . . . 106
4.3.1 4-ppb MHz-burst . . . 106
4.3.2 50-ppb GHz-burst . . . 112
. . . 114

4.3.3 Plasma and critical density discussion 116
4.4 Pump-probe shadowgraphy combined with Mach-Zehnder interferometry 119
4.4.1 MHz-burst with 4 pbb 119
4.4.1.1 In-volume experiment 119
4.4.1.2 Plume expansion 122
4.4.2 GHz-burst with 50 pbb 124
4.4.2.1 In-volume experiment 124
4.4.2.2 Plume expansion 126

Conclusion & Perspectives **129**

List of publications **134**

Bibliography **147**

A Multi-GHz burst irradiation in AF-32 glass **149**

B Exploration of a 16 GHz-burst frequency **151**

C Vortex beam MHz-burst **154**

D Melted layer generation on Ta6V **157**

E Reshaping with surface melting **160**

List of Figures

1 Representation schématique du set-up expérimental utilisé pour le faisceau de Bessel. 4
2 Representation schématique de la procédure de synchronisation. . . . 6
3 Representation schématique de la ligne à retard du montage experimental pompe-sonde. BBO : barium borate crystal. 7
4 Representation schématique du montage experimental pompe-sonde combiné au faisceau de Bessel. 8
5 Imagerie pompe–sonde dans du verre Soda-lime en régime rafale MHz, avec 4 impulsions par rafale et une énergie de 270 µJ par rafale. Les délais étudiés s'étendent de 0 ns à 100 ns pour une seule rafale appliquée, avec un pas minimal d'acquisition de 1 ns 9
6 Imagerie pompe–sonde dans du verre Soda-lime en régime rafale GHz, avec 50 impulsions par rafale et une énergie de 270 µJ par rafale. Les délais étudiés s'étendent de 0 ns à 100 ns pour une seule rafale appliquée, avec un pas minimal d'acquisition de 1 ns 11

1.1 Schematic representation of the band structure in conductor, semiconductor and insulator. 30
1.2 Evolution of the characteristics length as function of the Thermal diffusion time for various alloys. (Values used from Section 2.4.1. . . . 32
1.3 Schematic representation of the photoionization mechanisms. 34
1.4 Schematic representation of the carrier excitation mechanisms. 35
1.5 Intensity profile of the central core of a quasi-Bessel-Gauss beam along the propagation axis Z. 44
1.6 Intensity profile of the central core along the propagation axis Z with the effect of the rounding tip. 45

2.1 Schematic representation of the temporal structure and energy distribution of the three laser operating regimes available with the laser system. 49
2.2 Schematic representation of the experimental setup used for automated power control. 51
2.3 Evolution of the transmitted power as a function of the half-wave plate angle. 51
2.4 Schematic representation of the experimental setup used with a Gaussian beam. B.S: Beam Splitter, B.E: Beam Expander. 52
2.5 Schematic representation of the experimental setup used with a quasi Bessel–Gauss beam. 54
2.6 Schematic representation of the synchronization procedure. 56

2.7 Schematic representation of the pump-probe delay line setup. BBO : barium borate crystal. 57
2.8 Schematic view of the setup for shadowgraphy experiments. 59
2.9 Workflow of the data processing applied to pump–probe shadowgraphy measurements. 60
2.10 Schematic view of the experimental setup for shadowgraphy combined with a Mach-Zehnder interferometer. 61
2.11 Workflow of the data processing applied to pump–probe shadowgraphy measurements coupled with the Mach-Zehnder interferometer. . . 62
2.12 Example of images acquired with the Mach-Zehnder interferometer. . 62
2.13 Example of filtering applied to the FFT maps. 63
2.14 Example of colormaps obtained with the MZI workflow from the images in Figure 2.12. 64
2.15 Example of electron density map. Colorbar units: $10^{19}\,\mathrm{m}^{-3}$. 65
2.16 Schematic representation of the experimental setup used for chemical etching. 66
2.17 Schematic of laser scanning tracks, illustrating the spot-to-spot (S-2-S) and line-to-line (L-2-L) distances. where Φ is the beam spot size. 68

3.1 Schematic view of the experimental setup used for polishing experiments. B.S : Beam Splitter, B.E : Beam Expander, Cam : Camera, Inf.Max : Infini Max, Obj: Objectiv, M : Mirror, S: Sample. 71
3.2 SEM top view of pristine 316L stainless steel sample surface. 72
3.3 Optical microscope images of vortex beam surface modifications with increasing number of pulses-per-burst, as a function of energy and spot size. (a) 50 ppb, (b) 100 ppb, (c) 200 ppb, (d) 400 ppb, (e) 800 ppb. 75
3.4 SEM images of vortex beam surface modification with increasing number of pulse-per- burst for 92 μm spot size and 340 µJ burst energy. (a) 50 ppb,(b) 100 ppb,(c) 200 ppb,(d) 400 ppb with a magnification of 3 kx. 77
3.5 Optical microscope images of 316L samples showing the influence of spot-to-spot overlap using a vortex beam on the surface quality for 800 ppb GHz-burst for three burst energies of 170, 238, and 340 µJ, respectively. 78
3.6 Optical microscope images of 316L samples showing the line-to-line influence using a vortex beam on the surface quality for 800 ppb GHz-burst with three burst energies of 170, 238, and 340 µJ, respectively. . 79
3.7 Optical microscope images of gaussian beam surface modification with increasing number of pulse-per-burst values as a function of energy and spot size. 81
3.8 Optical microscope images of 316L samples showing the spot-to-spot influence on the surface quality for 800 ppb GHz-burst for four burst energies of 85, 170, 238, and 340 µJ, respectively. 83
3.9 Optical microscope images of 316L samples showing the line-to-line influence on the surface quality for 800 ppb GHz-burst for four burst energies of 85, 221, 255, and 389 µJ, respectively. 84

3.10 **a**) Left axis: Evolution of the engraved depth obtained in 316L with short (purple triangles) and long (green triangles) GHz-bursts as a function of the cumulative dose. Right axis: Evolution of the surface roughness R_a ISO 21920 for short (red squares) and long (blue squares) GHz-bursts as a function of the dose. Errors are estimated to 5 μm for depth measurements. (**b**) SEM top view of surface obtained in 316L after laser irradiation with 50 ppb for a dose of 36 $J \cdot mm^{-2}$, and at a magnification of x136. (**c**) SEM top view of surface obtained in 316L after laser irradiation with 50 ppb for a dose of 36 $J \cdot mm^{-2}$, and at a magnification of x5,000. 85
3.11 (**a**) Evolution of the surface roughness R_a ISO 21920 and S_a ISO 25178 as a function of the number of passes on 316 L for 800 ppb GHz-bursts at 400 kHz, 46.8 µJ per burst, S-2-S = 5 μm, L-2-L = 1.2 μm. (**b**) SEM top view of the 316L surface obtained after laser irradiation with 800 ppb, and at a magnification of x5,000. 87
3.12 Surface roughness R_a variation as a function of the the S-2-S overlap for 316 L samples under GHz-burst irradiation with 800 ppb and 2.3 µJ per burst with, **(a)** L-2-L = 75 %; **(b)** L-2-L = 97 %. 89
3.13 Surface roughness R_a evolution as a function of the number of passes for 316L steel samples under GHz-burst irradiation with 800 ppb and S-2-S = 5 μm for: (a) L-2-L = 1.2 μm, 400 kHz, 46.8 µJ per burst (the red dashed line indicates the initial surface roughness) (b) L-2-L = 12 μm, 2.3 µJ per burst; and (c) L-2-L = 1.2 μm, 2.3 µJ per burst. 90
3.14 Evolution of surface roughness R_a as a function of the dose in 316L stainless steel, with S-2-S = 5 μm, 800 ppb GHz-burst (**a**) for L-2-L = 97 % (1,2 μm), and (**b**) for L-2-L = 75 % (12 μm). 92
3.15 SEM top view of 316L sample at iso-dose with S-2-S = 16 μm, L-2-L = 12 μm, 800 ppb GHz-burst. 93

4.1 Top row: 3D intensity profile. Middle row: top view of the 3D intensity profile. Bottom row: 2D axial intensity profile along the Bessel beam propagation length. (**a**)–(**d**) Z-intensity profiles of a Bessel beam measured for beam entrance diameters of 1.5, 3, 6, and 9 mm, respectively. Z-axis is in mm and ranges from [0-8],[0-35], [0-300], [0-200], respectively. 96
4.2 Bessel–Gauss Z-intensity profiles measured for a beam entrance diameter of 9 mm with divergences of (**a**) 1 mrad, (**b**) 6 mrad, and (**c**) 14 mrad. 98
4.3 Optical microscope side views of modifications obtained in fused silica after laser irradiation with a Bessel beam with single pulse or burst, respectively, at an energy ranging from 15 to 255 µJ. (**a**) Single-pulse mode, (**b**) 4 ppb MHz-burst, and (**c**) 50 ppb GHz-burst. The pitch between two modifications of identical energy is 50 µm. The white line at the top of each image indicates the initial surface. Insets on the right show magnified views of the highest-energy modification. . . 100

4.4 Evolution of the modification depth obtained in fused silica with a single pulse/burst as a function of energy in the range from 15 to 128 µJ, in single-pulse mode and 15 to 255 µJ for 4 ppb MHz-burst, and 50 ppb GHz-burst. For each energy, at least 4 modifications were measured. 101
4.5 Optical microscope images of the modifications obtained in fused silica after laser irradiation with one single pulse or burst, respectively, with an energy ranging from 15 to 255 µJ, in (**a**) Single pulse mode, (**b**) 4 ppb MHz-burst, and (**c**) 50 ppb GHz-burst and after 1 h of KOH etching. 102
4.6 (**a**) Evolution of the modification depth obtained in fused silica after a single pulse (before chemical etching) and of the hole depth after chemical etching as a function of the pulse energy, ranging from 15 to 140 µJ, for different etching times. (**b**) Evolution of the modification depth obtained in fused silica after a single MHz-burst (before chemical etching) and of the hole depth after chemical etching as a function of the burst energy, ranging from 15 to 140 µJ, for different etching times. 104
4.7 Void microstructure obtained in fused silica with one single GHz-burst (50 ppb) of 255 µJ without chemical etching. Top surface is on the left. 106
4.8 Pump-probe imaging in Soda-Lime glass in MHz-burst regime with 4 pulses per burst and burst energy of 270 µJ with delays ranging from 0 ns to 100 ns for a single burst applied. Minimal delay investigated between measurements was 1 ns. 107
4.9 (**a**) Measurement of the first acoustic wave velocity inside the bulk of Soda-Lime glass. (**b**) Final modification obtained with MHz-burst in Soda-Lime glass. (**c**) View of compression/acoustic wave induced by the laser-matter interaction at 58 ns in MHz-burst. 109
4.10 Pump-probe absorbance measurement in Soda-Lime glass in MHz-burst with 4 pulses per burst and bursts energy of 270 µJ with delays ranging from 0 ns to 100 ns for a single burst applied. 110
4.11 Pump-probe imaging in Soda-Lime glass in GHz-burst regime with 50 pulses per burst and burst energy of 270 µJ with delays ranging from 0 ns to 100 ns for a single burst applied. Minimal delay investigated between measurements was 1 ns. 113
4.12 Pump-probe absorbance measurement in Soda-Lime glass in GHz-burst with 50 pulses per burst and burst energy of 270 µJ with delays ranging from 0 ns to 100 ns for a single burst applied. 115
4.13 Evolution of electron number density profile inside a femtosecond laser-irradiated glass by a Bessel-beam with MHz-burst of 4 ppb and burst energy of 270 µJ. 117
4.14 Evolution of electron number density profile inside a femtosecond laser-irradiated glass by a Bessel-beam with GHz-burst of 50 ppb and burst energy of 270 µJ. 118

4.15 Pump-probe imaging in Soda-Lime glass combined with Mach-Zehnder interferometry in MHz-burst regime with 4 pulses per burst and burst energy of 270 µJ with delays ranging from 0 ns to 100 ns for a single burst applied. Minimal delay investigated between measurement was 1 ns. First row of images is phase shift measurement in rad and second row is reconstructed free electron density in $10^{19} cm^{-3}$. 120
4.16 Free electron density calculated over time from pump-probe interferometry in Soda-Lime glass in MHz-burst with 4 pulses per burst and burst energy of 270 µJ with delays ranging from 0 ns to 100 ns for a single burst applied. 122
4.17 Pump-probe imaging in Soda-Lime glass combined with Mach-Zehnder interferometry in MHz-burst regime with 4 pulses per burst and burst energy of 270 µJ with delays ranging from 50 ns to 100 000 ns for a single burst applied. 123
4.18 Pump-probe imaging in Soda-Lime glass combined with Mach-Zehnder interferometry in GHz-burst regime with 50 pulses per burst and burst energy of 270 µJ with delays ranging from 0 ns to 100 ns for a single burst applied. Minimal delay investigated between measurement was 1 ns. 125
4.19 Free electron density calculated over time from pump-probe interferometry measurement in Soda-Lime glass in GHz-burst mode with 50 pulses per burst and burst energy of 270 µJ with delays ranging from 0 ns to 100 ns for a single burst applied. 126
4.20 Pump-probe imaging in Soda-Lime glass combined with Mach-Zehnder interferometry in GHz-burst regime with 50 pulses per burst and burst energy of 270 µJ with delays ranging from 50 ns to 10 000 ns for a single burst applied. 127

A.1 Optical microscope side-view images of laser-induced modifications in AF-32 glass obtained for different numbers of applied bursts at a burst energy of 255 μJ. 149

B.1 Experimental setup used with the 16 GHz OURAL laser system. . . . 151
B.2 Binocular image of the hole drilling experiment on 316L with 16 GHz bursts (a) and in CW regime (b) for drilling times of 10 µs up to 1 s generated with the OURAL laser system. 152
B.3 Binocular microscope image of thermal wave-like surface structures generated using the 16 GHz OURAL laser system. The laser scanning direction is perpendicular to the observed surface modulation. 153

C.1 Optical microscope images of vortex beam surface modifications with increasing number of pulses per burst, as a function of energy and spot size in MHz-burst mode with (a) 4 ppb,(b) 8 ppb,(c) 16 ppb,(d) 32 ppb. 155

D.1 Optical microscope images of spot-to-spot influence on surface quality for a gaussian beam, 800 ppb GHz-burst, for 4 burst energies, 85, 170, 238 and 340 μJ and a spot diameter of 91 μm. 158

D.2 Optical microscope images of spot-to-spot influence on surface quality for 800 ppb GHz burst with Vortex beam, for 4 burst energies, 85, 170, 238 and 340 μJ, and a spot diameter of 71 μm. 159
D.3 Optical microscope images of line-to-line influence on surface quality for 800-ppb GHz-burst with vortex beam shaping, for 3 burst energies, 85, 170, and 238 μJ, and a spot diameter of 71 μm. 159

E.1 Optical microscope images of reshaping through surface melting on AL7075, illustrated through a Shrek-like figure. 250 µJ, 2000 $m \cdot s^{-1}$, 10 000 passes, hatch of 12 µm. 160

Introduction

The development of ultrafast laser sources has profoundly reshaped laser–matter interaction studies and enabled major advances in laser-based material processing [3, 4]. Femtosecond laser pulses, characterized by their extremely short duration giving high peak intensity, allow for highly localized energy deposition. This high peak intensity, is in dielectrics, often mediated by non-linear absorption mechanisms [5]. These characteristics make ultrafast lasers particularly suited for high-precision micromachining, where strict control over affected volumes and minimal collateral damage are required. At the same time, the ultrashort interaction times inherent to femtosecond laser irradiation provide direct access to transient physical processes occurring on timescales comparable to electron excitation, plasma formation, and early lattice dynamics [6, 7, 8]. A key advantage of ultrafast laser processing lies in its fundamentally different thermal behavior compared to longer-pulse regimes. Energy deposition occurs much faster than thermal diffusion, which strongly limits heat propagation into the surrounding material [9, 10]. As a result, femtosecond laser irradiation typically produces sharply defined features with reduced molten material, limited resolidification artifacts, and a mini-mized heat-affected zone. These properties have driven the widespread adoption of ultrafast lasers for precision processing of both metallic and dielectric materials, especially in applications where surface quality, dimensional accuracy, and structural integrity are critical [11, 12, 13]. Over the past decade, significant progress in ultrafast laser technology—including increases in average power, repetition rate, and long-term operational stability—has considerably broadened the range of accessible applications [14]. Despite these developments, ultrafast lasers are not systematically the preferred option for industrial manufacturing, mainly due to limitations in throughput. Due to their high energy i.e. high fluence, it often leads to side-effects while high average power i.e. high repetition rate means heat accumulation. So in conventional single-pulse or low-repetition-rate operating regimes, ultrafast laser sources often require slows processes and thus, do not always fully exploit their available average power, leading to limited processing efficiency. Moreover, the high level of spatial accuracy achievable with femtosecond lasers is often accompanied by increased processing times, which can restrict throughput. Together with the relatively high cost of ultrafast laser systems, these factors have motivated the development of strategies aimed at improving efficiency while maintaining the advantages of ultrafast laser–matter interaction. Rather than relying on increased pulse energy or average power, the most promising strategies to address this challenge focus on engineering how laser energy is distributed in space and time. Spatial beam engineering techniques, such as beam multiplexing, aim to increase throughput through parallelization by dividing a single high-power beam into multiple sub-beams [15]. In parallel, beam shaping approaches modify the spatial intensity distribution of the

laser in order to tailor energy deposition to the targeted physical mechanism or material geometry, often improving precision, stability, and process reproducibility [16, 17, 18]. Temporal beam shaping provides a complementary and effective pathway toward improving energy coupling efficiency. By restructuring the laser emission into bursts composed of closely spaced pulses, the cooperative effect between successive pulses can be exploited. In the MHz repetition-rate regime, pulses may interact with a material that remains partially heated or transiently modified by preceding pulses, thereby reducing energy losses due to thermal diffusion [19, 20]. Extending this approach toward higher repetition rates, up to hundreds of MHz or even the GHz regime, further intensifies these cooperative effects and may lead to highly efficient material modification with a limited macroscopic thermal footprint. [21, 22, 23]. The simultaneous control of spatial and temporal energy delivery offers additional degrees of freedom for tailoring laser–matter interactions. By combining adapted beam geometries with high-repetition-rate burst structures, it becomes possible to access interaction regimes that differ fundamentally from conventional ultrafast processing, both in terms of plasma formation and subsequent material response. However, the practical benefits of these regimes remain strongly dependent on material properties, laser parameters, and processing configuration, and are not yet fully understood. Among spatial beam-shaping techniques, Bessel beams occupy a unique position due to their characteristic non-diffraction-limited propagation and elongated focal region [24]. Their intensity distribution enables energy deposition over extended depths and micron-scale spot, making them particularly suitable for high-aspect-ratio structuring and bulk modification of transparent materials. Previous studies have demonstrated that a single ultrafast laser pulse shaped as a Bessel beam can induce deep, well-confined nano-scale modifications in glass, highlighting the extreme localization of energy achievable with this approach [10]. Beyond single-pulse processing, repeated irradiation with short MHz-burst with Bessel enables the formation of continuous modified volumes that can be exploited for cutting and separation of transparent materials through stress-induced fracture mechanisms [25]. For advanced applications such as nano-structuring [26] or precision drilling [27, 28], tightly focused Bessel beams are often required. In practice, achievable focusing conditions are constrained by optical damage thresholds and geometrical limitations. Modifying the beam focusing not only affects the diameter of the central core but also alters the laser–plasma interaction, influencing energy deposition efficiency and the resulting material response. While spatial beam shaping governs where energy is delivered, temporal pulse structuring determines how the material responds to that energy. At low repetition rates, each ultrafast pulse interacts with a material that has largely returned to its initial thermodynamic state, resulting in highly reproducible but comparatively inefficient processing. In contrast, burst-mode operation allows successive pulses to interact with an already excited or partially heated material, improving energy coupling and reducing dissipative losses [23]. For most materials, minimizing thermal dissipation between pulses requires repetition rates on the order of several hundred MHz, naturally leading to GHz-burst regimes. Early reports highlighted substantial gains in ablation efficiency and, in some cases, a surprisingly limited heat-affected zone when operating in the GHz-burst regime [17]. The central objective of this thesis is to improve the efficiency, controllability, and physical understanding of ultrafast laser processing through the combined use of spatial and temporal beam shaping, with particular emphasis on

Bessel beams and MHz- and GHz-burst regimes. The work addresses both metallic and dielectric materials, with the aim of linking fundamental interaction mechanisms to practical surface functionalization and micro-structuring strategies. By combining systematic processing studies with time-resolved optical diagnostics, this manuscript seeks to clarify the role of burst-mode irradiation and tailored beam geometries in ultrafast laser–matter interactions, and to establish robust processing frameworks compatible with both high precision and improved throughput. To provide the necessary foundation, the manuscript first introduces the theoretical background and current state of the art relevant to ultrafast laser–matter interaction. The physical mechanisms governing femtosecond laser processing are reviewed, with particular emphasis on burst-mode irradiation and surface functionalization concepts. This discussion establishes a coherent scientific framework for interpreting the experimental results presented throughout the thesis. The experimental approaches developed during this PhD are then described, including the femtosecond laser systems, micromachining configurations, and diagnostic tools specifically designed for the studies reported here. The associated metrology methods, analytical techniques, and sample preparation procedures are introduced, along with the materials investigated, thereby defining a complete methodological basis for the subsequent investigations. Building on this framework, the functionalization of metallic materials is examined through the lens of femtosecond burst-mode laser polishing of AISI 316L stainless steel. Various processing strategies are explored in order to assess the influence of beam shaping, burst configuration, spatial overlap, and initial surface state on polishing efficiency and surface quality. Gaussian and vortex beam configurations are first compared through single-burst experiments to identify their respective effects on material response. The role of spot-to-spot and line-to-line overlaps is then investigated to evaluate their contribution to surface smoothing, while long GHz-burst configurations are considered to explore the impact of extended energy deposition. Additional parameters, such as the number of scanning passes and initial surface roughness, are examined to assess cumulative effects and process robustness. The discussion concludes with considerations on scalability and industrial relevance. Finally, the thesis addresses the functionalization of dielectric materials using femtosecond laser irradiation, with a particular focus on Bessel-beam processing and time-resolved diagnostics. The influence of key parameters governing Bessel beam generation and propagation is first analyzed to establish controlled energy deposition conditions in transparent materials. Laser-induced modifications are then investigated across single-pulse, MHz-burst, and GHz-burst regimes, complemented by a chemical etching study to evaluate the coupling between laser modification and post-processing. These results motivate preliminary investigations toward single-GHz-burst drilling of high-aspect ratio micro-holes for surface or sub-surface structuring which could be highly interesting for anti-reflective applications [13]. To gain deeper insight into the underlying interaction dynamics, pump–probe shadowgraphy is employed to characterize the temporal evolution of laser-induced plasmas in both MHz- and GHz-burst regimes. The analysis is further refined through the combination of shadowgraphy with Mach–Zehnder interferometry, enabling in-volume interaction studies and plume expansion measurements. The comparative investigation of burst regimes provides complementary insight into burst-dependent energy deposition, plasma behavior and matter ejection, reinforcing the broader understanding of dielectric responses under ultrafast burst-mode irradiation.

Chapter 1

Theoretical background

This chapter presents the theoretical background underlying the different topics addressed in this work. It first introduces the fundamental electronic and thermal properties of solids, with a particular focus on metals and dielectric materials. These properties provide the basis for understanding their response to laser irradiation.

The discussion then turns to the physical description of light–matter interaction under extreme conditions, where high intensities and ultrashort timescales lead to strongly nonlinear and nonequilibrium phenomena. In this context, the interaction of ultrafast laser pulses with matter is examined through the main ionization mechanisms and carrier relaxation processes that govern energy deposition.

Subsequently, the chapter reviews strategies for controlling laser energy deposition through temporal and spatial beam shaping. Both approaches are essential for tailoring the interaction regime and optimizing material modification.

Finally, an overview of the applications in surface functionalization is presented, with particular emphasis on burst-mode laser processing. This emerging approach offers new opportunities for enhancing processing efficiency and achieving advanced surface functionalities.

1.1 Metals

This section first focuses on metals, for which the free electron gas model provides a convenient description of optical absorption. The two-temperature model is then introduced to describe the non-equilibrium dynamics between electrons and the lattice under ultrafast excitation. Finally, thermal conductivity and energy diffusion mechanisms are discussed, as they play a crucial role in determining heat accumulation and material modifications. Metals constitute a fundamental reference system for understanding ultrafast laser–matter interaction. Their high density of free carriers leads to efficient optical absorption and rapid energy redistribution, making their response to femtosecond irradiation comparatively well understood. In particular, the electronic excitation, non-equilibrium dynamics, and subsequent thermal relaxation processes can be described using established theoretical frameworks such as the free electron gas approximation and the two-temperature model [29, 30].

Since this work also concerns dielectric materials, investigating the metallic case provides a valuable conceptual baseline. The mechanisms governing electronic absorption, energy transfer, and heat diffusion in metals highlight key physical principles that will later be contrasted with the fundamentally different behavior of

wide-bandgap materials.

1.1.1 Free electron gas

Metals are characterized by a high density of delocalized conduction electrons that can move almost freely within the periodic potential of the ion lattice, this behavior can be understood through the band structure in metals illustrated in Figure 1.1. In the simplest approximation, these electrons can be described as a free electron gas, where the valence electrons are treated as quasi-free particles obeying Fermi–Dirac statistics [31]. This approach successfully explains many optical and electrical properties of metals, particularly in the framework of the Drude model.

Within this description, the interaction between an incident electromagnetic field and the conduction electrons leads to collective oscillations of the electron gas. The optical response is governed by the complex dielectric function, which depends on the electron density and collision frequency.

Under ultrafast laser irradiation, energy absorption in a metal occurs through the linear excitation of conduction electrons. These electrons occupy states near the Fermi level, which represents the highest occupied energy level at zero temperature and remains the reference energy for electrons at room temperature. In metals, the valence band overlaps the Fermi level, meaning that electrons can move freely across it and find available empty states just above. As a result, they can interact linearly with photons and absorb their energy efficiently, since no bandgap restricts their excitation. Because the electron subsystem responds on femtosecond timescales [32], it can reach very high electronic temperatures while the lattice remains initially close to equilibrium. This non-equilibrium state forms the basis for describing energy relaxation in metals after the arrival of an ultrafast pulse.

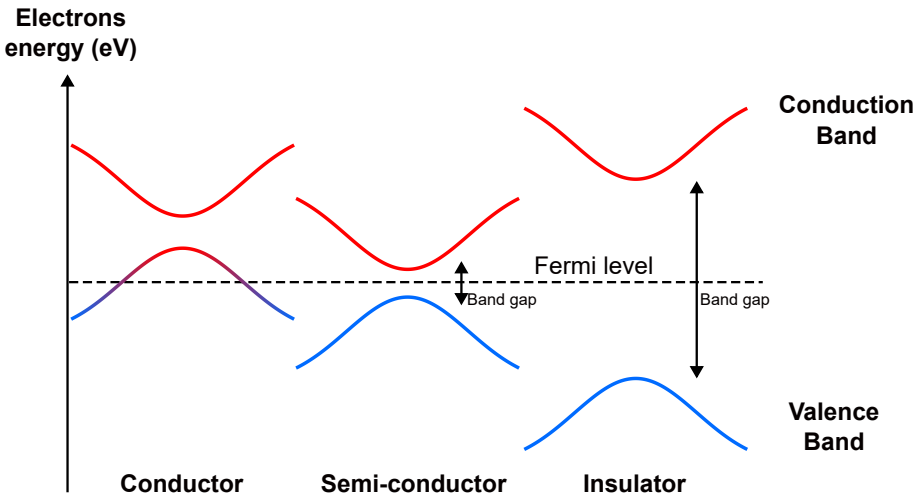

Figure 1.1: Schematic representation of the band structure in conductor, semi-conductor and insulator.

1.1.2 Two-temperature model

Following femtosecond excitation, the electron and lattice subsystems can no longer be assumed to be in thermal equilibrium. The absorbed laser energy is first deposited

into the electronic system, leading to a rapid increase in the electron temperature T_e. The lattice temperature T_l rises subsequently through electron–phonon coupling on picosecond timescales.

This nonequilibrium situation is commonly described using the two-temperature model (TTM) [33, 34], which treats electrons and lattice as two coupled thermal reservoirs:

$$C_e(T_e)\frac{\partial T_e}{\partial t} = \nabla \cdot (k_e \nabla T_e) - G(T_e - T_l) + S, \tag{1.1}$$

$$C_l\frac{\partial T_l}{\partial t} = \nabla \cdot (k_e \nabla T_e) + G(T_e - T_l), \tag{1.2}$$

where C_e and C_l are the electronic and lattice heat capacities, k_e is the electronic thermal conductivity, G is the electron–phonon coupling constant, and S represents the laser energy source term.

The TTM captures the essential physics of ultrafast laser heating in metals: rapid electronic excitation, followed by energy transfer to the lattice and eventual thermal diffusion. The characteristic electron–phonon relaxation time [35] typically lies in the picosecond range, defining the timescale over which the system returns toward thermal equilibrium, if the pulse duration is longer than the electron-phonon coupling time, a significant part of the pulse energy remains in the material even after matter ejection [36].

1.1.3 Thermal properties

Thermal transportation in metals is predominantly governed by conduction electrons. According to the Wiedemann–Franz law [37], the electronic thermal conductivity is proportional to the electrical conductivity, reflecting the fact that both charge and heat are transported by the same free-electron population. As a result, metals generally exhibit high thermal conductivities and, consequently, high thermal diffusivity (20 to 160 $\text{mm}^2.\text{s}^{-1}$) [38].

Under ultrafast laser excitation, the situation is initially non-equilibrium. The laser energy is first absorbed by the electronic subsystem, leading to a rapid increase in the electron temperature. During this stage, hot electrons can transport energy over distances exceeding the optical penetration depth before transferring it to the lattice through electron–phonon coupling. This ultrafast electronic heat transport modifies the spatial distribution of deposited energy and affects melting thresholds, stress generation, and the onset of ablation.

Once electron–lattice equilibrium is restored (typically on picosecond timescales), heat transportation can be described using classical Fourier diffusion (or Fourier heat conduction) governed by the lattice temperature gradient and the thermal properties of the material. In this regime, the relevant material parameter is the thermal diffusivity

$$\alpha = \frac{k}{\rho C},$$

where k is the thermal conductivity, ρ the density, and C the specific heat capacity [39].

In order to quantify heat redistribution over a characteristic length scale L [40], a useful estimate of the thermal diffusion time is

$$\tau_{\text{th}} \sim \frac{L^2}{4\alpha}. \tag{1.3}$$

This expression provides the order of magnitude of the time required for heat to diffuse over the distance L. Because α varies significantly between metals, the thermal confinement strongly depends on the material.

Figure Figure 1.2 presents the calculated diffusion time as a function of L for stainless steel 316, Ti6Al4V, Al 2024 and Al 7075, using their respective room-temperature thermal diffusivities. Aluminum alloys, characterized by high thermal diffusivity, exhibit the shortest diffusion times, whereas stainless steel and titanium alloys display slower heat redistribution due to their lower diffusivity. For micro-

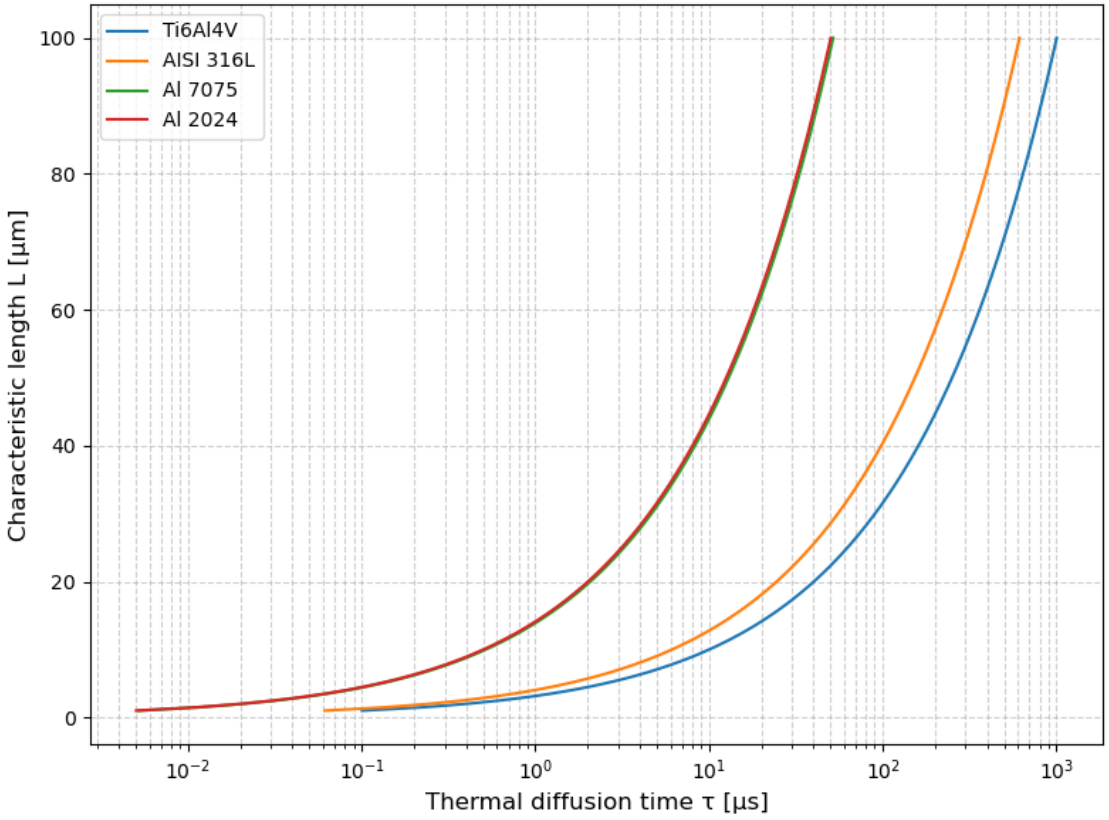

Figure 1.2: Evolution of the characteristics length as function of the Thermal diffusion time for various alloys. (Values used from Section 2.4.1.

metric length scales ($L \sim 1$ μm), the diffusion time ranges from sub-nanosecond values in aluminum alloys to several nanoseconds in steel and titanium alloys. For $L \sim 10$ μm, the characteristic time increases to tens or hundreds of nanoseconds depending on the material. This quadratic scaling highlights the strong dependence of thermal confinement on the interaction size, interaction time, inter-pulse delay, and the intrinsic material properties.

These considerations are particularly relevant in burst irradiation regimes. If the inter-pulse delay within the burst is shorter than τ_{th}, heat accumulation may occur within the interaction volume. Conversely, if the inter-pulse delay exceeds

the characteristic diffusion time, a significant fraction of the deposited energy can dissipate before the arrival of the next pulse. The comparison between τ_{th} and the burst repetition period therefore provides a quantitative framework for interpreting the transition between repetitive single pulse and cumulative thermal regimes.

1.2 Dielectrics

In contrast to metals, dielectrics are characterized by a fully occupied valence band separated from the empty conduction band by a wide bandgap originating from the periodic Coulomb potential generated by the ionic cores. The periodic Coulomb potential generated by the ionic lattice couples free-electron states that are degenerated in energy, particularly at the Brillouin zone boundaries. An illustration of the folded Brillouin zone can be found in Figure 1.1. This coupling lifts the degeneracy by splitting the electronic states into bonding and antibonding combinations, thereby opening energy gaps. The repetition of this process throughout reciprocal space leads to the formation of electronic energy bands separated by band gaps. This potential lifts the degeneracy of free-electron states and gives rise to energy bands and band gaps.

At equilibrium, the absence of free carriers results in negligible electrical conductivity and weak linear optical absorption at photon energies below the bandgap (few eV). Laser-induced excitation of dielectric materials can be achieved either by linear absorption with high photon energy (with UV or deep-UV laser beam for instance), or by non-linear absorption with high intensity. Indeed, under intense ultrafast laser irradiation, this situation changes dramatically as strong irradiation processes can transiently populate the conduction band as will be further discussed in Section 1.3.

1.2.1 Band structure

In wide-bandgap materials such as glass or crystal, the initially localized electronic structure leads to fundamentally different absorption and transport mechanisms compared to metals. The electronic properties of dielectrics are governed by their Fermi level. This Fermi level is typicaly located in between the conduction band and the valence band as illustrated in Figure 1.1. The bandgap energy E_g (typically several electronvolts) prevents thermal excitation of electrons into the conduction band at room temperature. As a result, the free carrier density is extremely low under equilibrium conditions. [41]

When interacting with femtosecond laser pulses, electrons can be promoted from the valence band to the conduction band if sufficient energy is provided, either by a single photon with energy matching the bandgap value ($E_{bg} = \hbar\omega$) or with sufficient intensity such that the electrons can simultaneously absorb two or more photons at the same time such that ($E_{bg} = n \times \hbar\omega$). More details about those mechanisms will be given in Section 1.2.2. The band structure therefore determines the ionization threshold, the effective mass of excited carriers, and the subsequent carrier dynamics.

1.2.2 Ultrafast Laser & Matter Interaction Regimes

Under intense laser irradiation, several ionization mechanisms may contribute to free carrier generation. For photon energies below the bandgap, multiphoton ionization (MPI) can occur when multiple photons are simultaneously absorbed to bridge the bandgap. At higher intensities, tunneling ionization becomes significant, where the strong electric field distorts the Coulomb potential (or band structure) sufficiently to allow electrons to tunnel into the conduction band. An illustration of these two phenomena can be found in Figure 1.3.

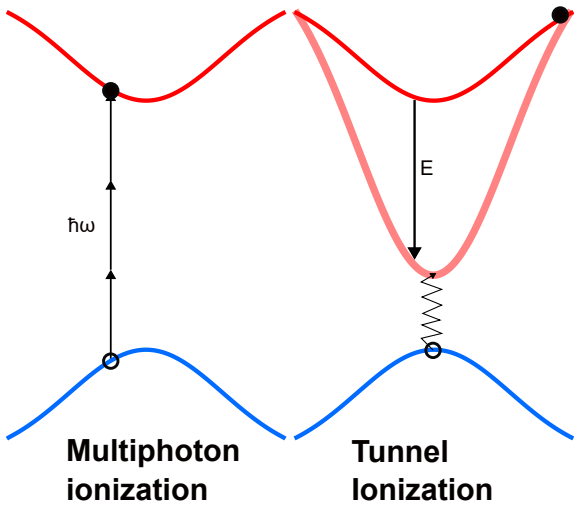

Figure 1.3: Schematic representation of the photoionization mechanisms.

The relative importance of these regimes is characterized by the Keldysh parameter γ, defined as

$$\gamma = \omega \sqrt{\frac{m^* E_g c \epsilon_0}{e^2 I}}, \tag{1.4}$$

where ω is the laser angular frequency, I the laser intensity, m^* the effective electron mass, E_g the bandgap energy, c the speed of light, e the electric charge of the electron and ϵ_0 the void permittivity [42].

The Keldysh parameter can be interpreted as the ratio between the tunneling time and the optical period. It provides a convenient criterion to distinguish ionization regimes:

- $\gamma \gg 1$: multiphoton ionization (perturbative regime),
- $\gamma \sim 1$: intermediate regime,
- $\gamma \ll 1$: tunneling ionization (strong-field regime).

Since $E \propto \sqrt{I}$, increasing the intensity reduces γ and progressively drives the interaction from multiphoton to tunneling ionization. In this work the Keldysh parameters have been estimated and are located between 1 and 10 for the various energy distributions investigated. Therefore, the primary absorption will be mainly driven by multiphoton ionization.

In addition to direct photoionization, impact (avalanche) ionization may further increase the carrier density [43] and will be in competition with both radiative

and non-radiative mechanisms that contribute to cooling down the free electron temperature and density. The interplay between these mechanisms governs the temporal evolution of the electron density and the onset of optical breakdown.

1.2.2.1 Multiphoton ionization

Multiphoton ionization is a perturbative nonlinear process in which k photons are simultaneously absorbed to overcome the bandgap energy:

$$k\hbar\omega \geq E_g.$$

The ionization rate scales as

$$W_{\mathrm{MPI}} \propto I^k,$$

where $k = E_g/\hbar\omega$ is the minimum number of photons required [44].

Because of this strong nonlinear dependence, MPI is highly localized in regions of highest intensity. It dominates at intensities where $\gamma \gg 1$[3]. However, MPI alone may not be sufficient to reach critical plasma density unless intensities are very high or the pulse duration is long enough.

1.2.2.2 Avalanche ionization

Avalanche ionization, also known as impact ionization, is a secondary process that amplifies the initially generated carrier population. Free electrons absorb energy from the laser field through inverse Bremsstrahlung [45] and gain sufficient kinetic energy (free carrier absorption) to ionize valence electrons via collisions (impact ionization) [46]. A schematic representation of the different mechanism can be found in Figure 1.4.

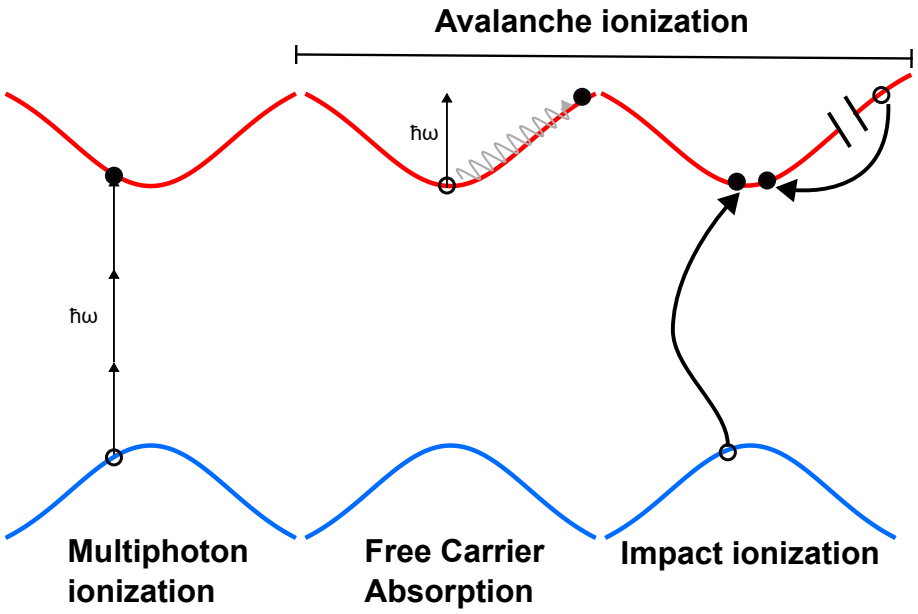

Figure 1.4: Schematic representation of the carrier excitation mechanisms.

The evolution of the electron density can be described by

$$\frac{dn_e}{dt} = W_{\mathrm{PI}} + \alpha n_e, \tag{1.5}$$

where W_{PI} represents the photoionization rate (MPI or tunneling) and α is the avalanche coefficient.

This mechanism leads to exponential growth of the carrier density, provided that the pulse duration exceeds the characteristic collision time. Avalanche ionization therefore plays a more significant role for longer pulses (picosecond regime) or at high repetition rates, where seed electrons are already present.

1.2.2.3 Carrier relaxation

Following excitation, the carrier population is in a highly nonequilibrium state. Relaxation proceeds through several stages characterized by distinct timescales.

On femtosecond timescales, electron–electron collisions lead to rapid thermalization within the conduction band, establishing a hot Fermi–Dirac distribution [47].

On picosecond timescales, energy is transferred from the electronic subsystem to the lattice through electron–phonon coupling [43, 48, 49]. This process governs lattice heating, stress generation, and potential phase transitions.

On longer timescales (picoseconds to nanoseconds), carrier recombination mechanisms reduce the free carrier density. These include:

- Radiative recombination,
- Defect-assisted (trap-mediated) recombination,
- Auger recombination at high carrier densities.

In dielectrics, defect formation such as self-trapped electrons and Frenkel defects can significantly alter relaxation pathways and lead to permanent structural changes [50, 51].

The competition between ionization, relaxation, and recombination ultimately determines whether the material response remains reversible (transient refractive index change) or evolves toward irreversible modification such as densification, void formation, or matter ejection (ablation).

1.3 Optical properties under extreme conditions

Under extreme excitation conditions, the transient generation of free carriers strongly modifies the optical properties of the material. Even in wide-bandgap dielectrics, a sufficiently high carrier density in the conduction band can induce metallic-like behavior during the pulse duration.

1.3.1 Drude model

Under intense ultrafast excitation, the transient population of free carriers strongly modifies the dielectric response of the material. Even wide-bandgap dielectrics can exhibit metallic-like optical behavior when a sufficiently high free electron density

is generated. The optical response of of the material can be described within the Drude formalism [52].

In this framework, the complex dielectric function is written as

$$\epsilon(\omega) = \epsilon_\infty - \frac{\omega_p^2}{\omega(\omega + i\nu)}, \tag{1.6}$$

where $\epsilon_\infty = n_0^2$ represents the background permittivity of the unperturbed material (with n_0 the linear refractive index), ω is the angular frequency of light considered ($\omega = 2\pi f = \frac{2\pi c}{\lambda}$), for the laser it's ω_l, ω_p is the plasma frequency defined as

$$\omega_p^2 = \frac{n_e e^2}{\epsilon_0 m^*}, \tag{1.7}$$

where n_e is the electron density, e the electric charge of the electron, ϵ_0 the void permittivity and m^* the effective mass of the electron, and ν is the effective collision frequency.

The collision frequency $\nu = 1/\tau$ (with τ the collision time) plays a crucial role in determining the dissipative character of the plasma response, which is related to the imaginary part of the dielectric function. From a physical point of view, ν accounts for collisions mechanisms between species, such as:

- Electron–phonon collisions (ν_{ep}), dominant process as the lattice temperature increases[53, 54, 35],
- Electron–electron collisions (ν_{ee}), which contribute to electrons thermalization, without major plasma relaxation effects as the momentum is conserved,
- Electron–ion collisions (ν_{ei}), particularly relevant at high ionization levels. This collision type can be subdivided into three categories, free-free (bremsstrahlung), bound-bound (discrete spectral lines) and free-bound (radiative combination), and are radiative emissions [55],
- Ion–ion collisions (ν_{ii}), mainly influencing the hydrodynamic evolution of the plasma.

The magnitude of ν determines the imaginary part of the permittivity and therefore the absorption. In the low-collision regime ($\nu \ll \omega$), the response of the plasma is predominantly non-absorbant to ω_l, leading mainly to refractive index changes and inducing phase shifts in the light propagating through the plasma. In contrast, when ν becomes comparable with or larger than ω, absorption increases significantly and energy deposition is enhanced.

In ultrafast laser excitation of dielectrics, ν is not a constant parameter but evolves dynamically with carrier density and lattice temperature. Immediately after ionization, electron–electron collisions dominate and a rapid thermalization within the conduction band occurs. As the electron–phonon interactions become increasingly important, the lattice heats up, increasing ν and modifying the optical absorption.

The Drude model therefore establishes a direct link between the transient carrier density, collisional dynamics, and measurable optical quantities such as reflectivity

with the real part of the complex dielectric function and absorption with the imaginary part of the complex dielectric function. This framework is particularly relevant for interpreting pump–probe and pump-probe interferometry experiments, where the transmission variation over time is linked to the dissipative character $\epsilon(\omega_l)$ and the phase variation is directly related to the real part of $\epsilon(\omega_l)$.

1.3.2 Critical plasma density

Under intense ultrafast excitation, the free electron density (n_e) increases, so the plasma angular frequency (ω_p) increases. When ω_p reaches the angular frequency ω_l, the corresponding free electron density, called the critical density is defined such that the real part of the dielectric function decreases to zero, leading to a transient dielectric-to-metal transition. When a sufficiently high density of free electrons is generated under intense laser irradiation, the optical response of the material can drastically change. A key quantity governing this transition is the critical plasma density.

According to the Drude model, the critical plasma density is reached when the corresponding plasma angular frequency is equal to the laser angular frequency. In these conditions, the real part of the dielectric function becomes zero. [55]:

$$\omega_p = \omega_l$$

Using the definition of the plasma frequency given in Equation (1.7),
the corresponding electron density defines the critical density n_c:

$$n_c = \frac{\epsilon_0 m^* \omega_l^2}{e^2}. \tag{1.8}$$

For $n_e < n_c$, the material remains transparent to ω_l (positive real permittivity), although absorption may increase. When $n_e \geq n_c$, the real part of the permittivity becomes zero or negative, and the material exhibits metallic-like behavior with strong reflection to ω_l. This shielding effect corresponds to a physical limit of the n_c value at the laser wavelength.

For near-infrared excitation (e.g., $\lambda = 1030$ nm), the critical density is typically found to be 1.05×10^{21} cm^{-3} [56].

The concept of critical density therefore provides a fundamental threshold separating weak perturbative regimes from strongly nonlinear plasma-driven regimes. It also serves as a reference scale when interpreting phase and absorption measurements in pump–probe experiments.

1.3.3 Refractive index modification

The generation of free carriers and the subsequent thermo-mechanical response of the material both contribute to transient modifications of the complex refractive index.

First, considering the contribution of the free carriers, the refractive index is defined by the dielectric function as

$$n = \sqrt{\epsilon}. \tag{1.9}$$

Using the Drude expression in Equation (1.6), the presence of free electrons induces a negative contribution to the real part of the permittivity. For moderate carrier densities ($\omega_p^2 \ll \omega^2$ and $\nu \ll \omega$), the refractive index variation can be approximated as

$$\Delta n_{plasma} \approx -\frac{n_e e^2}{2n_0 \epsilon_0 m^* \omega^2}. \tag{1.10}$$

This expression shows that free carrier generation induces a decrease of the refractive index. Physically, the oscillating electrons screen the incident electromagnetic field, reducing the effective polarization of the medium.

In addition to the index variation resulting from the free electron density, any transient variation of the matter density, such as thermal expansion or pressure waves generated may also induce a variation of the refractive index. [57, 58, 14].

Therefore, the total refractive index variation may be written schematically as

$$\Delta n = \Delta n_{\text{plasma}} + \Delta n_{\text{thermo-mechanical}}. \tag{1.11}$$

Disentangling these contributions is essential for interpreting time-resolved interferometric measurements, especially when probing timescales extending from femtoseconds to nanoseconds.

1.3.4 Relation between refractive index variation and pressure (Lorentz–Lorenz)

While the Drude model describes refractive index changes induced by free carriers, mechanical compression or rarefaction also modifies the refractive index through density variations. This effect can be quantified using the Lorentz-Lorenz relation [59]:

$$\frac{n^2 - 1}{n^2 + 2} = A\rho, \tag{1.12}$$

where n is the refractive index, ρ the material density, and A a constant related to the molecular polarizability.

Defining

$$F(n) = \frac{n^2 - 1}{n^2 + 2},$$

its derivative with respect to n is

$$\frac{dF}{dn} = \frac{6n}{(n^2 + 2)^2}.$$

For small perturbations,

$$\Delta F \approx \frac{6n}{(n^2 + 2)^2} \Delta n.$$

From Equation (1.12), variations in F are directly related to density variations:

$$\Delta F = A \Delta \rho.$$

Combining these expressions yields

$$\frac{6n}{(n^2+2)^2}\Delta n = A\Delta\rho.$$

Using Equation (1.12) to eliminate A, the following is obtained:

$$\frac{\Delta\rho}{\rho} = \Delta n \, \frac{6n}{(n^2+2)(n^2-1)}. \tag{1.13}$$

This relation is valid for small perturbations and assumes that the polarizability remains unchanged.

In the elastic regime, pressure is related to volume change via the bulk modulus K:

$$P = -K\frac{\Delta V}{V}. \tag{1.14}$$

Since mass is conserved,

$$\frac{\Delta\rho}{\rho} = -\frac{\Delta V}{V}.$$

Finally, the pressure can be expressed as

$$P = K\frac{\Delta\rho}{\rho}. \tag{1.15}$$

Combining Equation (1.13) and Equation (1.15) provides a direct link between the measured refractive index variation and the mechanically induced pressure:

$$P = K\,\Delta n \, \frac{6n}{(n^2+2)(n^2-1)} \tag{1.16}$$

This expression forms the basis for converting interferometric phase measurements into quantitative pressure estimations during pressure wave or plasma expansion experiments.

1.4 Temporal and spatial control of energy deposition

In ultrafast laser–matter interaction, controlling the deposited energy is not limited to adjusting the pulse energy or focusing conditions. Advanced beam engineering strategies enable precise control of both the spatial and temporal distribution of energy to optimize the response of the material or the micro-machining process. While spatial shaping governs intensity localization within the surface or focal volume, temporal shaping modifies the way energy is delivered in time, strongly influencing carrier dynamics, heat accumulation, plasma shielding, and ultimately material removal efficiency [60, 61, 62].

Among temporal shaping strategies, burst regimes, which refer to the sub-division of a single pulse into sub-pulses separated by controlled delays, have emerged as a powerful approach to tailor ultrafast energy deposition beyond the single-pulse configuration [63]. A more detailed explanation will be given in Section 2.1.

1.4.1 Temporal beam shaping

Temporal beam shaping refers to the modification of the temporal structure of a laser pulse or pulse sequence in order to control light–matter interaction mechanisms. In the ultrafast regime, where characteristic material response times range from femtoseconds (electron dynamics) to nanoseconds (thermal diffusion), the pulse-to-pulse delay becomes a key parameter.

By splitting a single pulse into a train of sub-pulses separated by controlled delays, it becomes possible to exploit cumulative effects within the burst, plasma dynamics, or transient thermodynamic states. This approach introduces additional degrees of freedom such as:

- number of pulses per burst,
- intra-burst repetition rate,
- energy distribution within the burst,
- burst duration,
- inter-burst repetition rate.

These parameters allow tailoring the interaction to match intrinsic material timescales such as carrier lifetime, electron–phonon coupling time, or thermal diffusion time [25, 64, 65].

1.4.1.1 MHz-burst

In the MHz-burst regime, the energy of a single pulse is divided in sub-pulses thus reducing the peak intensity and undesired non-linear effect. The pulse-to-pulse delay typically lies in the range of several nanoseconds. This timescale is comparable to plasma expansion and partial thermal diffusion times.

In this configuration, the first pulse generates free carriers and initiates material removal. The subsequent pulses may interact with:

- a partially expanded plasma plume
- a molten layer

Experimental studies have revealed complex behaviors such as alternating ablation efficiency with odd and even numbers of pulses per burst. This phenomenon is often attributed to particle ejection and plasma shielding: one pulse may be partially absorbed by the ablation plume, once the plume is gone, the surface will have a renewed surface interaction [20, 66].

In dielectrics, MHz-bursts have demonstrated improved processing quality. The short intra-burst delay limits lateral heat diffusion, confining thermal effects and minimizing the heat-affected zone. This regime is particularly advantageous for brittle materials such as glass, where controlled energy deposition is essential to avoid undesired fracture [17, 22, 25].

1.4.1.2 GHz-burst

The GHz-burst regime corresponds to intra-burst repetition rates on the order of 10^9 Hz, i.e. pulse-to-pulse delays of one nanosecond or less. At this timescale, heat diffusion between consecutive pulses becomes negligible.

In this regime, each pulse interacts with a surface or a volume that remains thermally excited by the previous one. This leads to a gentle cumulative temperature rise within the interaction volume with well-chosen burst parameters. Because less energy is required to bring already-heated material to the ablation temperature, material removal can occur at fluences below the single-pulse ablation threshold [63]. This behavior has been described as an ablation regime, where part of the energy deposition mainly occurs in a thin layer corresponding to the skin depth, and where part of the deposited energy is possibly carried away by the ejected material rather than diffused into the bulk. Compared to single-pulse irradiation:

- energy losses due to thermal diffusion are reduced
- ablation efficiency can increase significantly
- collateral thermal damage should be minimized

Nevertheless, at very high repetition rates, particle ejection and plasma shielding effects may increase. Therefore, optimization requires balancing pulse duration, pulse energy, repetition rate, and number of pulses per burst.

GHz-burst processing represents a distinct light–matter interaction regime, where ultrafast cumulative heating dominates over diffusive relaxation, enabling efficient and precise material removal [21, 63, 67, 68].

1.4.2 Spatial beam shaping

In addition to temporal control, the spatial distribution of laser intensity plays a central role in ultrafast laser–matter interaction. The deposited energy density, the excitation volume, and the resulting modification regime are strongly driven by the transverse and longitudinal structure of the optical field.

Spatial beam shaping consists in tailoring the amplitude and/or phase of the incident beam in order to modify its propagation properties and focal intensity distribution. By engineering the spatial profile, it becomes possible to control:

- the peak intensity
- the focal volume geometry and aspect ratio
- the depth of focus
- the symmetry of energy deposition
- number of sub-beams

Different beam profiles lead to fundamentally different interaction regimes. In the following, the three configurations relevant to ultrafast material processing and used within this work are discussed: Gaussian beams, quasi-Bessel–Gauss beams, and vortex beams generated using a vortex phase plate.

1.4.2.1 Gaussian beam

The Gaussian beam represents the fundamental transverse electromagnetic mode (TEM_{00}) of most laser systems relevant for ultrafast laser processing. Its intensity distribution in the transverse plane is given by

$$I(r,z) = I_0 \left(\frac{w_0}{w(z)}\right)^2 \exp\left(-\frac{2r^2}{w^2(z)}\right), \tag{1.17}$$

where r and z are the radial and height coordinate of a cylindrical system, I_0 is the peak intensity, w_0 is the beam radius at focus and $w(z)$ is the beam radius at position z. The beam divergence is governed by diffraction and characterized by the Rayleigh length

$$z_R = \frac{\pi w_0^2}{\lambda}, \tag{1.18}$$

which defines the characteristic propagation distance in free space over which the beam radius remains below $\omega_0\sqrt{2}$.

Gaussian beams provide strong intensity localization and high peak fluence, making them well suited for precision micromachining and nonlinear absorption processes. However, their short depth of focus limits the longitudinal extension of the modification zone. As a result, energy deposition is highly localized near the focal plane, which may lead to strong intensity gradients and sensitivity to focusing conditions.

Despite these limitations, Gaussian beams remain the reference configuration for material micro-machining / micro-processing with ultrafast lasers due to their simplicity and well-understood propagation behavior [10, 69].

1.4.2.2 Quasi-Bessel-Gauss beams

In contrast to Gaussian beams, Bessel beams exhibit a non-diffractive propagation behavior characterized by an extended depth of focus. An ideal Bessel beam possesses a transverse intensity profile described by a zeroth-order Bessel function:

$$I(r) \propto J_0^2(k_r r), \tag{1.19}$$

where J_0 is the zeroth-order Bessel function, k_r is the transverse wave vector component and r the radial coordinate [24, 70, 71].

In practice, ideal Bessel beams require infinite energy and are therefore physically unrealizable. Instead, quasi-Bessel–Gauss beams are generated experimentally using axicons [72, 73, 74] or spatial phase modulation [10, 75, 26, 76]. These beams preserve the narrow central core of an ideal Bessel beam while exhibiting a Gaussian envelope in the transverse direction, which ensures finite energy and results in a limited non-diffraction propagation length.

The key properties of quasi-Bessel–Gauss beams include:

- an extended focal region
- a narrow central core
- self-healing properties after partial obstruction

In ultrafast laser processing, the elongated interaction region enables the fabrication of high-aspect-ratio structures, deep modifications inside transparent materials, ablation-free glass cutting and improved drilling performance [24, 25, 77, 78]. The extended depth of focus significantly relaxes axial positioning tolerances relative to Gaussian beams. However, the presence of concentric side lobes may lead to additional energy deposition outside the central core, which must be considered when high precision is required [71].

Additionally, when a Bessel beam is generated from a Gaussian input beam, the intensity along the propagation axis is not uniform. The axial intensity distribution follows [72, 79]:

$$I(z) = \frac{8\pi P_0 \sin^2\theta}{\lambda\omega_0^2} z \exp\left[-2\left(\frac{z\sin\theta}{\omega_0}\right)^2\right] \tag{1.20}$$

Where P_0 is the incident peak power of the incoming Gaussian beam, θ is the angle of the axicon, λ is the laser wavelength, ω_0 is the beam radius at the axicon entry, and z is the height coordinate. The resulting curve can be found in Figure 1.5:

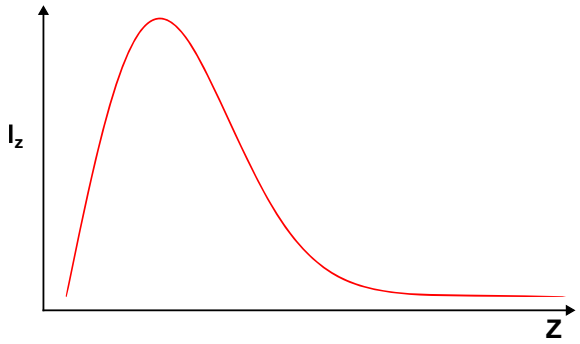

Figure 1.5: Intensity profile of the central core of a quasi-Bessel-Gauss beam along the propagation axis Z.

Another important feature of the Bessel beam is that, when generated through an axicon (conical lens) the tip is often rounded and behaves as a classical lens for the incoming wavefront as represented in Figure 1.6. The result is an additional interference between the conical wave and the spherical wave generated by the rounded tip leading to fluctuation in the Z-intensity profile compared to the ideal case [72]. The longitudinal extension of the central core, often referred to as the non-diffractive length, is approximately given by [70] :

$$L \approx \frac{w_0}{\tan\theta}, \tag{1.21}$$

where w_0 is the radius of the incident Gaussian beam and θ is the axicon angle.

1.4.2.3 Vortex phase plate

Vortex beams are structured light fields carrying orbital angular momentum (OAM). They can be generated by introducing an azimuthal phase modulation of the form

$$\Phi(\theta) = \ell\theta, \tag{1.22}$$

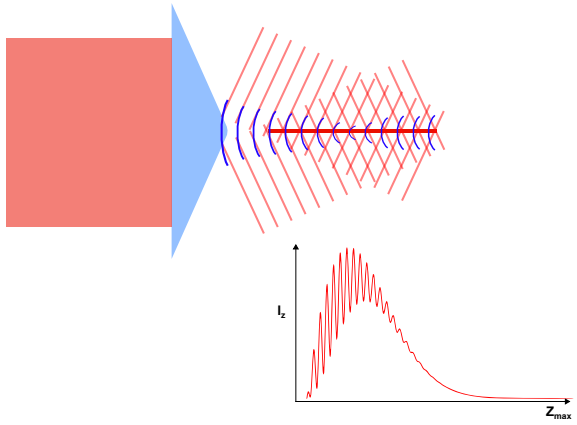

Figure 1.6: Intensity profile of the central core along the propagation axis Z with the effect of the rounding tip.

where θ is the azimuthal angle and ℓ is the topological charge. A vortex phase plate imposes thus a helical phase structure onto an incoming beam.

As a consequence of the phase singularity at the beam center, the intensity profile exhibits a ring-shaped distribution with a zero-intensity core. The resulting beam carries an orbital angular momentum of $\ell\hbar$ per photon [16, ?].

In ultrafast material processing, vortex beams enable:

- ring-shaped energy deposition
- controlled generation of hollow microstructures (donut-like)
- angular momentum transfer to matter

The absence of intensity at the beam center modifies the local energy density distribution and can significantly affect laser matter interaction and material removal dynamics [80]. By adjusting the topological charge ℓ, the diameter of the intensity ring and the spatial distribution of deposited energy can be controlled.

Vortex beams therefore provide an additional degree of freedom for engineering light–matter interaction beyond conventional Gaussian illumination and can even be combined with Bessel beam shaping in order to use the even order [26].

1.5 Applications and surface functionalization

Ultrafast laser processing has become a versatile and powerful tool for tailoring the physical and chemical properties of material surfaces. Owing to the extremely short pulse duration, energy deposition occurs on timescales shorter than thermal diffusion, enabling highly localized material modifications with minimal heat-affected zones and excellent processing quality [5, 29, 81]. This capability makes femtosecond lasers particularly suitable for precise surface structuring and functionalization.

More generally, femtosecond laser technology offers several advantages for advanced manufacturing processes. It enables localized, contactless, and environmentally friendly processing without the need for chemical reagents or masks. In addition, laser processing is highly flexible and compatible with modern industries

[82], including aerospace [60], medical devices [83, 84], electronics [85], and optical systems [86].

Laser-induced surface modifications can alter a wide range of functional properties, including wettability [87], optical reflectivity, friction, adhesion, antibacterial behavior, or biological compatibility. Therefore, surface engineering aims either at improving existing surface properties or introducing entirely new functionalities. This can be achieved by modifying the surface morphology or by altering the chemical composition of the near-surface region.

Laser-based technologies allow a broad spectrum of surface engineering processes. These include direct laser ablation processes such as cleaning, engraving, deep ablation, or surface texturing [29], as well as micro- and nano-structuring techniques such as laser-induced periodic surface structures (LIPSS)[88, 89], direct laser interference patterning (DLIP)[90] or metal polishing by surface melting [11, 91, 92]. Such surface modifications enable numerous functionalities including anti-reflective surfaces [13], enhanced light absorption [93], controlled wettability [87], antibacterial surfaces [12], or anti-icing coatings [94]. In addition, laser-based processes can also involve multi-perforation for permeability or acoustic control, as well as surface melting for polishing or surface smoothing [91, 95].

These laser-assisted processes offer several advantages from a sustainability perspective. Many of them are single-step processes that do not require masks, chemical treatments, or additional finishing steps. Furthermore, they can operate without coating layers and sometimes without material removal, which reduces waste, simplifies the manufacturing workflow, and saves energy. However, simultaneously achieving high throughput, high precision, and high processing quality remains a key challenge for many industrial applications [96, 97].

One approach to address this challenge consists in optimizing laser parameters such as wavelength [98], pulse duration [74], fluence, or polarization in order to maximize energy deposition while minimizing unwanted side effects. Another strategy relies on spatial [25] or temporal beam shaping [25, 64, 65], which provides additional degrees of freedom to control the interaction between the laser radiation and the material. In this context, exploring new regimes of laser–matter interaction remains a major research direction for expanding the range of achievable surface functionalities.

1.5.1 Thesis context: Burst approaches for ultrafast laser-based material processing

In addition to single-pulse irradiation, burst laser processing has emerged as an efficient approach for controlling surface modification dynamics. In burst regimes, a sequence of ultrashort pulses is delivered with a controlled intra-burst delay, allowing successive pulses to interact with a surface that has not yet fully relaxed [23].

This temporal structuring of the energy deposition can significantly influence the ablation dynamics. The first pulse typically generates free carriers and initiates heating or material removal, while the following pulses interact with an excited surface, a transient molten layer, or an expanding plasma plume. As a result, cumulative effects may enhance energy absorption and modify the resulting surface morphology [61].

In particular, the use of GHz burst regimes has recently emerged as a promis-

ing alternative for improving laser material processing. In this configuration, each high-intensity pulse is replaced by a train of lower-intensity pulses with intra-burst repetition rates on the order of several gigahertz, while the repetition rate between bursts typically remains in the range of tens of kilohertz. The delay between two pulses inside the burst is therefore shorter than the typical thermal relaxation time of the material, leading to a beneficial preheating of the interaction zone. This cumulative heating effect can significantly improve the material removal rate and the achievable aspect ratio of laser-machined structures, even for fluences below the ablation threshold defined for a single pulse [19, 22, 67].

At the same time, the relatively long delay between two successive bursts leaves sufficient time for heat dissipation, preserving the high processing quality typically associated with femtosecond laser machining. Another advantage of this regime is the reduction of undesirable nonlinear propagation effects such as air breakdown during surface processing or premature energy deposition before the geometrical focus in transparent materials.

Burst processing has therefore been shown to improve several aspects of laser surface and sub-surface structuring, including ablation efficiency, surface quality, and reproducibility of laser-induced patterns. By controlling parameters such as the number of pulses per burst [64], the intra-burst repetition rate, and the temporal envelope of the burst, it becomes possible to tailor the energy deposition dynamics and access new regimes of laser–matter interaction.

Overall, burst-mode ultrafast laser processing represents a promising strategy for improving surface structuring efficiency and expanding the range of achievable surface functionalities in modern laser-based manufacturing technologies. This PhD thesis has been carried out in this context, with the aim of investigating burst-modes applied to ultrafast laser processing as a strategy to control energy deposition.

Chapter 2

Materials & methods

In this chapter, an introduction of the technical aspects of the experiments and experimental setups used throughout this work is given. The chapter begins with the presentation of the laser system developed by Amplitude, which enabled the investigation of a wide range of irradiation regimes, from single-pulse operation to long GHz-bursts, including various MHz-burst configurations. This is followed by a description of the large-area micro-machining station employed in the experiments.

This station was used in conjunction with several beam-shaping configurations, starting from the conventional Gaussian beam, and extending to quasi-Bessel–Gauss beams and vortex beams. These spatial beam-shaping techniques were applied to different types of experiments, such as surface polishing, surface modification and ablation, as well as interferometric measurements. The chapter also introduces the different devices and automation procedures implemented during the three years of this PhD work. All measurement equipments and characterization methods used to analyze the experiments are presented. Finally, the last part of this chapter is dedicated to the samples and materials investigated in this study.

2.1 Laser system

The main laser system used during this PhD work is a prototype version of a commercial product developed by Amplitude, based on the Tangor 100 W. The system is capable of operating in three distinct regimes: the repetitive single-pulse regime, the MHz-burst regime, and the GHz-burst regime. These operating modes are schematically illustrated in Figure 2.1.
In all three regimes, the laser delivers pulses or bursts of pulses at a central wavelength of 1030 nm, with a maximum pulse or burst energy of up to 500 µJ. The repetition rate can reach up to 2 MHz, corresponding to a maximum average power of 100 W. Each operating mode, however, presents specific characteristics.

In the repetitive single-pulse (SP) regime, the laser delivers isolated pulses with a minimum pulse duration of 480 fs. In the MHz-burst regime, the laser is capable of producing bursts containing between 2 and 32 pulses per burst (ppb), with an intra-burst repetition rate of 40 MHz (i.e., a pulse-to-pulse delay of 25 ns) and the minimum pulse duration remains 480 fs. Finally, in the GHz-burst regime, the laser delivers bursts containing between 50 and 800 ppb, with an intra-burst repetition rate of 1.28 GHz and the minimum pulse duration in this regime is 505 fs.

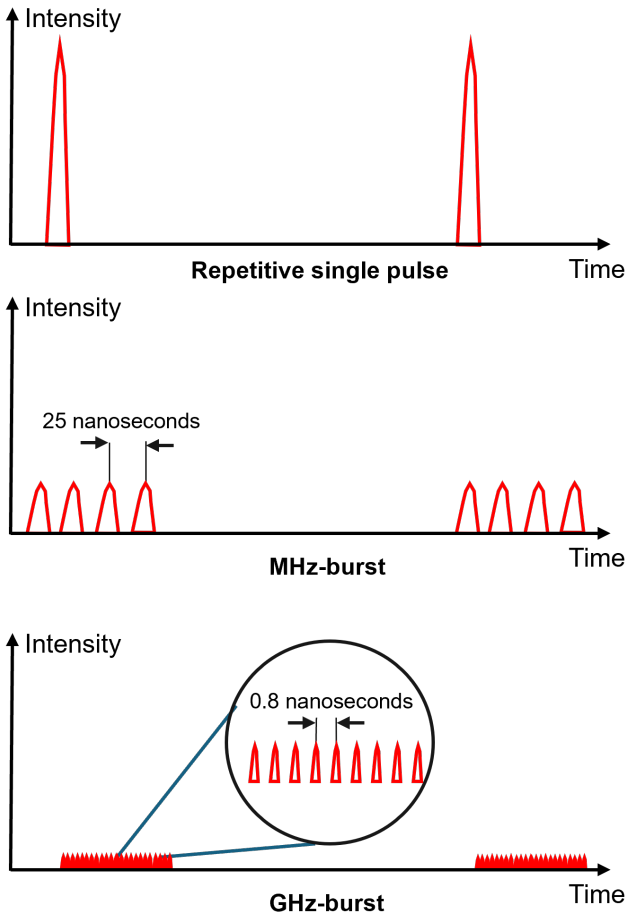

Figure 2.1: Schematic representation of the temporal structure and energy distribution of the three laser operating regimes available with the laser system.

The pulse duration can be adjusted by the compressor in the laser system allowing to achieve pulse durations of up to 2.5 ps in all regimes. In both the MHz- and GHz-burst modes, the energy distribution within a burst can be tailored. Four different burst profiles are available: gain-depleted bursts, decreasing bursts, increasing bursts, and flat bursts. In this work, all experiments performed in MHz- and GHz-burst regimes were carried out using the flat-burst configuration. This configuration is generated using an arbitrary waveform generator (AWG) to pre-compensate for gain depletion occurring in the amplification stages by changing the diffraction efficiency of the in-built acousto-optic modulator (AOM).

At the output of the laser, the beam has a Gaussian spatial profile with a diameter of approximately 3 mm. The beam profile was measured and found to be consistent with the certificate of conformance (COC) provided by the manufacturer. The laser beam was then guided to the micromachining workstation through a series of reflective mirrors. The total transmission from the laser output to the workstation ranged between 90 % and 95 %, depending on the optical path length used for beam delivery. This aspect will be discussed in more detail in Section 2.2.4.3.

2.2 Micromachining workstation

This section describes the large-area micromachining workstation used throughout this PhD work. This workstation was specifically designed to provide a high level of flexibility, enabling the implementation of a wide range of diagnostics and experimental configurations in order to gain insight into the physical processes involved in laser–matter interaction under burst irradiation.

The workstation is called FemtoWeld and is based on a granite gantry architecture specified by CELIA, designed by ALPhANOV, and manufactured by Microplan. The use of a granite structure ensures high mechanical stability and vibration damping, which are essential for precise laser processing and time-resolved diagnostics. The laser beam is injected from the rear side of the workstation and propagates towards the front through dedicated apertures machined in the granite structure.

After entering the workstation, the beam is routed using reflective optics towards the processing module. Depending on the experimental configuration, this module enables either conventional Gaussian beam delivery or quasi-Bessel–Gauss beam shaping, both of which are detailed in the following subsections. Additional optical components such as automated power control, or pump–probe diagnostics can be implemented on the station while specific modules can be used to accommodate various experiments, such as chemical etching and surface polishing under controlled atmosphere.

The different experimental configurations implemented on this workstation, together with the associated diagnostics and data-processing methods, are presented in the following subsections.

2.2.1 Automated laser power control

The use of a system enabling precise and repeatable beam attenuation is essential for systematic laser–matter interaction studies. In order to eliminate human-induced variability in laser power management, an automated power control unit was implemented upstream the workstation.. This unit is composed of a motorized rotation stage (Newport / Thorlabs, URS100BCC/K10CR1) coupled with a half-wave plate, and a polarizing beam splitter (PBS). The transmitted laser power was characterized using a power meter (PM) (Gentec, Maestro controller coupled with a UP19K-50F-W5-D sensor). A schematic representation of the setup is shown in Figure 2.2.

The calibration procedure is based on Malus' law [99], which relates the transmitted intensity of linearly polarized light. Transposed to our experimental configuration, this corresponds to measuring the intensity of linearly polarized light transmitted through a beam splitter as a function of the angular orientation of a quarter-wave plate:

$$T(\theta) = T_{max} \cos^2(\theta), \tag{2.1}$$

where T is the transmission (expressed in percent), T_{max} is the maximum transmission (100 %), and θ is the angular position of the quarter-wave plate expressed in radiant.

In the case of this experiment a half-wave plate was used instead of a quarter-wave plate, thus adding a factor 2 to the angle in Equation (2.1). In practice, the zero degree of the half-wave plate is not aligned with the zero position of the rotation stage. The experimental data were therefore fitted using the following modified

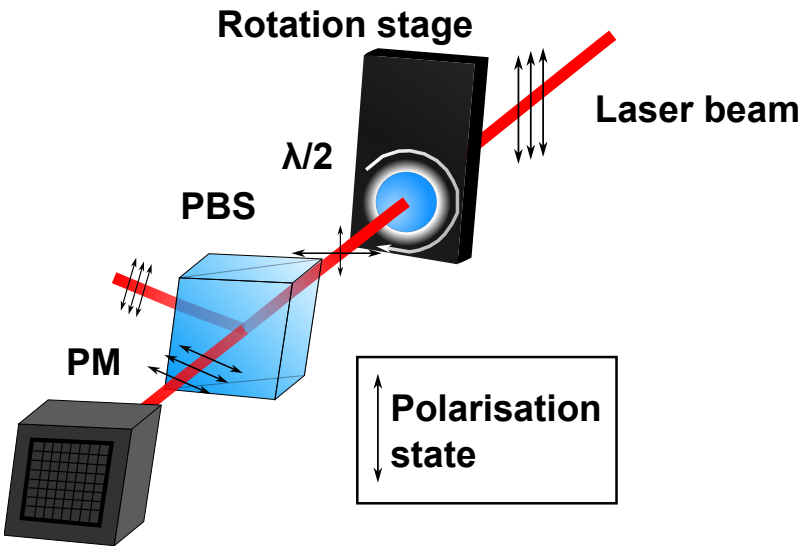

Figure 2.2: Schematic representation of the experimental setup used for automated power control.

expression:

$$T(\theta) = T_{max} \cos^2(2 * \theta + \phi), \tag{2.2}$$

where ϕ is an angular offset. The fitting procedure was performed using a custom Python script. The experimental data and fitted curve are shown in Figure 2.3, and the offset angle was found to be -0.652 rad.

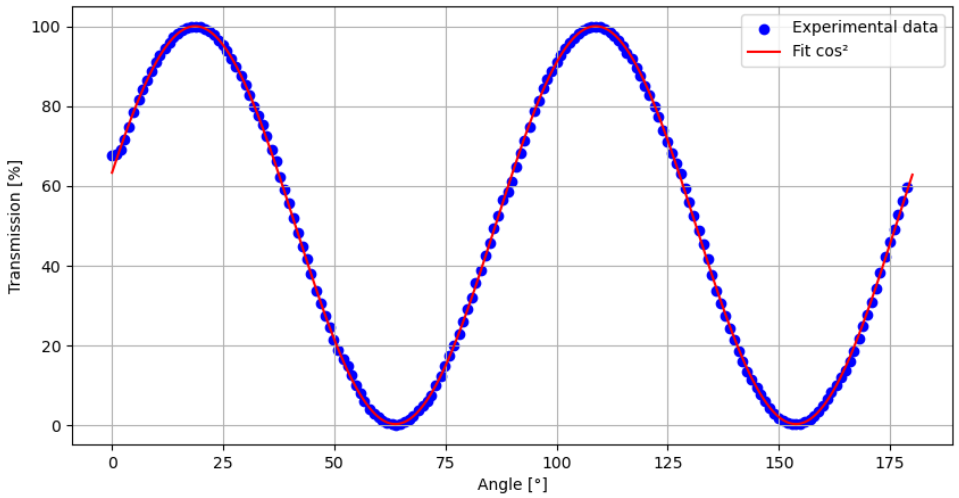

Figure 2.3: Evolution of the transmitted power as a function of the half-wave plate angle.

This calibration leads to the following expression for the transmission:

$$T(\theta) = 100 \cos^2(2\,\theta - 0.652). \tag{2.3}$$

Using this relation, the inverse function can be computed in order to determine the half-wave plate angle required to achieve any given transmission:

$$\theta = \frac{\cos^{-1}\left(\sqrt{\frac{T}{100}}\right) - 0.652}{2}. \tag{2.4}$$

With the automated and calibrated power control in place, the following subsection describes the Gaussian beam configuration used as the reference setup throughout this work.

2.2.2 Set-up with Gaussian beam

The conventional Gaussian beam configuration was used throughout this work for surface polishing experiments, pump–probe shadowgraphy measurements, and as the reference configuration for all subsequent beam-shaping approaches. While the precise optical arrangements are detailed in the corresponding subsections, a general overview of the Gaussian beam setup is provided in Figure 2.4.

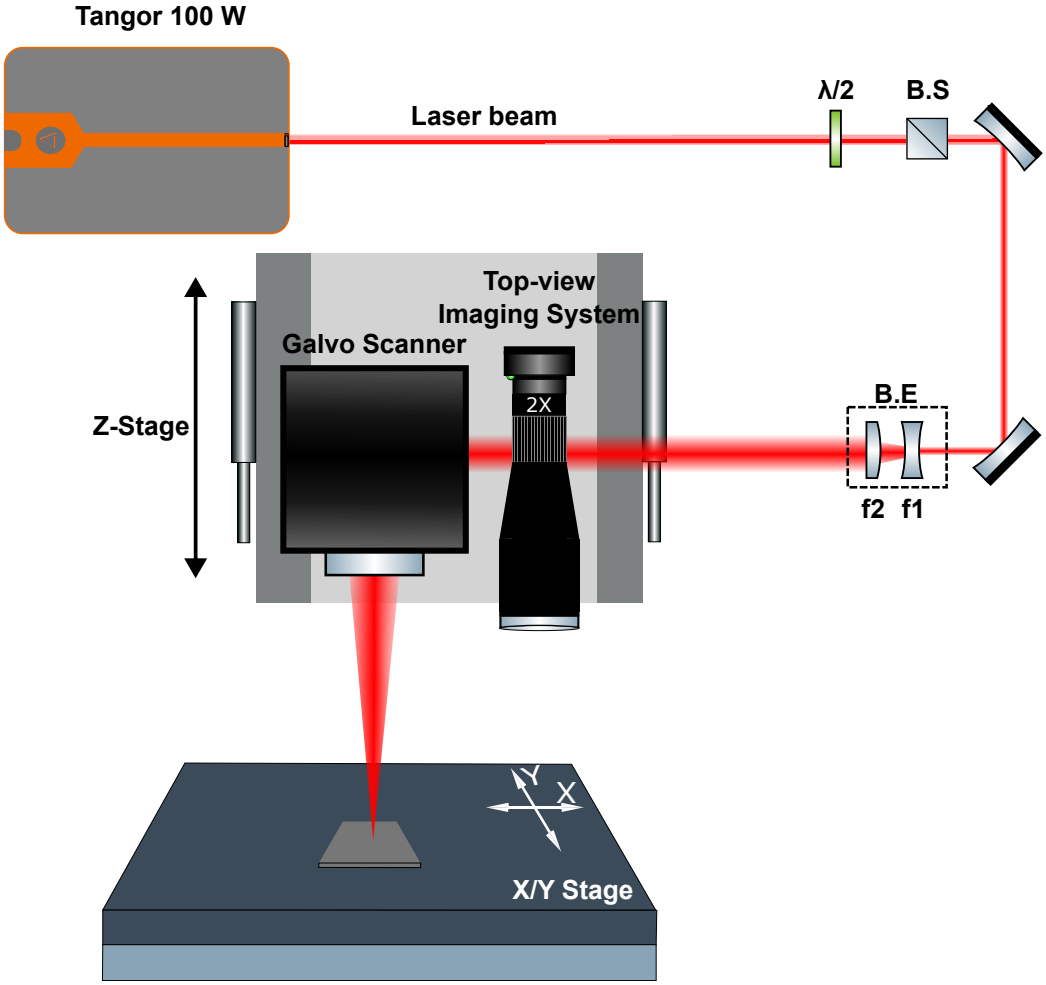

Figure 2.4: Schematic representation of the experimental setup used with a Gaussian beam. B.S: Beam Splitter, B.E: Beam Expander.

As shown in Figure 2.4, a beam expander (B.E) composed of two lenses was used to adjust the beam diameter to a desired value by adjusting the ratio of their

focal lengths. The beam was then delivered to the entrance of the scanner module. The latter consists of a galvo-scanning system; in this work, two different scanners were used: a Scanlab scanner (intelliSCAN III 14, SCANLAB, Germany) and a LASEA scanner (LS-Scan XY 20, LASEA, Belgium), combined with several f-theta lenses. Unless otherwise specified, an f-theta lens with a focal length of 100 mm was used. This lens provides a processing field of view of up to 56.5×56.5 mm^2, an entrance pupil size of 12 mm and a focal spot diameter ranging from 18.0 to 21.5 µm, depending on the incident beam diameter.

The scanner module was mounted on a motorized Z-axis stage (Alio Industries, Arvada, CO, USA, AI-LM-10000-I-PLT-LP), allowing precise adjustment of the focal position relative to the sample surface. The workstation was also equipped with a top-view imaging system consisting of a long-working-distance microscope (Infinity, InfiniMax KX with MX5 objective) coupled to a CMOS camera (Basler acA1440-220uc, 1440×1080 pixels, pixel size 3.45 µm, 227 fps, global shutter). This system enabled accurate positioning of the focal plane on the sample surface.

In addition, a monolithic XY motorized stage (Alio Industries, AI-LM-20000-XY-I-LP) was used to laterally position the sample with respect to the scanner and imaging system, as well as to perform controlled translations during machining experiments. The entire setup was mounted on a stiff granite base to ensure mechanical stability and experimental repeatability. The translation stages, laser gate, laser parameters, image acquisition, and laser power control unit were fully automated and controlled using DMCpro software (v1.0.8, Direct Machining Control, Vilnius, Lithuania), providing precise and repeatable control over all experimental parameters.

While the Gaussian beam configuration serves as the reference setup, additional beam shaping was implemented to generate quasi Bessel–Gauss beams, enabling an extended depth of focus and tailored energy deposition. The corresponding experimental setup is described below.

2.2.3 Set-up with Quasi Bessel-Gauss beam

In this subsection, the experimental implementation of the quasi Bessel–Gauss beam used in this work is described. The theoretical background of Bessel and Bessel–Gauss beams, together with their physical properties, was presented in Section 1.4.2.2. Here, the focus is exclusively placed on the optical setup, alignment procedure, and practical limitations associated with the experimental realization. A schematic view of the experimental setup is provided in Figure 2.5.

As shown in the schematic view of the experimental setup in Figure 2.5, the laser beam is guided to the Bessel module using a series of reflective mirrors. The Bessel module is mounted on the previously described granite gantry and attached to a motorized Z-axis stage, as introduced in Section 2.2.2. The Gaussian beam first passes through a beam expander, allowing precise adjustment of the beam diameter before beam shaping.

The expanded Gaussian beam then propagates through an axicon with an apex angle of 170° (or corresponding to a 5° base angle, depending on the notation), resulting in the generation of a quasi Bessel–Gauss beam. At this point, the primary generated Bessel beam exhibits large transverse and longitudinal dimensions, which are not suitable for bulk modification in dielectric materials. To address this

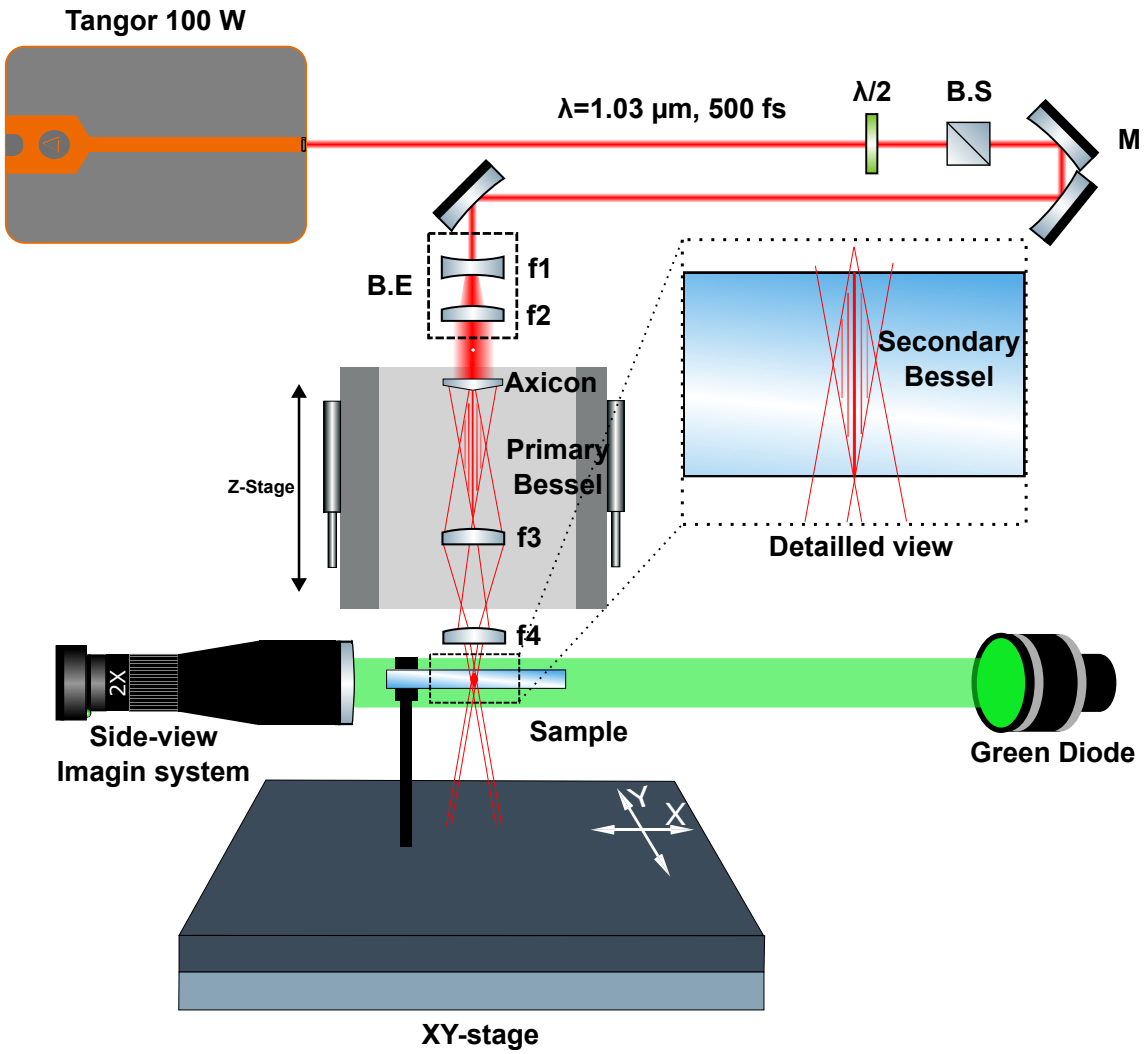

Figure 2.5: Schematic representation of the experimental setup used with a quasi Bessel–Gauss beam.

limitation, the beam subsequently propagates through a 4f optical system. This system reduces the transverse dimensions of the primary Bessel beam by a factor of 12.5, into a smaller secondary Bessel beam with zeroth-order of 3 µm in diameter, enabling bulk laser modification inside dielectric materials.

In addition to the Bessel module, the setup is equipped with a side-view imaging system that allows direct lateral observation of the interaction region during processing. This system relies on a green diode emitting at 520 nm and a long-working-distance InfiniMax microscope, equipped with an optional 2× ring, and a 520 nm bandpass filter. This configuration enables horizontal visualization through the sample while preventing saturation from the processing laser operating at 1030 nm.

Finally, the samples are mounted using various dedicated sample holders depending on the experimental configuration. These holders are fixed to the monolithic XY motorized stage described in the previous section. Additional manual Z-stage and axis-tilt stage for height and planarity setting can also be implemented.

2.2.4 Pump-probe shadowgraphy

In this work, a pump-probe shadowgraphy setup, which requires two synchronized laser pulses with a well-defined temporal delay for active imaging of the interaction zone, was developed for specific experiments in order to investigate laser-induced transient phenomena under burst irradiation. This diagnostics technique enables time-resolved visualization of material responses and plasma dynamics with a sub-nanosecond absolute uncertainty but a 500 fs-relative uncertainty.

The complete setup is divided into four subsections. First, the synchronization strategy between the pump and probe lasers is described. Then, the common optical components shared by the different diagnostics configurations, including the delay line system (Section 2.2.4.2), are introduced. Finally, two imaging configurations are presented: a classical shadowgraphy setup (Section 2.2.4.3) and a shadowgraphy configuration coupled with a Mach-Zehnder interferometer (Section 2.2.4.5).

2.2.4.1 Synchronization module

This subsection details the operating principle of the electronic synchronization module used in the pump-probe experiments. Similar synchronization strategies have previously been reported in the literature [1]. A schematic overview of the synchronization logic is shown in Figure 2.6.

Two laser systems are involved: a Tangor 100 laser, operating as the pump source, and a YUJA laser, used as the probe. The Tangor delivers up to 100 W average power, while the YUJA operates at 10 W. An optical leakage from the Tangor oscillator is injected into an optical fiber and used to seed the pre-amplifier and amplifier of the YUJA. At this oscillator stage, no burst structure is generated, and the YUJA is continuously seeded in the single-pulse regime.

This configuration allows both laser systems to share the same master oscillator and clock frequency, independently of the burst regime selected on the Tangor. As a result, the two lasers remain perfectly synchronized over time, with no temporal walk-off. The master oscillator operates at a repetition rate of 40 MHz, corresponding to a minimum temporal separation of 25 ns between consecutive pulses.

The Tangor pulses are subsequently amplified and temporally structured to produce either single pulses, MHz-bursts, or GHz-bursts and act as the pump, whereas the YUJA delivers single pulses acting as a probe. The pump and probe pulses have a duration of approximately 500 fs, a central wavelength of 1030 nm, and linear polarization.

Since the YUJA laser cannot be externally triggered, it is operated as the master system, while the Tangor acts as the slave. The synchronization procedure aims at synchronizing the output of the two laser systems such as on target the two pulses overlap spatially and temporally with a zero (0) delay at first. This procedure then consists of the following steps :

- **Task 0:** Both laser systems share the same master clock.
- **Task 1:** Manual selection of the pulse injected into the slave amplifier by adjusting the delay of the first pulse picker (Delay 1 = +4.2 µs). Due to electronic limitations of the delay generator (minimum delay ∼75 ns), the

next available pulse at the amplifier repetition rate is selected.[1]

- **Task 2:** Manual selection of the pulse extracted from the slave amplifier using the second pulse picker (Delay 2 = +4.995 ms). Again, the next available pulse is selected due to electronic timing constraints (Here the delay is (5 ms - 5 µs).
- **Task 3:** The Nth pulse of the master laser triggers the $(N+1)^{\text{th}}$ pulse of the slave laser, enabling fine temporal adjustment. The delay applied in Task 1 can be modified in steps of $n \times 25$ ns, while the delay applied in Task 2 can be adjusted in steps of $n \times 5$ µs, allowing extended temporal exploration.

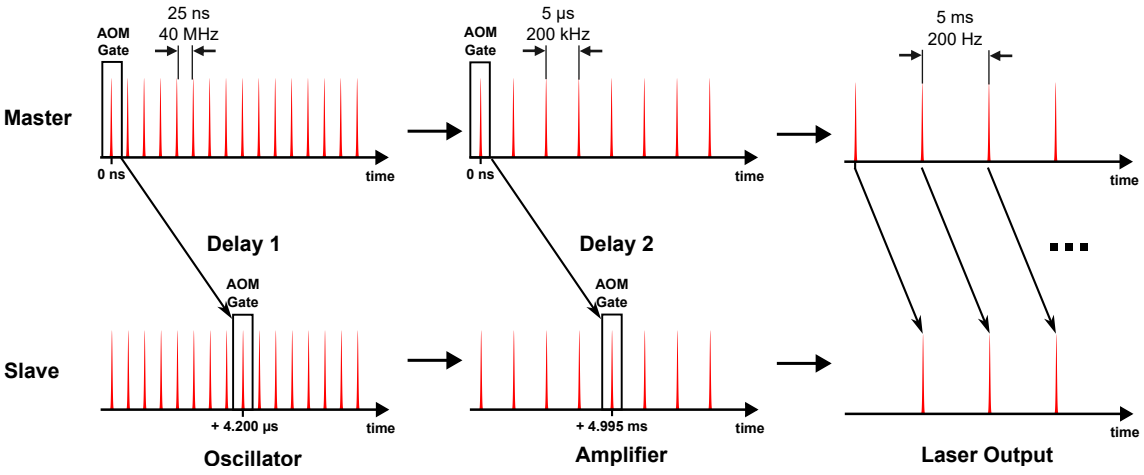

Figure 2.6: Schematic representation of the synchronization procedure.

2.2.4.2 Delay lines

This subsection describes the optical delay line system used to control the fine temporal delay (below 25 ns) between the pump and probe pulses, as the electronics module is limited the fundamental oscillator frequency (40 MHz - 25 ns). A schematic representation of the delay line configuration is shown in Figure 2.7. The above mentioned two laser sources are involved in this setup: the Tangor 100 laser, used as the pump, and the YUJA laser, used as the probe, as introduced in the previous subsection [1].

The probe beam is injected into the delay line module and routed using a sequence of mirrors. After reflections on mirrors M1 and M2, the beam passes through a polarizing beam splitter (PBS). At this stage, the probe polarization is adjusted such that the beam is fully transmitted through the PBS. The beam then propagates towards a motorized translation stage (DDS300, Thorlabs, Germany) providing a maximum travel length of 300 mm.

Four mirrors (M3, M4, M7, and M8) are mounted on the translation stage to form a folded optical path. After transmission through the PBS, the beam is successively reflected by mirrors M3 and M4 towards mirrors M5 and M6, which redirect it to

[1]The delay is not exactly +4.485 µs (5 µs - 25 ns) due to an intrinsic offset between the pulse pickers when no external triggering is applied.

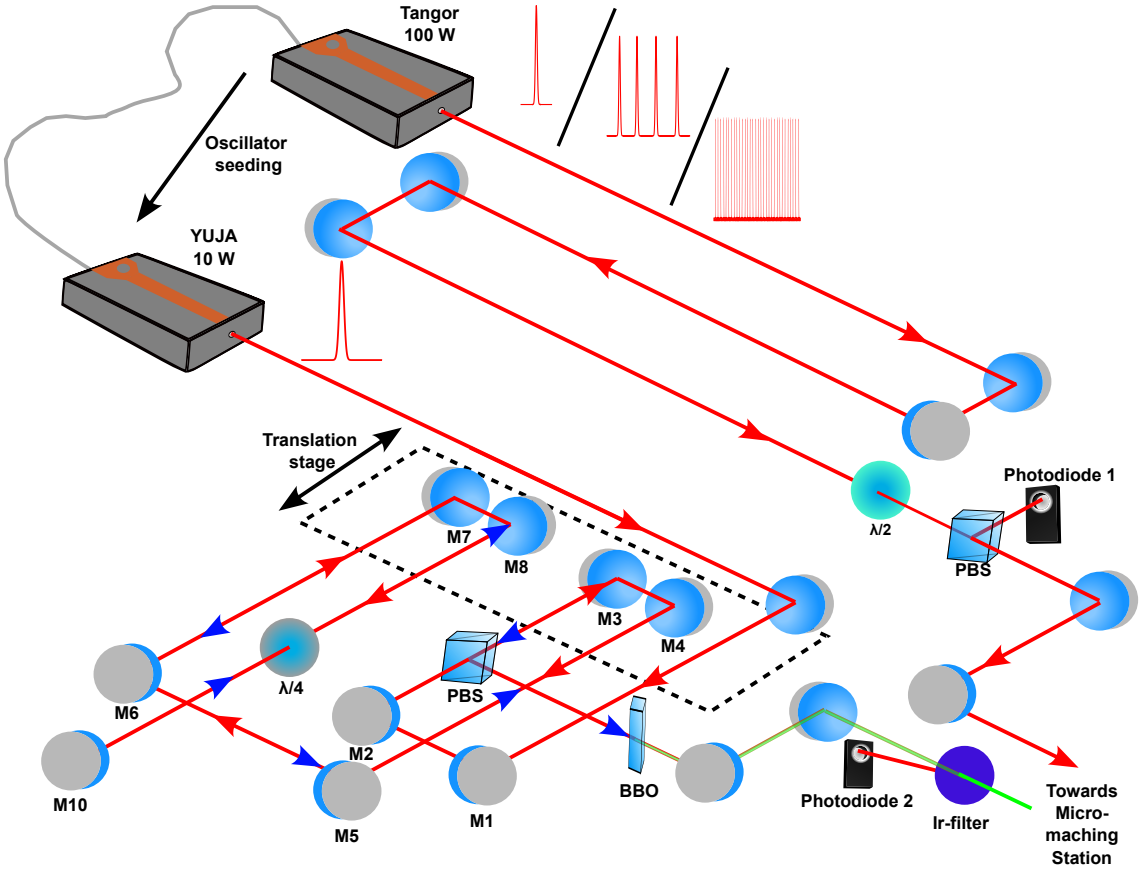

Figure 2.7: Schematic representation of the pump-probe delay line setup. BBO : barium borate crystal.

mirrors M7 and M8. Following this path, the beam passes through a quarter-wave plate and is reflected by mirror M10, aligned at normal incidence. The beam then retraces the same optical path in reverse, passing through the quarter-wave plate a second time, resulting in a total phase shift of $\pi/2$.

Upon returning to the PBS, the polarization state of the beam is rotated such that it is now reflected towards a nonlinear BBO crystal, where second-harmonic generation (SHG) occurs. After the BBO crystal, the probe beam consists of approximately 30 % of frequency-doubled light at 515 nm and 70 % of the fundamental wavelength at 1030 nm, which is not perfectly optimized but suitable for the experiment.

The residual infrared component of the beam is separated using an angled IR filter and collected by a fast photodiode (Alphalas, UPD-35-IR2-P), which is connected to a 4 GHz oscilloscope (WaveRunner 9404, Teledyne LeCroy). This detection scheme enables real-time monitoring of the probe arrival time and precise calibration of the optical delay.

Using the motorized translation stage, the probe delay can be continuously adjusted over a temporal range of approximately 8 ns. This configuration requires precise optical alignment to ensure that variations in the optical path length, corresponding to 2.4 m of beam propagation, do not result in beam clipping or spatial

drift at the output.

The pump beam, in contrast, is delivered to the machining station via an extended optical path to compensate for the delay introduced by the propagation of the probe seed through the optical fiber used to seed the YUJA laser. The length of this pump delay line is adjustable, and multiple optical path configurations are implemented to bridge the temporal gap between the maximum mechanical delay provided by the translation stage and two consecutive pulses of the master oscillator. Electronic delays can be set in increments of 25 ns, while the mechanical delay line provides a continuous adjustment range of approximately 8 ns. Three pump path configurations, corresponding to optical path differences of 0, -8 m, and -16 m, ensure continuous temporal coverage between 0 and 25 ns. Immediately before reaching the station, a half-wave plate and a polarizing beam splitter are used to divert a small fraction of the pump beam toward an identical fast photodiode, also connected to the 4 GHz oscilloscope. This photodiode is positioned such that, after the PBS, the pump and probe beams traverse essentially the same optical distance, within ± 3 mm, which corresponds to an absolute delay uncertainty of $\pm$ 10 ps.

2.2.4.3 Shadowgraphy

This subsection describes the classical pump–probe shadowgraphy setup used to investigate laser-induced modifications. A schematic view of the experimental setup is shown in Fig. 2.8.

The pump beam exits the station via mirror M1 and is directed sequentially through mirrors M2 to M5. Beyond M5, the beam enters the Bessel module previously described in Section 2.2.3.

The probe beam exits the station via mirror M1v and is directed toward M2v. At this stage, the probe beam is at a different height than the pump. To achieve lateral observation, a custom U-shaped machined breadboard was implemented in the micro-machining workstation, at the appropriate height. The beam then continues through M3v and M4v before passing a polarizing beam splitter (PBS) (In this set-up the PBS is used as a mirror but will be used in the Mach-Zenhder set-up). The polarization is adjusted to ensure total reflection toward M5v, causing the probe beam to overlap with the pump beam and collect imaging information of the laser-induced modifications. Finally, the beam is imaged by a long-distance microscope (Infinity, InfiniMax KX with MX6 objective), equipped with a 2× ring and three 515 nm bandpass filters (two FWHM 40 nm, one FWHM 10 nm) to reduce the intensity of plasma generated by the pump and a BASLER camera (CMOS 1/2.9" 1440x1080p 220fps, minimal exposition time of 21 µs) .

A delay control unit, consisting of three delay generators (Aerodiode Tombak), is used to synchronize the pump and probe beams, and to trigger the camera. The first two devices control the delays corresponding to Task 1 and Task 2 (see Section 2.2.4.1), while the third serves as a gate for both lasers and triggers image acquisition for the microscope imaging system. The latter used the generated gate signal from the XY-stage controller and reproduced it with perfect form and an adjustable delay.

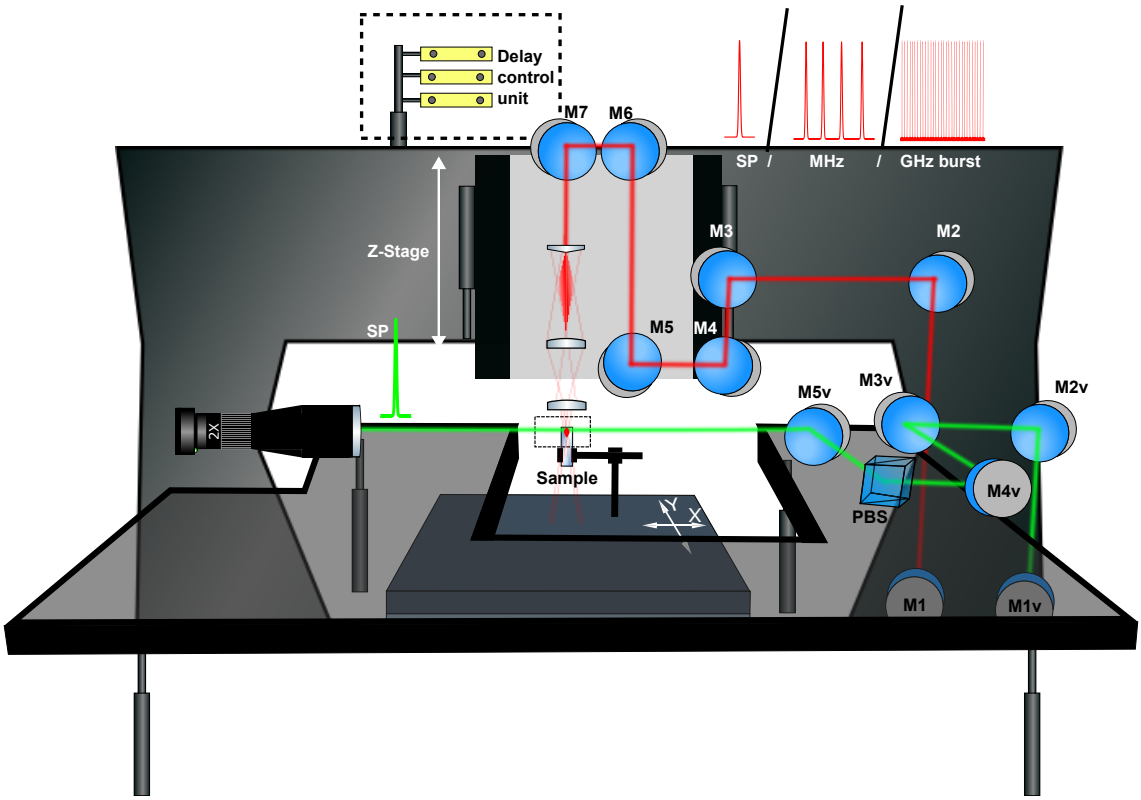

Figure 2.8: Schematic view of the setup for shadowgraphy experiments.

2.2.4.4 Data processing for shadowgraphy

This section describes the data processing workflow applied to the shadowgraphy measurements presented in Section 2.2.4.3. The different processing steps are summarized in Fig. 2.9.

For each investigated delay, two images are acquired. The first image, referred to as the background image, is recorded with the probe and without the pump. The second image, referred to as the modification image, is acquired with the probe and the pump laser inducing a modification in the sample.

Both images are processed using a Fast Fourier Transform (FFT) and an inverse FFT (iFFT). The FFT/iFFT procedure is used exclusively to retrieve the complex representation of the images, without applying any spatial filtering. Each processed image can therefore be written as:

$$z_i(x,y) = r_i(x,y)e^{i\phi_i(x,y)}, \tag{2.5}$$

where r_i represents the amplitude and ϕ_i the phase of the complex signal at any given x,y of the image and the i denote the category of the image, either background or modification.

The modification image is then normalized by the background image according to:

$$\begin{aligned} z_m &= r_m e^{i\phi_m}, \quad z_b = r_b e^{i\phi_b}, \\ \frac{z_m}{z_b} &= \frac{r_m}{r_b} e^{i(\phi_m - \phi_b)}. \end{aligned} \tag{2.6}$$

In the present work, the quantity of interest is the relative attenuation of the probe beam induced by the plasma since the phase difference $\phi_m - \phi_b$ remains

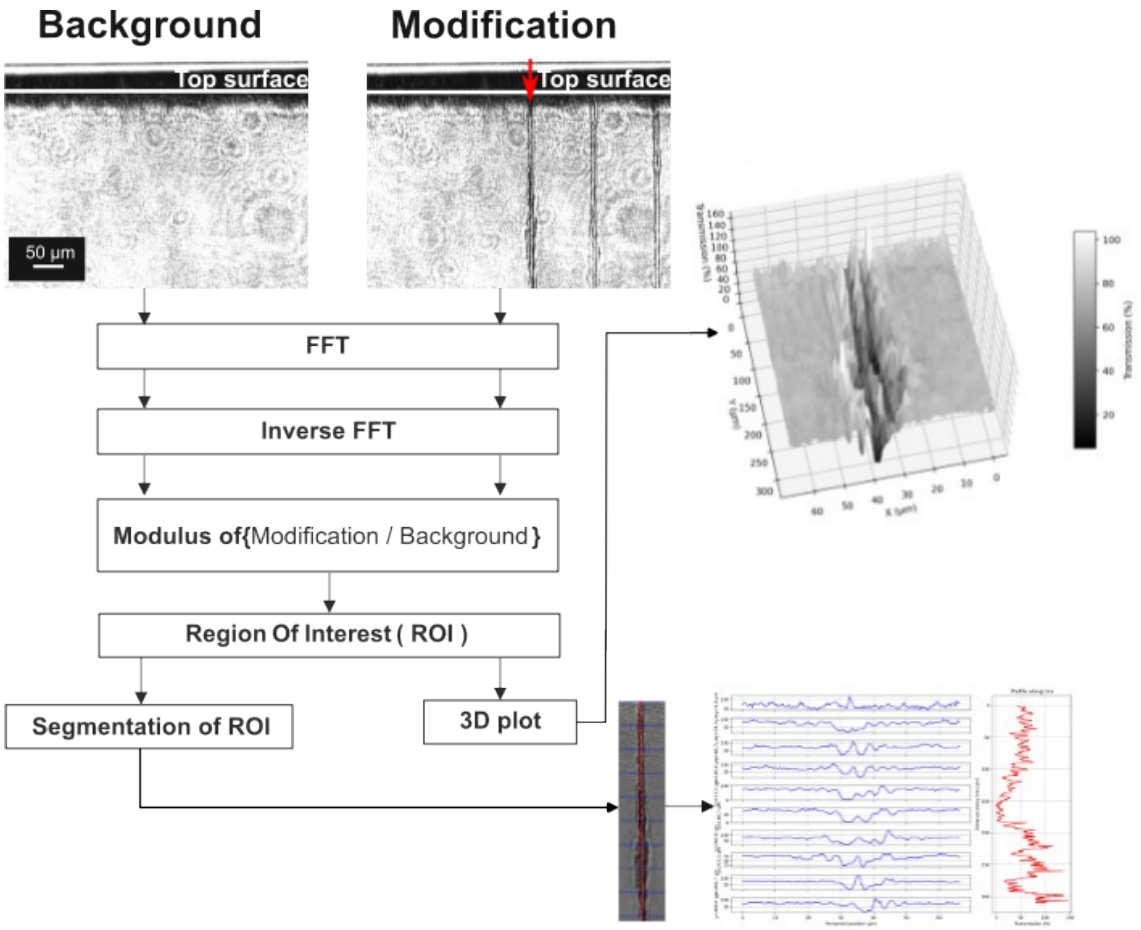

Figure 2.9: Workflow of the data processing applied to pump–probe shadowgraphy measurements.

negligible in the present experimental conditions as no artificial structured light is induced and thus, no characteristic frequencies are present in the image. This information is extracted from the amplitude of the normalized signal, given by:

$$\left|\frac{z_m}{z_b}\right| = \frac{r_m}{r_b}. \tag{2.7}$$

After normalization, a region of interest (ROI) is selected. Two types of analysis are then performed. First, the ROI is segmented using multiple horizontal line profiles, as illustrated in Fig. 2.9. The pixel values along these lines are extracted to generate one-dimensional transmission profiles. Second, the ROI is rendered as a three-dimensional map to visualize the spatial distribution of probe attenuation.

All extracted data are expressed in terms of normalized transmission, corresponding to the fraction of probe intensity transmitted through the laser-induced plasma at the time of acquisition. While classical shadowgraphy provides quantitative information on probe attenuation, additional phase-sensitive diagnostics are required to retrieve confirmed plasma properties. This motivates the implementation of a Mach–Zehnder interferometer, described in the following section.

2.2.4.5 Mach-Zehnder interferometer

This section describes the pump-probe shadowgraphy setup combined with a Mach-Zehnder interferometer (MZI), used to investigate laser-induced modifications and retrieve the electron density. A schematic view of the experimental setup is shown in Fig. 2.10. The pump beam follows the exact same optical path as described in Section 2.2.4.3. The probe beam also follows the same path as previously described

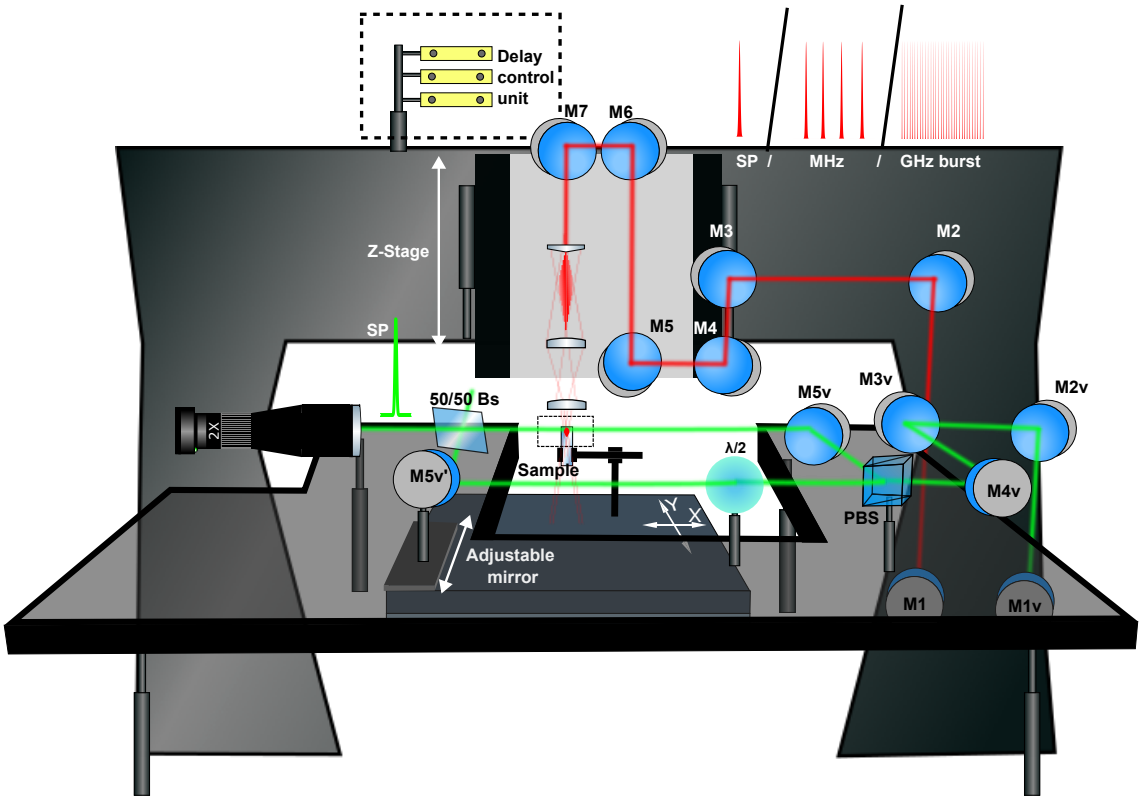

Figure 2.10: Schematic view of the experimental setup for shadowgraphy combined with a Mach-Zehnder interferometer.

until it reaches the polarizing beam splitter (PBS). In this configuration, the polarization is adjusted to ensure a 50/50 beam splitting. Fifty percent of the probe beam are directed toward mirror M5v, where they briefly overlap with the pump beam and collects imaging information of the laser-induced modifications. The remaining 50% are directed toward a half-wave plate to ensure that both interferometer arms have identical polarization states, allowing interference.

After the half-wave plate, the reference arm reaches mirror M5v', which is mounted on a manual translation stage with a travel range of 10 mm. This stage is used to accurately adjust the optical path length difference between the two interferometer arms. The two beams are then recombined using a 50/50 beam splitter and imaged by a long-distance microscope (InfiniMax KX with MX6 objective), equipped with a 2× ring and three 515 nm bandpass filters (two with a FWHM of 40 nm and one with a FWHM of 10 nm) to reduce the plasma emission generated by the pump. The interference pattern is recorded using a CMOS camera (Basler, 1/2.9", 1440×1080 pixels, 220 fps).

To obtain a stable interference pattern, both spatial and temporal overlap be-

tween the two interferometer arms must be carefully achieved. A delay control unit identical to the one described in Section 2.2.4.3 is also implemented to synchronize the pump and probe beams and trigger image acquisition.

2.2.4.6 Data Processing for Mach-Zehnder Interferometry

This section describes the data processing workflow applied to the interferometry measurements obtained with the setup presented in Section 2.2.4.5. The workflow is summarized in Fig. 2.11.

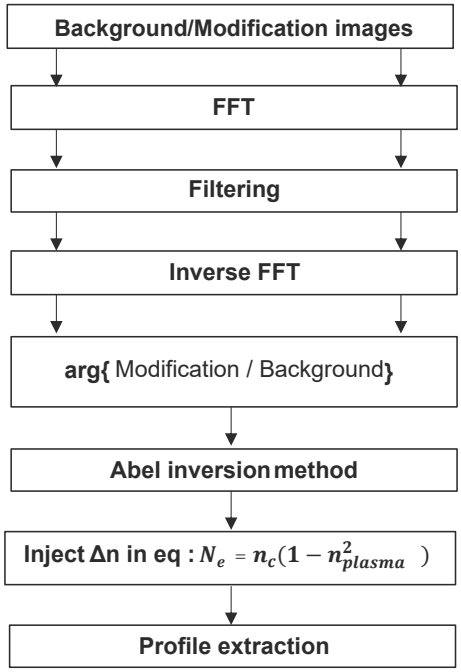

Figure 2.11: Workflow of the data processing applied to pump–probe shadowgraphy measurements coupled with the Mach-Zehnder interferometer.

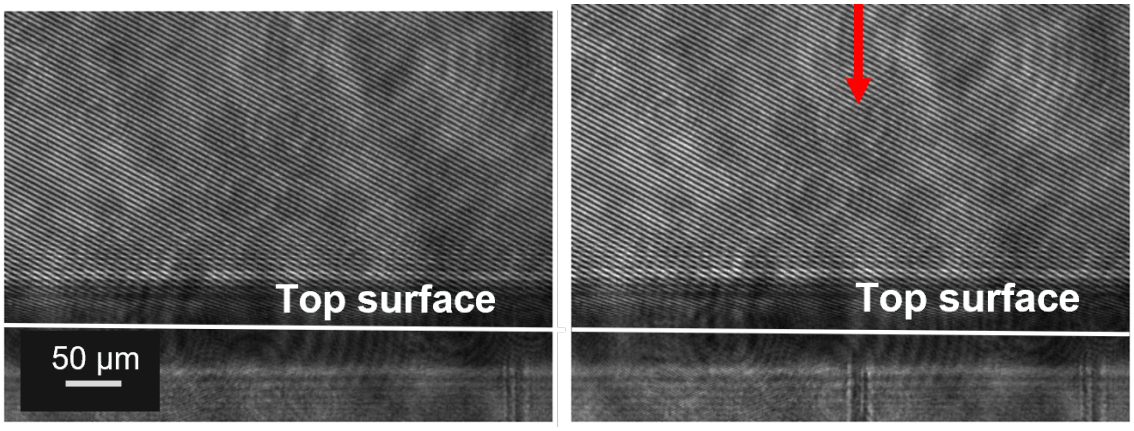

(a) Background image. (b) Modification image.

Figure 2.12: Example of images acquired with the Mach-Zehnder interferometer.

For each investigated delay, two images are acquired. The background image (Fig. 2.12a) is recorded with the probe and without the pump, while the modification

image (Fig. 2.12b) is recorded with the probe and pump laser inducing a modification in the sample.

Both images are processed using a Fast Fourier Transform (FFT). The resulting Fourier space representation is shown in Fig. 2.13a. A radial Hanning filter [7], defined in Eq. (2.9), is then applied to isolate the first-order frequency corresponding to the fringe pattern. After filtering, an inverse FFT (iFFT) is applied to recover the filtered spatial domain signal.

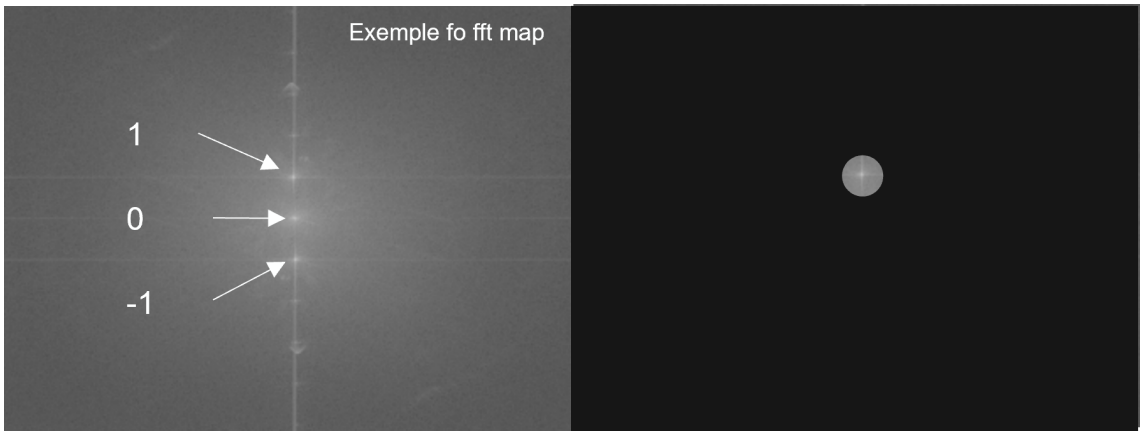

(a) FFT maps obtained with MZI. (b) Filtered FFT maps.

Figure 2.13: Example of filtering applied to the FFT maps.

The radial distance is defined as:

$$\Delta r = \sqrt{(f_x - f_{0x})^2 + (f_y - f_{0y})^2}, \tag{2.8}$$

where f_x and f_y are the frequency component in the FFT image while f_{0x} and f_{0y} are the coordinates of the first order peak, and the radial Hanning filter is:

$$H(\Delta r) = \begin{cases} \frac{1}{2}\left[1 + \cos\left(\pi \frac{\Delta r}{r_0}\right)\right], & \Delta r < r_0 \\ 0, & \text{otherwise,} \end{cases} \tag{2.9}$$

where r_0 is the filter width.

Each processed image can be expressed as a complex signal:

$$z_i = r_i e^{i\phi_i}, \tag{2.10}$$

where r_i is the amplitude and ϕ_i the phase.

The modification image is divided by the background image:

$$\begin{aligned} &z_m = r_m e^{i\phi_m}, \quad z_b = r_b e^{i\phi_b}, \\ &\frac{z_m}{z_b} = \frac{r_m}{r_b} e^{i(\phi_m - \phi_b)}. \end{aligned} \tag{2.11}$$

The relative phase shift of the probe beam induced by the plasma is obtained from:

$$\arg\left(\frac{z_m}{z_b}\right) = \phi_m - \phi_b. \tag{2.12}$$

After division, the phase difference maps are obtained and all maps are renormalized by subtracting an off-set, which is defined as the average value in a zone unaffected by the physical phenomena, such that the image background of the obtained images corresponds to zero dephasing. The phase maps are then deconvoluted along the propagation axis of the probe beam. In the simple 2D case the relation between the phase shift and the change in refractive index is given by Equation (2.13). However, under the assumption of cylindrical symmetry, an inverse Abel transformation can be applied [14, 100]. The results are shown in Fig. 2.14b.

$$\Delta n = \frac{\lambda}{2\pi L} \times \Delta\phi \tag{2.13}$$

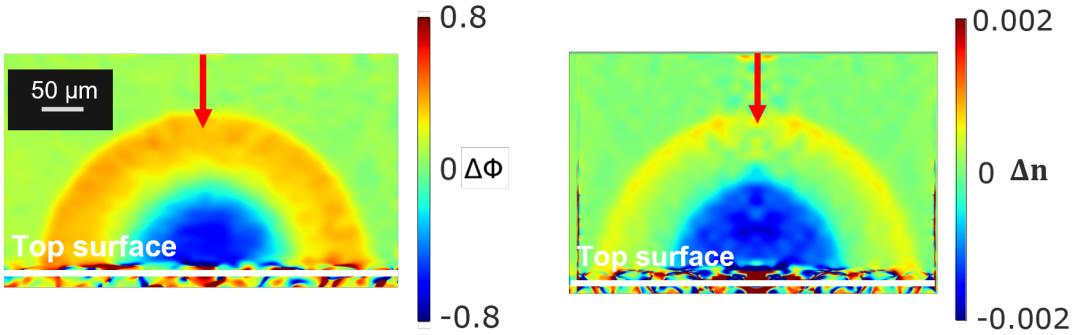

(a) Phase map. Colorbar units: rad.

(b) Refractive index change map.

Figure 2.14: Example of colormaps obtained with the MZI workflow from the images in Figure 2.12.

Finally, the electron density map is calculated from the refractive index maps using:

$$\begin{aligned} \eta_{\text{plasma}} &= \eta_{\text{air}} + \Delta\eta, \\ N_e &= n_c(1 - \eta^2_{\text{plasma}}), \end{aligned} \tag{2.14}$$

where η_i is the refractive index of the species i, N_e the electron plasma density and n_c the critical plasma density. The resulting electron density map is shown in Fig. 2.15.

2.3 Measuring equipments, sample preparation & methods

In this section, the different measurement equipments used throughout this work are introduced. The section is divided into two parts. The first part presents the tools for laser beam characterization , while the second part describes the equipment for sample characterization.

2.3.1 Laser beam characterization tools

Accurate knowledge of the laser beam parameters is critical in laser processing experiments to ensure reproducibility and consistency of the results. Key parameters

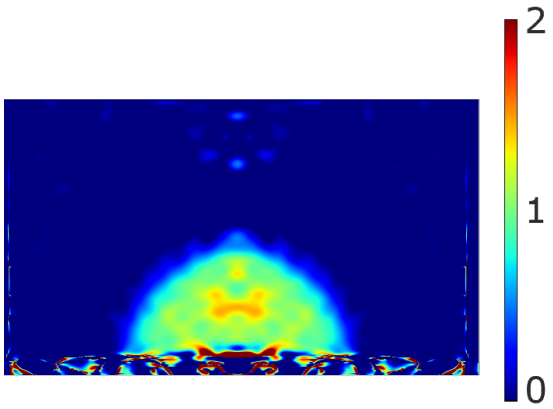

Figure 2.15: Example of electron density map. Colorbar units: $10^{19}\,\mathrm{m}^{-3}$.

such as pulse duration, pulse energy, beam size, and focal spot size must therefore be carefully characterized. In addition, the use of spatial beam shaping requires a detailed analysis of the spatial energy distribution.

The following instruments were used for laser beam characterization:

- **Power meter:** used to measure the average power and derive the energy per pulse (UP19K-50F-W5-D0, MAESTRO, Gentec).
- **Autocorrelator:** used to measure the pulse duration (ROC Single-Shot Autocorrelator, FemtoEasy).
- **CMOS camera:** used to measure the beam profile ($1/e^2$) and derive the numerical aperture or divergence of the beam (DAT-WinCamD LCM4). The CMOS camera was coupled with a homemade calibrated magnification system of up to 20x magnification for accurate measurement of the micro-beam.
- **Home-made Z-profiling:** A dedicated measurement method was developed based on a custom Python scripted which coupled the CMOS camera and a motorized translation stage (BB300, Thorlabs), enabling precise axial scanning and three-dimensional reconstruction of the Bessel beam intensity profile.

2.3.2 Etching set-up

In this work, chemical etching was employed for specific experiments in order to reveal or enhance laser-induced modifications. The experimental setup used for the etching process is shown in Figure 2.16. It consists of an ultrasonic bath with temperature control, allowing operation up to 90 °C.

To limit thermal gradients with the surrounding environment, the bath temperature was set to 55 °C. The samples were immersed for a defined duration in an aqueous potassium hydroxide (KOH) solution with a concentration of 10 $\mathrm{mol{\cdot}L^{-1}}$, while ultrasonic agitation was applied to ensure homogeneous etching conditions. After the etching process, the samples were removed from the solution and thoroughly cleaned with acetone.

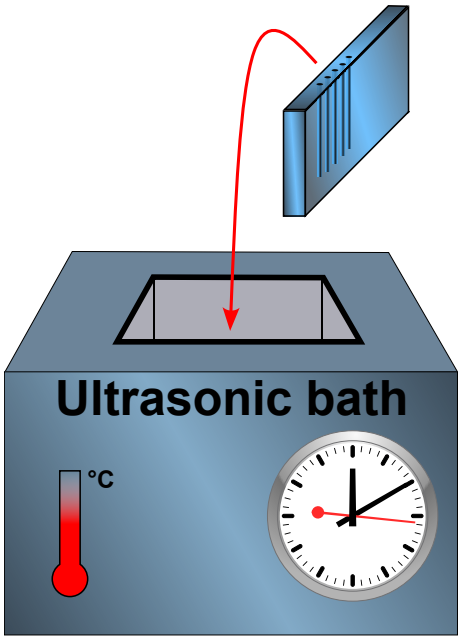

Figure 2.16: Schematic representation of the experimental setup used for chemical etching.

2.3.3 Sample characterization

The experiments presented in this work were carried out on various materials, including metals, semiconductors, and dielectrics. Each material required specific characterization techniques adapted to its optical and structural properties. The measurement tools used are listed below.

- **Optical microscope:** used to measure hole depths in dielectric materials and to obtain close-up images for polishing experiments. The measuring microscope used was an MF-B1010D (Mitutoyo), equipped with encoders allowing measurements with an accuracy of 2.2 µm over 1 mm, 2.4 over 10 mm, and 3.2 mm over 100 mm. The measuring field is 100 x 100 mm^2 in the XY plan. Several objectives were available (3×, 10×, 20×, and 50×).

- **Confocal microscope:** used to measure surface roughness and surface topography for polishing experiments. This technique was generally not suitable for dielectric samples due to insufficient reflected signal. The instrument used was a Smartproof 5 (ZEISS), equipped with objectives ranging from 2.5× to 100×. The 50x objective was the most used and displays the following caracteristic: 0.95 NA, 0.22 µm of optical resolution, 0.13 µm of spatial resolution in XY, a field of view of 225 × 225 µm and a vertical and horizontal uncertainty of 0.1 µm over a 1 mm measurement.

- **Scanning Electron Microscope (SEM):** used to analyze surface morphologies of all samples, with a particular focus on metallic samples and polishing experiments. The SEM used was a TESCAN (SEM EDX EBSD) microscope. It also provides elemental analysis capabilities with a spatial resolution of approximately 10 μm.

2.3.4 Methods

Surface roughness and ISO standards: In this work, surface roughness measurements were performed using the optical profilometer described above. Several roughness parameters were extracted to characterize the surface morphology, following ISO standards (ISO 21920 and ISO 25178).

Two main categories of roughness parameters are commonly used: line-based measurements, denoted by R_{xxx}, and surface-based measurements, denoted by S_{xxx}. Both approaches are relevant and are used throughout this work. However, line-based parameters are more widely adopted in both scientific literature and industrial practice and are therefore prioritized for comparison.

Once these two categories are defined, several sub-parameters can be introduced, each describing a specific aspect of the surface morphology.

- The most commonly used parameter is R_a or S_a, defined as the arithmetic mean height, i.e., the average of the absolute profile deviations along the sampling length:
$$R_a = \frac{1}{l} \int_l |Z(x)| \, dx, \tag{2.15}$$

- The second parameter is R_q or S_q, defined as the root mean square deviation of the profile:
$$R_q = \sqrt{\frac{1}{l} \int_l Z^2(x) \, dx}, \tag{2.16}$$

- The parameter R_z or S_z corresponds to the maximum height difference of the profile and is defined as the vertical distance between the highest peak and the deepest valley:
$$R_z = \max(Z) - \min(Z).$$

- The skewness, R_{sk} or S_{sk}, provides information on the asymmetry of the height distribution. A negative skewness indicates a surface dominated by valleys, whereas a positive value indicates a surface dominated by peaks:
$$R_{sk} = \frac{1}{R_q^3} \left[\frac{1}{l} \int_l Z^3(x) \, dx \right], \tag{2.17}$$

- Finally, the kurtosis, R_{ku} or S_{ku}, characterizes the sharpness of the height distribution. Values greater than 3 indicate a surface dominated by sharp peaks, while values below 3 correspond to smoother height variations:
$$R_{ku} = \frac{1}{R_q^4} \left[\frac{1}{l} \int_l Z^4(x) \, dx \right], \tag{2.18}$$

Overlap Computation: This paragraph presents the definition and computation of the area overlap for the laser scanning experiments. The schematic shown in Figure 2.17 illustrates all the parameters required to calculate the cumulative dose.

The spot-to-spot distance (S-2-S) corresponds to the center-to-center distance between consecutive pulses along a scanning line (x-axis), while the line-to-line distance (L-2-L) corresponds to the distance between adjacent scanning lines along the

y-axis. From these distances, the number of points along the X-axis (N_x) and Y-axis (N_y) can be determined.

With the average laser power (P_{mean}) and the pulse repetition frequency (f_{rep}), pulse or burst energy can be calculated as:

$$E_{\text{burst}} = \frac{P_{\text{mean}}}{f_{\text{rep}}}$$

Finally, the cumulative dose is obtained from the number of pulses and burst energy:

$$\text{Dose (J.mm}^{-2}) = E_{\text{burst}} \times N_x \times N_y \tag{2.19}$$

This metric provides a consistent measure of the total energy delivered per unit area and will be used for comparison throughout the following sections.

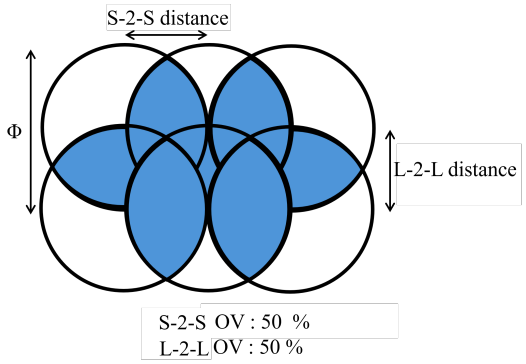

Figure 2.17: Schematic of laser scanning tracks, illustrating the spot-to-spot (S-2-S) and line-to-line (L-2-L) distances. where Φ is the beam spot size.

2.4 Materials of interest

The interaction between ultrashort laser pulses and matter strongly depends on the material properties, such as the thermal conductivity, melting temperature, and band gap. In this work, a broad range of materials was investigated, including metals, dielectrics, and semiconductors. The materials used throughout this work, and their material properties are presented in the following.

2.4.1 Metals

The investigated metals are listed below, together with their main physical properties and typical fields of application.[2]

- **Stainless steel AISI 316L**: Austenitic chromium–nickel-molybdenum stainless steel with low carbon content, offering excellent corrosion resistance, particularly in non-oxidizing acids and chlorine-containing environments. Its melting ranges between 1370 and 1400° C, and its thermal conductivity is approximately 16.3 $\text{W m}^{-1}\,\text{K}^{-1}$ at 23° C. This material is widely used in the petrochemical, biomedical, and optical industries.

[2]All data was taken from the component data sheet from the GoodFellow website

- **Titanium alloy Ti-6Al-4V (TA6V)**: A titanium-aluminium-vanadium alloy combining high mechanical strength with low density and good corrosion resistance. Its melting lies between 1600 and 1650° C, and its thermal conductivity is about 5.8 $\mathrm{W\,m^{-1}\,K^{-1}}$ at 23° C. Typical applications include aeronautics, biomedical implants, and high-performance mechanical components.

- **Aluminium alloy 2024**: An aluminium–copper alloy primarily used for its high mechanical strength and good fatigue resistance. It exhibits a melting temperature around 510° C and a thermal conductivity of approximately 121 $\mathrm{W\,m^{-1}\,K^{-1}}$ at 25° C. This alloy is mainly employed in the aeronautical industry and other applications requiring a high strength-to-weight ratio.

- **Aluminium alloy 7075**: An aluminium–zinc alloy known for its very high specific strength. Its melting ranges from 447 to 635° C, with a thermal conductivity of about 130 $\mathrm{W\,m^{-1}\,K^{-1}}$ at 20° C. It is widely used in transportation industries, including aerospace, automotive, and marine applications.

2.4.2 Dielectrics

- **Soda-lime glass**: One of the most widely used commercial alkaline glasses, representing approximately 80 % of global glass production. Its typical composition is around 70 % SiO_2, 15 % Na_2O, and 9 % CaO, although variations may occur between batches. Soda-lime glass has a relatively low softening temperature of about 750° C [101] and a high thermal expansion coefficient of $9 \times 10^{-6} K^{-1}$ [102], making it sensitive to thermal shock. Its optical band gap is approximately 3.9 eV [103].

- **Fused silica**: A synthetic, non-crystalline material composed almost exclusively of SiO_2. It undergoes high-temperature treatments (around 2000° C) to reduce impurities and structural defects. Fused silica exhibits a very low thermal expansion coefficient of $0.6 \times 10^{-6} K^{-1}$ [102], providing excellent resistance to thermal shock and steep thermal gradients. Its softening temperature is about 1665° C [101], and it has a wide band gap of approximately 9 eV [104].

- **AF32 glass**: An alkali-free aluminoborosilicate glass developed by Schott and widely used in the electronics and display industry for substrates and cover glasses. Its typical composition is based on SiO_2–B_2O_3–Al_2O_3, without alkali oxides, providing high chemical durability and excellent thermal stability. AF32 glass exhibits a softening temperature of approximately 970° C [105]. Its coefficient of thermal expansion is relatively low, about $3.2 \times 10^{-6}\,\mathrm{K^{-1}}$ in the temperature range 20–300° C [105], offering good resistance to thermal shock compared to soda-lime glass.

Chapter 3

Surface processing of metallic materials

In this chapter, the main goal is to investigate the response or the morphology changes of metallic surfaces under laser irradiation operating in burst mode for metals[1], in order to identify potential applications and limitations. The burst modes studied are MHz- and GHz-bursts, which combine pulse durations of hundreds of femtoseconds with burst durations in the range of hundreds of nanoseconds. This allows for both high processing precision (fs) and high ablation rates (ns).

It should be noted that the pulse-to-pulse delays within the bursts (0.8 ns in the GHz-burst with a pulse repetition rate of 1.28 GHz, and 25 ns in the MHz-burst with a pulse repetition rate of 40 MHz) are significantly shorter than the heat diffusion times over the length of 25 μm in metals ($\sim$ 8 µs for Al alloys, and 100–160 µs for AISI 316L and Ti6Al4V, respectively) computed from Eq. (1.3). Cumulative energy deposition and heat accumulation are therefore expected.

This chapter provides a comparative study between the different GHz-burst regimes. Firstly, laser polishing of AISI 316L was investigated regarding the influence of beam spot size, burst energy, and burst shape, using Gaussian and vortex beam profiles. Secondly, a double-step process based on a first laser milled surface followed by a polishing step using long bursts is then presented. An optimization of the molten layer generation is then performed using these long GHz-bursts. Further tests have been carried out, notably a study of the single spot interaction in MHz-burst mode and the molten layer generation on Ti6Al4V which are presented in Appendices C and D, respectively. Finally, some preliminary material reshaping results are presented for Al7075 using the GHz-burst mode in Appendix E.

3.1 Investigation of different beam shapes

AISI 316L steel alloy is widely used in the industry. It would be highly interesting to have a single laser-based machine-tool with the capability to carry out an engraving step (material removal) and a finishing step (polishing) without replacing the sample between the two steps. So, laser polishing which is based on the principle of melting a thin surface layer is used in order to reduce the roughness due to surface tension forces. This process has been already reported using longer pulses, as it allows

[1]Only 316L AISI will be presented in this chapter as other metals are presented in Appendix and follow the same general trend.

the study of surface modification under controlled energy deposition. Following the recommendations in [96], a cover gas was applied during polishing to improve surface quality and reduce oxidation. The gas delivery system was designed with a circular base and an open top, providing a homogeneous flow over the target through eight distribution pipes each delivering the gas through a low-density and porous aluminum floor, and the gas rate was adjusted with a control valve integrated into the experimental setup.

To accommodate the gas cover, the standard setup presented in Fig. 2.4 was modified, as illustrated in Fig. 3.1. This setup provides a controlled environment for systematic investigations of polishing under different beam and burst conditions.

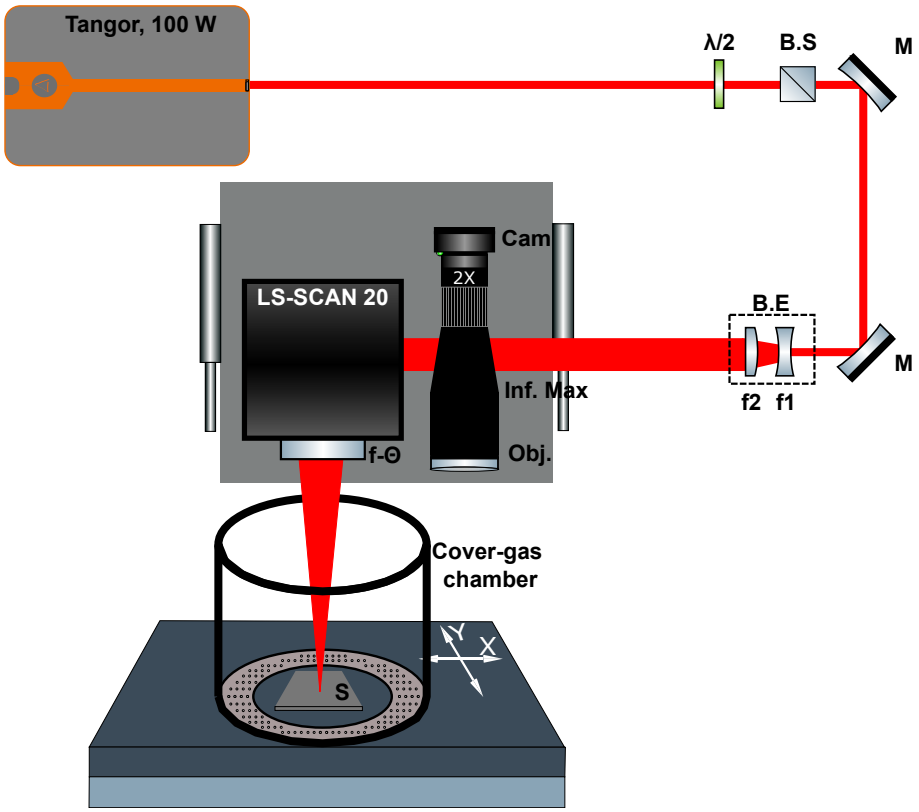

Figure 3.1: Schematic view of the experimental setup used for polishing experiments. B.S : Beam Splitter, B.E : Beam Expander, Cam : Camera, Inf.Max : Infini Max, Obj: Objectiv, M : Mirror, S: Sample.

The first metal investigated in this study is AISI 316L stainless steel. For reference, this alloy exhibits a melting temperature in the range of 1370–1400 °C and a thermal conductivity of approximately 16.3 $\mathrm{W\,m^{-1}\,K^{-1}}$ at 23 °C. Based on these properties, the characteristic thermal diffusion time over a length scale of 20 μm—corresponding approximately to the laser spot size— is on the order of ∼8 µs.

This diffusion time is significantly longer than the intra-burst pulse-to-pulse delays used in both, MHz- and GHz-burst regimes, leading to pronounced heat accumulation during a burst. Moreover, heat accumulation can also occur between successive bursts [9]. While such behavior can be beneficial by smoothing temperature gradients, it may also become detrimental in the case of excessive energy

deposition [106].

SEM images of the pristine AISI 316L surface are shown in Fig. 3.2. The images were acquired at magnifications of 500× and 5 000×, corresponding to fields of view of 556 μm and 55.6 μm, respectively. The surface appears highly smooth and exhibits only minimal defects.

Quantitative surface measurements obtained using a confocal microscope are summarized in Table 3.1 and Table 3.2 according to ISO 25178-2 (surface measurements) and ISO 21920 (linear measurements), respectively. The measured arithmetic roughness is $R_a = 0.05$ μm and root mean square roughness is $R_q = 0.08$ μm. In addition, the skewness, defined by R_{sk} indicates that the surface presents more peaks than valleys, as the value is positive equaling 2.9. The high kurtosis value R_{ku} (19.6) indicates that the surface roughness is dominated by isolated peaks. Those characteristics are typical of a mirror-like surface finish.

Unless otherwise stated, this surface condition is used as the reference for all subsequent experiments.

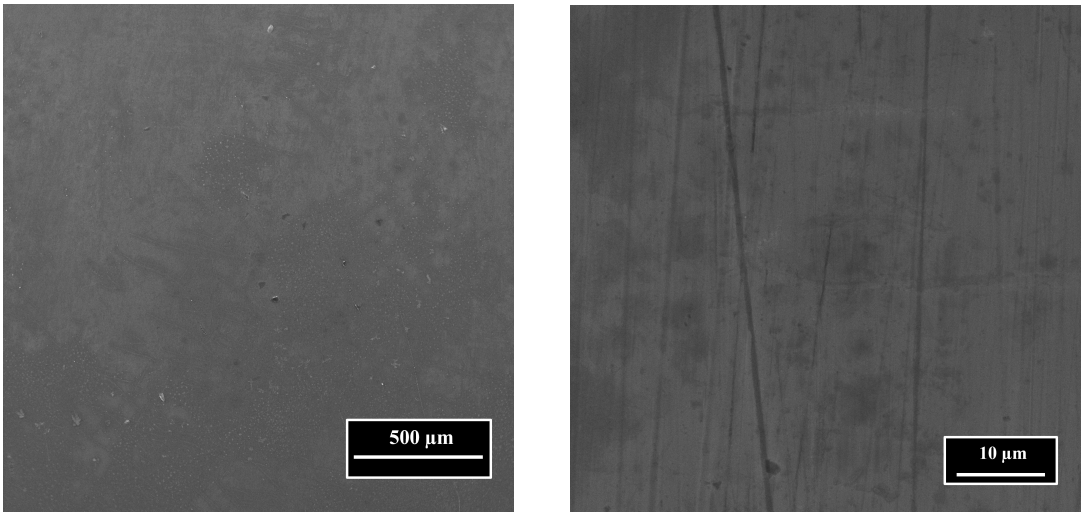

(a) Magnification of ×500. (b) Magnification of ×5000.

Figure 3.2: SEM top view of pristine 316L stainless steel sample surface.

S_a	S_q	S_{sk}	S_{ku}	S_z
0.049	0.063	1.12	30	5.22

Table 3.1: Areal surface measurements according to ISO 25178-2.

R_a	R_q	R_{sk}	R_{ku}	R_z
0.05	0.08	2.9	19.6	0.71

Table 3.2: Linear surface measurements according to ISO 21920.

The study begins with the interaction of the metal with a vortex beam, followed by the same experiment using a gaussian beam. After identifying optimal processing parameters for single-burst irradiation, the influence of horizontal and vertical

overlap is investigated. Based on these results, experiments using long GHz-bursts in a double-step process are conducted. Finally, an optimization of processing parameters is then performed using long GHz-bursts.

3.1.1 Vortex beam

In this section, the results obtained with a laser beam, spatially shaped using a vortex phase mask carrying an orbital angular momentum of $m = 1$, as explained in Section 1.4.2.3 are presented. The underlying physical mechanism of this beam-shaping method has also been detailed in Section 1.4.2.3. The objective of this section is to identify optimal processing parameters through a systematic, step-by-step experimental investigation based on visual analysis.

3.1.1.1 Single burst study

The primary motivation for using an vortex beam profile lies in its potential thermal advantages. In particular, the presence of a hollow intensity distribution is expected to promote smoother radial thermal gradients, leading to a more stable and controllable process. Such benefits have already been demonstrated in continuous-wave laser welding of metals [107, 108, 109]. It should be noted, however, that this beam-shaping configuration was implemented relatively late in the course of this work. Consequently, the vortex beam was not explored as extensively as the Gaussian configuration.

The first step of the study focuses on the impact of a single burst on the sample surface. To this end, several beam spot sizes were investigated by translating the target along the optical axis using the Z-translation stage, thereby defocusing the beam at the surface. For each spot size, the burst energy was varied in steps of 8.5 µJ. In addition, for each parameter set, the number of pulses per burst (ppb) was investigated from 50 to 800 ppb.

The resulting surface modifications were characterized using an optical microscope equipped with a 20× objective. Representative results obtained in the GHz-burst configuration are presented in Fig. 3.3. The corresponding results for the MHz-burst regime are provided in Appendix C

By inspecting the first burst configuration shown in Fig. 3.3a, several characteristic features can be identified. For the smallest beam spot size (54 μm) corresponding to fluences[2] from 9 to 15 $J{\cdot}cm^{-2}$, a circular molten region is observed, with a distinct dark feature at its center. This central structure is likely associated with a material protrusion or spike, or may result from a Marangoni effect as well (also called thermo-capillary convection). This arises when a temperature gradient induces a gradient in surface tension (from liquid zone to solid zone), and the matter flows from the cold zone to the hot zone [110].

As the burst energy is reduced and thus the fluence, the depth and extent of the molten peripheral ring gradually decrease, and the central feature becomes less pronounced. When increasing the beam spot size and thus reducing the fluence from 8 to 5 $J \cdot cm^{-2}$, the "thermal pressure", induced by rapid surface heating is reduced due to the lower energy density. At a spot size of 100 μm, the vortex beam primarily melts the outer ring, while the central region remains unaffected.

[2]The fluence have been computed assuming a full circle surface.

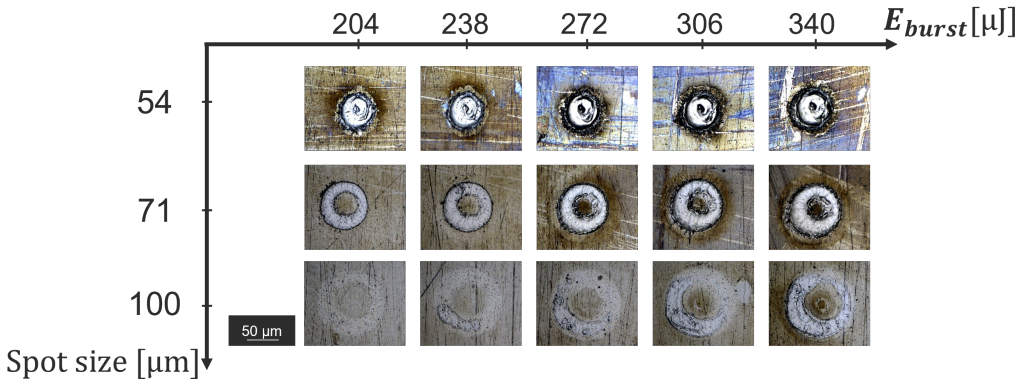

(a) 50 ppb.

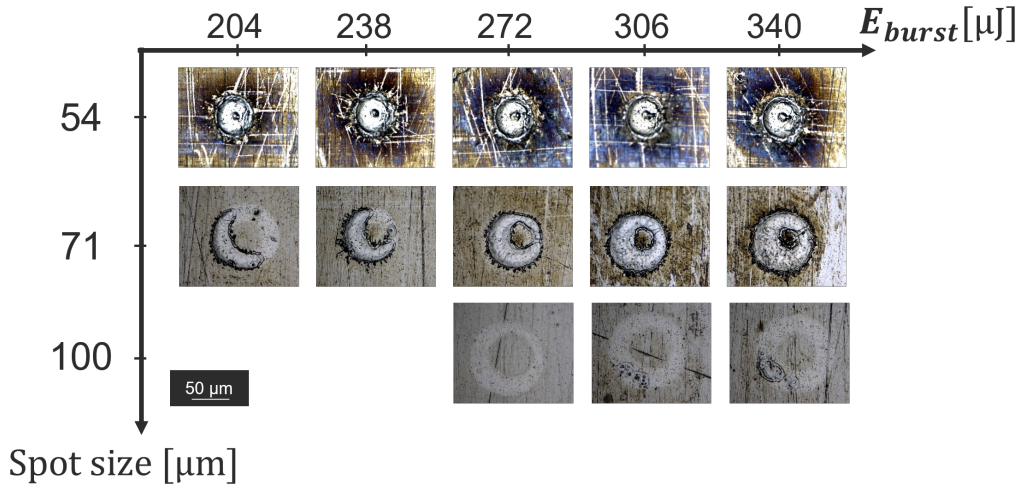

(b) 100 ppb.

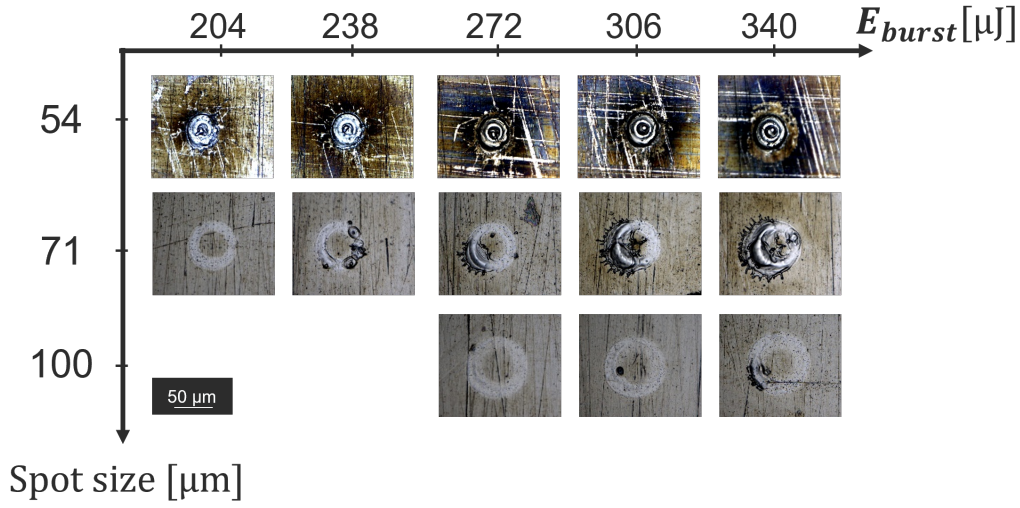

(c) 200 ppb.

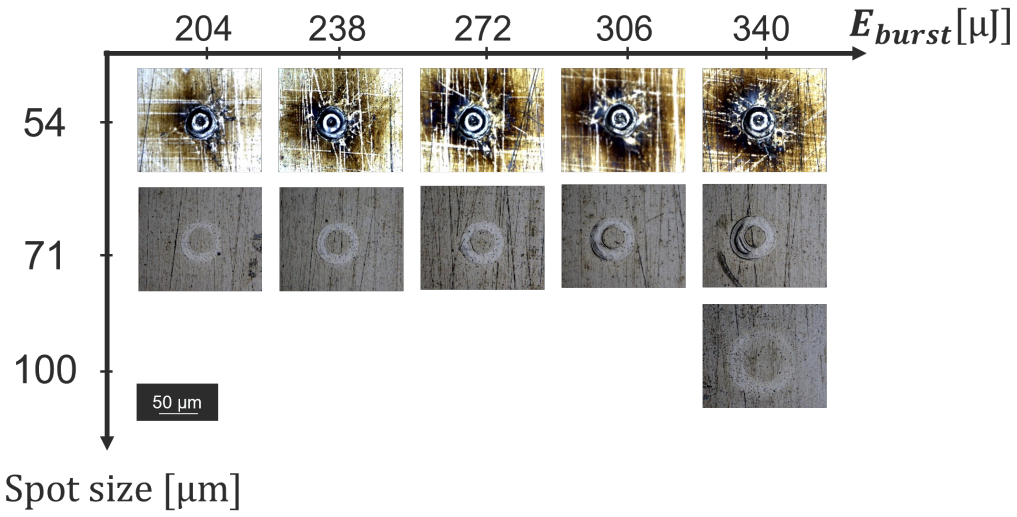

(d) 400 ppb.

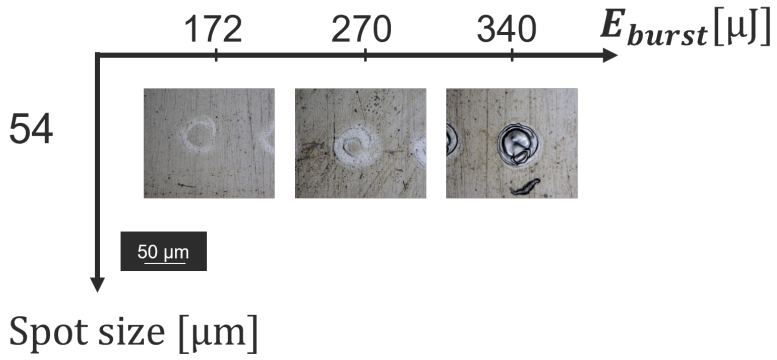

(e) 800 ppb.

Figure 3.3: Optical microscope images of vortex beam surface modifications with increasing number of pulses-per-burst, as a function of energy and spot size. (a) 50 ppb, (b) 100 ppb, (c) 200 ppb, (d) 400 ppb, (e) 800 ppb.

This results in a well-defined vortex molten zone surrounding a pristine core. A similar behavior is observed for a beam spot size of 136 μm (fluence of 3 to 4 $J \cdot cm^{-2}$).

Increasing the number of pulses per burst to 100 ppb (Fig. 3.3b) leads to comparable trends. For the smallest spot size, a molten pool with a central feature is still observed; however, the overall size of the molten region appears reduced compared to the 50 ppb configuration for the same fluence of 9 - 15 $J \cdot cm^{-2}$. At a spot size of 71 μm, the central region remains largely unaffected. At lower burst energies, the molten region becomes increasingly inhomogeneous, which can be attributed to residual non-uniformities of the vortex phase mask used. For the largest spot size investigated (100 μm), the molten region nearly vanishes.

This general trend persists as the number of pulses per burst is further increased to 200 ppb and 400 ppb, as shown in Fig. 3.3c and Fig. 3.3d. At small beam spot sizes, excessive energy deposition leads to strong melting, while the outer radius

of the molten region decreases with an increasing number of pulses per burst. For larger spot sizes, melting remains confined to the periphery, leaving the central region unaffected.

Finally, the 800 ppb configuration (Fig. 3.3e) reveals a markedly different behavior. A homogeneous molten pool is obtained, characterized by the absence of a central spike and minimal spatter at the edges. This configuration appears to provide the most stable and uniform melting conditions. However, a slight reduction in burst energy (at 314 μJ) immediately leads to the disappearance of the molten region and only leaves the shallow melting, indicating a narrow processing window for this regime.

An additional investigation was performed to further analyze the central feature observed in the previous configurations. SEM images were acquired at a magnification of 3k×. The resulting images for the 50, 100, 200, and 400 ppb configurations are presented in Fig. 3.4.

By inspecting Fig. 3.3a, Fig. 3.3b, Fig. 3.3c, and Fig. 3.3d, a common feature can be identified: spatter is systematically observed at the periphery of the molten region. However it seems that the droplet size at the periphery increases with the number of pulses in the burst, meanwhile the number of droplets decreases with increasing pulses-per-burst number. The central pillar-like structure is not present in all images, as it appears to be relatively fragile and may be altered during sample handling and transfer between the experimental setup and the SEM facility at ALPhANOV. Similar pillar or tubular structures induced by vortex beams have already been reported in the literature [26, 80].

Overall an increase of the number of pulses per burst alter the light-matter interaction at equivalent fluence.

3.1.1.2 Influence of overlap

Based on the single-burst study, the 800 ppb configuration was selected, as it provides a more gradual energy deposition, resulting in reduced spatter formation and fewer surface protrusions. The influence of burst overlap was therefore investigated using this configuration.

Spot-to-spot overlap The spot-to-spot overlap (S-2-S) was first studied using a beam spot size of 54 μm and a repetition frequency of 20 kHz. The overlap was varied from 0 % to 97 % for three burst energies: 170 µJ, 238 µJ, and 340 µJ. Therefore, any melting at 170 µJ and 238 µJ would be attributed to heat accumulation with spatial overlap. The corresponding surface morphologies are shown in Fig. 3.5.

For all investigated energies and low overlap values, surface morphologies similar to those obtained in the single-spot configuration (Fig. 3.3e) are observed. At the highest burst energy of 340 µJ, increasing the spot-to-spot overlap rapidly leads to unstable seams. In the range between 32 % and 45 %, the distance between successive spots remains too large to ensure surface homogenization. An optimal regime is identified at 72 % overlap, where a continuous seam is obtained, although early signs of thermal instabilities are already visible.

For a burst energy of 238 µJ, individual spots remain clearly distinguishable up to 45 % overlap. Between 59 % and 91 %, homogeneous and stable seams are obtained. However, increasing the overlap beyond 97 % results in excessive

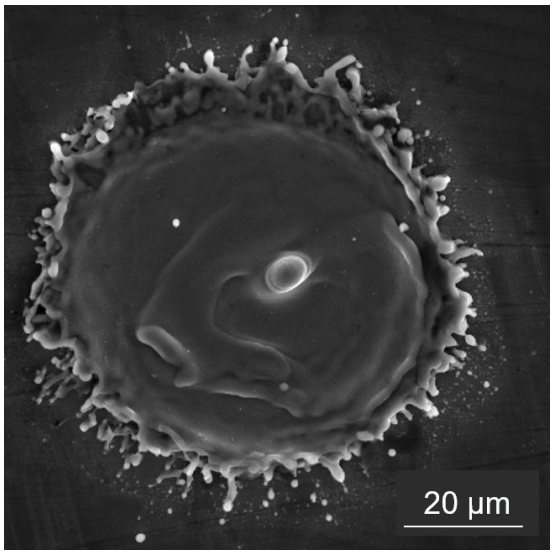

(a) 50 ppb.

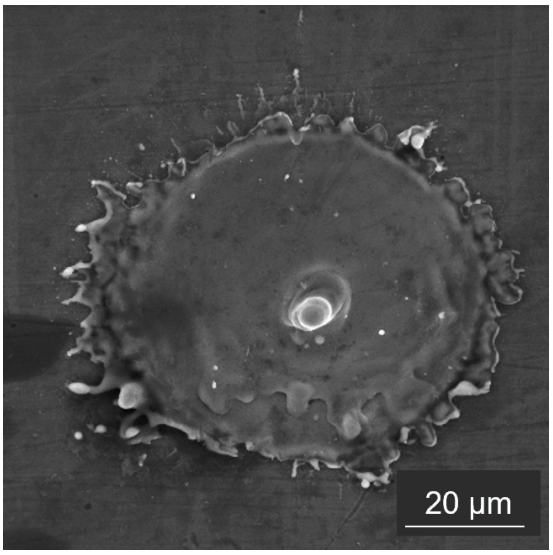

(b) 100 ppb.

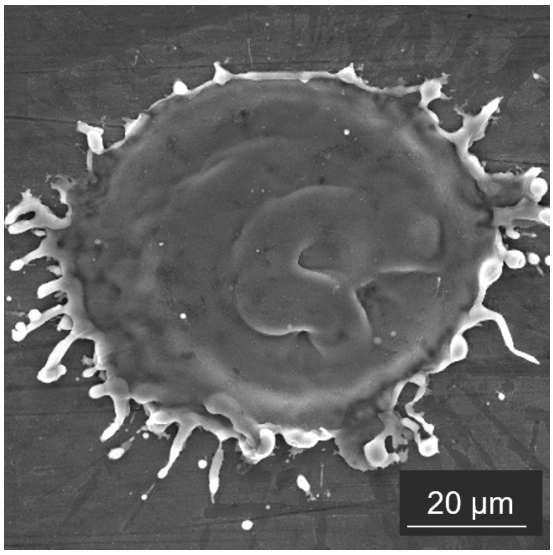

(c) 200 ppb.

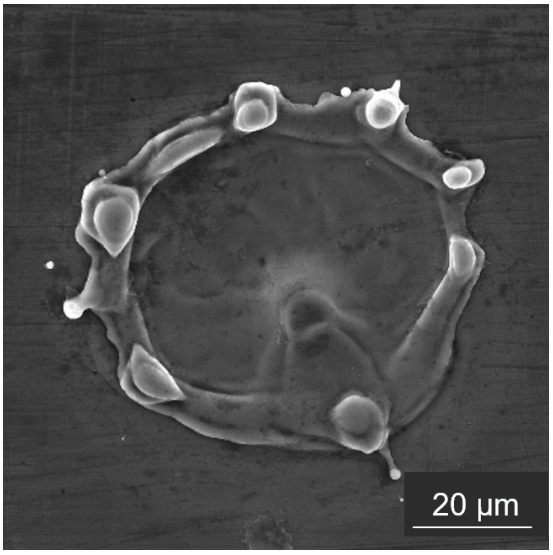

(d) 400 ppb.

Figure 3.4: SEM images of vortex beam surface modification with increasing number of pulse-per- burst for 92 μm spot size and 340 µJ burst energy. (a) 50 ppb,(b) 100 ppb,(c) 200 ppb,(d) 400 ppb with a magnification of 3 kx.

heat accumulation, leading to the formation of a heat-affected zone accompanied by strong surface oxidation.

A similar behavior is observed for the lowest burst energy of 170 µJ. Homogeneous seams are obtained for overlaps ranging from 72 % to 91 %, while higher overlap values again lead to overheating and oxidation effects.

Based on these observations, a spot-to-spot overlap of 72 % was selected for subsequent experiments but another interesting working point would have been, 238 µJ per burst with 97 % overlap, where a thinner and stable melting layer is also produced.

Line-to-line overlap With the spot-to-spot overlap fixed, the influence of the line-to-line (L-2-L) overlap was investigated. Two configurations were considered:

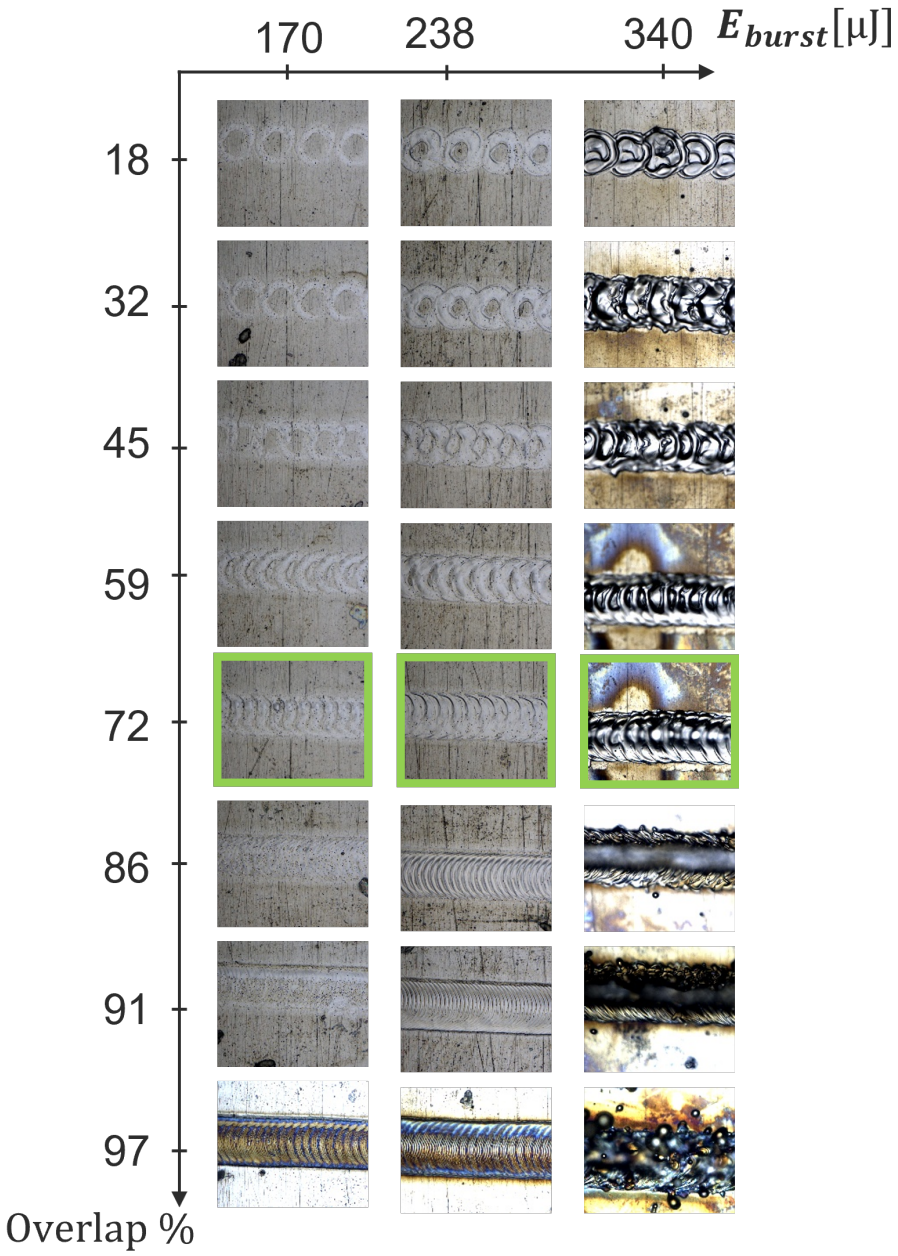

Figure 3.5: Optical microscope images of 316L samples showing the influence of spot-to-spot overlap using a vortex beam on the surface quality for 800 ppb GHz-burst for three burst energies of 170, 238, and 340 µJ, respectively.

a 10 % overlap, and a 75 % overlap. Burst energies of 170 µJ, 238 µJ, and 340 µJ were tested for each configuration. The results are shown in Fig. 3.6.

It can be directly observed that a 10 % line-to-line overlap produces surface morphologies closely resembling those obtained for a single line. In contrast, a 75 % overlap results in a significantly more structured surface. In this case, the material does not appear to form a smooth molten region for any of the investigated energies; instead, the surface exhibits a rough morphology, as if each laser spot generated an individual molten pool rather than contributing to a continuous molten track. This behavior leads to a rough visual aspect and heterogeneous-like surface. Further

investigation regarding surface roughness measurement and characterization will be presented in Section 3.2.

These results show that the effect of burst energy, spot-to-spot overlap, and line-to-line overlap are strongly correlated and cannot be considered as independent processing parameters.

Having explored the influence of a vortex beam profile on surface modification, it is interesting to compare these results with those obtained using a classical Gaussian beam. The following section therefore presents the investigations for the same experimental approach using a Gaussian beam profile, which serves as a reference configuration due to its simplicity and widespread use.

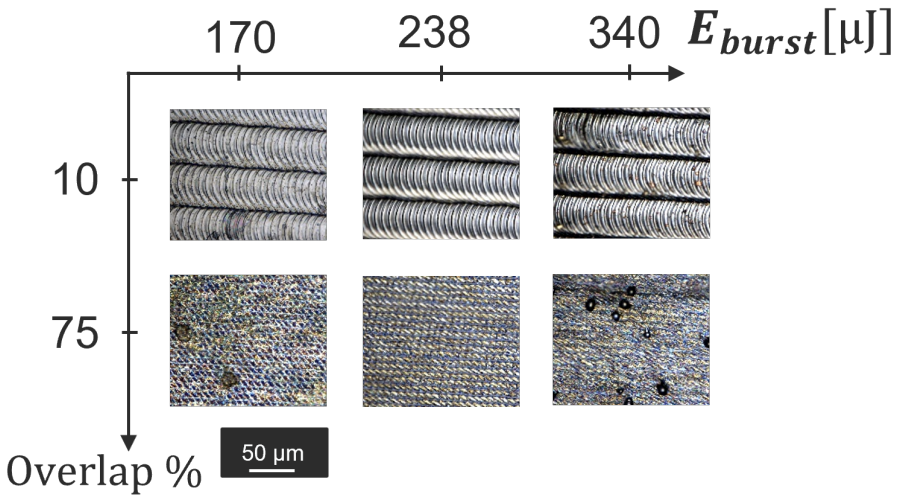

Figure 3.6: Optical microscope images of 316L samples showing the line-to-line influence using a vortex beam on the surface quality for 800 ppb GHz-burst with three burst energies of 170, 238, and 340 µJ, respectively.

3.1.2 Gaussian beam

In this section, the laser beam is a classical gaussian beam. The objective of this section is to identify optimal processing parameters through a systematic, step-by-step experimental investigation based on visual analysis.

3.1.2.1 Single-burst study

The first step of the study focuses on the impact of a single burst on the sample surface. To this end, several beam spot sizes were investigated by translating the target along the optical axis using the Z-translation stage, thereby defocusing the beam at the surface. For each spot size, the burst energy was varied in steps of 8.5 µJ. In addition, for each parameter set, both the number of pulses per burst and the burst repetition regime were investigated, considering both MHz-burst and GHz-burst modes.

The resulting surface modifications were characterized using an optical microscope equipped with a 50× objective. Representative results obtained in the GHz-burst configuration are presented in Fig. 3.7.

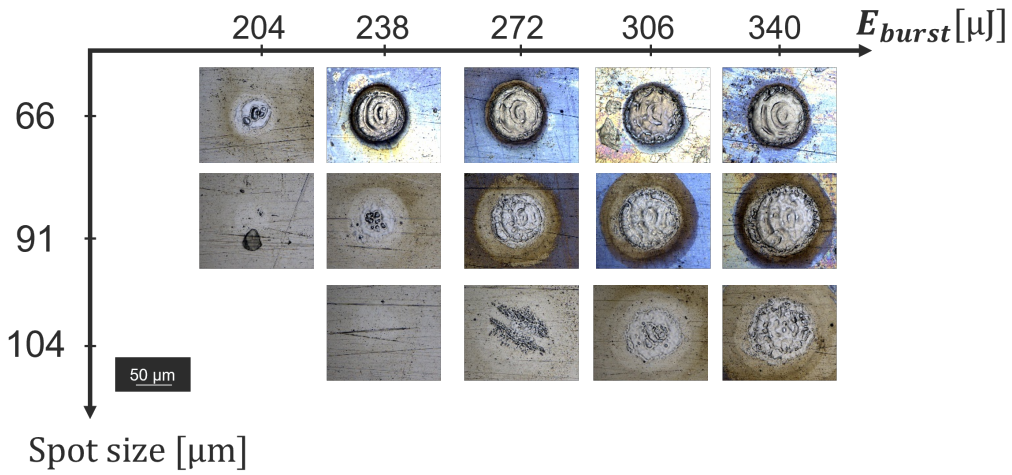

(a) 50 ppb.

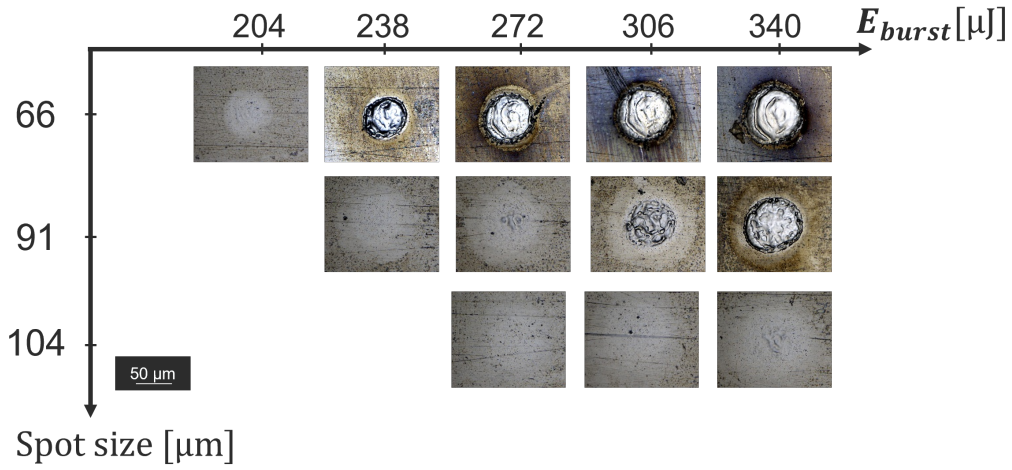

(b) 100 ppb.

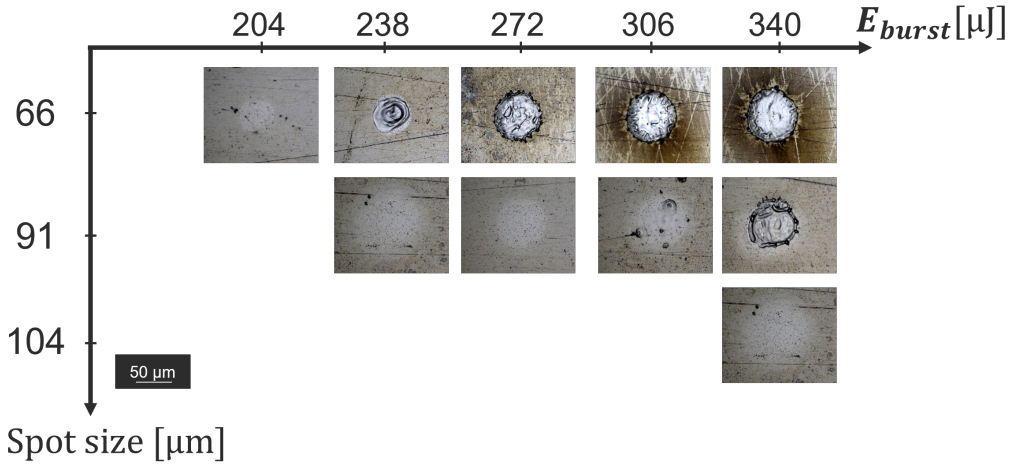

(c) 200 ppb.

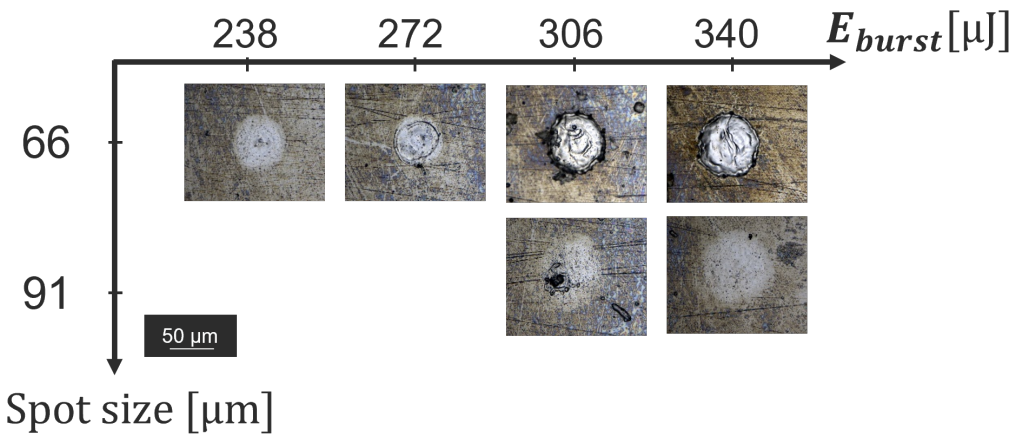

(d) 400 ppb.

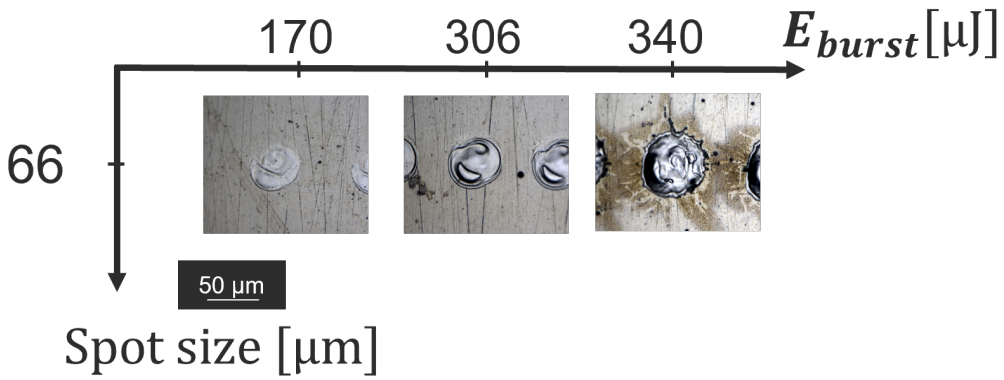

(e) 800 ppb.

Figure 3.7: Optical microscope images of gaussian beam surface modification with increasing number of pulse-per-burst values as a function of energy and spot size.

By inspecting the first burst configuration shown in Fig. 3.7a (50 ppb), several characteristic features can be identified. For the smallest beam spot size (66 μm), a circular molten region is observed, and no distinct features emerge. As the energy is lowered, the size of the melted zone is reduced (fluence from 6 to 10 $J \cdot cm^{-2}$).

At a spot size of 91 μm, the gaussian beam primarily melts the central core, while the external region is heated but not melted. Here also, as the burst energy is reduced, the size of the molten pool is reduced as well (fluence from 3 to 6 $J \cdot cm^{-2}$). A similar behavior is observed for a beam spot size of 104 μm (fluence of 2 $J \cdot cm^{-2}$).

Increasing the number of pulses per burst to 100 ppb (Fig. 3.7b) leads to comparable trends. For the smallest spot size and highest energy a re-solidified area with the appearance of a higher reflectivity and smoother re-solidified surface. As the burst energy is reduced, the size of the melted pool is reduced and no trace of melting is obtained at 204 µJ. The overall size of the molten region appears equal compared to the 50 ppb configuration. At a spot size of 91 μm, the molten region looks more disturbed. Increasing the beam spot size to 104 μm results in a very slight molten area for 340 µJ.

This general trend persists as the number of pulses per burst is further increased

to 200 ppb and 400 ppb, as shown in Fig. 3.7c and Fig. 3.7d. For small spot sizes, high energy deposition leads to strong melting, while the surrounding remains pristine. For larger spot sizes, melting is shifted toward higher burst energy values with barely any visible at 306 μJ and 104 μm spot size. Increasing the number of pulses per burst leads to similar results.

3.1.2.2 Impact of overlap

Based on the single-burst study, the 800 ppb configuration was selected, as it enables a more gradual energy deposition due to the energy being dispensed over a longer time and thus a more gradual heating process. The influence of burst overlap was subsequently investigated.

Spot-to-spot overlap The spot-to-spot overlap was studied using a beam spot size of 92 μm and a repetition frequency of 20 kHz. The overlap was varied from 0 % to 97 % for four burst energies: 85 µJ, 170 µJ, 238 µJ, and 340 µJ. The corresponding results are shown in Fig. 3.8.

For all energies and low overlap values, surface morphologies similar to those observed in the single-burst configuration (Fig. 3.7e) are obtained. At the highest burst energy of 340 µJ, increasing the overlap rapidly leads to unstable seams and localized ablation of the track.

For a burst energy of 238 µJ, individual spots remain clearly distinguishable up to 86 % overlap. Between 86 % and 91 %, the seams appear homogeneous and stable. However, increasing the overlap beyond 97 % results in excessive heat accumulation, leading to the formation of holes within the track.

At a burst energy of 170 µJ, individual spots remain visible up to 86 % overlap, although with a more uniform appearance. Between 86 % and 91 %, stable and smooth seams are obtained. At 97 % overlap, oxidation effects similar to those observed for the vortex beam configuration (Section 3.1.1.2) are identified.

Finally, for the lowest burst energy of 85 µJ, for overlaps ranging from 18 % to 59 % a small modified zone is detected but appears discontinuously, as the overlap increases from 72 % to 91 % a thin and smooth molten layer is generated. At 97 % overlap, oxidation effects again become apparent.

Based on these observations, a spot-to-spot overlap of 91 % was selected for the subsequent experiments.

Line-to-line overlap With the spot-to-spot overlap fixed, the influence of the line-to-line overlap was investigated. Three configurations were considered: a 10 %, a 50 % and a 75 % overlap. Burst energies of 85 µJ, 221 µJ, 255 µJ, and 289 µJ were tested for a repetition rate of 20 kHz. The results are shown in Fig. 3.9.

A 10 % line-to-line overlap produces surface morphologies similar to those obtained for a single line at burst energies of 85 µJ and 221 µJ. At higher energies, surface degradation becomes apparent. A 50 % overlap leads to comparable results for the two lowest energies.

Increasing the line-to-line overlap to 75 % results in a significantly more structured surface. In this regime, each individual molten line seems to overlap entirely with the previous one, thus leaving only the edges of the previous melted line, and

thus, leading to a rough and heterogeneous surface. A potential strategy to mitigate this effect would be to increase the inter-burst repetition frequency in order to enhance thermal accumulation, although this would increase the risk of overheating.

As observed for the vortex beam configuration, these results confirm that the effect of burst energy, spot-to-spot overlap, and line-to-line overlap are strongly correlated and cannot be considered as independent processing parameters. After this first section about visual inspection of the generated surface and the different links present between each parameters, a more in-depth study is performed using surface characterization diagnostic.

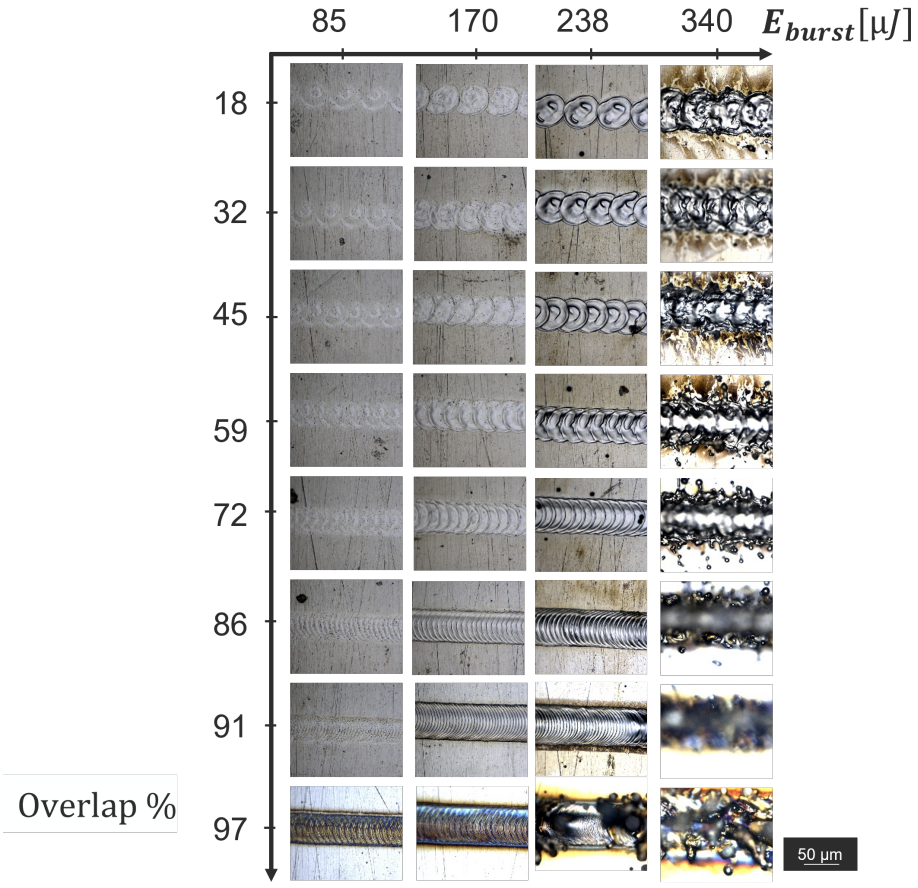

Figure 3.8: Optical microscope images of 316L samples showing the spot-to-spot influence on the surface quality for 800 ppb GHz-burst for four burst energies of 85, 170, 238, and 340 µJ, respectively.

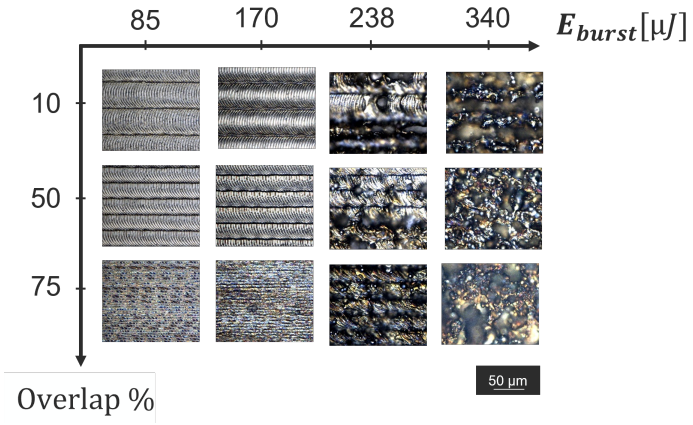

Figure 3.9: Optical microscope images of 316L samples showing the line-to-line influence on the surface quality for 800 ppb GHz-burst for four burst energies of 85, 221, 255, and 389 µJ, respectively.

Overall, the observations performed in this section provided valuable insight on the correlation between the induced effect of each parameter, such as S-2-S, L-2-L, burst duration, beam spot size, and beam shape. The two beam shapes investigated, vortex and gaussian, showed only small differences in their respective behavior based on this simple visual analysis leading to a focus on gaussian beams in the subsequent studies. Additionally, the polishing process has been identified as a cumulative process where burst-to-burst irradiation results in a heat accumulation but can be detrimental if this heat accumulation is too pronounced.

3.2 Investigation of the potential of long GHz-burst

In this section, two different studies are presented: first, a double-step process based on a first laser milling step followed by a finishing/polishing step on the milled surface is presented in Section 3.2.1.1 and Section 3.2.1.2. Then, a single-step polishing process on pristine stainless steel samples is presented in Sections 3.2.2 to 3.2.4, including the investigation of the influence of key processing parameters such as S-2-S overlap, burst repetition rate, and number of passes on the resulting surface roughness through tests with two different L-2-L overlaps. These effects are analyzed starting from a mirror-like surface, as shown in Section 3.1, and compared with the results obtained on samples that were milled before polishing (double-step process).

3.2.1 Combined laser milling-polishing approach

In this part, a proof-of-concept for an all-in-one approach combining ablation and polishing using GHz-bursts is presented. First, results dealing with ablation depth as a function of cumulative dose for short (50 ppb) or long (800 ppb) bursts are presented. The corresponding surface roughness (R_a) results are displayed in Section 3.2.1.2. The purpose at this stage is to remove matter, not to polish. In a second step, the resulting surface from the first step is polished using long GHz-

bursts. The influence of the number of passes in the second step is analyzed for 100 μm-deep cavities in Section 3.2.1.2

3.2.1.1 Laser milling step

In this subsection, the ablation depth obtained with short and long GHz-bursts on pristine stainless steel 316 L surface (shown in Figure 3.2) will be presented as a function of the cumulative dose (defined in Section 2.3). The change in cumulative dose is linked to a change in the energy contained in a burst ranging from 9 µJ to 94 µJ. The burst length chosen for this study is 50 ppb for the short burst and 800 ppb for the long burst, respectively. Each ablation trial was performed by engraving a 2x2 mm square, with 165 passes and a hatch of 10 μm uni-directional rotated by 60° each pass (55 passes at each angle). The burst repetition rate was kept constant at 400 kHz, and the marking speed was set to 1 $m{\cdot}s^{-1}$ thus providing a S-2-S overlap of 88 % (i.e. of 2.5 μm). The sample was placed at the focal plane thanks to the off-axis camera, and thus a spot size of 21.5 μm was used and no re-focalisation was performed during the process. The surface roughness was determined using the method described in 2.3 and the depth of engraving was also determined with the confocal microscope.

Figure 3.10a presents the relationship of the engraved depth and the surface roughness (R_a) as a function of the cumulative dose, as defined in Equation (2.19). The downward-pointing triangles represent the engraved depth (left black-labeled axis) for burst durations of 50 ppb and 800 ppb, while the crosses correspond to the surface roughness (R_a), which is represented along the right red-labeled axis.

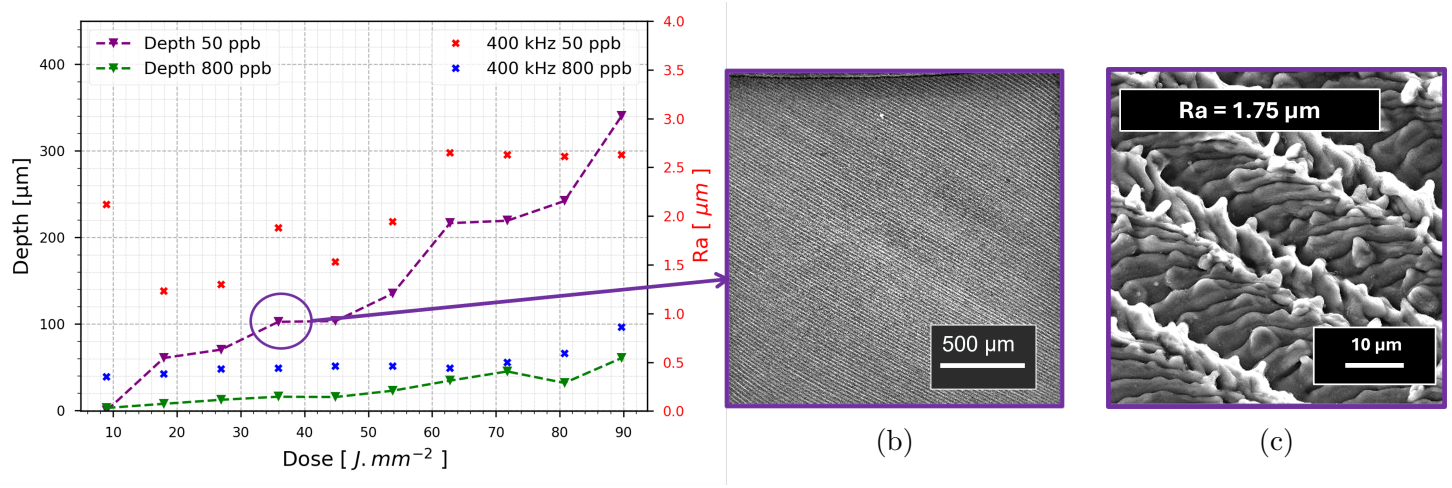

(a) (b) (c)

Figure 3.10: **a**) Left axis: Evolution of the engraved depth obtained in 316L with short (purple triangles) and long (green triangles) GHz-bursts as a function of the cumulative dose. Right axis: Evolution of the surface roughness R_a ISO 21920 for short (red squares) and long (blue squares) GHz-bursts as a function of the dose. Errors are estimated to 5 μm for depth measurements. (**b**) SEM top view of surface obtained in 316L after laser irradiation with 50 ppb for a dose of 36 $J \cdot mm^{-2}$, and at a magnification of x136. (**c**) SEM top view of surface obtained in 316L after laser irradiation with 50 ppb for a dose of 36 $J \cdot mm^{-2}$, and at a magnification of x5,000.

Starting with the engraving depth, one can observe that as the cumulative dose

(which here scales with the effective fluence) increases, the depth of engraving also increases for both configurations. However, a clear distinction can be made between the 50 ppb and 800 ppb curves. Specifically, the engraving depth for the 50 ppb curve increases at a rate of 4.75 $\mu m \cdot J^{-1} \cdot mm^2$, while the 800 ppb curve shows a much lower rate of 0.85 $\mu m \cdot J^{-1} \cdot mm^2$ showing a completely different interaction with the surface. Indeed, the resulting engraved squares from the 50 ppb and 800 ppb configuration exhibit different surface morphologies. In the case of the 800 ppb configuration, the surface appears melted and "smooth", while in the 50 ppb configuration the surface is rough as shown in Figure 3.10b and the close-up view in Figure 3.10c.

Turning to the surface roughness, a trend is noticed: the surface roughness increases with the dose, as reported in [111]. In this study, the depth of engraving increases, related here solely to fluence, also leading to the surface roughness deterioration. For the 50 ppb configuration, the surface roughness reaches up to 2.6 μm, whereas with the 800 ppb configuration, the surface roughness is about 0.5 μm below a dose of 70 J·mm^{-2} and increases up to 0.9 μm above. This decrease in roughness measured at 800 ppb is obtained at the expense of a reduced engraving depth (3 to 5 times lower compared to 50 ppb). It must be noted that the energy levels used for engraving are significantly lower than those studied in [67] (10 $\times$ less for the maximal burst energy values).

For the subsequent section, the selected laser parameters to achieve a cavity depth of 100 μm are chosen. This set of parameters corresponds to the encircled point in Figure 3.10a, the reference surface for the following polishing process with long GHz-bursts (see Section 3.2.1.2) as illustrated on the SEM images in Figure 3.10b. In these images, the final pass hatching angle is observed, zooming in reveals the individual tracks with an observable 50 % overlap. Additionally, the individual recast marks generated by each molten pool (i.e. each burst) are visible, contributing to the surface roughness. Ideally, for minimal roughness, the recast marks would not be visible, producing a single smooth track [112]. Looking at Table 3.3, which gives the different roughnesses obtained before and after milling, it appears that the R_a value is degraded to 1.37 μm, similarly R_q = 1.72 μm. The neutral value of skewness ($R_{sk} = 0.03$) indicates that there is an equilibrium between peaks and valleys while the kurtosis (R_{ku} = 3.11) indicates that the roughness is distributed more uniformly across the surface. Finally the R_z value is found to be 10.82 μm.

	R_a [μm]	R_q	R_{sk}	R_{ku}	R_z [μm]
Pristine	0.05	0.08	2.9	19.6	0.71
Milled	1.37	1.72	0.03	3.11	10.82

Table 3.3: Linear surface measurements of engraved surface according to ISO 21920.

3.2.1.2 Laser polishing step

This section investigates the polishing process applied to the previously engraved surfaces (the one identified on Figure 3.10a with a purple circle). The influence of the number of passes of subsequent polishing on the final surface roughness is evaluated.

All experiments were conducted at a fixed burst repetition rate of 400 kHz, using the GHz-burst mode with 800 ppb and a total burst energy of 46.8 µJ. The laser spot size was 45.3 μm, with a spot-to-spot (S-2-S) distance of 5 μm and a line-to-line (L-2-L) spacing of 1.2 μm. Those specific parameters were chosen based on a preliminary investigation.

The results are presented in Figure 3.11a, which shows the surface roughness as a function of the number of polishing passes. It is important to note that both the engraving and polishing steps were performed using the same burst repetition rate and energy. However, the burst duration and spot size were adjusted to perform the polishing process (the focus is set 600 μm below the target surface). The red dashed

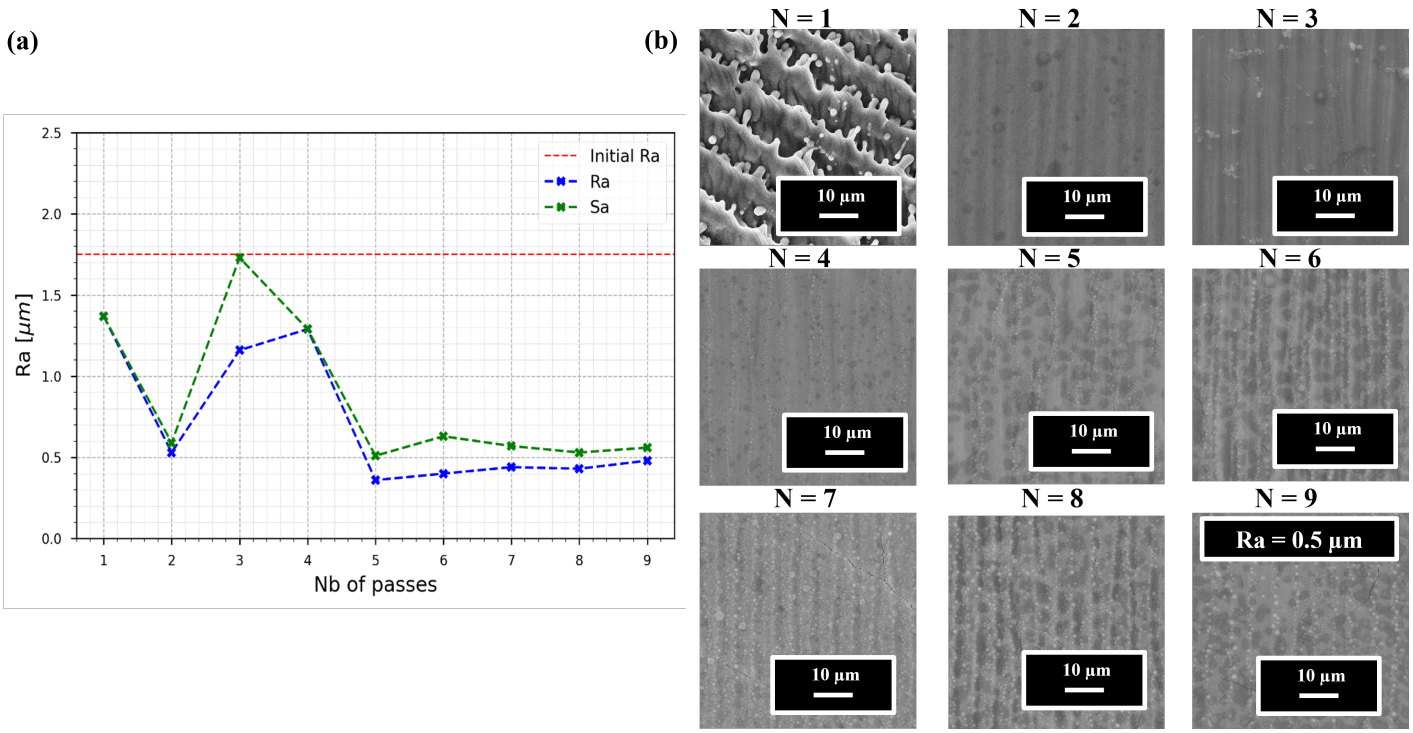

Figure 3.11: (**a**) Evolution of the surface roughness R_a ISO 21920 and S_a ISO 25178 as a function of the number of passes on 316 L for 800 ppb GHz-bursts at 400 kHz, 46.8 µJ per burst, S-2-S = 5 μm, L-2-L = 1.2 μm. (**b**) SEM top view of the 316L surface obtained after laser irradiation with 800 ppb, and at a magnification of x5,000.

line in Figure 3.11a, corresponds to the surface roughnesses (R_a) after laser milling and before laser polishing. This reference value is 1.75 μm. The x-axis indicates the number of polishing passes N, ranging from 1 to 9, used for polishing after the engraving process (described in Section 3.2.1.1), while the y-axis shows the surface roughness (R_a in blue and S_a in green). The R_a values were measured using the method described in Section 2.3, while the S_a values were extracted directly from the stitched 3D images.

Both R_a and S_a curves follow a similar trend and show comparable magnitudes, although S_a tends to be slightly higher overall. Figure 3.11b displays SEM top-view images (5,000× magnification) of the surface after each number of passes.

At N=1, the surface exhibits early signs of melting but largely retains its original morphology as in Figure 3.10ac. After N=2, a significantly smoother surface is

achieved, with a roughness that is reduced to 0.5 μm. Interestingly, at N=3 and N=4, roughness increases to 1.15 and 1.25 μm, respectively, although this variation is not clearly reflected in the corresponding SEM images. This anomaly is attributed to the formation of thermal surface waviness with a periodicity of a few hundred microns which subtly increased the measured roughness without drastically altering the visual appearance of the surface. A binocular image of such thermal wave can be seen in Appendix B, Figure B.3.

From N=5 onward, a clear plateau is observed: the surface roughness stabilizes just below 0.5 μm and does not significantly improve with additional passes. The SEM images for passes N=5 to N=9 reveal the emergence of small white microspheres and larger dark spots. These features appear embedded within the surface but do not lead to increased surface roughness. Their exact origin remains undetermined and further investigations are required to explain their content and their appearance. Looking at Table 3.4, which gives the different roughness obtained

	R_a [μm]	R_q	R_{sk}	R_{ku}	R_z [μm]
Milled	1.37	1.72	0.03	3.11	10.82
Polished	0.47	0.60	-0.16	2.97	2.81

Table 3.4: Linear surface measurements of laser polished surface with 9 passes according to ISO 21920.

before and after laser polishing, it appears that the R_a value is improved from 1.37 μm to 0.47 μm, similarly goes from R_q = 1.72 μm to 0.6 μm. The skewness (R_{sk}) remains neutral maintaining an equilibrium between peaks and valleys while the kurtosis (R_{ku}) is reduced by a small margin from 3.11 to 2.97 indicating that the roughness is distributed even more uniformly across the surface. Finally, the R_z value is reduced from 10.82 μm to 2.81 μm, thus leading to an overall improvement in the surface quality of the engraved surface.

To summarize this Section, GHz-burst laser ablation combined with GHz-burst laser polishing effectively reduces the surface roughness of the engraved samples to 34 % of the initial roughness after the milling process. It has also reduced the R_q, R_{sk}, R_z by 50 % or more. The time efficiency of this approach is noteworthy, as only the burst length and the spot size were modified between the ablation step and the polishing step, while key parameters such as intra-burst frequency as well as burst energy and frequency remained unchanged [112].

3.2.2 Influence of the spot-to-spot overlap

This section investigates the influence of the spot-to-spot (S-2-S) overlap on surface roughness by systematically varying the burst repetition rate and scanning speed, keeping the number of passes to 1 and using the pristine surface presented in Figure 3.2. Experiments were conducted using two distinct line-to-line (L-2-L) overlaps of 97 % and 75 % (1.2 μm and 12 μm), respectively. The burst length and burst energy were kept constant at 800 ppb and 2.3 µJ, respectively, with a spot size of 45.3 μm on the sample. Those parameters have been selected based on a preliminary study on this surface morphology. The tested repetition rates were 50, 100, 200, 400, and 800 kHz, combined with scanning speeds ranging from 100 to 1400 mm·s^{-1}, resulting in S-2-S overlaps ranging from 73 % to 97 %.

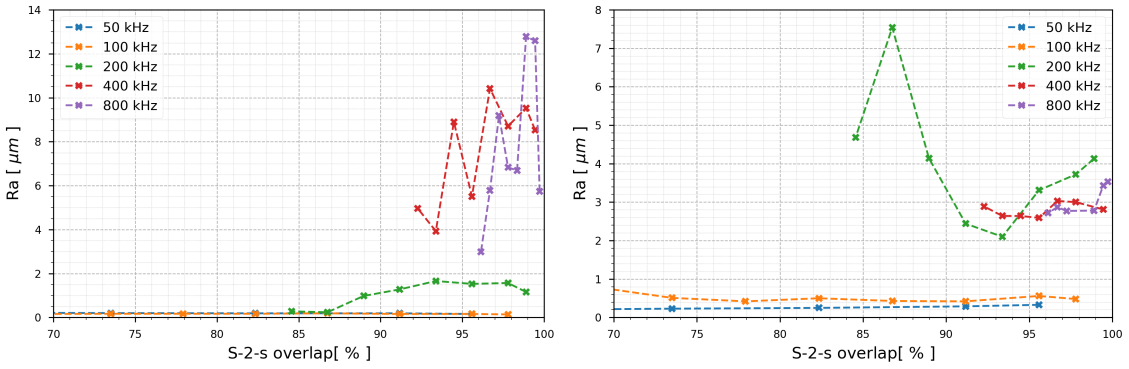

Figure 3.12: Surface roughness R_a variation as a function of the the S-2-S overlap for 316 L samples under GHz-burst irradiation with 800 ppb and 2.3 µJ per burst with, **(a)** L-2-L = 75 %; **(b)** L-2-L = 97 %.

Figure 3.12a presents the results for an L-2-L overlap of 75 %. The yellow and blue curves (which is behind the yellow curve), corresponding to 50 kHz and 100 kHz, respectively, show minimal changes in surface roughness across the range of S-2-S overlaps. These two burst repetition rates induce only a slight "cleaning" effect, without any significant surface degradation nor improvement.

At 200 kHz (green curve), the initial two data points show relatively low surface roughness. However, as the S-2-S overlap increases beyond 87 %, a noticeable rise in roughness occurs, eventually plateauing around an R_a of 2 μm. In contrast, the results at 400 kHz and 800 kHz (red and purple curves) reveal a strong negative impact on the surface quality even at the first test points—at overlaps of 93 % and 96 %, the surface roughness already reaches 5 μm and 2.8 μm, respectively. As the overlap increases further, the surface roughness rises significantly, reaching values as high as 11 μm and 13 μm for S-2-S overlaps exceeding 96 % and 98 %. This trend indicates a transition to a more thermally-driven interaction regime, leading to pronounced surface degradation.

Turning to Figure 3.12b, which corresponds to an L-2-L overlap of 97 %, a different behavior is observed. As in the previous case, the 50 kHz and 100 kHz curves show negligible impact, with only a thin, uniform melt layer forming—insufficient for effective polishing. For 200 kHz, the surface initially exhibits a sharp increase in roughness at low overlaps. This is followed by a decrease to an R_a of approximately 2.5 μm at an S-2-S overlap of 84 %, before rising again to about 4 μm at 98 % overlap. This fluctuation is attributed to recast layer formation at low overlap values and probably thermally induced instabilities at higher ones. The smaller L-2-L spacing of 1.2 μm leads to an increased surface roughness and surface irregularities due to localized melt accumulations at the track edges.

Finally, for 400 kHz and 800 kHz, both curves show a similar trend. The surface roughness starts high—around 3 μm and 2.7 μm, respectively—and remains roughly constant as the S-2-S overlap increases. Unlike in Figure 3.12a, where the roughness increases sharply at these burst repetition rates. Furthermore, the higher overlap also exhibits high fluctuation on the surface, yielding persistently in low surface quality [112].

3.2.3 Influence of the number of passes

This section explores the effect of the number of passes on the final surface roughness starting from the pristine surface shown in Figure 3.2. Experiments were carried out using two different line-to-line (L-2-L) overlaps: 75 % and 97 %. The burst length was fixed at 800 ppb, and two burst energies of 2.3 µJ and 46.8 µJ, respectively, were tested. Burst repetition rates of 50, 100, 200, 400, and 800 kHz were evaluated in combination with scanning speeds ranging from 250 to 4000 mm·s^{-1}, resulting in a constant spot-to-spot (S-2-S) overlap of 91.6 %.

The surface roughness results are shown in Fig. 3.13.

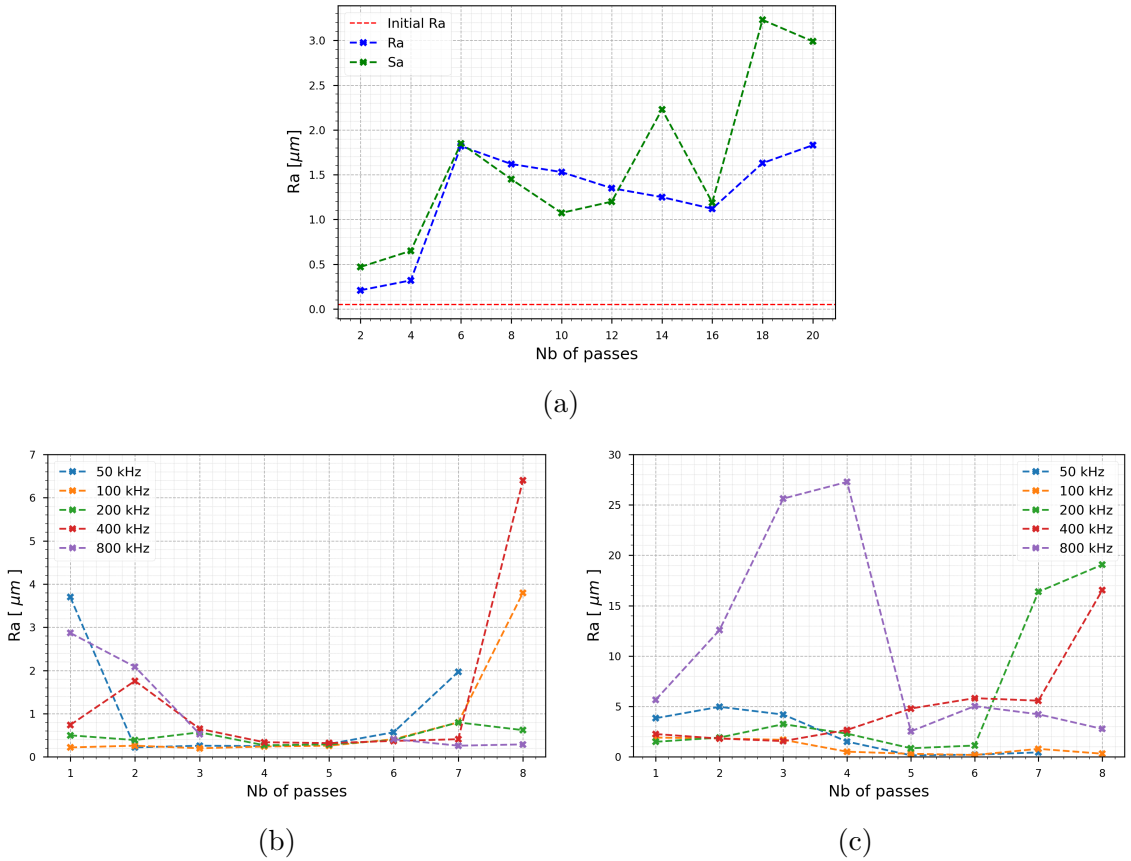

(a)

(b)

(c)

Figure 3.13: Surface roughness R_a evolution as a function of the number of passes for 316L steel samples under GHz-burst irradiation with 800 ppb and S-2-S = 5 μm for: (a) L-2-L = 1.2 μm, 400 kHz, 46.8 µJ per burst (the red dashed line indicates the initial surface roughness) (b) L-2-L = 12 μm, 2.3 µJ per burst; and (c) L-2-L = 1.2 μm, 2.3 µJ per burst.

Figure 3.13a illustrates the effect of the number of passes for processing the pristine surface using the same parameters as used for the polishing process in the double step process (Section 3.2.1.1), which were 400 kHz burst repetition rate, L-2-L = 97 %, and a burst energy of 46.8 µJ. The red dashed line represents the initial surface roughness. In contrast to the results from Section 3.2.1.1, where the surface roughness was reduced with increasing passes, here R_a increases progressively. This indicates a different polishing behavior under identical parameters, depending on the initial surface condition. Additionally, R_a and S_a values closely match throughout, validating the consistency of our surface roughness measurements.

Fig. 3.13b shows the evolution of surface roughness for an L-2-L distance of 12 μm. Observing all tested burst repetition rates together, a three-phase trend is observed. Initially, up to N=3, the roughness values exhibit high variability, ranging from 0.22 μm to 3.7 μm. Between N=3 and N=6, a stable plateau forms, with R_a values between 0.22 μm and 0.55 μm, indicating a temporary stabilization of the surface quality. Beyond N=6, a new regime emerges, marked by a gradual increase in roughness. For example, at 400 kHz and N=8, the roughness reaches a maximum of 6.4 μm.

In contrast, Fig. 3.13c presents the results for a smaller L-2-L spacing of 1.2 μm (i.e a higher dose). Here, the surface roughness increases immediately from N=1, with R_a values ranging from 1.5 μm to 5.7 μm. For burst repetition rates of 50, 100, 200, and 400 kHz, the roughness decreases until around N=4, reaching a minimum of approximately 0.5 μm for 100 kHz. However, 800 kHz behaves differently as the roughness rises sharply, peaking at 27 μm by N=4. After this point, the trends diverge. While the 200 kHz and 400 kHz curves continue to rise steadily—reaching 19 μm and 16 μm (out of range in the graph), respectively, by N=8 the 800 kHz curve unexpectedly decreases to 2.78 μm at the same pass number.

From the data presented in this section, it can be inferred that the effectiveness of the polishing process strongly depends on the initial surface state. Although identical parameters were used, starting from a mirror-like surface (as in Fig. 3.13c) resulted in an increase in roughness, whereas the same settings applied to a previously laser milled surface (Section 3.2.1.1) led to the formation of a smooth resolidified molten layer and a reduction in R_a below 0.5 μm with multiple passes. Thus, a polishing step, i.e. generation of a melted layer, after milling requires a much higher dose than the generation of a melted layer on a pristine surface, 46.8 μJ were required for the milled surface compared to only 2.3 μJ for the pristine surface, and no absolute recipe can be designed out of this study. In order to approach such recipe, one should do an in-depth study on the impact of the surface morphology on the light-matter interaction leading to the melting.

Furthermore, a comparison between Fig. 3.13a and Fig. 3.13b suggests that lower initial surface roughness benefits more from a reduced dose, achieved here through larger L-2-L spacing—which appears to promote the formation of a smoother molten layer and better surface finish [112].

3.2.4 Scalability

This section investigates the scalability, through increase of the repetition rate and speed with the same ratio, of the single step polishing process with respect to the final surface roughness. Experiments were conducted using two different line-to-line (L-2-L) overlaps of 75 % and 97 %, respectively. The burst length was fixed at 800 ppb, with burst energies ranging from 9.8 to 93.75 µJ.

Five different burst repetition rates—50, 100, 200, 400, and 800 kHz—were assessed in combination with scanning speeds between 100 and 1400 mm·s^{-1}, maintaining a constant spot-to-spot (S-2-S) overlap of 91.6 % (equivalent to a 5 μm spacing).

The results are presented in Figure 3.14a for L-2-L = 1.2 μm and in Figure 3.14b for L-2-L = 12 μm. Additionally, the SEM images corresponding to the results shown in Figure 3.14a are provided in Figure 3.15.

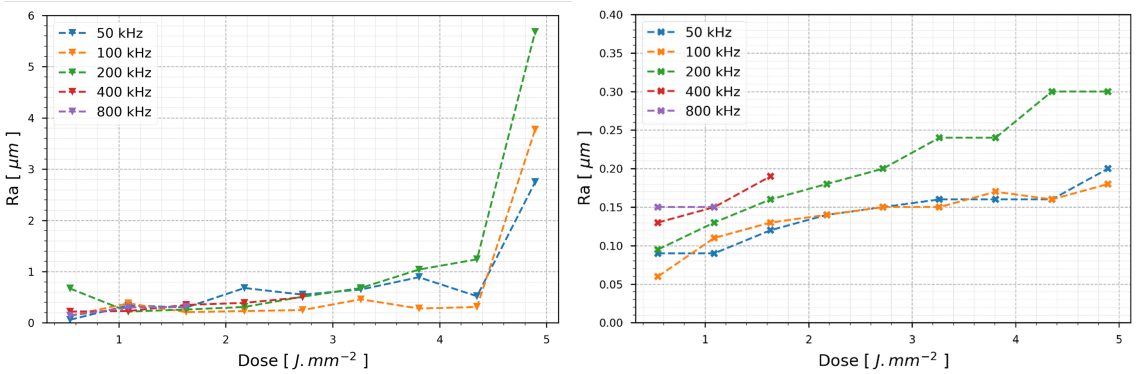

(a) (b)

Figure 3.14: Evolution of surface roughness R_a as a function of the dose in 316L stainless steel, with S-2-S = 5 μm, 800 ppb GHz-burst (**a**) for L-2-L = 97 % (1,2 μm), and (**b**) for L-2-L = 75 % (12 μm).

Figure 3.14a illustrates the evolution of surface roughness for an L-2-L distance of 1.2 μm as a function of the deposited dose, adjusted by varying the burst energy. Across all tested burst repetition rates, a clear trend is evident: from 0.5 J.mm^{-2} to approximately 3.3 J.mm^{-2}, the surface roughness values increase gradually, reflecting minor surface modifications. However, in the range of 3.8 J.mm^{-2} to 4.3 J.mm^{-2}, a higher variability is observed across all burst repetition rates, indicating a critical energy threshold where the process becomes less stable. Beyond 4.3 J.mm^{-2}, the increasing dose leads to significant fluctuations, causing pronounced roughness due to excessive localized heating. These observations confirm that the scalability is generally maintained for this L-2-L distance, as similar outputs are obtained across varying burst repetition rates when the S-2-S overlap remains constant, suggesting process acceleration through higher repetition rates is feasible.

For L-2-L = 12 μm, as shown in Figure 3.14b, the surface roughness follows a similar pattern. The roughness gradually increases for doses from 0.5 J.mm^{-2} to 5.4 J.mm^{-2}, demonstrating consistent scalability, as the outputs remain comparable across burst repetition rates under the same S-2-S overlap condition.

Finally, Figure 3.15 offers a more detailed view of the surface morphology across varying dose levels, here directly linked to burst energies. In the blue-highlighted region, representing 0.5 J.mm^{-2} for all repetition rates, minimal surface alteration is observed. However, the red-highlighted region, corresponding to higher energy levels (3.3 J.mm^{-2} to 5.4 J.mm^{-2}), reveals significant fluctuations, including micro-sphere formation and track wobbling, indicative of a too high energy transfer. Interestingly, the intermediate region, particularly for 400 kHz and 800 kHz, exhibits the smoothest track formation, though edge effects still induce artificial roughness [112].

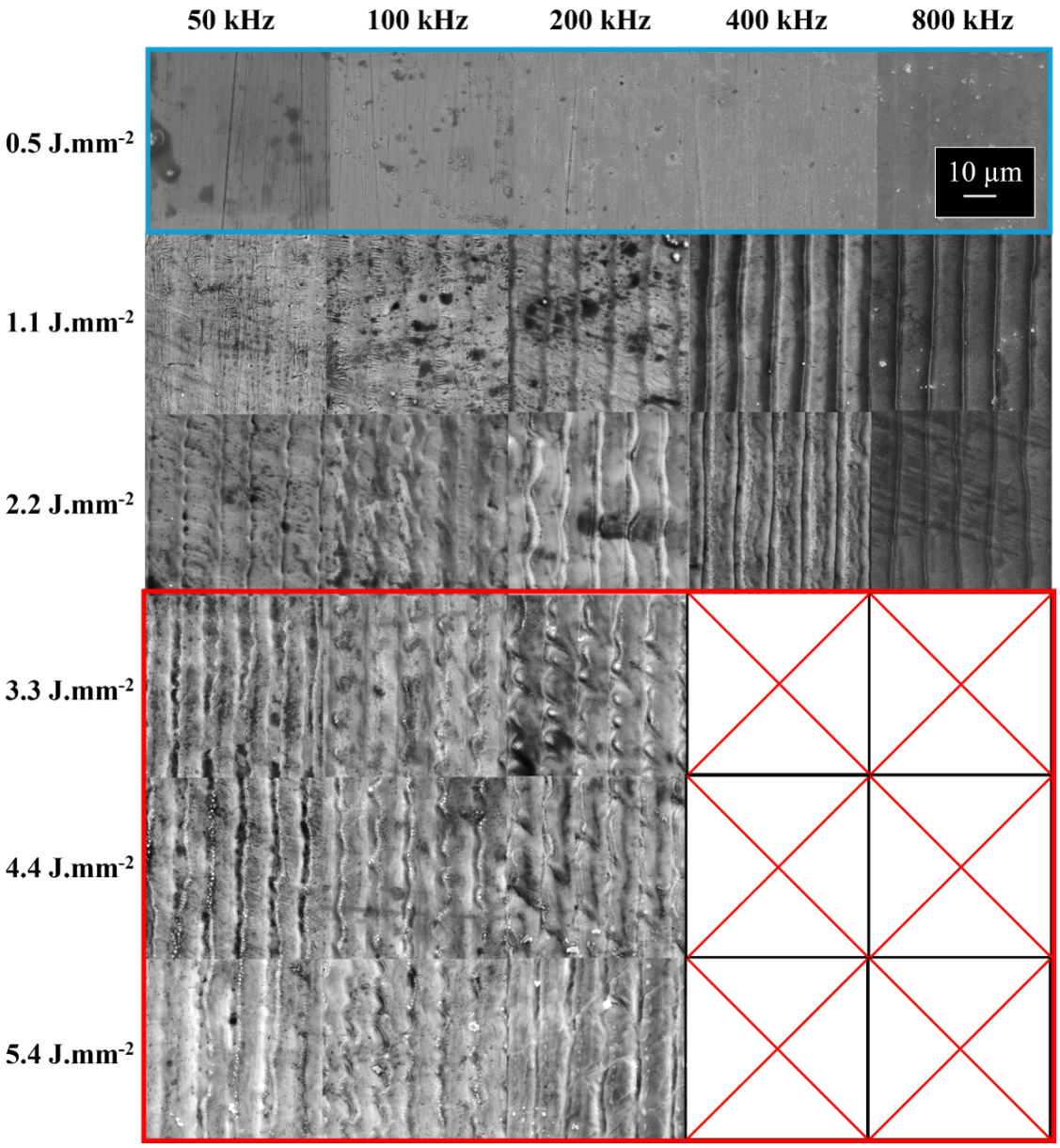

Figure 3.15: SEM top view of 316L sample at iso-dose with S-2-S = 16 μm, L-2-L = 12 μm, 800 ppb GHz-burst.

To summarize, this study has thoroughly demonstrated the feasibility and scalability of GHz-burst laser polishing for enhancing the surface quality of metallic materials. The initial proof-of-concept confirmed the fundamental viability of the GHz-burst regime, highlighting the ability of this approach to effectively control the surface morphology and demonstrating its potential to reduce roughness without excessive thermal damage when parameters are precisely controlled. The studies on the number of passes underline the importance of controlling the cumulative energy input. Results show that while multiple passes can significantly enhance surface finish, the required number of passes is highly dependent on the initial surface roughness, showing a tenfold increase in the burst energy required to smooth a much rougher surface (Ra of 1.75 µm). However, excessive repetition of passes can introduce thermal stresses, potentially compromising the material's integrity. This

insight is critical for applications with stringent surface specifications, where precision is paramount. Finally, the scalability investigation demonstrated the adaptability of GHz-burst laser polishing across varying repetition rates and marking speeds, achieving a 16× proportional speed increase with 800 kHz at 1.4 $m.s^{-1}$ without sacrificing surface quality. These results pave the way for integrating this technology into high-throughput manufacturing systems, addressing critical industry demands. Collectively, these findings establish GHz-burst laser polishing as a powerful and adaptable tool for next-generation manufacturing. Moving forward, efforts should focus on refining energy distribution strategies, integrating real-time feedback systems, and minimize edge effects.

Chapter 4

Dielectric materials functionalization

In this chapter, the main goal is to investigate the response or the morphology changes of dielectric materials under laser irradiation operating in burst mode combined with Gauss-Bessel beam shaping, in order to identify potential applications and limitations. The burst modes studied are MHz- and GHz-bursts, which combine pulse durations of hundreds of femtoseconds with burst durations in the range of hundreds of nanoseconds. This allows for both high processing precision (fs) and high ablation rates (ns).

A comparative study between the single pulse and burst regimes is provided, with MHz-bursts with 4 ppb and GHz-bursts with 50 ppb. Firstly, the influencing parameters concerning the generation of the Bessel beam are presented in Section 4.1. Secondly, a direct comparison between the regime of the Bessel beam induced bulk modification in fused silica is presented in Section 4.2. This study is directly linked with a chemical etching study of the induced bulk modifications in Section 4.2.2. Thirdly, a pump-probe shadowgraphy experiment is presented, in order to characterize the main differences previously identified between the MHz- and GHz-burst. This study is subdivided, with a classical pump-probe shadowgraphy study in Section 2.2.4, and studying the in-bulk modification with a pump-probe technique coupled with a Mach-Zehnder interferometer in Section 4.4 investigating in-bulk modifications and plasma plume dynamics. Moreover, a study on multi-burst irradiation is performed on AF32 glass which is presented in Appendix A.

4.1 Bessel beam intensity profile: influencing parameters

This section presents a parametric study aiming on identifying the key parameters influencing the axial intensity profile of a Bessel beam. In particular, the effect of the rounded tip—introduced in Section 1.4.2.2—on the longitudinal intensity distribution is investigated using the experimental setup described in Section 2.3.1.

The study is conducted in two steps. First, the influence of the entrance beam diameter on the resulting Bessel beam profile is examined. Second, for a fixed entrance beam size, the effect of the divergence of the incoming beam is analyzed.

The experimental setup used for this study is a modified version of the configu-

ration presented in Figure 2.5. In this arrangement, the Bessel module was aligned parallel to the optical table, allowing precise measurements along the translation axis. Additionally, a 2f-2f/4f imaging system with a 1x-magnification was used in order to retrieve its intensity further down along the optical line reproducing our Bessel module.

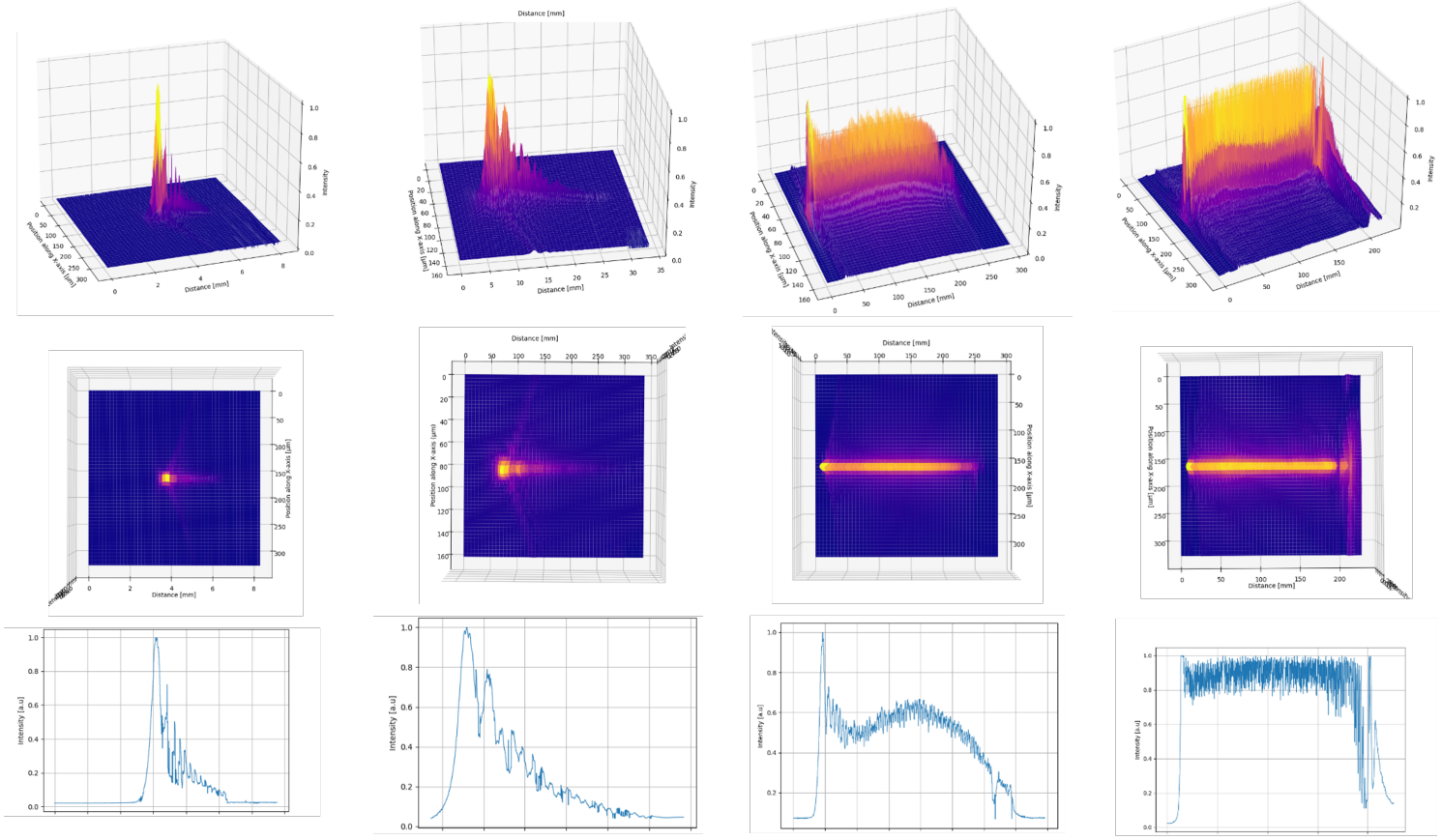

(a) (b) (c) (d)

Figure 4.1: Top row: 3D intensity profile. Middle row: top view of the 3D intensity profile. Bottom row: 2D axial intensity profile along the Bessel beam propagation length. (**a**)–(**d**) Z-intensity profiles of a Bessel beam measured for beam entrance diameters of 1.5, 3, 6, and 9 mm, respectively. Z-axis is in mm and ranges from [0-8],[0-35], [0-300], [0-200], respectively.

The results, composed of 2D reconstructions of the Bessel beam along xz, are presented in Figure 4.1 for various entrance beam diameters on the axicon. The beam diameter was adjusted by moving a short focal length plano-convex lens before the axicon. This lens increases the divergence of the beam. The first row of images is a angled 3D view of the intensity profile, the second row is a zx view of the intensity profile while the third row is a 2D plot of the intensity profile along the z direction. As discussed in Section 1.4.2.2, in contrast to an ideal phase mask, the use of a physical axicon inevitably introduces real-world limitations, the most

prominent being the rounded-tip effect [72].

In this experiment, an axicon with 170° angle is used, the rounded tip has been measured to exist over a 300 μm diameter. For a beam entrance diameter of 1.5 mm (Figure 4.1a), the central core of the Gaussian beam (which contains 7.7 % of the pulse energy and corresponds to an intensity above 92 % of the maximum pulse intensity) goes through the rounded-tip. This portion of the beam behaves as if focused by a conventional lens, resulting in a strongly asymmetric Z-intensity profile characterized by a high initial intensity peak followed by a rapid decay.

Increasing the entrance beam diameter to 3 mm (Figure 4.1b) decreases the contribution of the central core going through the round-tip, a noticeable increase in the effective depth of focus of the Bessel beam is observed, indicating a partial redistribution of the energy toward the conical region of the axicon.

For an entrance beam diameter of 6 mm (Figure 4.1c), a clear transition in the Z-intensity profile is observed. Although a strong intensity spike remains at the beginning of the propagation, it is followed by a quasi-plateau region. In this configuration, the rounded-tip contribution is reduced, allowing the axial intensity profile to approach more closely the theoretical Bessel-gauss beam behavior.

Finally, for an entrance beam diameter of 9 mm (Figure 4.1d), the Z-intensity profile becomes nearly flat over the entire propagation length of the Bessel beam. Only a small residual intensity spike is observed near the entrance, rapidly giving way to a uniform axial intensity distribution. This behavior can be attributed to the fact that only a minor fraction of the incident beam now propagates through the rounded tip of the axicon.

Across all configurations, a common feature can be identified: the wavefront passing through the rounded tip generates a circular wave that interferes with the conical wavefront shaped by the axicon. This interference results in longitudinal intensity oscillations rather than a perfectly smooth Z-profile. The amplitude of these oscillations increases as the entrance beam is smaller in diameter, so as a larger fraction of the incident energy passes through the rounded tip. Therefore, it is better to cover the full entrance aperture/pupil of the axicon to minimize this detrimental effect, as shown in Figure 4.1d.

As the beam diameter in the previous experiment was adjusted by moving a lens, it also led to an increase in the divergence of the beam. So, it is important to measure the influence of the beam divergence on the Bessel beam intensity profile. The results of the divergence study are presented in Figure 4.2. In this investigation, the beam entrance diameter was fixed at 9 mm, as this configuration previously demonstrated a quasi Z-flat Bessel intensity profile. The divergence of the incoming beam was then adjusted using additional lenses, allowing controlled variation of the beam divergence.

Three divergence angles were investigated: 1 mrad, 6 mrad, and 14 mrad with a beam entrance size of 9 mm. The first Z-intensity profile is obtained for a divergence of 1 mrad (Figure 4.2a). The profile exhibits a quasi-uniform axial intensity profile with superimposed oscillations along the propagation axis.

When the divergence is increased to 6 mrad (Figure 4.2b), a quasi-flat intensity region is still observed over the first half of the Bessel propagation length, followed by a sharp decrease in intensity. This abrupt drop is attributed primarily to a slight misalignment of the optical system during the experiment. Evidence of this misalignment can be observed in the middle row of Figure 4.2b, where a leakage of

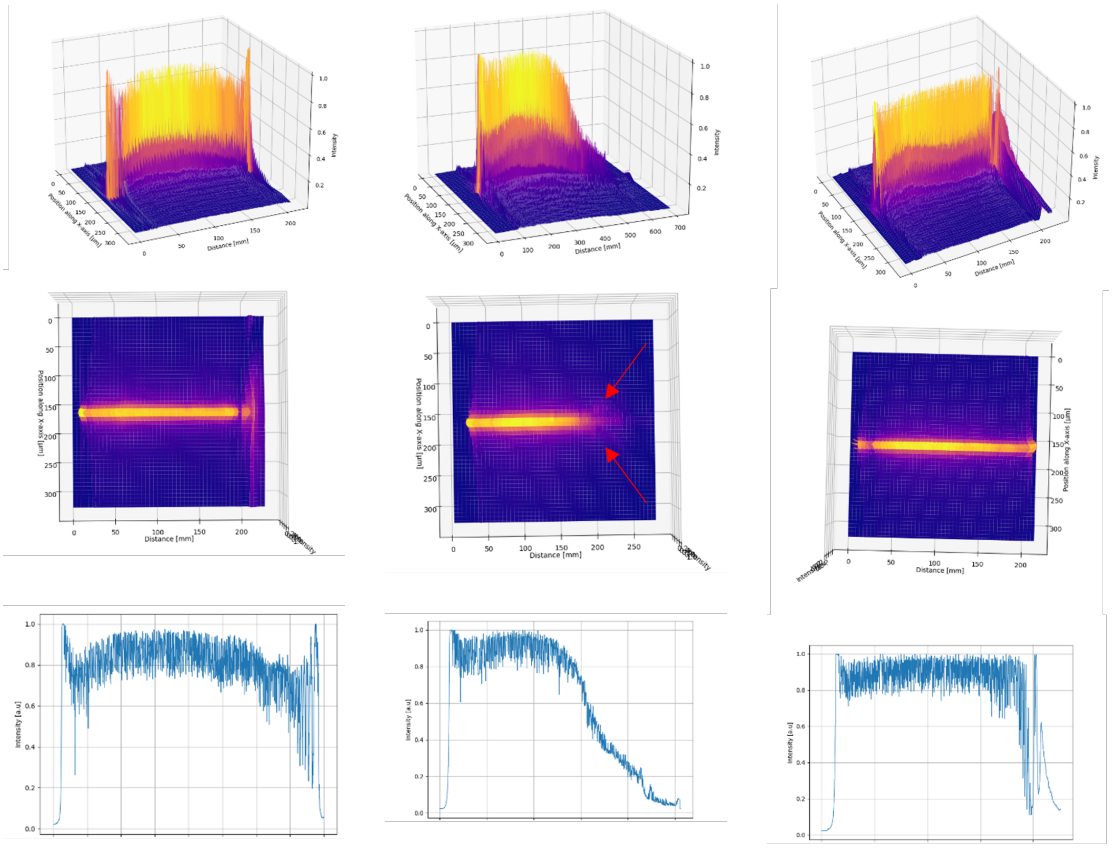

Figure 4.2: Bessel–Gauss Z-intensity profiles measured for a beam entrance diameter of 9 mm with divergences of (**a**) 1 mrad, (**b**) 6 mrad, and (**c**) 14 mrad.

intensity from the tail of the Bessel beam is visible compared to the other configurations (highlighted by the red arrows).

For the largest divergence angle of 14 mrad (Figure 4.2c), the Z-intensity profile closely resembles that obtained for the 1 mrad configuration. An almost Z-flat axial intensity distribution is recovered, with oscillations extending over the entire propagation length of the Bessel beam.

Overall, within the investigated range, the divergence of the incoming beam appears to have a minor influence on the axial intensity uniformity of the Bessel beam, provided that the optical alignment is carefully maintained.

4.2 Bessel beam induced in-bulk modifications

In this section, the modifications induced by laser irradiation by a Bessel beam within the bulk material are first examined and compared across the three regimes using either a single pulse or a burst, as detailed in Section 4.2.1. Subsequently, the evolution of the etching rate as a function of etching time is presented, together

with a detailed analysis of the etching-induced bulk modifications in Section 4.2.2. The etching depths obtained in the SP and MHz-burst regimes are then compared. Finally, it is demonstrated that the GHz-burst regime enables direct hole formation using a single burst, constituting a remarkable result that paves the way toward chemical-free, single-step, high-aspect-ratio TGV fabrication (see Section 4.2.3).

4.2.1 Single Pulse / MHz-burst / GHz-burst

The purpose of this section is to investigate the mechanisms related to sub-surface modification, induced in glass after laser irradiation using a Bessel beam configuration, for future sub-surface structuring. In the upcoming section, the modification depths produced after laser irradiation in fused silica are presented as a function of the energy contained in a pulse or burst, ranging from 15 µJ to 255 µJ. Each modification was repeated four times on the same sample with a pitch of 50 µm to ensure reliability of the results. The bulk modification was observed in-situ using the side-view system. It can be noticed that modifications generated by a low-energy Bessel beam originate from the middle of the interaction region and subsequently expand toward the top and rear surfaces. For etching purposes, the Bessel beam was initially fully positioned inside the medium, producing a modification at 255 µJ. Subsequently, by moving the Z-stage along the irradiation axis, 30 % of the Bessel beam was positioned above the top surface of the sample, such that only 70 % of the maximum interaction length contributed to modification formation inside the material so that the rising front and intensity variations introduced by the round-tip on the longitudinal intensity profile are located in air above the target surface, and do not interact with the glass material. This positioning ensured, for all experimental series and burst energies, that the modifications reached the top surface for the subsequent etching step, as described in Section 2.3.2. The resulting modifications obtained in the single-pulse (SP), MHz-burst, and GHz-burst regimes are shown in Figure 4.3.

The images in Figure 4.3 were acquired using an in situ long-distance microscope equipped with a 1.4× zoom lens and were reconstructed by stitching multiple images together. The inserts on the right are images/micrographs obtained using the optical measuring microscope equipped with a 50× objective. In Figure 4.3a and Figure 4.3b, corresponding to the SP and MHz-burst regimes, respectively, visible modifications were produced across the entire investigated energy range. From Figure 4.3a, it is observed that increasing energy leads to deeper and darker modifications in the images, indicating a stronger material alteration. The magnified views shown in Figure 4.3a and Figure 4.3b provide detailed observations of the modifications obtained at the highest SP and burst energies, 128 μJ and 255 μJ, respectively. These modifications appear thin and elongated, with small bubbles distributed along their length in the SP regime. In the MHz-burst regime, similarly elongated structures are observed, although the bubbles appear larger. The bubble size could not be quantified accurately with the available optical microscope.

In contrast, in Figure 4.3c, corresponding to the GHz-burst regime, a clear energy threshold for modification formation is observed. Reproducible modifications are obtained for burst energies of 165 µJ and above. Below this threshold, the modifications generated by a single GHz-burst are weak, poorly reproducible, and do not reach the sample surface. Although applying multiple bursts can produce

modifications comparable to those obtained at higher energies, this case is not considered in the present study. Since the pulse energy is distributed over a burst of 50 sub-pulses (2 µJ–5.1 µJ per sub-pulse), nonlinear absorption requires higher peak intensity to initiate modification. Between 165 µJ and 225 µJ per GHz-burst, consistent modifications are observed with increasing depth as a function of burst energy. In Figure 4.3c, the hole morphology corresponding to a burst energy of 255 µJ in the GHz-burst regime is shown, revealing a straight, taper-free, and continuous channel. However, cracks are observed around the periphery of this modification, which will be discussed in Section Section 4.2.3. The morphology of these modifications is distinctly different from those obtained in the SP and MHz-burst regimes where a collar of tiny bubbles is observed. It may be hypothesized that these bubbles correspond to material ejection or void formation induced by the strong compression/expansion dynamics associated with the GHz-burst regime combined with Bessel beam shaping. This hypothesis is further discussed in the following section.

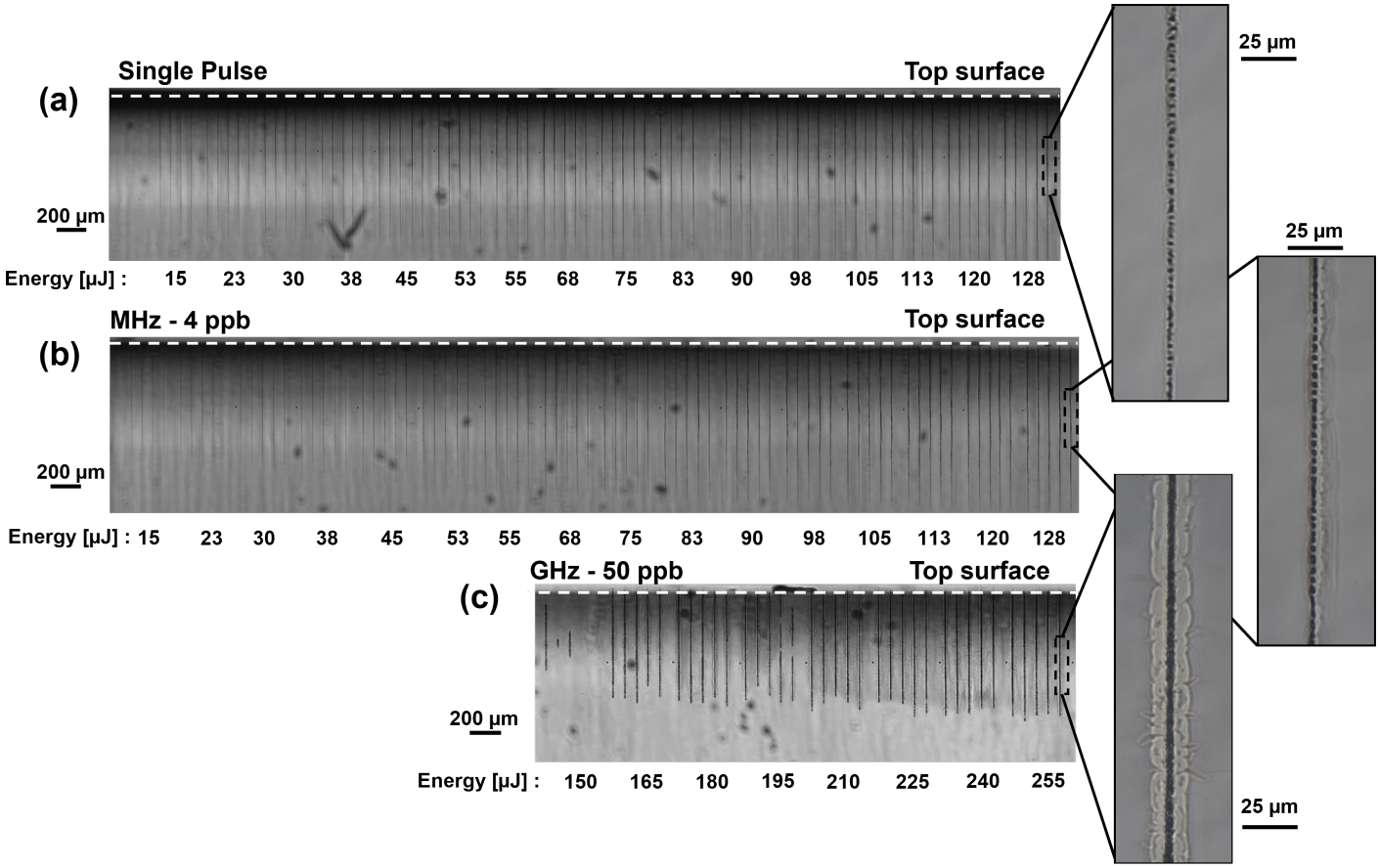

Figure 4.3: Optical microscope side views of modifications obtained in fused silica after laser irradiation with a Bessel beam with single pulse or burst, respectively, at an energy ranging from 15 to 255 µJ. (**a**) Single-pulse mode, (**b**) 4 ppb MHz-burst, and (**c**) 50 ppb GHz-burst. The pitch between two modifications of identical energy is 50 µm. The white line at the top of each image indicates the initial surface. Insets on the right show magnified views of the highest-energy modification.

Figure 4.4 shows the evolution of the depth of the laser-induced modifications over the full energy range for the three regimes. The uncertainty in the depth measurement was estimated to be ±5 µm, and the error bars are not displayed on

this graph since they would not be visible. From this figure, a similar behavior between the SP (blue triangles) and the MHz-burst (red diamonds) regimes can be observed, consistent with Figure 4.3. Moreover, a clear trend is observed from 15 µJ to 55 µJ, with the depth increasing at a rate of 5.25 µm/µJ for both regimes. However, an offset in the initial modification depth is observed between these two regimes. This shift can be explained by the fact that the energy is distributed among four pulses in the MHz-burst configuration. As a result, the intensity of an individual pulse is four times lower and the non-linear absorption is reduced. Consequently, the modifications are induced at higher energy compared to the classical SP regime for identical size. This effect is particularly pronounced in fused silica, a dielectric material with a relatively large band gap (9 eV) [104].

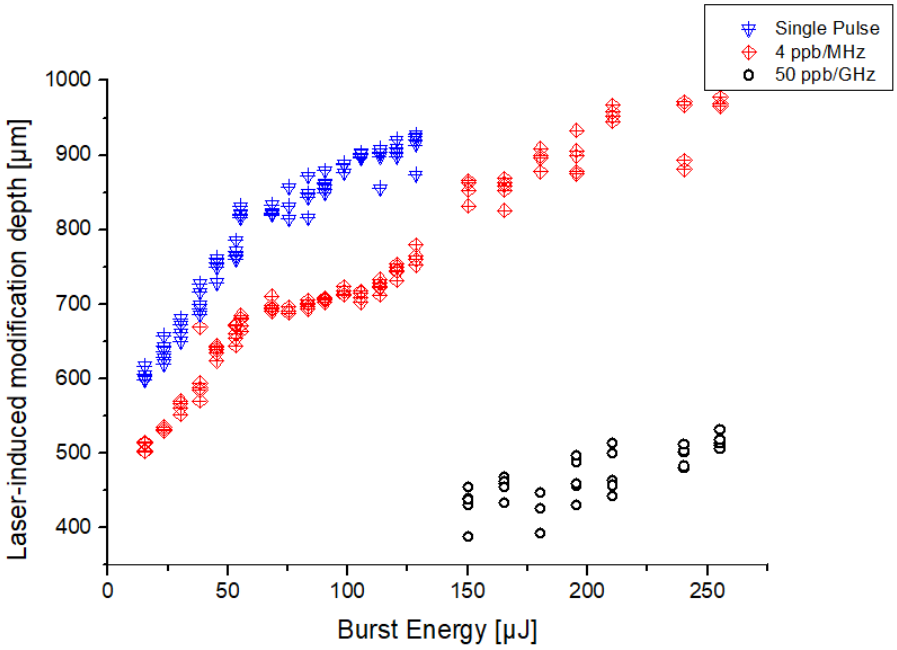

Figure 4.4: Evolution of the modification depth obtained in fused silica with a single pulse/burst as a function of energy in the range from 15 to 128 µJ, in single-pulse mode and 15 to 255 µJ for 4 ppb MHz-burst, and 50 ppb GHz-burst. For each energy, at least 4 modifications were measured.

For both, the SP and MHz-burst regimes, an energy of 55 µJ appears to represent a threshold beyond which the rate of increase of the modification depth decreases to 1.45 µm/µJ. It is also observed that both regimes are capable of producing modifications longer than 900 µm. This is particularly noteworthy, as nearly 1 mm deep modifications are achieved even though the Bessel beam is not fully confined within the sample. Higher energies were investigated in the MHz-burst regime compared to the SP regime. This choice was made because increasing the energy to similar levels in the SP regime would have resulted in air breakdown and potential damage to the optical setup.

Finally, when considering the GHz-burst results (black circles), shorter modifications are observed, starting from approximately 400 µm and reaching about 500 µm for a burst energy of 255 µJ, corresponding to a rate of 1.19 µm/µJ, which is significantly lower than the values obtained for the SP and MHz-burst regimes. In the GHz-burst configuration, the energy is distributed among 50 pulses with a pulse-

to-pulse delay of 0.8 ns. Consequently, the intensity of each individual sub-pulse is substantially lower than in the SP and MHz-burst regimes, resulting in weaker non-linear propagation effects. Moreover, the extremely short pulse-to-pulse delay promotes cooperative interactions between sub-pulses, leading to strong thermal accumulation within the burst. This behavior could explain the distinct response observed in the GHz-burst regime, where direct void formation occurs instead of extended internal modifications.

4.2.2 Etching study

In this section, the results of chemical etching in KOH are presented using the same samples containing the laser-induced modifications described in the previous subsection. As mentioned in Section 2.3.2, the samples were etched in a 10 mol·L^{-1} KOH solution for 30 min, 1 h, and 2 h. Microscope images of the samples after 1 h of etching are shown in Figure 4.5. All images were acquired using a long-distance microscope equipped with a 1.4× zoom lens.

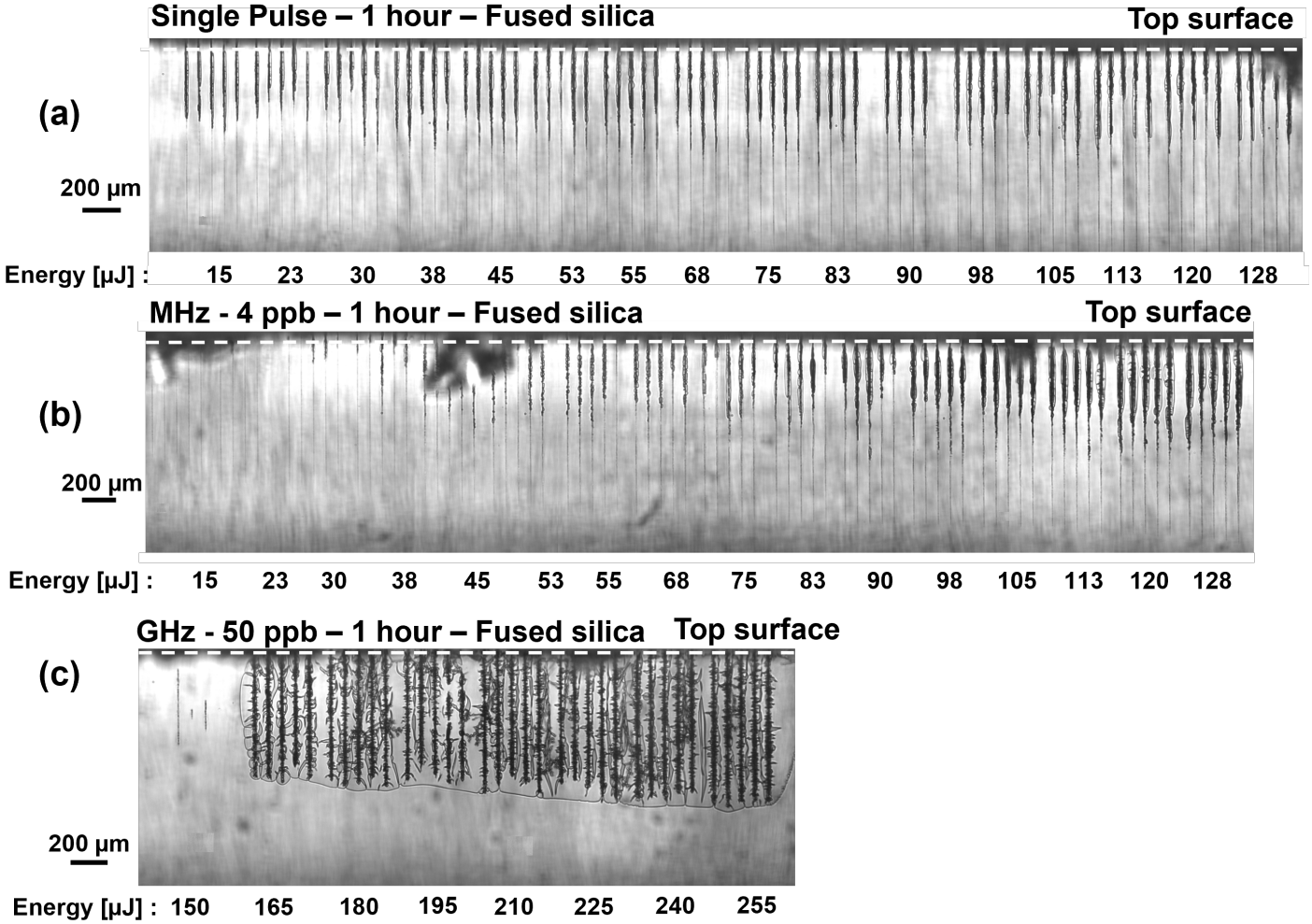

Figure 4.5: Optical microscope images of the modifications obtained in fused silica after laser irradiation with one single pulse or burst, respectively, with an energy ranging from 15 to 255 µJ, in (**a**) Single pulse mode, (**b**) 4 ppb MHz-burst, and (**c**) 50 ppb GHz-burst and after 1 h of KOH etching.

From the images, thicker black lines can be distinguished and are attributed to the etched regions, whereas thinner black lines correspond to the bulk-modified regions unaffected by the etching process. The etched depths were measured as the lengths of the thicker black lines. Figure 4.5 illustrates the evolution of the etching-induced modifications as a function of the energy per SP (Figure 4.5a) or per burst (MHz-burst, Figure 4.5b; GHz-burst, Figure 4.5c).

In the SP regime, a slow increase in modification depth is observed with increasing energy. A slightly larger variance in the etched depths is also observed for identical laser parameters compared to the results presented in Figure 4.3. In the MHz-burst regime (Figure 4.5b), a clear difference from the SP regime is observed, with no reproducible etched lines below a burst energy of 55 µJ. At higher burst energies, the etching depth increases slowly, similarly to the SP regime, although the etched holes appear wider. Finally, Figure 4.5c presents the etched modifications obtained in the GHz-burst regime. After 1 h, etching proceeds along the entire length of the modification and also attacks the surrounding bulk material, leading to crack formation. The same behavior is observed after 30 min and 2 h. This confirms that the structure produced by a single GHz-burst corresponds to a true elongated void reaching the surface rather than a simple bulk modification. Consequently, chemical etching is not required in the GHz-burst regime.

The evolution of etching depth across the energy range is shown in Figure 4.6a for SP and in Figure 4.6b for MHz-burst. Empty symbols correspond to laser-induced modifications before etching (from Figure 4.3) and are included for comparison, whereas filled symbols represent etched modifications. Results for the GHz-burst regime are not included, as etching does not further modify the holes produced directly by laser irradiation, as previously discussed. In Figure 4.6, a similar evolution of etching depth is observed for both SP and MHz-burst regimes. In the SP regime, after 30 min of etching, no measurable effect is observed for pulse energies below 100 µJ. For higher energies, significant deviations in etched depth are observed within the same energy group. After 1 h of etching, a clear cut-off appears. Below 40 µJ per pulse, the etching effect remains weak and no clear modifications are observed, similarly to the 30 min results. Above 40 µJ, the etched depth rapidly increases to approximately 400 µm and continues to increase slightly with pulse energy. For energies above 100 µJ, fluctuations decrease significantly and the etched depth tends to saturate.

This behavior is confirmed by the etching rates. During the first hour, an etching rate of 300 µm/h is obtained at 68 µJ and reaches 606 µm/h at 128 µJ in the SP regime. During the second hour, however, the etching rate decreases and the averaged etching rate over the two hours decreases below 100 µm/h at 38 µJ and reaches 315 µm/h at 128 µJ, indicating a saturation effect with the rate reduced by approximately a factor of two compared to the first hour. Compared to values reported in the literature, an increased etching rate is observed during the first hour [113, 114], whereas values after 2 h remain typical. Considering the etching conditions, pristine fused silica is expected to exhibit an etching rate of approximately 150 nm/h [115]. The selectivity, defined as $S = (R + \epsilon)/\epsilon$ [113], quantifies the enhancement of etching in laser-modified material relative to pristine material, where R is the modified etching rate and ϵ the pristine etching rate. A selectivity of 2103:1 is obtained after 2 h, representing, to the best of current knowledge, the highest value reported in the literature.

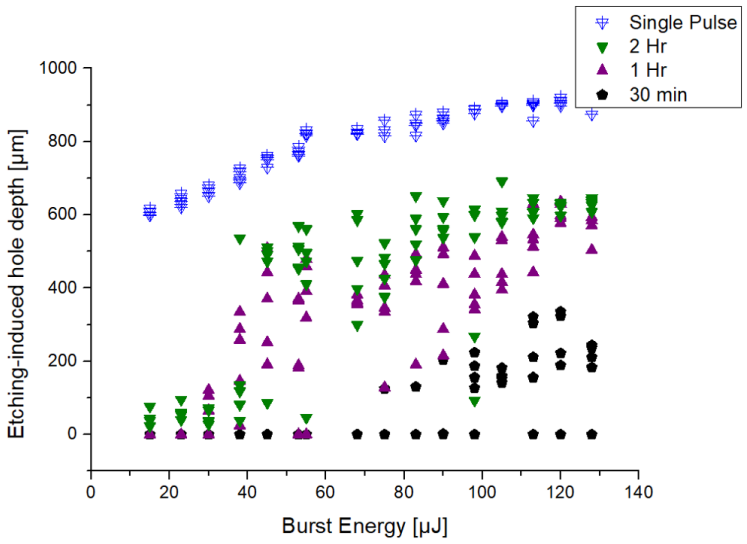

(a)

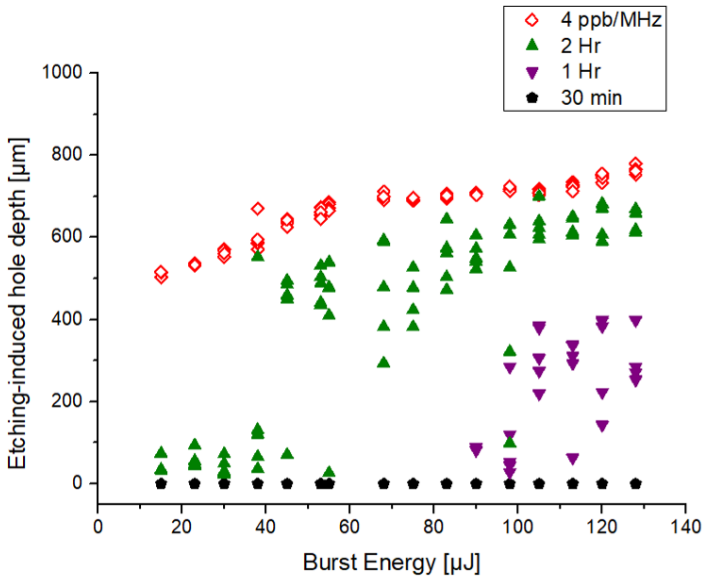

(b)

Figure 4.6: (**a**) Evolution of the modification depth obtained in fused silica after a single pulse (before chemical etching) and of the hole depth after chemical etching as a function of the pulse energy, ranging from 15 to 140 µJ, for different etching times. (**b**) Evolution of the modification depth obtained in fused silica after a single MHz-burst (before chemical etching) and of the hole depth after chemical etching as a function of the burst energy, ranging from 15 to 140 µJ, for different etching times.

For the MHz-burst regime, the results are shown in Figure 4.6b. After 30 min of etching, similarly to the SP regime, no etching is observed. After 1 h, only modifications produced with burst energies above 100 µJ exhibit consistent etching, with depths ranging from 100 µm to 300 µm and significant shot-to-shot fluctuations, accompanied by increased cracking at the edges. The resulting holes are also smaller compared to those obtained in the SP regime. After 2 h of etching, a behavior similar to the SP regime is observed. Below 40 µJ, etched depths remain below 100 µm

and are weakly visible. Above 40 µJ, the etched depth rapidly increases, reaching values between 400 µm and 600 µm for a burst energy of 140 µJ with relatively low fluctuations.

Overall, a slight increase in etching depth is observed in the MHz-burst regime. During the first hour, an etching rate of 75 µm/h is measured at 98 µJ, increasing rapidly to 300 µm/h at 105 µJ. Beyond this value, the rate remains relatively stable, reaching 315 µm/h at 128 µJ. However, during the second hour, the behavior differs from the SP regime. While the rate decreases below 100 µm/h at 38 µJ, it increases again above 315 µm/h at 113 µJ and reaches a maximum of 322 µm/h at 128 µJ. This indicates that the saturation depth has not yet been reached in the MHz-burst configuration, as the etching rate after 2 h remains higher than during the first hour. The calculated selectivity for the MHz-burst regime (4 ppb) reaches 2230:1, exceeding the SP result by 6 %. This small difference could be justified by the fact that the bulk modification in SP and MHz-burst are more or less the same. This selectivity value is, to the best of current knowledge, the highest reported value.

To compare the three regimes, the maximum laser-induced modification length, etched depth, etching rate, and selectivity in fused silica are summarized in Table 4.1. The maximum modification depths correspond to 128 µJ in the SP regime and in MHz-burst regimes. The maximum etched depths are obtained after 2 h of etching for 100 µJ in both SP and MHz-burst regimes. The highest etching rates over 1 h and 2 h are obtained at 128 µJ in the SP regime and at 105 µJ and 128 µJ, respectively, in the MHz-burst regime.

Regime	**Max. modification depth [µm]**	**Max. etched depth [µm]**	**Etching rate (1 h) [µm/h]**	**Etching rate (2 h) [µm/h]**	**Selectivity**
SP	930 (128 µJ)	650 (100 µJ)	606 (128 µJ)	315 (128 µJ)	2103:1
MHz-burst	950 (225 µJ)	680 (100 µJ)	300 (105 µJ)	322 (128 µJ)	2230:1
GHz-burst	525 (225 µJ)	–	–	–	–

Table 4.1: Summary of the maximum laser-induced modification depth, etched depth, etching rate, and selectivity obtained in fused silica for single-pulse (SP), MHz-burst, and GHz-burst regimes.

4.2.3 Towards direct TGV-drilling with single GHz-burst

As the combination of the GHz-burst and the Bessel beam directly produces an elongated void, the potential for direct, single-step, and dry hole drilling is investigated in this subsection. As detailed in Section 4.2.1, all modifications were previously performed with approximately 70 % of the Bessel beam positioned inside the sample to ensure a relatively uniform energy distribution for the etching study as a function of pulse energy. Additional experiments were conducted with the entire Bessel beam placed inside the sample in order to maximize the interaction length within the material. In this configuration, longer modifications were produced, clearly exceeding the 525 µm length reported in Figure 4.4.

As shown in Figure 4.7, a single-shot irradiation in pristine fused silica enabled the formation of a hole 730 µm in length with an entrance diameter of 4 µm, corresponding to an aspect ratio of 182:1. However, cracks were observed around the

periphery of the affected zone along the hole, likely resulting from material removal or void formation induced by the single GHz-burst. This behavior intrinsically limits the minimum spacing between adjacent holes that can be produced without inducing significant damage to the surrounding bulk material. Consequently, this process may be suitable for the fabrication of hole matrices in bulk materials with thicknesses below 700 µm and very small hole diameters (< 5 µm), provided that relatively large spacing (> 50 µm) is maintained, depending on the targeted application.

An important advantage of this approach is that hole formation is achieved in a single step, as the structure is generated directly by a single GHz-burst without requiring any post-process etching. This capability of direct drilling using a single GHz-burst in a Bessel beam configuration opens the way toward on-the-fly glass drilling of through-holes, as required for TGV fabrication [116].

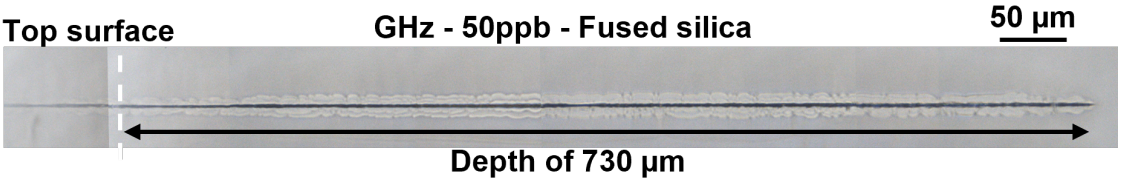

Figure 4.7: Void microstructure obtained in fused silica with one single GHz-burst (50 ppb) of 255 µJ without chemical etching. Top surface is on the left.

4.3 Pump probe shadowgraphy

In this section, a pump-probe shadowgraphy experiment is presented, investigating the main differences previously identified in Section 4.2.1 between MHz-burst and GHz-burst laser–matter interaction. The MHz-burst regime is first analyzed in Section 4.3.1, followed by the GHz-burst configuration in Section 4.3.2. The single pulse regime was not investigated as it presented a higher risk of damage for the laser due to the need of deactivating a safety feature inside the laser for this experiment.

The optical setup described in Figure 2.8 was used. Bessel beam shaping was implemented using the configuration presented in Figure 2.5 with a beam entrance size of 9 mm, and a burst energy of 270 µJ was applied. Temporal sampling was performed from the pump–probe temporal overlap, determined using the oscilloscope (Figure 2.7), up to 100 ns, with a temporal resolution of 1 ns. The data analysis methods used in this section are detailed in Section 2.2.4.

4.3.1 4-ppb MHz-burst

In the following section, shadowgraphy images obtained after laser irradiation in Soda-Lime glass are presented as a function of the pump–probe delay. The same experiment has been attempted in Fused silica, but due to the surface quality of the manually polished side-surface of fused silica, the viewing quality was not sufficient for the pump-probe set-up, whereas the Soda-Lime samples presented sufficient side-surface quality for laser irradiation and imaging. Each delay was repeated five times on the same sample with a pitch of 50 µm between tests to ensure repeatability. Initially, the delay was varied from 0 to 8 ns in 1 ns steps using the delay-line translation stage. The delay was then shifted using the first pulse picker so that

the new zero corresponded to 25 ns, after which the translation stage again scanned an 8-ns window. This procedure was repeated until reaching 100 ns. Finally, the optical pump line was adjusted to shift the zero delay to 9 ns, and the full cycle was repeated twice to obtain a complete mapping of delays between 0 and 100 ns.

A global overview of the experiment for the 4-ppb configuration is shown in Figure 4.8. The top of the figure displays a time axis spanning 0–100 ns, with major ticks every 10 ns and minor ticks every 1 ns. For clarity, the MHz-burst temporal structure (4 ppb) is schematically represented on the axis. The amplitude is arbitrary, but the temporal spacing is accurate, with sub-pulses located at 0, 25, 50, and 75 ns. Below the axis, a compilation of shadowgraphy images at different delays is grouped into phases. In the MHz-burst regime, eight phases can be identified by visual inspection, divided into two categories: absorption phases, characterized by reduced transmission and labeled Abs. (i), and relaxation phases, characterized by increased transmission and labeled Rlx. (i).

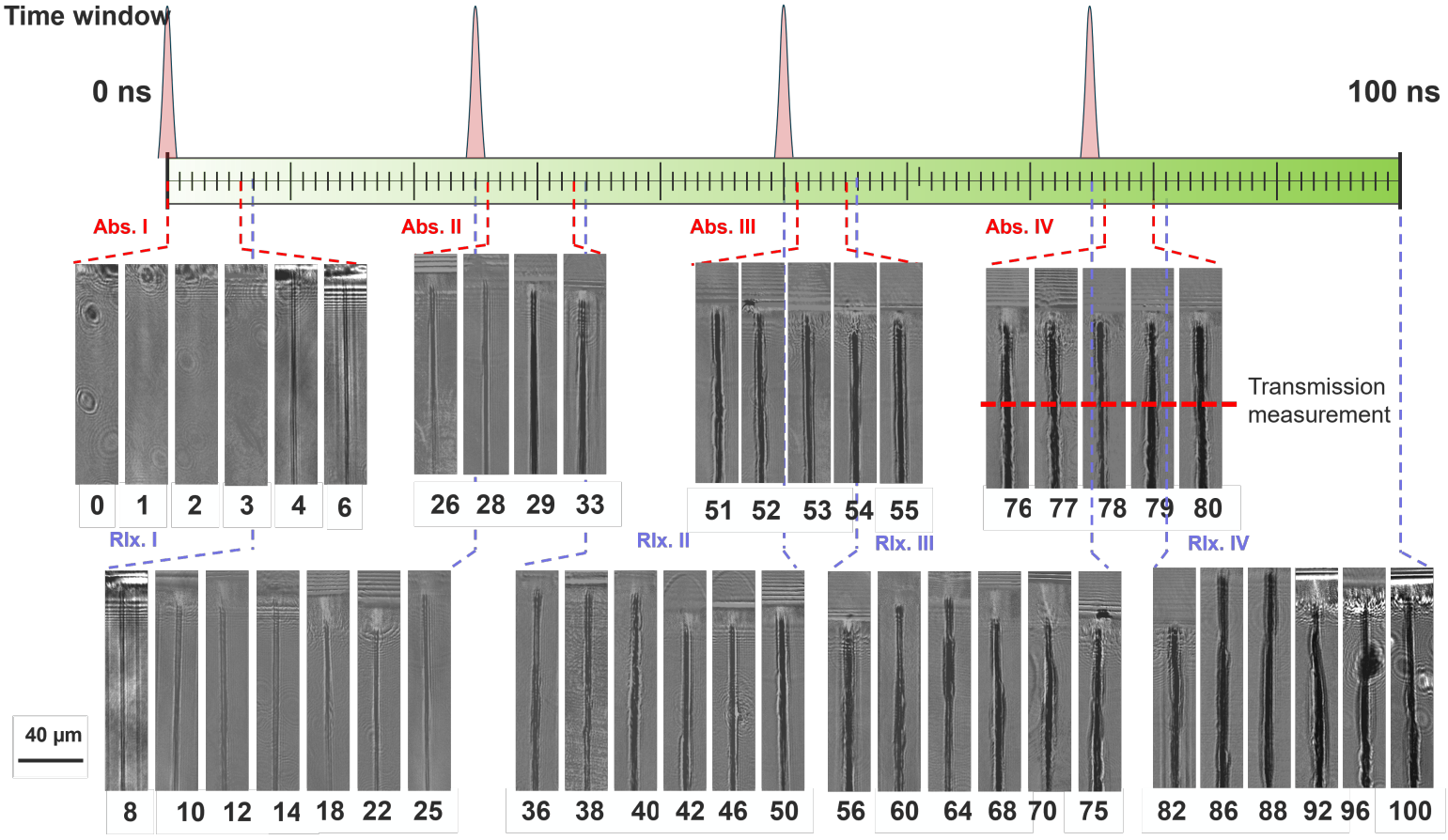

Figure 4.8: Pump-probe imaging in Soda-Lime glass in MHz-burst regime with 4 pulses per burst and burst energy of 270 µJ with delays ranging from 0 ns to 100 ns for a single burst applied. Minimal delay investigated between measurements was 1 ns.

From visual inspection, the first pulse arrives at 0 ns. The corresponding image shows no observable modification, and similar observations hold for delays of 1–3 ns. As our observation system used a magnification of 5.8x with an estimated numerical aperture (NA) of 0.1, this yields a lateral resolution of 2.2 µm according to [59].

This is limiting the interpretation of the results, but had been chosen to have a large enough field of view of the Bessel beam. Thus, it is believed that the interaction may be ongoing but not detectable at our current NA. At 4 ns, a darkening of the central region appears, likely caused by densification induced by the first pulse. At 6 ns, a compression wave becomes visible along the elongated bulk modification. This marks the end of the first absorption phase, defined by the absorption of the probe beam, and the beginning of the first relaxation phase.

At 8 ns, the compression wave is still visible, indicating a strong pressure gradient in the bulk [57]. Tracking its propagation across successive images yields an acoustic velocity of 5.72 µm·s^{-1} (5.72 km·s^{-1}) as presented in Figure 4.9a alongside the visual aspect of this compression wave in Figure 4.9c. This value is consistent with reported elastic wave velocity values in Soda-Lime glass [2, 117]. This suggests that the pressure generated by the first pulse remains below the 5 GPa threshold for inelastic response [58]. During this first relaxation phase (Rlx. I), the central region expands and brightens up to 25 ns, indicating progressive relaxation in the absence of continued laser induced pressure.

At 25 ns, the second pulse initiates the second absorption phase (Abs. II), spanning approximately 26–33 ns. The previously relaxing region is re-excited, producing renewed darkening of the core, with maximum absorption of the probe observed near 29 ns.

At 35 ns, the second relaxation phase (Rlx. II) begins, marked by increasing transmission and the emergence of a second acoustic wave propagating outward at approximately 5.69 km s^{-1}. However, the transmission does not recover to the same level as during Rlx. I, which means that there is a cumulative effect pulse after pulse.

The third pulse arrives at 50 ns, initiating Abs. III. A stronger and more homogeneous darkening of the core is observed, peaking around 55 ns. The third relaxation phase (Rlx. III) begins near 56 ns, again accompanied by an acoustic wave with a measured velocity of 5.75 km s^{-1}. The core gradually brightens between 56 and 75 ns.

At 75 ns, when the fourth pulse arrives, a white wavy structure appears at the edge of the core, possibly indicating the onset of crack appearance in the bulk along the Bessel beam. The fourth absorption phase (Abs. IV) begins at 76 ns, showing additional darkening that quickly saturates. The white structure remains visible in subsequent images, and peak absorption occurs near 80 ns.

The final relaxation phase (Rlx. IV) starts at 81 ns. An acoustic wave is detected at 82 ns, propagating at 5.85 km s^{-1}. The core region remains relatively stable until about 92 ns, when a reduction in core diameter is observed. At 100 ns, the structure has not fully relaxed for this configuration. A representative image of the final modification is shown in Figure 4.9b.

From those images, a linear profile is extracted and fitted to determine the minimal transmission values (i.e. the darkest pixel on each transverse profile) at each nanosecond of the interactions. This transmission value is then used to compute the absorbance, which should not be confused with the absorption coefficient which will be discussed later. The absorbance is defined as:

$$\alpha = ln(\frac{1}{\Delta T}) \tag{4.1}$$

with ΔT being the measured transmission [8, 118, 119]. Some disciplines use

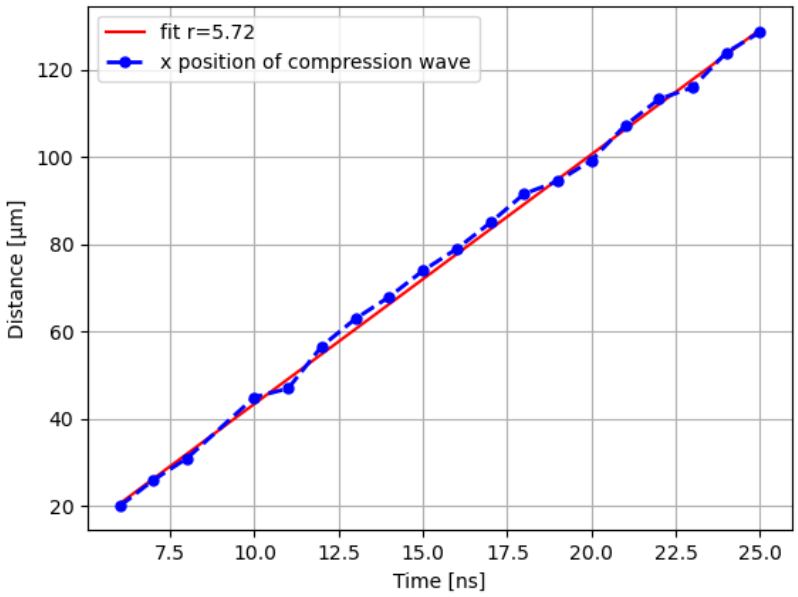

(a)

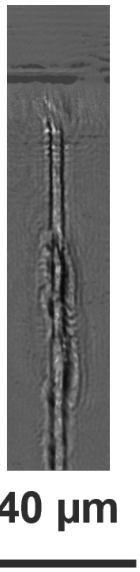

(b)

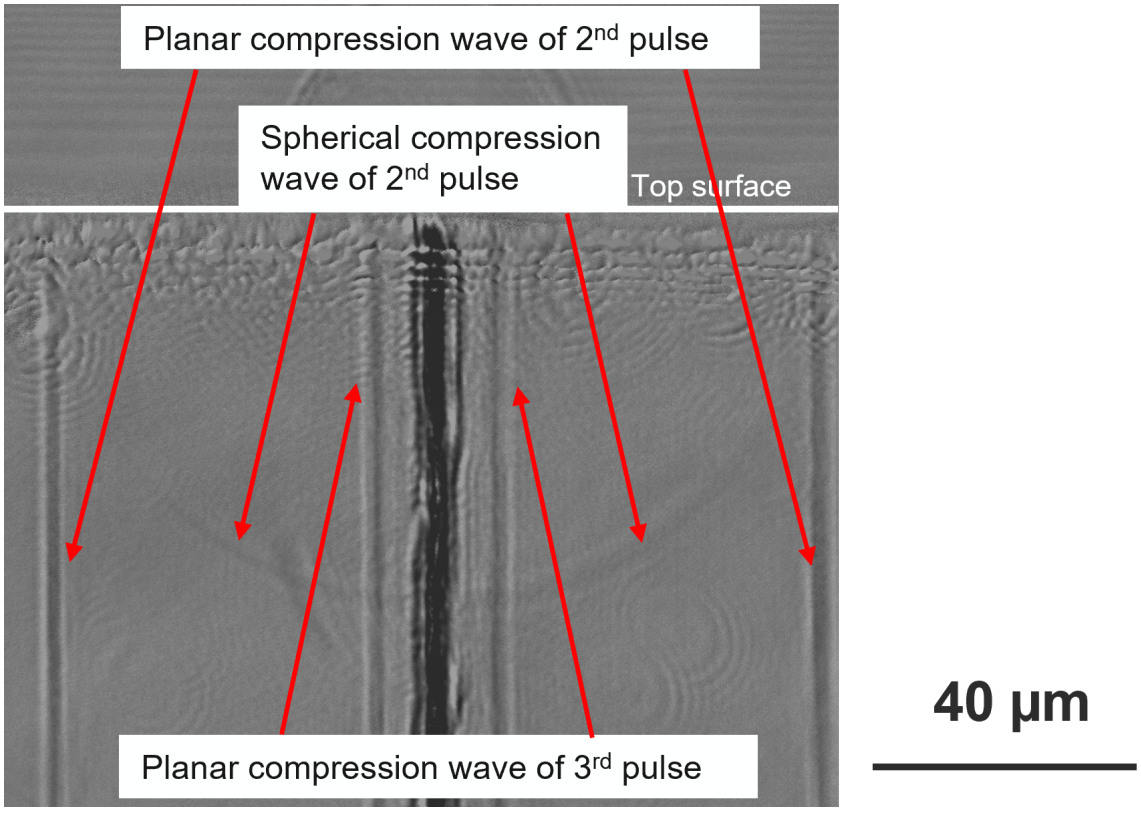

(c)

Figure 4.9: (**a**) Measurement of the first acoustic wave velocity inside the bulk of Soda-Lime glass. (**b**) Final modification obtained with MHz-burst in Soda-Lime glass. (**c**) View of compression/acoustic wave induced by the laser-matter interaction at 58 ns in MHz-burst.

by convention the base 10 for the logarithmic absorbance rather than the Neperian absorbance [120] but Neperian is used in this work. These values are then plotted against time in Figure 4.10. This Figure displays the time delay between the pump and probe as the x-axis, the y-axis is the absorbance, a dimensionless unit, a schematic representation of the burst repartition in time is displayed on the x-axis. The eight phases discussed previously are also indicated in this Figure. Finally, the data points are represented by empty circles and represent the mean value of the transmission for a given delay over the five repeated measurements. The y-bars around each point represent de standard deviation over the 5 measurements compared to the mean. Additionally, for visual representation, the different absorption phases are manually fitted by Equation (4.2) while the relaxation phases are manually fitted by Equation (4.3).

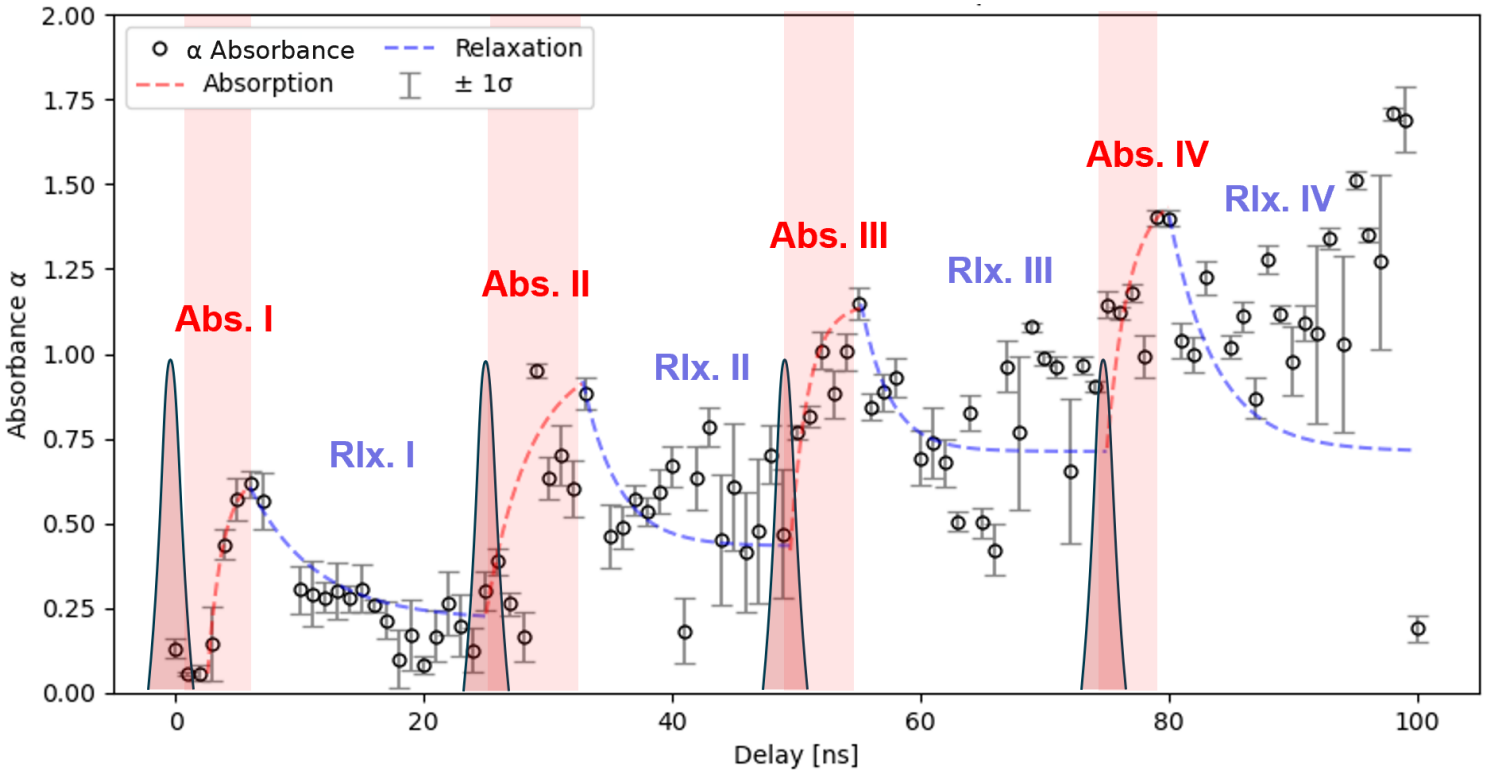

Figure 4.10: Pump-probe absorbance measurement in Soda-Lime glass in MHz-burst with 4 pulses per burst and bursts energy of 270 µJ with delays ranging from 0 ns to 100 ns for a single burst applied.

$$Abs(i) = A(i)e^{\frac{t_0 - t}{\tau}} + C(i) \tag{4.2}$$

$$Rlx(i) = A(i)e^{\frac{t_0 - t}{\tau}} + C(i) \tag{4.3}$$

where A is the amplitude, t_0 the starting time of the fit, τ the characteristic time of the exponential and C a constant.

At delays between 0 and 3 ns, the absorbance remains low at approximately 0.1, which defines the baseline level. As shown in the previous figure (Figure 4.8), the Abs. I phase begins with an increase in absorbance and reaches its maximum absorption at 7 ns. The absorption dynamics are well described by the fitted curve,

	Abs. I	**Abs. II**	**Abs. III**	**Abs. IV**	**Rlx. I**	**Rlx. II**	**Rlx. III**	**Rlx. IV**
t [ns]	2.6 - 6	25 - 32.8	49.5 - 55.2	75 - 80	6 -25	32.8 - 49.5	55.2 - 75	80 - 100
A	-0.965	-0.91	-0.74	-0.772	0.49	0.49	0.44	0.702
τ [ns]	1.22	3.58	1.42	1.78	5.38	2.82	2.3	3.74
t_0 [ns]	2	24.4	49.5	75	4.8	32.8	55.2	80
C	0.647	1	1.147	1.478	0.215	0.433	0.712	0.712

Table 4.2: Summary of parameters used for the fitting of Figure 4.10.

corresponding to an exponential rise of the absorbance. The fitting parameters are summarized in Table 4.2, yielding a characteristic time of 1.22 ns. The maximum absorbance measured during this phase is 0.6.

Immediately afterward, the Rlx. I phase begins. The relaxation was fitted using an exponential decay. During this first relaxation phase, the absorbance decreases rapidly from 0.6 to 0.3 between 7 and 9 ns, followed by a slower decrease from 0.3 to 0.11 between 9 and 24 ns.

The second pulse arrives at 25 ns, marking the onset of the Abs. II phase. The absorbance rises sharply from 0.11 to 0.96 between 28 and 29 ns. Following this absorption stage, fluctuations are observed between 29 and 33 ns, with the absorbance ending around 0.89 before entering the next phase.

The Rlx. II phase starts at 33 ns with an absorbance of 0.89 and rapidly decreases to an average value of 0.53 between 35 and 41 ns. Over the 41–50 ns interval, the average absorbance reaches approximately 0.46. However, significant fluctuations are observed, and the data do not closely follow the fitted curve. A second rise seems to occur after each relaxation leading to a second relaxation phase. This interpretation of the curves has not been studied for the MHz-case.

At 50 ns, the third pulse reaches the sample, causing a sudden rise in absorbance from 0.46 to 0.8 between 50 and 51 ns. The absorbance continues to increase, reaching 1.15 at 55 ns. In this phase, the data exhibit reduced fluctuations and follow the handmade fitting more closely.

The Rlx. III phase then extends from 55 to 75 ns. The exponential decay relaxation model (blue curve) does not accurately reproduce the data. Initially, the absorbance decreases nearly linearly from 1.15 to 0.78 between 55 and 60 ns, followed by a decrease from 0.78 to 0.66 between 66 and 74 ns.

At 75 ns, the fourth and final pulse arrives, producing a rise in absorbance from 0.66 to 1.41 between 75 and 80 ns. The Rlx. IV phase begins immediately after 80 ns, with the absorbance reducing from 1.41 to 0.87 between 80 and 86 ns. Beyond this point, strong fluctuations appear. The absorbance increases abruptly rising to 1.72 at 99 ns before decreasing to a minimum of 0.19 at 100 ns. The value at 100 ns shows relatively low variance compared to the 86–99 ns interval. According to the exponential decay (blue curve), the absorbance at the end of this interval should be closer to 0.7, indicating a significant deviation from the measured data. Thus, this part of the experiment should be considered with caution.

Combining the observations from Figure 4.8 and Figure 4.10, a clear pulse-to-pulse accumulation is observed in the MHz regime, although the 25 ns delay between successive pulses still allows partial relaxation between pulses. The delay between pulse arrival and the onset of strong absorption can be attributed to a thermo-

elastic response of the bulk. Following energy deposition, no significant absorption is observed before 3 ns, most likely due to the limited spatial resolution of the imaging system. Around 4 ns, a transient absorption becomes detectable together with the emergence of an acoustic wave, indicating the formation of a confined high-pressure, high-temperature and densified state. Between 4 and 8 ns, the absorption progressively increases, suggesting a delayed build-up of a compressed, heated and electronically excited state rather than an instantaneous structural modification. This behavior reflects the finite time required for pressure confinement, electronic and structural defect generation, and energy redistribution within the interaction volume. The measured delay between pulse arrival and maximal absorbance is approximately 4 ns, suggesting that an intra-burst repetition rate on the order of 250 MHz may maximize energy accumulation in the bulk of Soda-Lime glass.

Additionally, the Rlx. III and Rlx. IV phases show high variance in the measured data and could be associated with the white wavy and vertical structure appearing in Figure 4.8. The onset of bulk cracking may induce strong variability in the transmission measurement, as fracture formation allows partial pressure release while introducing significant optical scattering. Since crack formation appears to occur at slightly different times across measurements, this may explain the observed fluctuations in transmission. Under these conditions, the assumption of purely exponential relaxation becomes insufficient, as thermo-mechanical coupling and structural heterogeneity could start to govern the relaxation dynamics.

4.3.2 50-ppb GHz-burst

In the following section, the presentation of the shadowgraphy experiment continues with the GHz-burst regime. The images obtained after laser irradiation in Soda-Lime glass are presented as a function of the pump–probe delay in Figure 4.11, and the acquisition method is the same as listed in the previous section.

A global overview of the experiment for the 50-ppb GHz-burst configuration is shown in Figure 4.11. The top of the figure displays a time axis spanning 0–100 ns, with major ticks every 10 ns and minor ticks every 1 ns. For clarity, the GHz-burst temporal structure (50 ppb) is schematically represented on the axis. The absolute amplitude is arbitrary, but the temporal shape illustrates the energy distribution as measured on the oscilloscope [1]. The temporal spacing is also accurate, with sub-pulses located between 0 and 40 ns with a spacing of 0.8 ns (1.25 GHz intra-burst repetition rate). Below the axis, a compilation of shadowgraphy images at different delays is grouped into phases. In the GHz-burst regime, only two phases are identified by visual inspection, compared to the MHz-burst. These two phases are divided into two categories: absorption phases, characterized by reduced transmission and labeled Abs. (i), and relaxation phases, characterized by increased transmission and labeled Rlx. (i).

From visual inspection, the first sub-pulse arrives at 0 ns. The corresponding image shows no observable modification, and similar observations hold for delays between 1 and 13 ns. As previously stated, our observation system used a magnification of 5.8× with an estimated NA of 0.1, yielding a lateral resolution of 2.2 µm according to [59] as before. Thus, it is believed that the interaction may already be ongoing but remains undetectable at our current NA. However, when comparing the delays between the MHz- and GHz-burst configurations, a difference of about

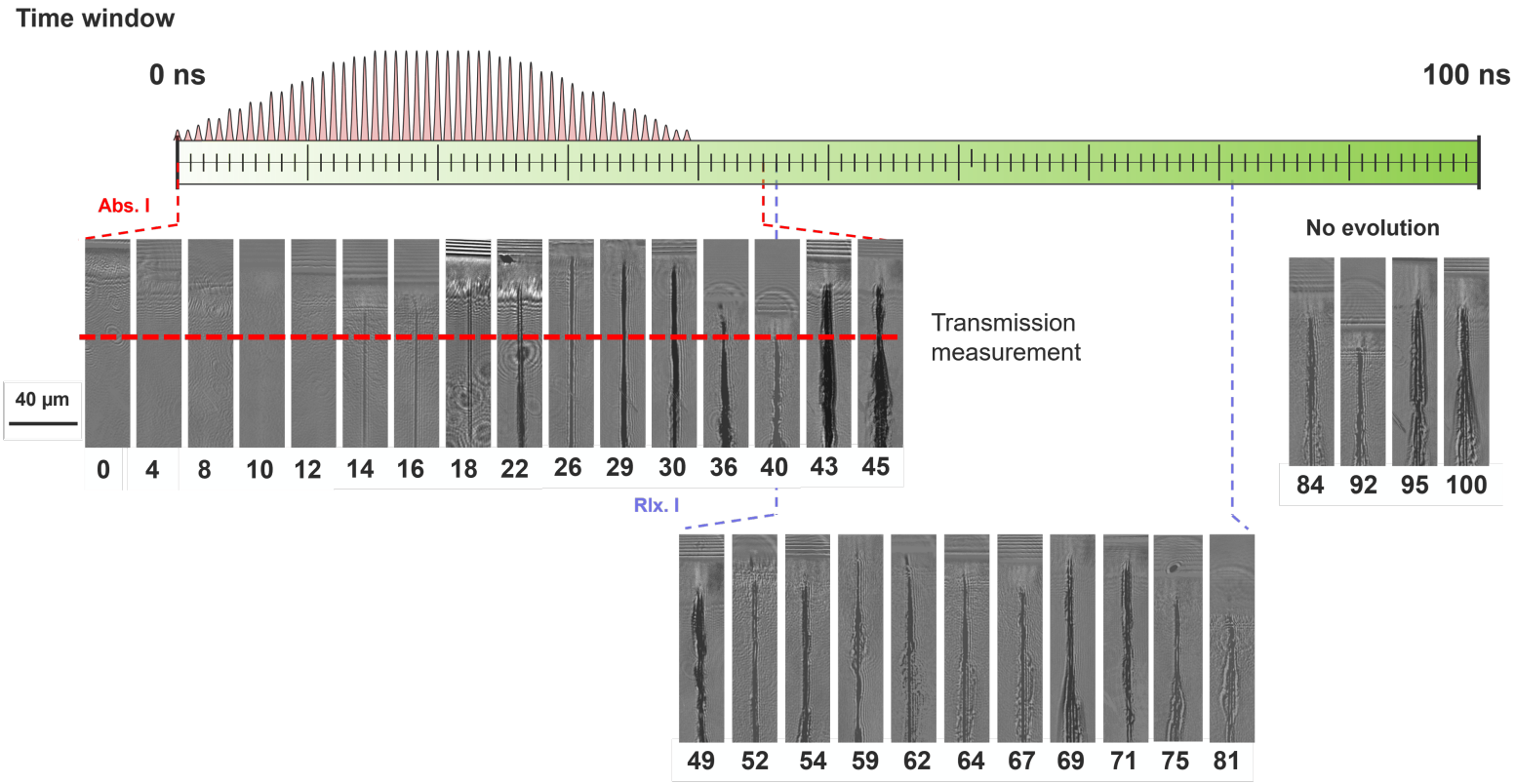

Figure 4.11: Pump-probe imaging in Soda-Lime glass in GHz-burst regime with 50 pulses per burst and burst energy of 270 µJ with delays ranging from 0 ns to 100 ns for a single burst applied. Minimal delay investigated between measurements was 1 ns.

10 ns is observed. Assuming that the first few nanoseconds of the interaction are not visible with our system, it can be inferred that the first detectable interaction occurs around 13 ns after the first pulse.

At 14 ns, a darkening of the central region appears, likely caused by densification induced by the sixteenth or seventeenth pulse. At 16 ns, a compression wave becomes visible. Compared to the pressure wave observed in the MHz regime, its amplitude appears lower, as it is barely visible in the images. At longer delays, the pressure wave is seen to consist of multiple smaller waves equally spaced by approximately 4.5 µm. The pressure-wave velocity is measured at 5.6 $km \cdot s^{-1}$, indicating an elastic regime [2, 58, 117]. Dividing this spatial period by the acoustic velocity yields a temporal spacing of 0.8 ns, confirming that the periodic acoustic emission is synchronized with the sub-pulse sequence of the GHz-burst. This also shows that, even under short periodic laser induced pressure, the Soda-Lime glass releases an acoustic wave every 0.8 ns.

From 14 ns to 26 ns, the transmission decreases, corresponding to the region between the 17th and 33rd pulses of the burst, where the pulse energy is highest. At 29 ns, the transmission at the core of the interaction further decreases. After this point, the transmission appears to saturate at a low value, while the width of the affected core continues to increase up to about 44–45 ns. It should be noted that the GHz burst temporally ends at around 40 ns. The image at 45 ns appears to mark the end of the first and only absorption phase.

The relaxation phase (Rlx. I) then begins after 45 ns. At 49 ns, the central core region appears reduced. At 52 ns, no region of very low transmission remains compared to 49 ns, indicating progressive relaxation in the absence of continued pressure induced by the expanding plasma. At 59 ns, cracks become visible along the sides of the interaction region. Between 59 ns and 81 ns, additional cracks appear, but the overall shape remains nearly unchanged, although a central region of reduced transmission is still visible. It can already be noted that these cracks are morphologically different from those observed in the MHz-burst regime as they appear extended on a larger region.

After approximately 82 ns, no further evolution is observed from one nanosecond to the next, suggesting that the interaction is completed and that the images correspond to the final modification morphology.

From this first visual inspection, it can already be inferred that the material response to the incoming burst (MHz vs GHz) is significantly different.

From those images, a linear profile is extracted and fitted to determine the minimal transmission values at each nanosecond of the interactions. This transmission value is then used to compute the absorbance thanks to Equation (4.1) with ΔT being the measured transmission [8, 118, 119]. The latter are then plotted against time in Figure 4.11. This Figure displays the time delay between the pump and probe as the x-axis, the y-axis is the absorbance, a dimensionless unit, a schematic representation of the burst repartition in time is displayed on the x-axis. In this graph four phases can be identified compared to the previous visual analysis, two Absorption phases and two Relaxation phases which is surprising. The data points are shown as empty circles and represent the mean transmission for a given delay averaged over five repeated experiments. The y-bar around each point represents the standard deviation over the five measurements compared to the mean. For visual guidance, the Absorption phase I is manually fitted using:

$$Abs(I) = A(I) \times (\frac{t - t_0}{b})^2 + C(I) \tag{4.4}$$

For the Relaxation phase I the following is used:

$$Rlx(I) = A(I) \times (\frac{t - t_0}{b})^2 + C(I) \tag{4.5}$$

While Equation (4.2) is used for Absorption phase II and using Equation (4.3) the Relaxation phase II is fitted. Those types of fit where chosen as they seem to better represent the data distribution but no physical explanation could have been extrapolated from this.

Between 0 and 8 ns, the absorbance remains low at approximately 0.05, defining the baseline. As observed previously, the Abs. I phase begins around 14 ns, although the data indicate that the absorbance increase starts slightly earlier, around 8-10 ns. After this point, the absorbance increases slowly between 11 and 15 ns, followed by a nearly linear increase between 15 and 23 ns, increasing from 0.04 to 1.06. After 23 ns, a change in measurement repeatability is observed. The absorbance appears to saturate with a slight decreasing trend, resulting in an absorbance decreasing from 1.06 to 0.48 at 40 ns. After this, a sudden rise in absorbance occurs going from 0.48 to 1.46 at 45 ns.

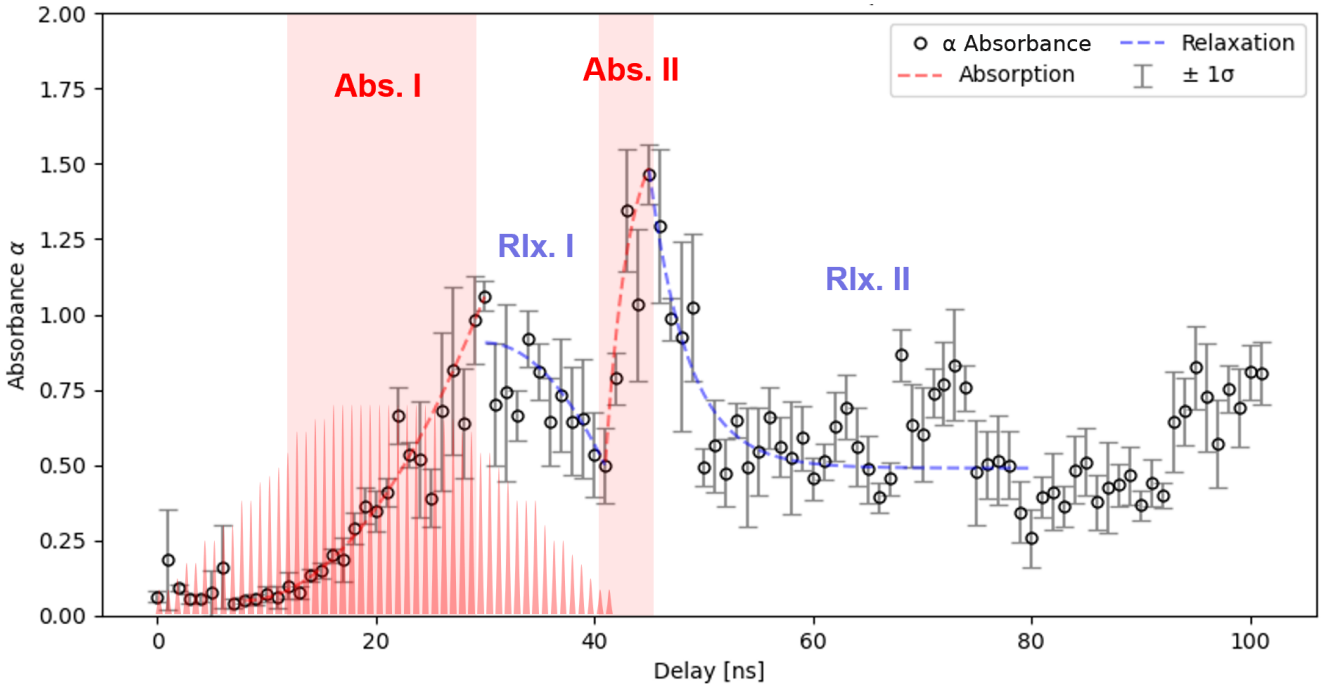

Figure 4.12: Pump-probe absorbance measurement in Soda-Lime glass in GHz-burst with 50 pulses per burst and burst energy of 270 µJ with delays ranging from 0 ns to 100 ns for a single burst applied.

	Abs. I	**Rlx. I**	**Abs. II**	**Rlx. II**
t [ns]	8-30	30-41	41-45	45-80
A	0.36	-0.31	-1.16	0.99
τ [ns]	–	–	2.12	3.59
b	13.15	9.32	–	–
t_0 [ns]	8	30	41	45
C	0.05	0.906	1.664	0.49

Table 4.3: Summary of parameters used for the fitting of Figure 4.12.

In the GHz-burst case, the absorption dynamics clearly deviates from the exponential behavior assumed in the MHz-burst case, for this reason the first absorption phase described above was fitted using a quadratic curve with the parameters found in Table 4.3. This difference likely arises from the specific nature of the GHz-burst regime, where the core is continuously excited every 0.8 ns by sub-pulses of lower intensity compared to the MHz-burst. After this first absorption phase, and while being still irradiated by the end of the burst, a decrease of absorbance is noticed and fitted using a quadratic curve and denoted as Rlx. I. This observation is surprising but shows a standard deviation similar to the other measurements indicating maybe a period of transition in the interaction, cracking may be an explanation but the high absorbance doesn't allow for direct observation of the central region. Then right after this small relaxation phase, a second absorption phase with rapid increase of absorbance is identified. The change in transmission between these two phases can also be identified through a change in morphologies between the 36, 40 and 43 ns of Figure 4.11 and may be explained by a change in the different mechanisms

involved. This time the absorption phase is fitted with the exponential as previously mentioned. Immediately afterward, the Rlx. II phase begins. The relaxation is fitted using an exponential decay. During this phase, the absorbance decreases rapidly from 1.46 to 0.55 between 45 and 50 ns, followed by a slower decrease from 0.55 to 0.5 between 50 and 80 ns. Between 80 ns and 100 ns, a slight increase in absorbance is observed; however, as shown in Figure 4.11, the interaction is already completed, and only the final modification remains, so this region is not considered further. Overall, the data follow the different fit reasonably well, phase Abs. I and Rlx. I are surprisingly well described by the quadratic fit, while Rlx. II seems to obey the classical exponential decay even though a weak oscillation can be seen between 70 and 76 ns.

Combining the observations from the MHz- and GHz-burst experiments, a clear pulse-to-pulse accumulation is also observed in the GHz-burst regime. However, unlike the MHz-burst, the 0.8 ns delay between successive sub-pulses does not allow any partial relaxation on the nanosecond timescale. The delay between pulse arrival and the onset of strong absorption—much longer than in the MHz-burst regime—can be attributed to two factors. First, the relatively low intensity of the first 18–20 pulses likely delays the build-up of a thermally and mechanically confined state driven by cumulative excitation. Second, as discussed for the MHz-burst regime, the limited spatial resolution of the imaging system may also contribute.

4.3.3 Plasma and critical density discussion

In the following section, the shadowgraph experiment is extended to the analysis of both the MHz-burst and GHz-burst regimes through the attempt of extracting the free-electron density. The data obtained in the previous section are then fitted using the model described in [8, 118] in order to relate the measured absorption to the transient electron density.

As detailed in Section 1.3.1, electron–collision processes are responsible for the increase in the imaginary part of the refractive index and thus, in the absorption coefficient linked to the absorbance, thereby inducing absorption of the probe beam. The relationship between the absorption coefficient and the probe absorbance is given by Equation (4.6):

$$A = \frac{1}{d} \ln\left(\frac{1}{\Delta T}\right) \tag{4.6}$$

where d is the characteristic size of the investigated object estimated to be constant in our case and of value 10 μm. The absorption coefficient can also be expressed as a function of the plasma frequency, as written in Equation (4.7), assuming a Drude-type free-electron response:

$$A = \frac{\tau}{n_g c} \frac{\omega_p^2}{1 + \omega^2 \tau^2} \tag{4.7}$$

where n_g is the refractive index of the considered glass and where the plasma frequency is defined as:

$$\omega_p = \sqrt{\frac{n_e e^2}{\epsilon_0 m_e}} \tag{4.8}$$

Using this formalism, the transient electron density can be reconstructed from the measured transmission dynamics using the following formula[1]:

$$n_e = \frac{A \times n_g \times c}{\tau} \times (1 + (\omega^2 \times \tau^2)) \times (\frac{m_e \times \epsilon_0}{e^2}) \tag{4.9}$$

The estimated transient electron density is represented in Figure 4.13 for the 4-ppb MHz-burst case and in Figure 4.14 for the GHz-burst using the characteristic time of the exponential decay in Table 4.2 for the MHz-burst of 3.74 ns and in Table 4.3 for the GHz-burst of 3.59 ns. The error bars were derived from the standard deviation of the absorbance data and estimating the error on τ of 25 % based on the data point distribution and assuming no cross-terms between the two values.

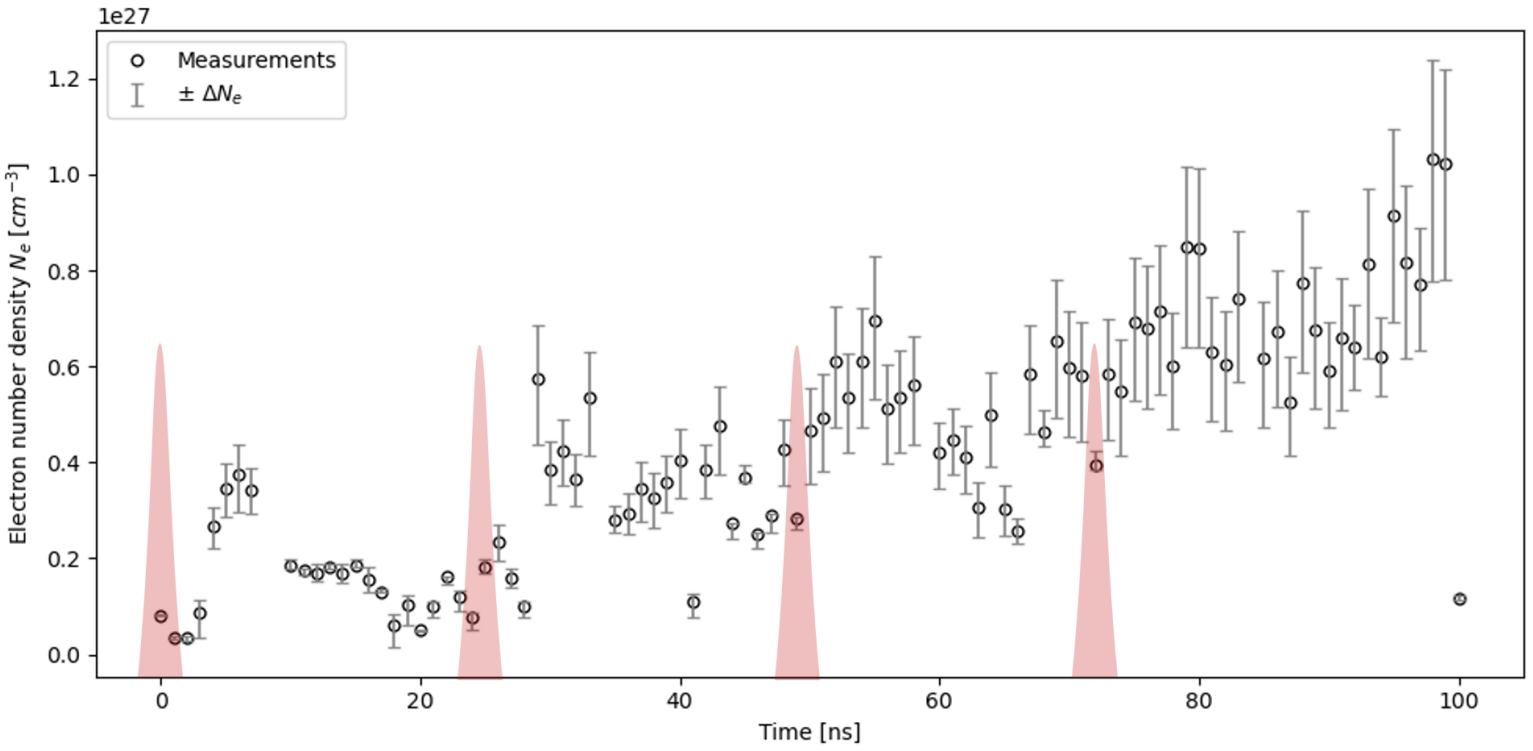

Figure 4.13: Evolution of electron number density profile inside a femtosecond laser-irradiated glass by a Bessel-beam with MHz-burst of 4 ppb and burst energy of 270 µJ.

For the 4-ppb MHz-burst regime, the Figure is superimposed with a temporal representation of the four pulses within the burst. The overall trends remain consistent with those observed in the previous section. Using a pump at 1030 nm, Equation (1.8) yields a critical plasma density of $1.05 \times 10^{21} cm^{-3}$, however looking at Figure 4.13 the maximal electron density retrieved is $1.03 \times 10^{27} cm^{-3}$, which is 6 orders of magnitude higher and thus non-physical. Comparing to typical relaxation times found in literature for Soda-Lime glass, one can find the value of $\tau = 1.82$ fs [8]. This value is also 6 orders of magnitude higher than the one measured in

[1]This formula yields a one dimensional value, by assuming a cubic symmetry one can derive the 3D electronic distribution.

our experiment which falls in the ns range. Looking now at the factor of $\omega^2\tau$, the following relation can be established

$$\omega^2\tau >> 1$$

This directly implies that this model (Drude) is insufficiently developed in order to describe the decrease of transmission observed in this experiment. Therefore, the decrease of transmission should not rely only on free electron generation. Transient defects such as Self-trapped exciton or Frenkel defects should be involved in the absorption and the subsequent decay over several tens of nanoseconds.

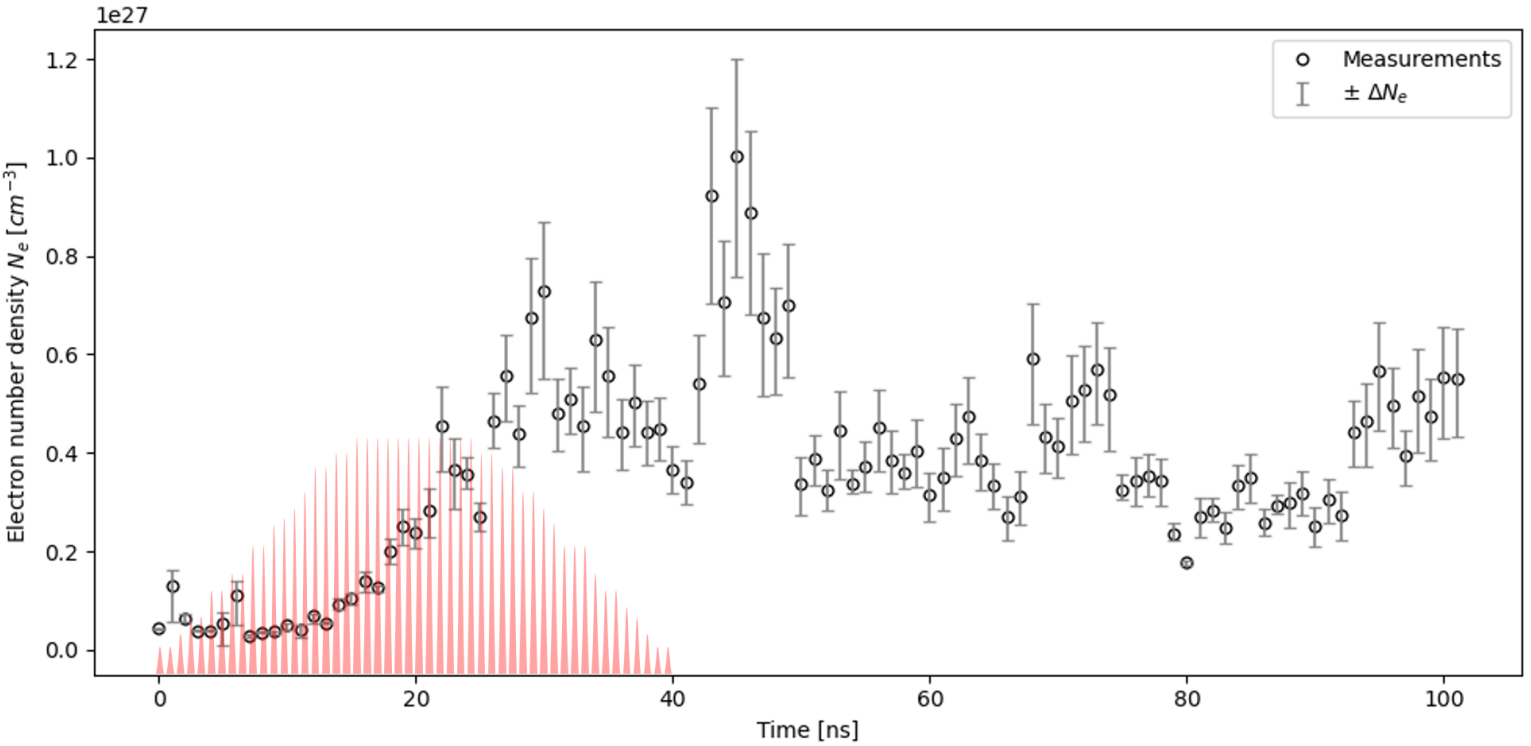

Figure 4.14: Evolution of electron number density profile inside a femtosecond laser-irradiated glass by a Bessel-beam with GHz-burst of 50 ppb and burst energy of 270 µJ.

For the 50-ppb GHz-burst regime, the Figure is superimposed with a temporal representation of the 50 pulses within the burst as well as their amplitude envelope. As in the MHz-burst case, the overall trends are consistent with the transmission analysis presented previously and the same comment can be made concerning the order of magnitude of the calculated free electron density.

Overall, although both burst regimes generate dense absorbing elements, such as free carriers or defects such as electron-hole pairs or Frenkel defects, their temporal dynamics differ substantially. In the MHz-burst regime, the observed electron/defect density builds up in a stepwise manner, with partial relaxation occurring between successive pulses. In contrast, the GHz-burst regime exhibits a rapid and more continuous accumulation of electrons/defects within a much shorter timescale, limiting relaxation between sub-pulses. This difference in temporal "plasma" build-up is expected to enhance energy confinement and promote stronger local heating in the

GHz-burst case. Consequently, even if the magnitude of electron densities remain unknown (because the Drude model is not consistent to describe the measured decrease of transmission), the distinct temporal evolution of the observed absorbing object may explain the markedly different final morphologies observed between the MHz- and GHz-burst regimes, in particular the transition from internal modifications to direct void formation.

4.4 Pump-probe shadowgraphy combined with Mach-Zehnder interferometry

In this section, pump-probe shadowgraphy combined with a Mach-Zehnder interferometer is employed to investigate the key differences previously identified in Section 4.2.1 between MHz- and GHz-burst laser-matter interaction. The objective is to further investigate the results obtained in Section 4.3 through phase-resolved measurements such as investigating the in-bulk electron density as well as retrieving the electronic density of the plume at the surface of the sample.

The MHz-burst regime is first analyzed in Section 4.4.1. A two-step approach is adopted: an in-volume study (Section 4.4.1.1) followed by an analysis of plume expansion in air (Section 4.4.1.2). The GHz-burst configuration (Section 4.4.2) is investigated using the same methodology, with the in-volume analysis presented in Section 4.4.2.1 and plume dynamics discussed in Section 4.4.2.2.

The optical setup described in Figure 2.10 was used. Bessel beam shaping was implemented using the configuration presented in Figure 2.5, with a burst energy of 270 µJ. Temporal sampling was performed from pump-probe temporal overlap (determined using the oscilloscope, and the fast photodiode, see Figure 2.7) up to 100 ns, with a temporal resolution of 1 ns for the in-volume experiments. For plume expansion measurements, the delay was controlled exclusively via the two AOMs, with a minimum step of 25 ns and a maximum investigated delay of 100 µs. The optical delay line (0-8 ns) was not used since the plume expansion occurs on longer timescales. Data processing procedures are detailed in Section 2.2.4.6.

4.4.1 MHz-burst with 4 pbb

4.4.1.1 In-volume experiment

In this section a global overview of the experiment for the 4-ppb configuration is shown in Figure 4.15 for Soda-Lime glass. The top of the Figure displays a time axis spanning 0–100 ns, with major ticks every 10 ns and minor ticks every 1 ns. For clarity, the MHz-burst temporal structure (4 ppb) is schematically represented on the axis. The amplitude is arbitrary, but the temporal spacing is accurate, with sub-pulses located at 0, 25, 50, and 75 ns. Below the axis, a compilation of retrieved phase images and retrieved electron densities at different delays is displayed. In the MHz-burst regime, eight phases were previously identified, divided into four absorption and relaxation phases, characterized by an increase and decrease in absorbance. These phases are represented in the color of the link from the time bar to the images with a red link indicating that the image is related to an absorption phase while a blue link indicates a relaxation phase. The first row of images corresponds to the measured phase shift and the color bar ranges from -1 to 1 rad, the second row of

images displays the retrieved electron density assuming a square symmetry over the 2D space[2], the color bar displayes ranges from 0 to 10×10^{19} cm^{-3} (well below the critical plasma density of $1.05 \times 10^{21} cm^{-3}$).

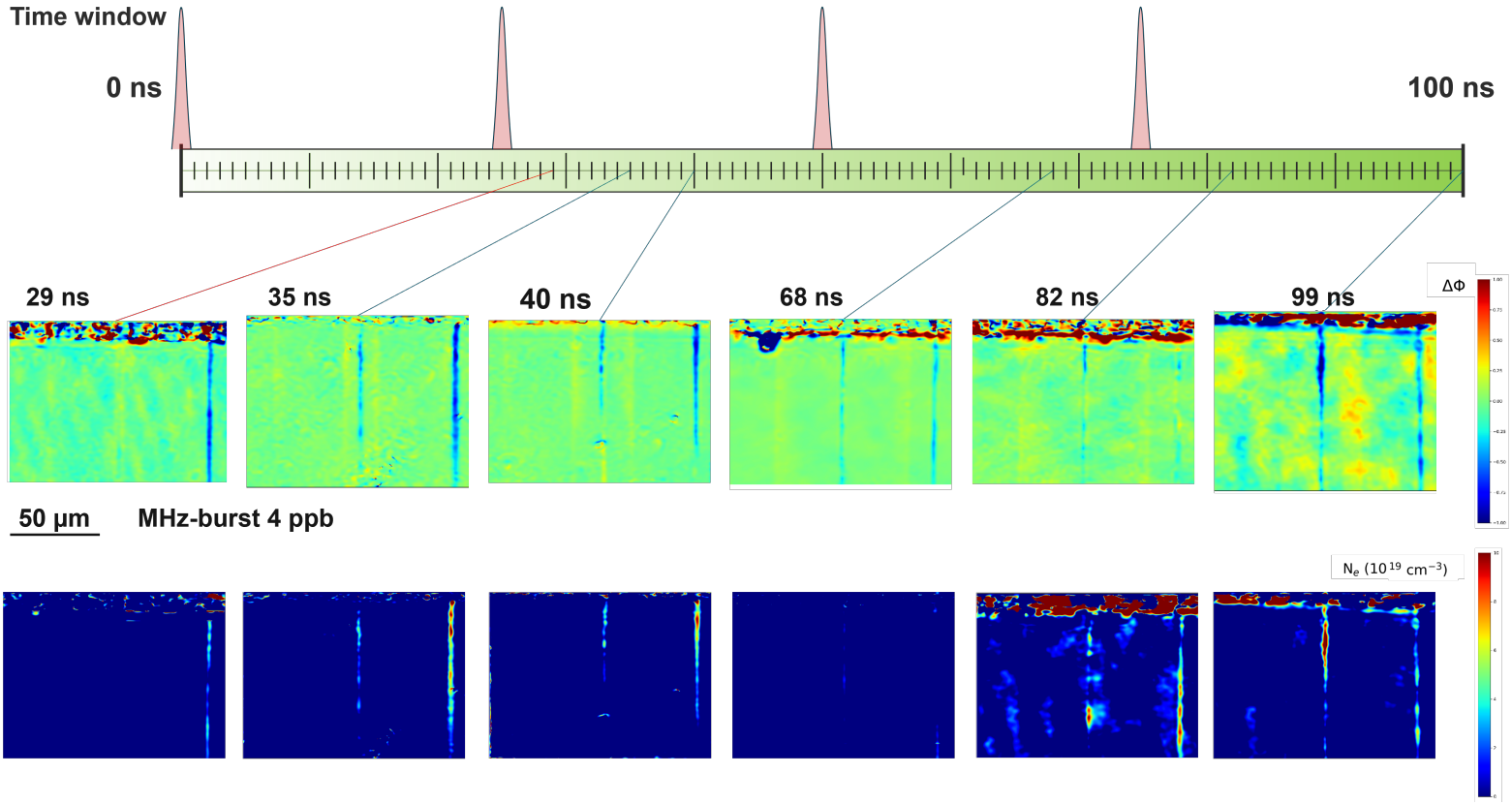

Figure 4.15: Pump-probe imaging in Soda-Lime glass combined with Mach-Zehnder interferometry in MHz-burst regime with 4 pulses per burst and burst energy of 270 µJ with delays ranging from 0 ns to 100 ns for a single burst applied. Minimal delay investigated between measurement was 1 ns. First row of images is phase shift measurement in rad and second row is reconstructed free electron density in $10^{19} cm^{-3}$.

From the temporal sequence, the first pulse arrives at 0 ns and the second at 25 ns. No measurable phase variation is observed immediately after these pulses. The first detectable phase modification appears at 29 ns, indicating a delayed material response.

At 35 ns, a clearly defined compression wave becomes visible. Tracking its radial propagation across successive frames yields an acoustic velocity of 5.8 km s^{-1}, in agreement with reported longitudinal elastic wave velocities in Soda-Lime glass and consistent with the values obtained in the previous section.

The lateral extent of the compression front is approximately 10 µm. A phase shift of 0.17 rad is measured. Assuming a two-dimensional approximation (Equation (2.13)), this corresponds to a refractive index variation of $\Delta n = 1.4 \times 10^{-3}$.

Using the relation derived previously (Equation (1.13)), the corresponding density variation is estimated to be approximately 11.5 kg $\cdot$ m^{-3}, leading to a relative

[2]The Abel inversion wasn't used in this particular case as the studied structure was too small to use a cylindrical symmetry.

density increase of 0.46 %.

Finally, applying Equation (1.15) yields an estimated pressure of approximately 200 MPa. This value remains well below the typical compressive strength of Soda-Lime glass, supporting the hypothesis that the material response remains within the elastic regime during this phase [25].

Analysis of the remaining delay times reveals a persistent line-like phase structure with relatively low phase shift. The corresponding electron density values extracted from these measurements remain close to zero, suggesting the lack of resolution from our system in characterizing the phase shift over the small region of the core interaction (10 µm) in this temporal window. From the classical pump-probe images, clear modifications were observed, combined together with the fact that the optical resolution of the imaging system is limited, a dephasing of above 2 π could be produced inside our lateral resolution [59, 121] thus, limiting our phase-shift map reconstruction.

An exception is observed at 99 ns, where a strong phase shift is detected, leading to an artificially high estimated electron density. However, inspection of the corresponding interferometric images shows that this signal likely originates from a permanent modification site, a post-mortem hole produced during the previous shot, and is very similar to the phase shift measured for the post-mortem hole visible on the right edge of the images at 29, 35, 40, 68 and 99 ns. The strong phase shift therefore results from static refractive index modification rather than from a transient plasma contribution. This confirms that the high value at 99 ns is an artifact related to the final morphology of the modification site and is not representative of the dynamic interaction.

As previously performed in Section 2.2.4, a horizontal line profile was extracted from the center of the interaction region in order to quantify the peak electron density as a function of delay time. The resulting temporal evolution is shown in Figure 4.16, an error bar of 10 % is applied to each data point.

For the 4-ppb MHz-burst regime, the temporal positions of the four sub-pulses are superimposed on the electron density plot. The extracted values are consistent with the qualitative observations: no positive electron density[3] is retrieved before approximately 40 ns, with measured values fluctuating around zero (within the noise level). Beyond this delay, the retrieved electron density exhibits significant shot-to-shot fluctuations, likely originating from reduced phase contrast rather than from intrinsic plasma dynamics [121]. The characteristic time of plasma dynamics for decay in Soda-Lime glass being well below the investigated time scale (1.82 fs [8] vs 3 ns), it could explain the lack of convincing results observed in this experiment.

[3]Negative electron density is an artifact induced by the measurement of a positive phase shift.

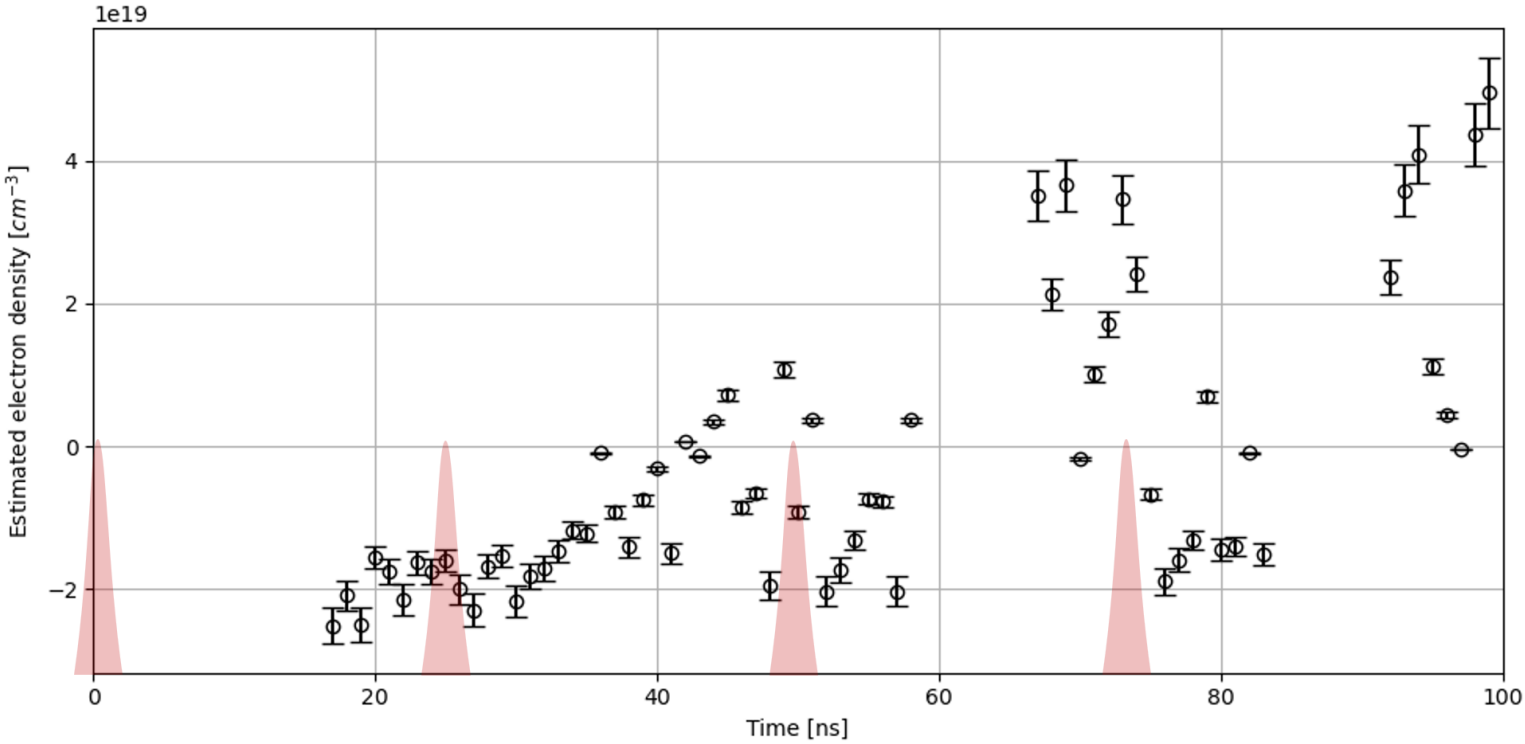

Figure 4.16: Free electron density calculated over time from pump-probe interferometry in Soda-Lime glass in MHz-burst with 4 pulses per burst and burst energy of 270 µJ with delays ranging from 0 ns to 100 ns for a single burst applied.

4.4.1.2 Plume expansion

In this section, the subject of interest is no longer the in-volume interaction but rather the plume expansion resulting from the in bulk interaction in Soda-Lime glass with 270 µJ. In order to perform this study the reference arm of the Mach-Zehnder interferometer (MZI) is shifted in order to obtain the fringe patterns in air, above the sample surface. A global overview of the experiment for the 4-ppb configuration is shown in Figure 4.17. The top row of the Figure displays a phase shift measurement spanning 50 – 100 000 ns, the color bar on the right ranges from -0.8 to 0.8 rad due to the modified volume being higher. On the bottom row, a compilation of retrieved electron density images at different delays is displayed, the color bar on the right ranges from 0 to 2×10^{19}cm^{-3}.

Looking at Figure 4.17, one notices a positive phase shift near the surface at 50 ns, corresponding to the initial expansion of the ejected matter/plasma plume expansion (in blue), pushing and heating the surrounding air (in red/yellow). At 100 ns the spherical compression wave is more noticeable yielding a positive dephasing of 0.7 rad, suggesting a densification. In the inside of the plume, a negative dephasing starts to be noticeable, suggesting a rarefaction instead. At 500 ns, the compression wave has traveled to the edge of the camera field, and the inner core displays a negative dephasing of -0.7 rad over the entire distance. The outer sphere (red/yellow) presents a higher dephasing than its inner sphere (blue) indicating a higher density in the former. At this stage, one can compute the speed of the ejected matter/plasma plume expansion and the compression wave from the images at 100

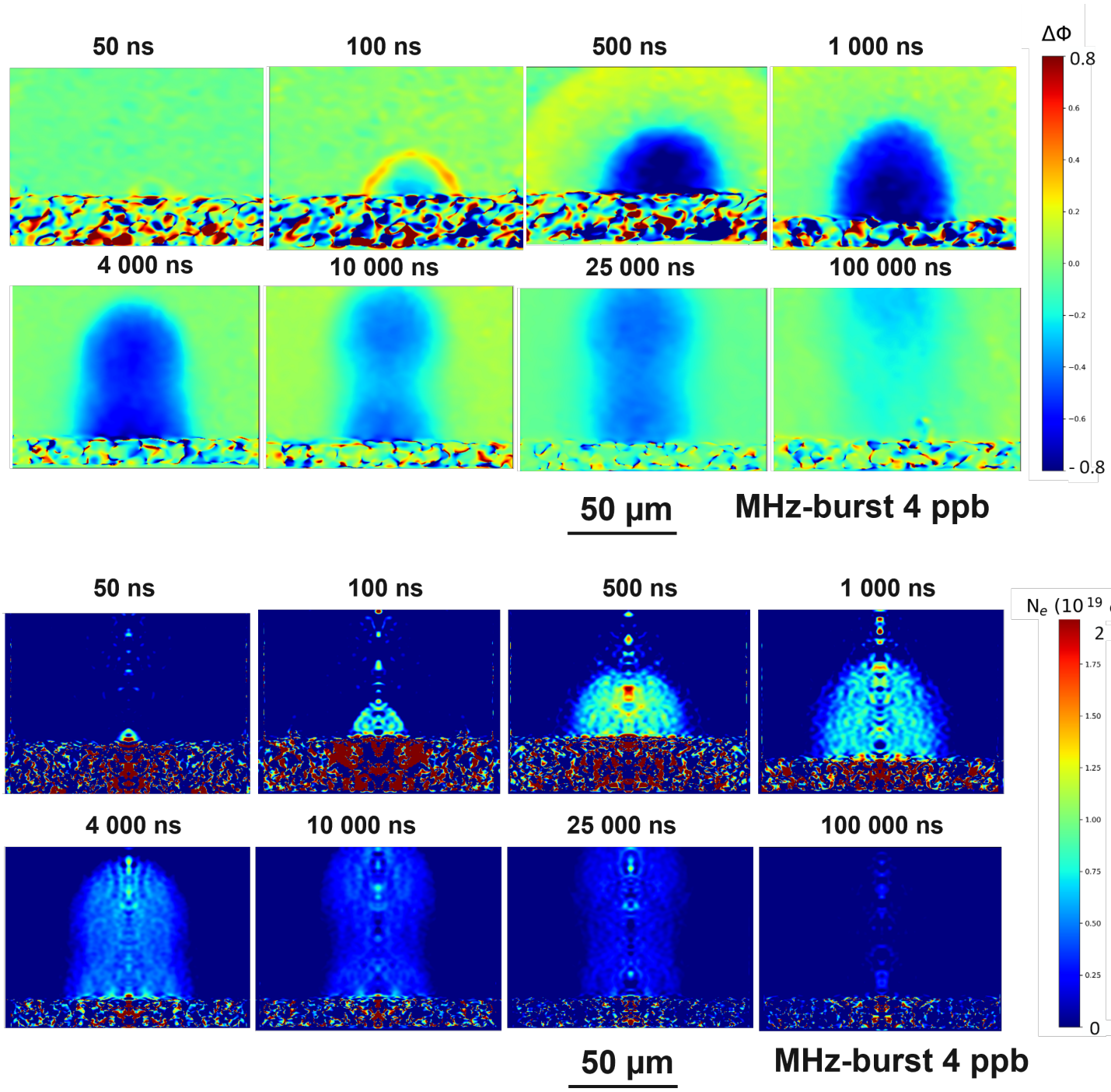

Figure 4.17: Pump-probe imaging in Soda-Lime glass combined with Mach-Zehnder interferometry in MHz-burst regime with 4 pulses per burst and burst energy of 270 µJ with delays ranging from 50 ns to 100 000 ns for a single burst applied.

ns and 500 ns yielding speeds along x and z of $v_x = 0.25$ and $v_z = 0.2\ km \cdot s^{-1}$, respectively, for the compression wave and $v_{x,z} = 0.1\ km \cdot s^{-1}$ for both directions of the ejected matter/plasma plume expansion, indicating an almost spherical propagation. Turning into polar coordinates in the plane xz, the speed along ρ which reads as $v_\rho = \sqrt{(v_x)^2 + (v_y)^2}$ yields $v_\rho = 0.3$ km·s^{-1}, for the compression wave (red/yellow) which is close to the speed of sound in air of 0.34 km·s^{-1} [122]. For the ejected matter/plasma plume expansion (blue) a value of $v_\rho = 0.14$ km·s^{-1} is

retrieved.

At 1 000 ns, the plume is expanding slightly in the Z-axis direction but with a similar dephasing in its center. At 4 000 ns, a change in morphology starts to be noticeable, the structure presents a wide base, then a waist and then a sphere, hinting at an elevation of the plume. At 10 000 ns, a first response is observed as the upper sphere is almost fully detached from the base, the dephasing is getting weaker also with a value around -0.4 rad. Finally, at 25 000 and 100 000 ns the ending of this interaction can be observed, with the object being seen leaving the camera field of view.

Looking at the bottom row of the Figure, the retrieved electron density can be investigated. The same morphologies are indeed retrieved from the phase shift images. At 50 ns, almost nothing is visible. It must be noted that due to the Inverse Abel transformation, artifacts are present around the symmetry axis. At 100 ns, the electron density is measured as 0.75×10^{19} cm^{-3}. At 500 ns, the maximal value in the density is observed with at mean value in the sphere of around 1×10^{19} cm^{-3} discarding the artifact on the symmetry axis. At 1 000 ns, the electron density is reduced due to the lateral size being wider and the dephasing being constant yielding a value of 0.6×10^{19} cm^{-3}. Then from 4 000 ns to 25 000 ns, the electron density drops and displays values of 0.5×10^{19} cm^{-3}, 0.25×10^{19} cm^{-3}, and 0.15×10^{19} cm^{-3}, respectively. At 100 000 ns, as the plasma plume is mostly outside the observation field, no electron density is retrieved.

This experiment informs us that some plasma plume is generated at the surface from the interaction with the 4-ppb MHz-burst, this plasma plume grows in density during the first 500 ns, and a pressure wave is released due to the expansion in air of this plasma plume. Starting from 1 000 ns, the plasma plume begins to fade and detaches from the initial surface. This jump in the plasma plume from the surface has already been characterized in air in [123] and is probably induced by the relatively high kinetic energy compared to the GHz-burst (50 ppb) since the pulse energy is sub-divided into only 4 pulses.

4.4.2 GHz-burst with 50 pbb

4.4.2.1 In-volume experiment

In this section, a global overview of the experiment for the 50-ppb configuration is shown in Figure 4.18. The top of the Figure displays a time axis spanning 0–100 ns, with major ticks every 10 ns and minor ticks every 1 ns. For clarity, the GHz-burst temporal structure (50 ppb) is schematically represented on the axis. The absolute amplitude is arbitrary, but the temporal shape illustrates the energy distribution. The temporal spacing is accurate, with sub-pulses located every 0.8 ns. Below the axis, a compilation of retrieved phase images and retrieved electron densities at different delays is displayed. In the GHz-burst regime, two phases were identified, divided into one absorption and one relaxation phase, characterized by reduced transmission and increased transmission. These phases are represented in the color of the link from the time bar to the images with a red link indicating that the image is related to an absorption phase while a blue link indicates a relaxation phase. The first row of images corresponds to the measured phase shift and the color bar ranges from -1 to 1 rad, the second row of images displays the retrieved electron density

assuming a square symmetry over the 2D space[4], the color bar displays ranges from 0 to 10×10^{19} cm^{-3}, which is still far below the critical density.

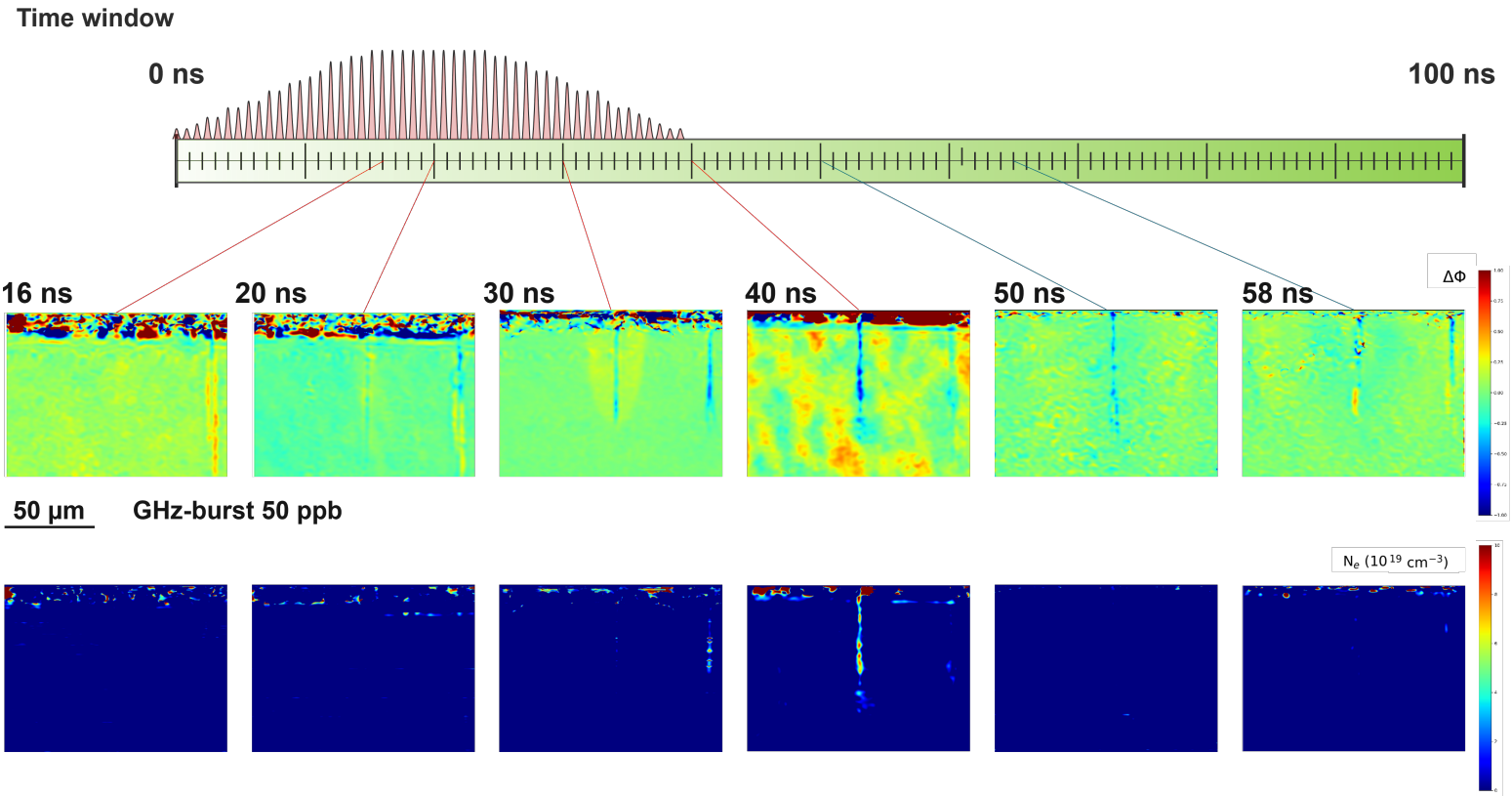

Figure 4.18: Pump-probe imaging in Soda-Lime glass combined with Mach-Zehnder interferometry in GHz-burst regime with 50 pulses per burst and burst energy of 270 µJ with delays ranging from 0 ns to 100 ns for a single burst applied. Minimal delay investigated between measurement was 1 ns.

From the temporal sequence, the first pulse arrives at 0 ns and no measurable phase variation is observed immediately after the first pulses. The first detectable phase modification appears around 20 ns, the phase shift produced by the plasma in the bulk is barely noticeable with phase shift values of less than 0.1 rad.

At 30 ns, a compression region seems to be visible around the bulk plasma generated by the Bessel beam, the phase shift in this region is measured at +0.2 rad. As the compression is small, it is not possible to accurately track the propagation over the images.

Analysis of the remaining delay times reveals a persistent line-like phase structure with relatively low amplitude. The corresponding electron density values extracted from these measurements remain close to zero, except at the 40-ns time delay where an electron density exceeding $5 \times 10^{19} cm^{-3}$ is retrieved indicating that our measurement system was not able to resolve and capture the small or big phase shift induced over the core region, even though the same morphology as in Section 4.3.2 was observed in the untreated images, which should yield in a measurable dephasing.

As previously performed in Section 4.3, a horizontal line profile was extracted from the center of the interaction region in order to quantify the peak electron

[4]The Abel inversion wasn't used in this particular case as the studied structure was too small to use a cylindrical symmetry as explained previously.

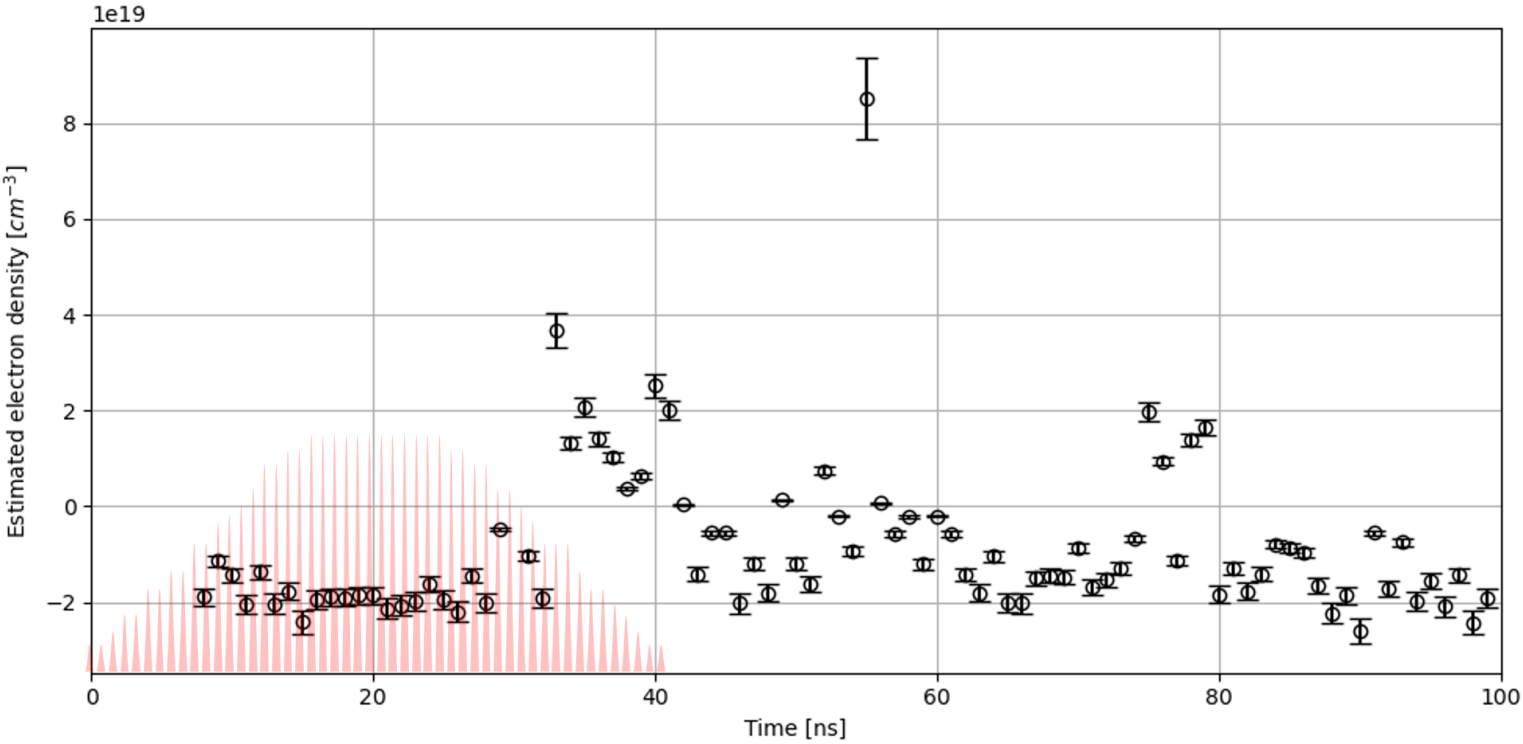

Figure 4.19: Free electron density calculated over time from pump-probe interferometry measurement in Soda-Lime glass in GHz-burst mode with 50 pulses per burst and burst energy of 270 µJ with delays ranging from 0 ns to 100 ns for a single burst applied.

density as a function of delay time. The resulting temporal evolution is shown in Figure 4.19, an error bar of 10 % is applied to each data point.

As for the 4-ppb MHz-burst regime, the temporal positions of the 50 sub-pulses are superimposed on the electron density plot. The extracted values are consistent with the qualitative observations: no positive electron density is retrieved before approximately 35 ns, with measured values fluctuating around zero (within the noise level). Beyond this delay, the retrieved electron density exhibits significant shot-to-shot fluctuations, likely originating from reduced phase contrast visibility rather than from intrinsic plasma dynamics.

4.4.2.2 Plume expansion

In this section, the subject of interest is no longer the in-volume interaction but rather the plume expansion resulting from the in-bulk interaction. In order to perform this study the reference arm of the MZI is shifted in order to obtain the fringe patterns in air above the sample surface. A global overview of the experiment for the 50-ppb configuration is shown in Figure 4.20. The top row of the Figure displays a phase shift measurement spanning 50 – 10 000 ns, the color bar on the right ranges from -0.8 to 0.8 rad. On the bottom row, a compilation of retrieved electron density images at different delays is displayed, the color bar on the right ranges from 0 to $2 \times 10^{19}\text{cm}^{-3}$.

The plume dynamics in the GHz-burst regime differs markedly from the MHz-

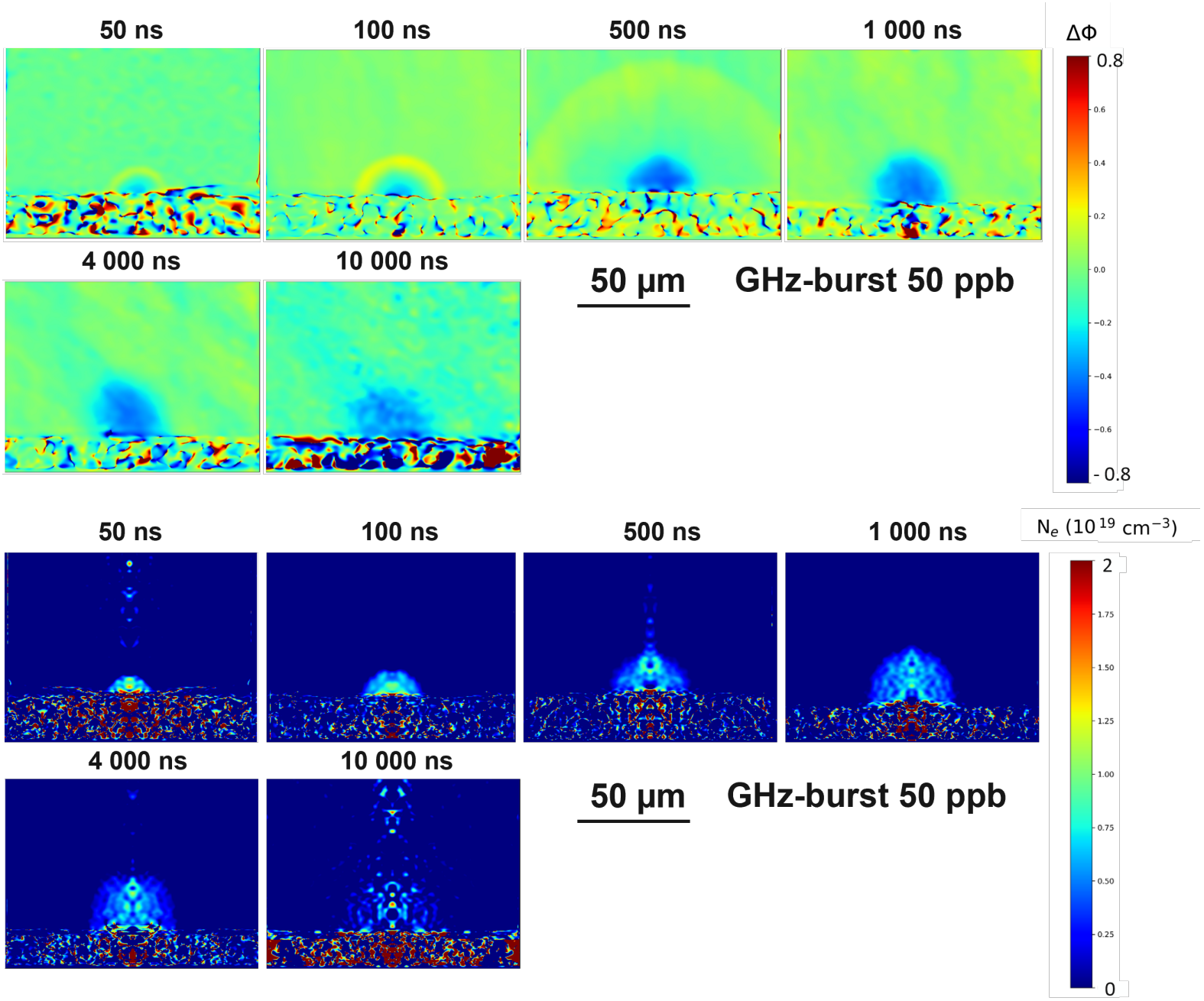

Figure 4.20: Pump-probe imaging in Soda-Lime glass combined with Mach-Zehnder interferometry in GHz-burst regime with 50 pulses per burst and burst energy of 270 µJ with delays ranging from 50 ns to 10 000 ns for a single burst applied.

burst configuration. A weak positive phase shift is observed near the surface at 50 ns, corresponding to the initial expansion the ejected matter/plasma plume expansion (in blue), pushing and heating the surrounding air (in red/yellow). From the top row it can be seen that the GHz-burst leads to a lower amount of ejected matter/plasma plume expansion compared to the MHz-burst which is surprising, as the former regime produces a channel and the latter does not (Section 4.2).

The maximum phase shift remains limited to approximately 0.2 rad at 100 ns, indicating a significantly lower induced pressure compared to the MHz-burst case.

One can compute the speed of the ejected matter/plasma plume expansion and

the compression wave from the images at 100 ns and 500 ns yielding speeds along x and z of $v_x = 0.2$ and $v_z = 0.16\ km \cdot s^{-1}$, respectively, for the compression wave (red/yellow) and $v_{x,z} = 0.05\ km{\cdot}s^{-1}$ for both directions of the ejected matter/plasma plume expansion wave, indicating a good spherical propagation. Turning into polar coordinates in the plane xz, the speed along ρ which reads as $v_\rho = \sqrt{(v_x)^2 + (v_y)^2}$ yields $v_\rho = 0.26$ km·s^{-1} for the compression wave (red/yellow), which is below the speed of sound in air of 0.34 km·s^{-1} [122] and below the speed found in the MHz-regime, this observation is consistent with the results found in [1, 124]. For the ejected matter/plasma plume expansion (blue) a value of $v_\rho = 0.07$ km·s^{-1} is retrieved.

From 500 ns onward, the phase contrast progressively decreases, and the structure expands laterally while its amplitude diminishes. This behavior suggests thermal diffusion and pressure relaxation rather than sustained plasma emission.

Importantly, no pronounced material ejection or surface jet is observed, in contrast to the MHz-burst regime. This difference can be attributed to the reduced energy per sub-pulse in the GHz-burst configuration, which limits the peak energy deposition and consequently the impulsive pressure at the surface.

Looking at the bottom row of the Figure the retrieved electron density can be investigated. The same morphologies are indeed retrieved from the phase shift images. At 50 ns, a small part exhibits a positive electron density of around $0.5{\times}10^{19}$ cm^{-3} . It must be noted that due to the Inverse Abel transformation, artifacts are present around the symmetry axis. At 100 ns, the electron density is measured as 1×10^{19} cm^{-3}. At 500 ns, the density value is decreasing around 0.5×10^{19} cm^{-3} discarding the artifact on the symmetry axis. At 1 000 ns, the electron density is reduced due to the lateral size being wider and the dephasing being constant yielding a value of 0.35×10^{19} cm^{-3}. Then from 4 000 ns to 10 000 ns, the electron density drops and displays values of 0.2×10^{19} cm^{-3} and almost 0 at 10 000 ns, respectively.

This experiment informs us that some plasma plume is generated at the surface from the interaction with the 50-ppb GHz-burst. This plasma plume grows in density during the first 100 ns and a pressure wave is released due to the expansion in the air of this plasma plume. Through the computation of propagation speed it has been identified that in the MHz-burst, the compression wave and plasma plume expansion being denser had a slightly increased velocity by 15 % (0.3 vs 0.26 km·s^{-1}) for the compression wave and a clearly higher velocity with an increase of 50 % for the plasma plume expansion. Starting from 500 ns, the plasma plume starts to fade but no jump from the surface is identified compared to the MHz-burst regime. The absence of jump of the plasma plume from the surface is probably induced by the relatively low kinetic energy induced by each individual pulse [124] compared to the MHz-burst since the pulse energy is sub-divided into 50 pulses resulting in lower expansion speed.

Conclusion & Perspectives

This work was carried out over a three-years period between the CELIA laboratory of the University of Bordeaux and ALPhANOV under a CIFRE contract. It benefited from close and sustained collaborations with industrial and academic partners, in particular ALPhANOV and Amplitude. These interactions are now structured within a joint laboratory based in Bordeaux which provides a formal administrative framework to support the already strong scientific and technological exchanges between the three entities (CELIA, ALPhANOV and Amplitude). The research topic was intentionally broad, allowing the exploration of multiple complementary directions within an emerging laser processing regime. At the beginning of this thesis, the GHz-burst regime was still largely unexplored in surface structuring, and the objective was therefore to investigate as many aspects and physical mechanisms as possible in order to contribute to a comprehensive understanding of this novel operating regime.

In the first chapter of this manuscript, the theoretical background required to understand the physical mechanisms involved in ultrafast laser–matter interactions were established. The electronic and thermal properties of solids were first introduced, with a distinction made between metals and dielectrics, highlighting key concepts such as band structure, charge carrier dynamics, and energy transport. The optical response of materials under extreme excitation conditions was then addressed through the presentation of fundamental models, including the Drude formalism, the concept of critical plasma density, and refractive index modifications induced by strong electronic excitation and pressure. Subsequently, the different interaction regimes associated with ultrafast laser irradiation were described, with particular emphasis placed on the ionization mechanisms governing energy absorption in wide bandgap materials, such as multiphoton ionization, avalanche ionization, and carrier relaxation processes. A significant portion of this chapter was devoted to the temporal and spatial control of energy deposition, with a particular focus on beam-shaping strategies. In particular, temporal beam shaping using burst modes at MHz and GHz repetition rates was introduced, as this approach constitutes a central aspect of the present work. Finally, an overview of the main applications of burst laser processing was given, especially in the context of surface functionalization, thereby providing a comprehensive framework for the experimental investigations presented in the subsequent chapters.

In the second chapter of this manuscript, the experimental methods and equipment implemented and used throughout the three years of this work were presented in detail. The laser system and the micromachining workstations used for the experiments are first described. Two main processing configurations were implemented: a

workstation based on Gaussian beam focusing and another one dedicated to Bessel beam generation. Both setups were mounted on the same granite gantry in order to enhance mechanical stability and to allow the integration of in-situ diagnostic tools. The importance of in-situ diagnostics for the understanding and optimization of laser–matter interaction processes was emphasized. In this context, a side-view imaging system was extensively used, enabling real-time transverse visualization of the interaction. This diagnostic approach provided essential insights and allowed initial hypotheses to be formulated regarding the underlying interaction mechanisms in the GHz-burst regime. In addition, a third set-up was implemented to perform pump–probe shadowgraphy measurements. The development of this setup required precise synchronization between a GHz-burst pump laser and a single-pulse probe laser, making its implementation particularly challenging. To achieve time delays of up to $+\infty$ with a temporal resolution on the order of a few hundred femtoseconds, a combination of optical and electronic delay lines was employed. This pump–probe configuration, coupled with the side-view imaging system, enabled a detailed investigation of the transient phenomena occurring during laser–matter interaction, as well as a systematic comparison between repetitive single-pulse, MHz-burst, and GHz-burst regimes. Finally, the sample preparation procedures, measurement techniques, and materials of interest investigated throughout such as pump-probe shadowgraphy, time-resolved interferometry and subsequent data processing used in this work were detailed, providing a comprehensive methodological framework for the results presented in the following chapters.

The third chapter was dedicated to the surface processing of metallic materials, through the prism of polishing of AISI 316L stainless steel using femtosecond laser irradiation in burst regimes. The different processing strategies explored in this chapter were structured around the influence of beam shaping, burst configuration, spatial overlap, and surface conditions on the polishing efficiency and surface quality. The polishing process was first investigated using a vortex beam and gaussian beam configuration. In this framework, a single-burst study was conducted in order to identify the fundamental effects of vortex and gaussian beam irradiation on the surface response of AISI 316L. Subsequently, the impact of spatial overlap was examined in detail, with specific attention paid to both spot-to-spot and line-to-line overlap conditions, allowing their respective roles in surface smoothing to be assessed. As no major differences have been identified in the thermal management of the treated surface the gaussian beam was selected to continue the study. The influence of extended burst durations was then explored through the use of long GHz-burst configurations with 800 ppb. This study aimed at assessing the potential of prolonged energy deposition for enhanced surface modification and polishing performance. In addition, the impact of the initial surface roughness on the polishing outcome was investigated. Test surfaces with controlled roughness were first generated through a first step of ablation with 50 ppb, thus degrading the pristine surface from a R_a of 0.05 µm to a R_a of 1.37 µm and an ablated depth of 100 µm, after which a second step generating a melted layer at the surface was performed with 800 ppb, in order to reduce the roughness, which managed to lower the roughness from R_a of 1.37 µm to 0.47 µm, which represents a decreasing of 34 % of the surface roughness. This demonstrated that it was possible to use a unique machine-tool to perform both tasks (engraving & finishing) and thus, a gain of potential time, efforts

and reproducibility. A dedicated polishing experiment/molten layer generation, was conducted to evaluate the dependence of the final surface quality on the initial surface conditions and reveals that parameters that were effectively producing a stable melted layer on R_a of 1.37 µm did not perform on the surface with R_a of 0.05 µm, but instead produced a surface with a R_a of 1.5 µm. Further parametric studies were carried out to analyze the influence of spot-to-spot overlap and the number of passes on the polishing process. These investigations provided insight into the accumulation effects associated with repeated laser exposure and scanning strategies. Finally, considerations related to the scalability of the polishing process were addressed. It has been identified that keeping all operating parameters constant but scanning speed and frequency, which should be increased by the same ratio, one could reproduce similar results up to a repetition frequency of 800 kHz and a speed of 1400 $mm{\cdot}s^{-1}$, investigated in this work and highlighting the potential of burst-mode femtosecond laser polishing for larger-scale and industrial applications.

The final chapter was devoted to the processing of dielectric materials using femtosecond laser irradiation, with an emphasis on Bessel beam laser processing and time-resolved diagnostics in the objective of future surface functionalization. The influence of the main experimental parameters associated with Bessel beam generation and propagation was first investigated through a study on the beam divergence and entrance size on the final intensity profile of the produced Bessel beam. This study was performed in order to establish a clear framework for controlled energy deposition inside dielectric materials and revealed that the beam entrance size was critical in order to minimize the effects of the rounded tip of the axicon and that a beam entrance size of 9 mm was relevant and producing almost a Z-flat Bessel beam. Bessel beam–induced modifications were then examined in detail. A comparative study was carried out using single-pulse, MHz-burst, and GHz-burst regimes to assess their respective impact on material modification. This study reveals a crucial difference between those regimes. Single pulse and MHz-burst both produce modifications with bubble like structures and additional cracks for the MHz-burst regime, while in GHz-burst mode a clear channel was generated with a single burst, accompanied by cracks around. In addition, a dedicated etching study was performed to analyze the interaction between laser-induced modifications and subsequent chemical processing steps. The results highlighted the similarities in the produced modifications between the single pulse and MHz-burst regimes yielding a similar etching rate and selectivity of above 2100:1 in both cases. The MHz-burst revealed a slightly higher selectivity value (6 %) probably due to the presence of cracks in the bulk compared to the single pulse regime. This study also confirmed that the modifications generated by the GHz-burst were clear channels as the etchant reached the bottom for all three etching times investigated (30 min, 1 hr and 2 hr). These investigations led to exploratory work toward single-shot GHz-burst drilling of through-glass vias (TGV), aiming at advancing high-aspect-ratio structuring capabilities in dielectric substrates. A clear blind channel has been produced in fused silica with a maximal depth of 730 µm. Additionally, TGV were realised in 300 µm thick AF32 samples. Time-resolved diagnostics were further employed through the implementation of pump–probe shadowgraphy experiments. These measurements were conducted for both, MHz-burst configurations with 4 pulses per burst and GHz-burst configurations with 50 pulses per burst. The temporal evolution of the induced modifications

was analyzed through the prism of the probe absorption, and reveals very different dynamics, with an 8 steps-like process for the MHz-burst and a quasi-continuous ramp for the GHz-burst, a detailed discussion was provided concerning potential plasma formation and the critical plasma density during laser–matter interaction in dielectrics. However it has been identified that the assumptions expressed in this work were not enough to explain the different mechanisms at play in this experiment. To deepen the understanding of the interaction dynamics, pump-probe shadowgraphy was combined with Mach–Zehnder interferometry. This combined diagnostic approach enabled both in-volume interaction experiments and plume expansion studies to be performed in MHz-burst and GHz-burst regimes. The comparison between these configurations provided complementary insight into the influence of burst parameters on energy deposition and plume dynamics by identifying two different behaviors between MHz-burst and GHz-burst, thereby reinforcing the understanding of the dielectric response under ultrafast burst-mode laser irradiation.

In this manuscript, the relatively new regime of light–matter interaction known as the femtosecond GHz-burst mode was experimentally investigated. Over the three years devoted to this doctoral work, the primary objective was to provide an extensive experimental study of GHz-burst laser processing in order to contribute to a deeper understanding of this emerging regime. Throughout this work, substantial efforts were dedicated to addressing this gap by contributing to the state of the art of femtosecond GHz-burst laser processing, as reflected in some already published peer-reviewed journal articles [112, 116], and some more to be submitted soon.

During this PhD, which spanned slightly less than three years, a significant number of processes were explored. However, many promising directions remain open and largely unexplored. While it would have been straightforward to extend the study across a wider range of materials for each investigated process, such an approach, although efficient, would likely have provided limited insight compared to more in-depth investigations of the underlying physics. Instead, several key avenues for future work emerge. In the case of laser–metal interactions, the pump–probe experimental setup, combining a pump in burst-mode and a single-pulse probe, is a highly valuable opportunity for further developments. For instance, adapting the system to include angled or side-view imaging could provide crucial insight into molten pool dynamics for metals. Such an approach would help clarifying the differences in melt pool formation and evolution between single-pulse and burst regimes (both MHz and GHz), which remain only partially understood. Capturing the transient behavior of the material from different perspectives could reveal subtle mechanisms governing material flow, instability formation, and energy deposition. On the dielectric side, the pump–probe setup could also be significantly improved. Enhancing the optical system—for example, by integrating higher-quality objectives or designing a more compact and stable configuration—would likely improve both, spatial resolution and signal reliability. This, in turn, would help address some of the interpretation challenges encountered throughout this work, particularly when dealing with complex light–matter interactions and rapidly evolving transient states. Additionally, transferring such a system upgrade to the pump-probe set-up coupled with the Mach-Zehnder interferometer would also highly benefit to better characterize the in-bulk interactions. On this note, a first study of classical pump-probe with

a Mach-Zehnder interferometer at the threshold energy would be very valuable to properly calibrate our results with classical literature and solidify our understanding and interpretation of complex results. Beyond experimental improvements, both metallic and dielectric studies would strongly benefit from the development of robust theoretical and numerical models. A comprehensive framework describing the interaction mechanisms under single-pulse, MHz-burst, and GHz-burst regimes is still lacking. Such models would not only support the interpretation of experimental observations but also guide future experiments by identifying key parameters and scaling laws. Ultimately, combining improved diagnostics with predictive modeling would enable a deeper and more systematic understanding of ultrafast laser–matter interaction phenomena.

On a more personal level, this PhD also provided the opportunity to engage with a wide range of topics that are not directly reflected in this manuscript. Through various collaborations and side projects, I was faced with diverse applications of ultrafast laser–matter interaction, as our group is providing transnational access within the European project Laser4EU as a member of the Laserlab network. These campaigns included studies on X-ray emission induced by ultrafast lasers and investigations of transient temperature changes in metals and dielectrics under different burst regimes. More applied work such as laser eye surgery and bone ablation has been carried out in collaboration with the CHU facilities. These experiences were particularly enriching, as they offered a broader perspective on both the scientific and practical potential of the techniques developed during this PhD. They highlighted the versatility of ultrafast laser systems across disciplines, ranging from fundamental physics to biomedical applications. Moreover, working in such varied contexts helped develop a more adaptable and interdisciplinary approach to problem-solving. Altogether, these contributions—although not detailed in this manuscript—played an important role in shaping my understanding of the field. They opened new perspectives on the possible directions for future research and emphasized the wide range of opportunities that can stem from the skills and expertise acquired throughout this work.

List of publications

Peer-reviewed journal articles :

1. Balage, P. Bonamis, G. Lafargue, M. **Guilberteau, T.** Delaigue, M. Hönninger, C. Qiao, J. Lopez, J. Manek-Hönninger, I. Advances in Femtosecond Laser GHz-Burst Drilling of GLasses: Inffluence of Burst Shape and Duration. Micromachines 2023, 14 (6), 1158.

2. Balage, P. **Guilberteau, T.** Lafargue, M. Bonamis, G.Hönninger, C. Lopez, J. Manek-Hönninger, I. Bessel Beam Dielectrics Cutting with Femtosecond Laser in GHz-BurstMode. Micromachines 2023, 14, 1650.

3. Balage, P. Lafargue, M. **Guilberteau, T.** Bonamis, G. Hönninger, C. Lopez, J. Manek-Hönninger, I. Comparative Study of Percussion Drilling in Glasses with a Femtosecond Laser in Single Pulse, MHz-Burst, and GHz-Burst Regimes and Optimization of the Hole Aspect Ratio. Micromachines 2023, 14, 1754.

4. Balage, P. Lafargue, M. **Guilberteau, T.** Bonamis, G. Hönninger, C. Lopez, J. Manek-Hönninger, I. Femtosecond Laser Percussion Drilling of Silicon Using Repetitive Single Pulse, MHz-, and GHz-Burst Regimes. Micromachines 2024, 15, 632.

5. Balage, P. Lopez, J. **Guilberteau, T.** , Lafargue, M. Bonamis, G. Hönninger, C. Manek-Hönninger, I. Through Glass Via Drilling Using GHz-burst of Femtosecond Pulses: Challenges and Implementation. Journal of Laser Micro/Nanoengineering, 2024 19, 1, 214.

6. **Guilberteau, T.** Balage, P. Lafargue, M. Lopez, J. Gemini, L. Manek-Hönninger, I. Bessel Beam Femtosecond Laser Interaction with Fused Silica Before and After Chemical Etching: Comparison of Single Pulse, MHz-Burst, and GHz-Burst. Micromachines 2024, 15,1313.

7. Lafargue, M. **Guilberteau, T.** Balage, P. Gavory, B. Lopez, J. Manek-Hönninger, I. In-Volume Glass Modification Using a Femtosecond Laser: Comparison Between Repetitive Single-Pulse, MHz Burst,and GHz Burst Regimes. Materials 2025, 18, 78.

8. Balage, P. **Guilberteau, T.** Lafargue, M. Bonamis, G. Hönninger, C. Lopez, J.Manek-Hönninger,I. Pump-Probe Imaging of Ultrafast Laser Percussion Drilling of Glass in Single Pulse, MHz- and GHz-Burst Regimes Adv. Mater. Interfaces 2025, 12, 2400853.

9. C. L. C. Lacoste, C. L. C. Catrix,E. Vallières,S. Hirsch-Passicos,A. **Guilberteau, T.**. Lafargue, M. Lopez,J. Manek-Hönninger,I. Fourmaux,S. Raffestin, D. d'Humières, E. Antici, P. Bardon, M. Experimental and numerical investigationof the impact of helical coil targets onlaser-driven proton and carbon accelerations. Matter Radiat. Extremes 2025, 10, 037602.

10. **Guilberteau, T.**; Husson, F.;Lafargue, M.; Lopez, J.; Faucon, M.;Gemini, L.; Manek-Hönninger, I. Long GHz-Burst Laser Surface Polishing of AlSl 316L Stainless Steel Parts Manufactured by Short GHz-Burst Laser Ablation. Nanomaterials 2025, 15,1343.

Peer-reviewed conference proceedings :

- M. Lafargue, **Guilberteau, T.**, P. Balage, B. Gavory, J. Lopez, I. Manek-Hönninger. Comparison of Laser-Induced Bulk Modifications in Glass by Femtosecond Pulses Using Single Pulses, MHz- and GHz-Bursts. Conference on Lasers and Electro-Optics/Europe (CLEO/Europe 2025) and EQEC 2025, Optica Publishing Group, paper cm_p_1 (2025)
- P. Balage, **Guilberteau, T.**, M. Lafargue, G. Bonamis, C. Hönninger, J. Lopez, I. Manek-Hönninger. Pump-probe shadowgraphy of glass drilling in different femtosecond burst regimes. Proc. SPIE 13350, Laser Applications in Microelectronic and Optoelectronic Manufacturing (LAMOM) XXX, 1335002 (2025)
- P. Balage, J. Lopez, M. Lafargue, **Guilberteau, T.**, G. Bonamis, C. Hönninger, I. Manek-Hönninger. Ultrafast laser drilling of through vias in gap materials using GHz-burst mode operation. Laser+ Photonics for Advanced Manufacturing 13005, 11–13 (2024)
- P. Balage, **Guilberteau, T.**, M. Lafargue, G. Bonamis, C. Hönninger, J. Lopez, I. Manek-Hönninger. Dielectrics cutting with Bessel beam in femtosecond GHz-burst regime. Proc. SPIE PC12872, Laser Applications in Microelectronic and Optoelectronic Manufacturing (LAMOM) XXIX, PC1287203 (2024)
- P. Balage, **Guilberteau, T.**, M. Lafargue, G. Bonamis, C. Hönninger, J. Qiao, J. Lopez, I. Manek-Hönninger. Advances on Percussion Drilling with Femtosecond Laser in GHz-burst Mode. EPJ Web of Conferences 287, 08005, EOSAM, Dijon, France (2023). `https://doi.org/10.1051/epjconf/202328708005`
- I. Manek-Hönninger, P. Balage, **Guilberteau, T.**, M. Lafargue, G. Bonamis, M. Delaigue, C. Hönninger, J. Lopez. Ultrafast laser micromachining with GHz bursts. Lasers in Manufacturing Conference, paper 1342 (2023)

Invited talk & Seminar

- I. Manek-Hönninger, **Guilberteau, T.**, M. Lafargue, L. Gemini, B. Gavory, J. Lopez. Surface treatment by ultrafast laser micromachning

in GHz-burst mode. European Materials Research Society Spring Meeting (EMRS), Strasbourg, France (2025)

- I. Manek-Hönninger, P. Balage, **Guilberteau, T.**, M. Lafargue, G. Bonamis, C. Hönninger, J. Lopez. Pump-probe shadography of glass drilling in different femtosecond burst regimes. Photonics West Conferences, SPIE-LASE, San Francisco, USA (2025)
- I. Manek-Hönninger, P. Balage, M. Lafargue, **Guilberteau, T.**, G. Bonamis, C. Hönninger, J. Lopez. Ultrafast Laser Proccessing with GHz-bursts. Procédés Laser pour l'Industrie (PLI), Bordeaux, France (2024)
- I. Manek-Hönninger, P. Balage, **Guilberteau, T.**, M. Lafargue, G. Bonamis, M. Delaigue, C. Hönninger, J. Lopez. Innovative femtosecond laser microprocessing of dielectrics with temporal and spatial beam shaping. Optics, Photonics and Lasers (OPL), Hiroshima, Japan (2023)

Oral presentations at conferences:

- Manek-Hönninger, I., Balage, P. **Guilberteau, T.**, Lafargue, M. Bonamis, G. Delaigue, M. Hönninger, C. Lopez, J. Ultrafast laser micromachining with GHz-bursts. Laser in Manufacturing LIM (2023).
- Balage, P., **Guilberteau, T.**,. Lafargue, M. Bonamis, G. Hönninger, C. Qiao, J. Lopez, J. Manek-Hönninger, I. Advances on percussion drilling with femtosecond laser in GHz-burst mode. EOSAM (2023).
- Balage, P., **Guilberteau, T.**, Lafargue, M. Bonamis, G. Hönninger, C. Lopez, J. Manek-Hönninger, I. GHz-burst Bessel beam dielectric materials cutting. PLI (2023).
- Manek-Hönninger, I., Balage, P. **Guilberteau, T.**, Lafargue, M. Bonamis, G. Delaigue, M. Hönninger, C. Lopez, J. ICAL EO (2023).
- Balage, P., **Guilberteau, T.**, Lafargue, M. Bonamis, G. Hönninger, C. Lopez, J. Manek-Hönninger, I. Dielectrics cutting with Bessel beam in femtosecond GHz-burst regime. Photonics West (2024).
- Balage, P., Lafargue, M. **Guilberteau, T.**, Bonamis, G. Hönninger, C. Lopez, J. Manek-Hönninger, I. Ultrafast laser drilling of through vias in gap materials using burst operation mode. Photonics Europe (2024).
- Balage, P., Lafargue, **Guilberteau, T.**, Bonamis, G. Hönninger, C. Lopez, J. Manek-Hönninger, I. Ultrafast laser drilling of through vias in gap materials using burst operation mode. LPM (2024).
- Balage, P., Lafargue, M. **Guilberteau, T.**, Bonamis, G. Hönninger, C. Lopez, J. Manek-Hönninger, I. Silicon processing with bursts of femtosecond pulses. Optique Normandie (2024).
- **Guilberteau, T.**, Balage,P. Lafargue,M. Husson,F. Valentin,M. Lopez,J. Gemini,L. Manek-Hönninger,I. Polishing of stainless steel with femtosecond GHz-burst laser. PLI (2024)

- **Guilberteau, T.**, Balage,P. Lafargue,M. Husson,F. Valentin,M. Lopez,J. Gemini,L. Manek-Hönninger,I. Polishing of stainless steel with femtosecond GHz-burst laser. Optique Normandie (2024)
- **Guilberteau, T.** Balage, P. Lafargue, M. Lopez, J. Gemini, L. Manek-Hönninger, I. Ultrafast Laser Bessel Beam Interaction with Fused Silica in Single Pulse, MHz-Burst, and GHz-Burst. PLI (2025)
- **Guilberteau, T.** Balage, P. Lafargue, M. Lopez, J. Gemini, L. Manek-Hönninger, I. Ultrafast Laser Bessel Beam Interaction with Fused Silica in Single Pulse, MHz-Burst, and GHz-Burst. LIM (2025)
- **Guilberteau, T.**, Lafargue,M. Lopez,J. Gemini,L. Manek-Hönninger,I.Polishing of metals with femtosecond GHz-burst laser. LIM (2025)
- **Guilberteau, T.**, Lopez,J. Lafargue Gemini,L. Manek-Hönninger,I.Pump-probe measurement of Bessel beam induced modification is Soda-Lime glass in Burst-regime. SPIE Europe (2026)

Poster presentations:

- Balage,P. Lafargue,M. **Guilberteau, T.**, Bonamis,G. Hönninger,C. Lopez,J. and Manek-Hönninger,I. Femtosecond laser processing: a comparison of single pulse, MHz-burst and GHz-burst drilling, Photonics West (2024)
- Balage,P. Lafargue,M. **Guilberteau, T.**, Bonamis,G. Hönninger,C. Lopez,J. and Manek-Hönninger,I. Challenges and solutions in femtosecond laser drilling of through vias in Gap materials in burst regime, Optique Normandie (2024)
- **Guilberteau, T.**, Balage,P. Lafargue,M. Husson,F. Valentin,M. Lopez,J. Gemini,L. Manek-Hönninger,I. Polishing of stainless steel with femtosecond GHz-burst laser Photonique TALENTS (2024)
- **Guilberteau, T.** Balage, P. Lafargue, M. Lopez, J. Gemini, L. Manek-Hönninger, I. Single shot modification in Fused Silica with Single Pulse, MHz-Burst, and GHz-Burst. Photonique TALENTS (2025)

Bibliography

[1] P. Balage, T. Guilberteau, M. Lafargue, G. Bonamis, C. Hönninger, J. Lopez, and I. Manek-Hönninger. Pump-probe imaging of ultrafast laser percussion drilling of glass in single pulse, mhz- and ghz-burst regimes. Advanced Materials Interfaces, 2025.

[2] Dennis E. Grady. Shock-wave properties of soda-lime glass. OSTI, 1996.

[3] Kévin Gaudfrin. Ablation laser par double impulsion pico-femtosecondes, mono-bichromatique, et multi-perforation de la silice fondue. PhD thesis, Université de Bordeaux, Bordeaux, France, dec 2020.

[4] J. Lopez, S. Niane, G. Bonamis, P. Balage, E. Audouard, C. Hönninger, E. Mottay, and I. Manek-Hönninger. Percussion drilling in glasses and process dynamics with femtosecond laser ghz-bursts. Optics Express, 30:12533, 2022.

[5] R. Gattass and E. Mazur. Femtosecond laser micromachining in transparent materials. Nature Photonics, 2:219–225, 2008.

[6] Y. Yu, L. Jiang, Q. Cao, B. Xia, Q. Wang, and Y. Lu. Pump-probe imaging of the fs-ps-ns dynamics during femtosecond laser bessel beam drilling in pmma. Optics Express, 23:32728–32735, 2015.

[7] Y. Hayasaki, S. Fukuda, S. Hasegawa, and S. Juodkazis. Two-color pump-probe interferometry of ultra-fast light-matter interaction. Scientific Reports, 7:10405, 2017.

[8] Xianglei Mao, Samuel S. Mao, and Richard E. Russo. Imaging femtosecond laser-induced electronic excitation in glass. Applied Physics Letters, 82(5):697–699, feb 2003.

[9] F. Bauer, A. Michalowski, T. Kiedrowski, and S. Nolte. Heat accumulation in ultra-short pulsed scanning laser ablation of metals. Optics Express, 23(2):1035–1043, 2015.

[10] F. Courvoisier, J. Zhang, M. Bhuyan, M. Jacquot, and J.M. Dudley. Applications of femtosecond bessel beams to laser ablation. Applied Physics A, 112:29–34, 2013.

[11] N. Li, P. Fan, Q. Zhu, B. Cui, J.-F. Silvain, and Y.F. Lu. Femtosecond laser polishing of additively manufactured parts at grazing incidence. SSRN Electronic Journal, 2022. Preprint, available at: `https://ssrn.com/abstract=4054170`.

[12] A. H. A. Lutey, L. Gemini, L. Romoli, M. Faucon, and R. Kling. Towards laser-textured antibacterial surfaces. Scientific Reports, 8:10112, 2018.

[13] A. Papadopoulos, E. Skoulas, A. Mimidis, G. Perrakis, G. Kenanakis, and E. Stratakis. Biomimetic omnidirectional antireflective glass via direct ultrafast laser nanostructuring. Advanced Materials, 31(31):1901123, 2019.

[14] V. Malka, C. Coulaud, J.P. Geindre, V. Lopez, Z. Najmudin, D. Neely, and Y. Amiranoff. Characterization of neutral density profile in a wide range of pressure of cylindrical pulsed gas jets. Rev. Sci. Instrum., 71:2329–2333, 2000.

[15] Arnold Gillner, Jan Finger, Philipp Gretzki, Michael Niessen, Thilo Bartels, and Markus Reininghaus. High power laser processing with ultrafast and multi-parallel beams. Journal of Laser Micro/Nanoengineering, 14(2):129–135, 2019.

[16] Takashige Omatsu et al. A new twist for materials science: The formation of chiral structures using the angular momentum of light. Advanced Optical Materials, 7(14):1801672, 2019.

[17] P. Balage, T. Guilberteau, M. Lafargue, G. Bonamis, C. Hönninger, J. Lopez, and I. Manek-Hönninger. Bessel beam dielectrics cutting with femtosecond laser in ghz-burst mode. Micromachines, 14:1650, 2023.

[18] K. Miyamoto, K. Sugioka, and K. Midorikawa. Bessel beam femtosecond laser processing of glass. Applied Physics A, 105:603–609, 2011.

[19] D. Metzner, P. Lickschat, C. Kreisel, T. Lampke, and S. Weißmantel. Study on laser ablation of glass using mhz to ghz burst pulses. Applied Physics A, 128:637, 2022.

[20] A. Žemaitis, M. Gaidys, P. Gečys, M. Barkauskas, and M. Gedvilas. Femtosecond laser ablation by bibursts in the mhz and ghz pulse repetition rates. Optics Express, 29(5):7641–7653, 2021.

[21] S. Hendow, H. Takahashi, M. Yamaguchi, and J. Xu. Enhanced ablation using ghz-pulsed fs laser. Proc. SPIE Laser Based Micro-Nanoprocessing XIV, 11268:1126809, 2020.

[22] P. Balage, J. Lopez, G. Bonamis, C. Hönninger, and I. Manek-Hönninger. Crack-free high-aspect ratio holes in glasses by top–down percussion drilling with infrared femtosecond laser ghz-bursts. International Journal of Extreme Manufacturing, 5:015002, 2023.

[23] K. Sugioka. Will ghz burst mode create a new path to femtosecond laser processing? International Journal of Extreme Manufacturing, 3:043001, 2021.

[24] S.N. Khonina, N.L. Kazanskiy, S.V. Karpeev, and M.A. Butt. Bessel beam: significance and applications — a progressive review. Micromachines, 11:997, 2020.

[25] K. Mishchik, R. Beuton, O. D. Caulier, S. Skupin, B. Chimier, G. Duchateau, B. Chassagne, R. Kling, C. Hönninger, and E. Mottay. Improved laser glass cutting by spatio-temporal control of energy deposition using bursts of femtosecond pulses. Optics Express, 25:33271–33282, 2017.

[26] Valeria Viviana Belloni, Mostafa Hassan, Luca Furfaro, Remo Giust, Anne-Magali Seydoux-Guillaume, Sergio Sao-Joao, and Francois Courvoisier. Single shot generation of high-aspect-ratio nano-rods from sapphire by ultrafast first order bessel beam. Laser & Photonics Reviews, 18(3), mar 2024.

[27] Y. Zhang, T. Koike, R. Yoshizaki, G. Ren, A. Shibata, S. Kiriake, R. Hasegawa, I. Nagasawa, K. Nagato, N. Sugita, and Y. Ito. Ultrahigh-speed laser drilling of transparent materials via transient electronic excitation. Science Advances, 11(24):1–10, 2025.

[28] F. He, J. Yu, Y. Tan, W. Chu, C. Zhou, Y. Cheng, and K. Sugioka. Tailoring femtosecond 1.5-μm bessel beams for manufacturing high-aspect-ratio through-silicon vias. Scientific Reports, 7:1–9, 2017.

[29] B.N. Chichkov, C. Momma, S. Nolte, F. von Alvensleben, and A. Tünnermann. Femtosecond, picosecond and nanosecond laser ablation of solids. Applied Physics A: Materials Science & Processing, 63(2):109–115, 1996.

[30] C. Momma, S. Nolte, N. Chichkov, F v. Alvensleben, and A. Tünnermann. Precise laser ablation with ultrashort pulses. Applied Surface Science, 109-110:15–19, 1997.

[31] S. Sh. Rekhviashvili. On the dimensional properties of electron gas. Russian Physics Journal, 50(8):789–792, 2007.

[32] Andrey V. Lugovskoy and Igor Bray. Ultrafast electron dynamics in metals under laser irradiation. Physical Review B, 60(5):3279–3287, 1999.

[33] Yiling Lian, Lan Jiang, Jingya Sun, Wenpan Tao, Zhicheng Chen, Gen Lin, Ziqian Ning, and Manlou Ye. Ultrafast dynamics and ablation mechanism in femtosecond laser irradiated au/ti bilayer systems. Nanophotonics, 12(24):4461–4473, 2023. PMCID: PMC11501701.

[34] C. D. Aeaby and Aditi Ray. Two-temperature model for ultrafast melting of au-based bimetallic films interacting with single-pulse femtosecond laser: Theoretical study of damage threshold. Physical Review B, 107(19):195402, 2023.

[35] D.J. Förster, B. Jäggi, A. Michalowski, and B. Neuenschwander. Review on experimental and theoretical investigations of ultra-short pulsed laser ablation of metals with burst pulses. Materials, 14(12):3331, 2021.

[36] E. Carpene. Ultrafast laser irradiation of metals: Beyond the two-temperature model. Physical Review B, 74(2):024301, 2006.

[37] Wen-Pin Hsieh, Chung-Hung Lin, Chao-Chih Chen, and Jen-Wei Chang. Testing the validity of the wiedemann-franz law for metals and alloys at high pressures. Applied Physics Letters, 125(25):252201, 2024.

[38] G. V. Samsonov, editor. Handbook of the Physicochemical Properties of the Elements. Springer, 1968.

[39] Riad Abas, M. Hayashi, and Seshadri Seetharaman. Thermal diffusivity measurements of some industrially important alloys by a laser flash method. International Journal of Materials Research, 98(6):535–540, 06 2007.

[40] R. Le Harzic, D. Breitling, M. Weikert, S. Sommer, C. Föhl, S. Valette, C. Donnet, E. Audouard, and F. Dausinger. Pulse width and energy influence on laser micromachining of metals in a range of 100 fs to 5 ps. Applied Surface Science, 249(1-4):322–331, 2005.

[41] Neil W. Ashcroft and N. David Mermin. Solid State Physics. Holt, Rinehart and Winston, New York, 1976.

[42] Rose Mary, Debaditya Choudhury, and Ajoy Kar. Applications of fiber lasers for the development of compact photonic devices. IEEE Journal of Selected Topics in Quantum Electronics, 20(5):1–13, 2014.

[43] N. Arnold and E. Cartier. Theory of laser-induced free-electron heating and impact ionization in wide-band-gap solids. Physical Review B, 46:15102–15115, 1992.

[44] E. E. Serebryannikov and A. M. Zheltikov. Quantum and semiclassical physics behind ultrafast optical nonlinearity in the midinfrared: The role of ionization dynamics within the field half cycle. Physical Review Letters, 113:043901, 2014.

[45] M. D. Perry, B. C. Stuart, P. S. Banks, M. D. Feit, V. Yanovsky, and A. M. Rubenchik. Ultrashort-pulse laser machining of dielectric materials. Journal of Applied Physics, 85:6803–6810, 1999.

[46] H. X. Deng, X. Xiang, W. G. Zheng, X. D. Yuan, S. Y. Wu, X. D. Jiang, F. Gao, X. T. Zu, and K. Sun. Theory of absorption rate of carriers in fused silica under intense laser irradiation. Journal of Applied Physics, 108:103116, 2010.

[47] Mousumi Upadhyay Kahaly, Saibabu Madas, Boris Mesits, and Subhendu Kahaly. Tunable ultrafast thermionic emission from femtosecond-laser hot spot on a metal surface by control of laser polarization and angle of incidence: A numerical investigation. Applied Surface Science, 643:158668, 2024.

[48] E. G. Gamaly. The physics of ultra-short laser interaction with solids at non-relativistic intensities. Physics Reports, 508:91–243, 2011.

[49] P. Balling and J. Schou. Femtosecond-laser ablation dynamics of dielectrics: basics and applications for thin films. Reports on Progress in Physics, 76:036502, 2013.

[50] P. Martin, S. Guizard, P. Daguzan, G. Petite, P. D'Oliveira, P. Meynadier, and M. Perdrix. Subpicosecond study of carrier trapping dynamics in wide-band-gap crystals. Physical Review B, 55:5799–5810, 1997.

[51] F. Théberge and S. L. Chin. Enhanced ablation of silica by the superposition of femtosecond and nanosecond laser pulses. Applied Physics A, 79(7):1505–1510, 2004.

[52] H. Kuzmany. The dielectric function. In Solid-State Spectroscopy. Springer, Berlin, Heidelberg, 1998.

[53] Fedor Akhmetov, Igor Milov, Igor A. Makhotkin, Marcelo Ackermann, and Jan Vorberger. Electron-phonon coupling in transition metals beyond wang's approximation. Physical Review B, 108:214301, 12 2023.

[54] J. K. Chen, W. P. Latham, and J. E. Beraun. The role of electron-phonon coupling in ultrafast laser heating. Journal of Laser Applications, 17(1):63–68, 02 2005.

[55] Heinrich Hora and George H. Miley, editors. Laser Interaction and Related Plasma Phenomena. Springer, 1984.

[56] A. Vogel, J. Noack, G. Hüttman, and G. Paltauf. Mechanisms of femtosecond laser nanosurgery of cells and tissues. Applied Physics B, 81:1015–1047, 2005.

[57] Akshay Joshi, Vatsa Gandhi, Suraj Ravindran, and Guruswami Ravichandran. An investigation of shock-induced phase transition in soda-lime glass. Journal of Applied Physics, 131(20):205902, may 2022.

[58] S. Bauer, F. Bagusat, E. Strassburger, M. Sauer, and S. Hiermaier. New insights into the failure front phenomenon and the equation of state of soda-lime glass under planar plate impact. Journal of Dynamic Behavior of Materials, 7:81–106, 2021.

[59] Max Born and Emil Wolf. Principles of Optics: Electromagnetic Theory of Propagation, Interference and Diffraction of Light. Cambridge University Press, Cambridge, 7th expanded anniversary edition edition, 2019.

[60] B. Wang, J. He, J. Yu, R. Pei, and C. Dai. Application of high efficiency polishing technology in manufacturing aero-engine components. Diamond and Abrasives Engineering, 38(3):75–80, 2018.

[61] S. Schwarz, S. Rung, C. Esen, and R. Hellmann. Enhanced ablation efficiency using ghz bursts in micromachining fused silica. Optics Letters, 46:282–285, 2021.

[62] H.D. Nguyen, E. Moreno, A. Rudenko, N. Faure, X. Sedao, C. Mauclair, J.-P. Colombier, and R. Stoian. Super-efficient drilling of metals with ultrafast non-diffractive laser beams. Scientific Reports, 12:2074, 2022.

[63] C. Kerse, H. Kalaycoglu, P. Elahi, B. Cetin, D. Kesim, O. Akçaalan, S. Yavas, M. Asik, B. Oktem, H. Hoogland, and O. Holzwarth, R. Ilday. Ablation-cooled material removal with ultrafast bursts of pulses. Nature, 537:84, 2016.

[64] P. Balage, G. Bonamis, M. Lafargue, T. Guilberteau, M. Delaigue, C. Hönninger, J. Qiao, J. Lopez, and I. Manek-Hönninger. Advances in femtosecond laser ghz-burst drilling of glasses: influence of burst shape and duration. Micromachines, 14:1158, 2023.

[65] B. Jaeggi, S. Remund, Y. Zhang, T. Kramer, and B. Neuenschwander. Optimizing the specific removal rate with the burst mode under varying conditions. JLMN - Journal of Laser Micro/Nanoengineering, 12(3):244–250, 2017.

[66] T. Kramer, Y. Zhang, S. Remund, B. Jaeggi, A. Michalowski, L. Grad, and B. Neuenschwander. Increasing the specific removal rate for ultra short pulsed laser-micromachining by using pulse bursts. Journal of Laser Micro/Nanoengineering, 12(2):107–114, 2019.

[67] G. Bonamis, E. Audouard, C. Hönninger, J. Lopez, K. Mishchik, E. Mottay, and I. Manek-Hönninger. Systematic study of laser ablation with ghz bursts of femtosecond pulses. Optics Express, 28(19):27702–27714, 2020.

[68] P. Elahi, Ö. Akçaalan, C. Ertek, K. Eken, F.Ö. Ilday, and H. Kalaycoglu. High-power yb-based all-fiber laser delivering 300 fs pulses for high-speed ablation-cooled material removal. Optics Letters, 43:3, 2018.

[69] W.R. Fahrner. Laser beam shaping. Springer Series in Optical Sciences, 170, 2013.

[70] G.S. Sokolovskii, V.V. Dudelev, S.N. Losev, M. Butkus, K.K. Soboleva, A.I. Sobolev, A.G. Deryagin, V.I. Kuchinskii, W. Sibbett, and E.U. Rafailov. Influence of the axicon characteristics and beam propagation parameter m^2 on the formation of bessel beams from semiconductor lasers. Quantum Electronics, 43:426–427, 2013.

[71] S. Mitra, M. Chanal, R. Clady, A. Mouskeftaras, and D. Grojo. Millijoule femtosecond micro-bessel beams for ultra-high aspect ratio machining. Applied Optics, 54:7358–7365, 2015.

[72] O. Brzobohatý, T. Čižmár, and P. Zemánek. High quality quasi-bessel beam generated by round-tip axicon. Optics Express, 16(17):12688–12700, 2008.

[73] J. Dudutis, P. Gečys, and G. Račiukaitis. Non-ideal axicon-generated bessel beam application for intra-volume glass modification. Optics Express, 24:28433–28443, 2016.

[74] J. Lopez, K. Mishchik, B. Chassagne, C. Javaux-Leger, C. Hönninger, E. Mottay, and R. Kling. Glass cutting using ultrashort pulsed bessel beam. In Proceedings of the ICALEO, page M404, Atlanta, GA, USA, 2015.

[75] B. Miao, L. Feder, J.E. Shrock, and H.M. Milchberg. Phase front retrieval and correction of bessel beams. Optics Express, 30(7), 2022.

[76] Runze Li, Xianghua Yu, Tong Peng, Yanlong Yang, Baoli Yao, Chunmin Zhang, and Tong Ye. Shaping the on-axis intensity profile of generalized bessel beams by iterative optimization methods. Journal of Optics, 20(8):085603, 2018.

[77] Z. Wang, L. Jiang, X. Li, N. Wang, Z. Yao, K. Zhang, and Y. Lu. High-throughput microchannel fabrication in fused silica by temporally shaped femtosecond laser bessel-beam-assisted chemical etching. Optics Letters, 43(1):1–4, 2018.

[78] Y. Matsuoka, Y. Kizuka, and T. Inoue. The characteristics of laser micro drilling using a bessel beam. Applied Physics A, 84:423–430, 2006.

[79] Valeria Belloni. Mise en forme spatiale et temporelle d'impulsions ultrabrèves pour l'ablation et la transformation de matériaux par laser. Thèse de doctorat, Université de Bourgogne Franche-Comté, Besançon, France, December 2023. Dirigée par François Courvoisier, FEMTO-ST Institute (UMR 6174).

[80] M. Zukerstein, J. Hrabovsky, J. Sladek, I. Mirza, Y. Levy, and N. M. Bulgakova. Formation of tubular structures and microneedles on silicon surface by doughnut-shaped ultrashort laser pulses. Applied Surface Science, 592:153228, aug 2022.

[81] K. M. Davis, K. Miura, N. Sugimoto, and K. Hirao. Writing waveguides in glass with a femtosecond laser. Optics Letters, 21(21):1729–1731, 1996.

[82] Z. Luo, Z. Zhang, F. Zhao, C. Fan, J. Feng, H. Zhou, F. Meng, X. Zhuang, and J. Wang. Advanced polishing methods for atomic-scale surfaces: A review. Materials Today Sustainability, 27:100841, 2024.

[83] D. Aslanidis, G. Roebben, J. Bruninx, and W. Van Moorleghem. Electropolishing for medical devices: Relatively new and fascinatingly diverse. Materials Science Forum, 394-395:169–172, 2002.

[84] J. O'Hara and F. Fang. Advances in micro cutting tool design and fabrication. International Journal of Extreme Manufacturing, 1:032003, 2019.

[85] Yu. D. Filatov. Polishing of precision surfaces of optoelectronic device elements made of glass, sitall, and optical and semiconductor crystals: A review. Journal of Superhard Materials, 42(1):30–48, 2020.

[86] Mingli Xie, Yipeng Pan, Zijun An, Shijun Huang, and Min Dong. Review on surface polishing methods of optical parts. Advances in Materials Science and Engineering, 2022.

[87] C. Sciancalepore, L. Gemini, L. Romoli, and F. Tantussi. Study of the wettability behavior of stainless steel surfaces after ultrafast laser texturing. Surface and Coatings Technology, 352:370–377, 2018.

[88] Jörn Bonse, Jürgen Krüger, Sören Höhm, and Arkadi Rosenfeld. Femtosecond laser-induced periodic surface structures. Journal of Laser Applications, 24(4):042006, 2012.

[89] F. Fraggelakis, G. Mincuzzi, J. Lopez, R. Kling, and E. Stratakis. Controlling 2d laser nanostructuring over large area with double femtosecond pulses. Applied Surface Science, 470:677–686, 2019.

[90] F. Ränke, A. F. Lasagni, and T. Kunze. High throughput laser surface microstructuring of polystyrene by combining direct laser interference patterning with polygon scanner technology. Materials Letters: X, 14:100144, 2022.

[91] M. Gaidys, A. Žemaitis, P. Gečys, and M. Gedvilas. Efficient surface polishing using burst and biburst mode ultrafast laser irradiation. RSC Advances, 13:3586–3591, 2023.

[92] A.M. Khalid Hafiz, E.V. Bordatchev, and R.O. Tutunea-Fatan. Influence of overlap between the laser beam tracks on surface quality in laser polishing of aisi h13 tool steel. Applied Surface Science, 261:806–814, 2012.

[93] A. Y. Vorobyev and C. Guo. Colorizing metals with femtosecond laser pulses. Applied Physics Letters, 92(4):041914, 2008.

[94] Annalisa Volpe, Caterina Gaudiuso, and Antonio Ancona. Laser fabrication of anti-icing surfaces: A review. Materials, 13(24):5692, 2020.

[95] A. Gisario, M. Barletta, and F. Veniali. Laser polishing: a review of a constantly growing technology in the surface finishing of components made by additive manufacturing. The International Journal of Advanced Manufacturing Technology, 120:1433–1472, 2022.

[96] C. Arnaud, A. Almirall, C. Loumena, and R. Kling. Potential of structuring and polishing with fiber laser on homogeneous metals. Journal of Laser Applications, 29(2):022501, 2017.

[97] A. Temmler, E. Willenborg, and K. Wissenbach. Design surfaces by laser remelting. Physica Procedia, 12:419–430, 2011.

[98] K. Gaudfrin, J. Lopez, R. Kling, and E. Audouard. Fused silica ablation by double ultrashort laser pulses with dual wavelength and variable delays. Optics Express, 30(22):40120–40132, 2022.

[99] Ioan Damian. Malus' law for a real polarizer. arXiv preprint, 2006. arXiv:physics/0603172.

[100] R. Álvarez, A. Rodero, and M.C. Quintero. An abel inversion method for radially resolved measurements in the axial injection torch. Spectrochimica Acta Part B: Atomic Spectroscopy, 57:1665–1680, 2002.

[101] K. Yamamoto, N. Hasaka, H. Morita, and E. Ohmura. Influence of the thermal expansion coefficient in laser scribing of glass. Precision Engineering, 34:70–75, 2010.

[102] Marvin J. Weber. Handbook of Optical Materials. Laser & Optical Science & Technology. CRC Press, 1 edition, 2003.

[103] O.D. Caulier, K. Mishchik, B. Chimier, S. Skupin, A. Bourgeade, C.J. Léger, R. Kling, C. Hönninger, J. Lopez, V. Tikhonchuk, and et al. Femtosecond laser pulse train interaction with dielectric materials. Applied Physics Letters, 107:181110, 2015.

[104] K. Obata, K. Sugioka, K. Toyoda, and K. Midorikawa. Enhance refractive index modification of fused silica by multiwavelength excitation process using f2 and krf excimer lasers. Opt. Lett., 27:330–332, 2002.

[105] SCHOTT AG. Electrical properties of schott glass. Technical datasheet, SCHOTT AG, Mainz, Germany, 2020. Technical information document.

[106] J. Lopez, K. Mishchik, G. Mincuzzi, E. Audouard, E. Mottay, and R. Kling. Efficient metal processing using high average power ultrafast laser. Journal of Laser Micro/Nanoengineering, 12(3), 2017.

[107] P. Haglund, I. Eriksson, J. Powell, and A. Kaplan. Surface tension stabilized laser welding (donut laser welding)—a new laserwelding technique. JOURNAL OF LASER APPLICATIONS, 25, 2013.

[108] Martin Ruthandi Maina, Yasuhiro Okamoto, Akira Okada, Matti Närhi, Jarno Kangastupa, and Jorma Vihinen. High surface quality welding of aluminum using adjustable ring-mode fiber laser. Journal of Materials Processing Technology, 258:180–188, aug 2018.

[109] Lin andKong Fanrong Mohammadpour, Masoud andWang and Radovan Kovacevic. Adjustable ring mode and single beam fiber lasers: A performance comparison. Manufacturing Letters, 25:50–55, aug 2020.

[110] T. Fuhrich, P. Berger, and H. Hügel. Marangoni effect in laser deep penetration welding of steel. Journal of Laser Applications, 13(5):178–186, 2001.

[111] A. Žemaitis, P. Gečys, and M. Gedvilas. Efficient ablation, further ghz burst polishing, and surface texturing by ultrafast laser. Advanced Engineering Materials, 26:2302262, 2024.

[112] T. Guilberteau, F. Husson, M. Lafargue, J. Lopez, M. Faucon, L. Gemini, and I. Manek-Hönninger. Long GHz-burst laser surface polishing of AISI 316l stainless steel parts manufactured by short GHz-burst laser ablation. Nanomaterials, 15(17):1343, 2025.

[113] Calum A. Ross, David G. MacLachlan, Debaditya Choudhury, and Robert R. Thomson. Optimisation of ultrafast laser assisted etching in fused silica. Optics Express, 26(19):24343–24356, 2018.

[114] V. Stankevičiūte, G. Račiukaitis, and P. Gečys. Chemical etching of fused silica after modification with two-pulse bursts of femtosecond laser. Optics Express, 29(20):31393–31408, 2021.

[115] H. Seidel, L. Csepregi, A. Heuberger, and H. Baumgärtel. Orientation dependence and behavior of passivation layers. Journal of The Electrochemical Society, 137:3612–3626, 1990.

[116] T. Guilberteau, P. Balage, M. Lafargue, J. Lopez, L. Gemini, and I. Manek-Hönninger. Bessel beam femtosecond laser interaction with fused silica before and after chemical etching: Comparison of single pulse, mhz-burst, and ghz-burst. Micromachines, (15):1313, 2024.

[117] D. Loison, J.-P. Guin, J.-C. Sangleboeuf, M. Nivard, E. Lescoute, A. Sollier, G. Seisson, D. Hebert, L. Berthe, and M. Boustie. Soda-lime glass behavior under laser shock. AIP Conference Proceedings, 1793:100036, 2017.

[118] Quan UN, Hong-bing Jiang, Yi Liu, Zhao-xin Wu, Hong Yang, and Qi-huang Gong. Diagnose parameters of plasma induced by femtosecond laser pulse in quartz and glasses. Frontiers of Physics in China, 1(1):67–71, 2006.

[119] J. Piard and J. Randon. L'absorbance : comment rendre sa compréhension plus lumineuse aux yeux des apprenant·es. Bulletin de l'Union des Professeurs de Physique et de Chimie, 2021. HAL open-access publication, hal-03929595.

[120] Wikipedia contributors. Absorbance. `https://en.wikipedia.org/wiki/Absorbance`, 2024. Accessed: 2024-09-12.

[121] Mitsuo Takeda, Hideki Ina, and Seiji Kobayashi. Fourier-transform method of fringe-pattern analysis for computer-based topography and interferometry. Journal of the Optical Society of America, 72(1):156–160, 1982.

[122] Lawrence E. Kinsler, Austin R. Frey, Alan B. Coppens, and James V. Sanders. Fundamentals of Acoustics. Wiley, 4th edition, 2000.

[123] DAVID B. GEOHEGAN. Time-resolved diagnostics of excimer laser-generated ablation plasmas used for pulsed laser deposition. In Excimer Lasers, pages 165–185. Springer, 1994. Chapter.

[124] M. Park, Y. Gu, X. Mao, C. P. Grigoropoulos, and V. Zorba. Mechanisms of ultrafast ghz burst fs laser ablation. Science Advances, 9:eadf6397, 2023.

Appendices

Appendix A

Multi-GHz burst irradiation in AF-32 glass

This annex presents the investigations on the influence of multi-burst irradiation on the final morphology of laser-induced modifications with a Bessel beam in AF-32 glass with the same optical set-up as in Section 4.2. The experiment was performed on samples with a thickness of 300 μm, using a burst energy of 255 μJ, a number of pulses per burst (ppb) of 50, and a repetition rate of 1 kHz. The corresponding results are presented in Figure A.1. For a single GHz-burst irradiation, the modi-

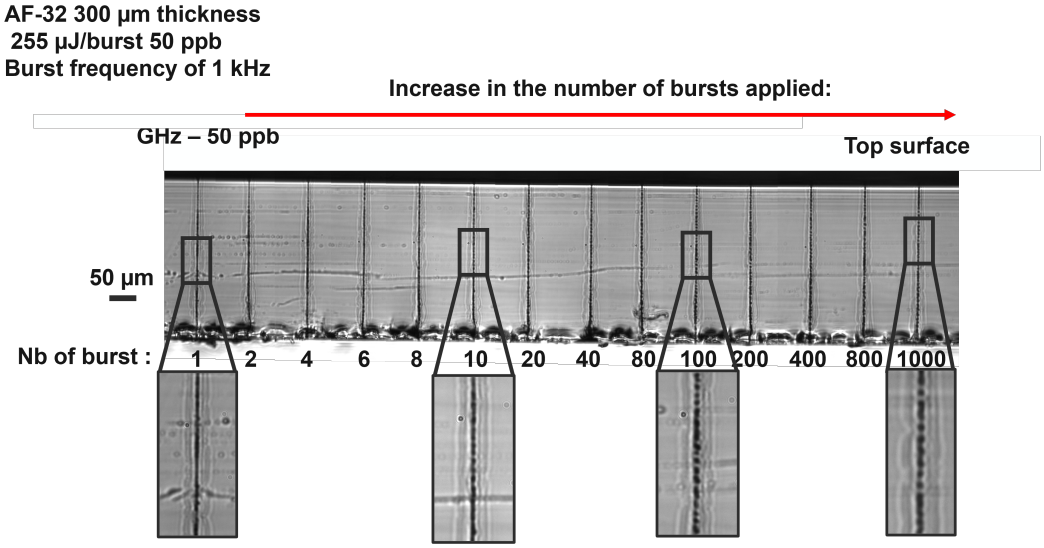

Figure A.1: Optical microscope side-view images of laser-induced modifications in AF-32 glass obtained for different numbers of applied bursts at a burst energy of 255 μJ.

fication morphology previously discussed in fused silica and shown in Figure 4.3 is clearly retrieved in AF-32 glass, confirming that the interaction regime is similar to that observed in other materials. However, when multiple bursts are applied at the same location, a progressive change of the morphology is observed. After 10 bursts, the first signs of bubble-like structures begin to appear within the laser-affected zone. As the number of bursts is further increased to N = 100 and N = 1000, this evolution continues, ultimately leading to the formation of a fully developed bubble-like structure, comparable to those typically observed in the single-pulse

(SP) and MHz-burst irradiation regimes. These observations demonstrate that the morphological differences between the GHz-burst and MHz-burst interaction regimes are strongly influenced by the cumulative energy deposition associated with multiple burst exposures. Consequently, the inherent differences in energy delivery dynamics between GHz-burst and MHz-burst irradiation play a central role in determining the final modification morphology.

Appendix B

Exploration of a 16 GHz-burst frequency

This section presents a preliminary investigation of the influence of multi-GHz burst-frequency irradiation on matter. The experiments were carried out using a home-built laser source, named OURAL, developed by the GOLF group at the CELIA laboratory. The OURAL laser is capable of delivering ultrafast pulse trains at repetition frequencies ranging from 8 to 16 GHz with a maximum average output power of 10 W in contrast to the intra-burst frequency of 1.28 GHz used for the GHz-bursts throughout all the other studies presented in this thesis. The beam diameter is first adjusted using a beam expander to ensure optimal operation of an acousto-optic modulator (AOM), as illustrated in the setup depicted in Figure B.1, which is used to temporally gate the pulse train and generate burst sequences. This burst regime has been employed for a preliminary study on stainless-steel surface polishing, as reported in an article under revision. The first trials were dedicated to

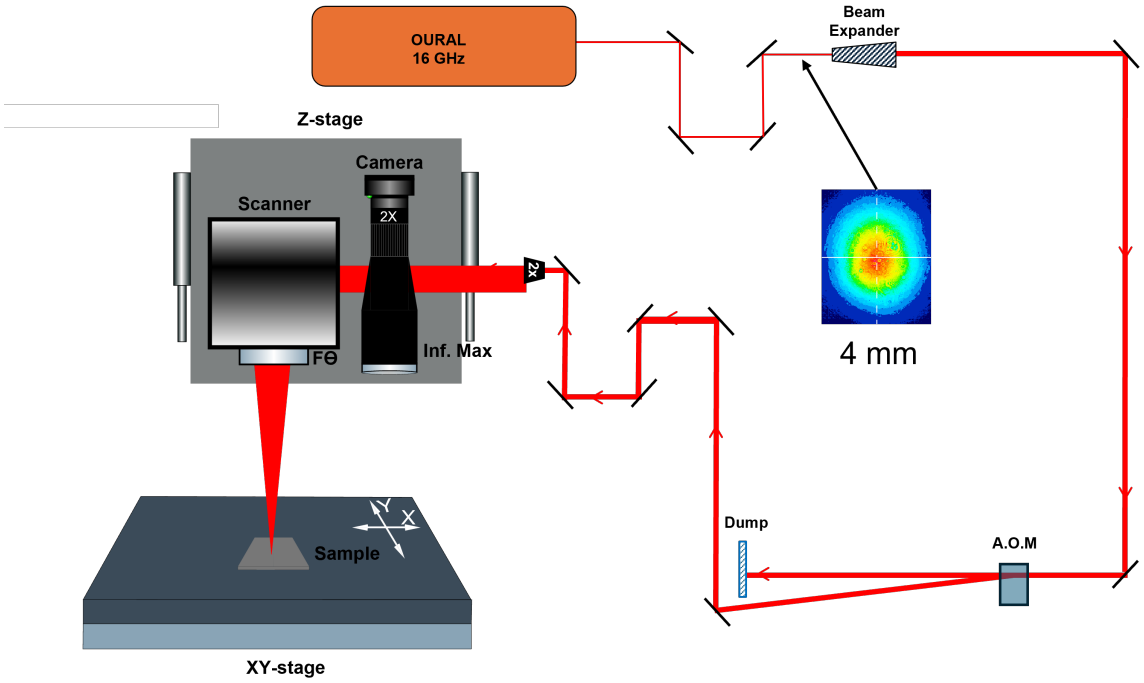

Figure B.1: Experimental setup used with the 16 GHz OURAL laser system.

drilling, and then the second trials were focused on the generation of a melted layer.

The OURAL laser can operate either in a continuous ultrafast pulse-train regime at 16 GHz or in a continuous-wave (CW) mode at a wavelength of 1030 nm. The experiment therefore consisted in comparing the laser-drilling behavior on stainless steel under these two irradiation regimes. For this purpose, an average power of 5.85 W was used, and holes were drilled with irradiation times ranging from 10 µs to 1 s in both configurations (16 GHz pulse train and CW). The resulting morphologies are presented in Figure B.2. No noticeable differences are observed between the holes produced under CW irradiation and those obtained using the 16 GHz pulse-train regime. This indicates that, under the investigated conditions, stainless steel does not exhibit a significant sensitivity to the temporal structure of the laser irradiation in this frequency range. This behavior can be explained by the fact that a repetition rate of 16 GHz corresponds to a pulse-to-pulse separation of approximately 62.5 ps, which is several orders of magnitude shorter than the characteristic thermal diffusion time in stainless steel (for 20 μm). As a result, the material response is governed by cumulative thermal effects, effectively smoothing out any distinction between the pulsed and continuous irradiation regimes. Additionally, during the melting layer

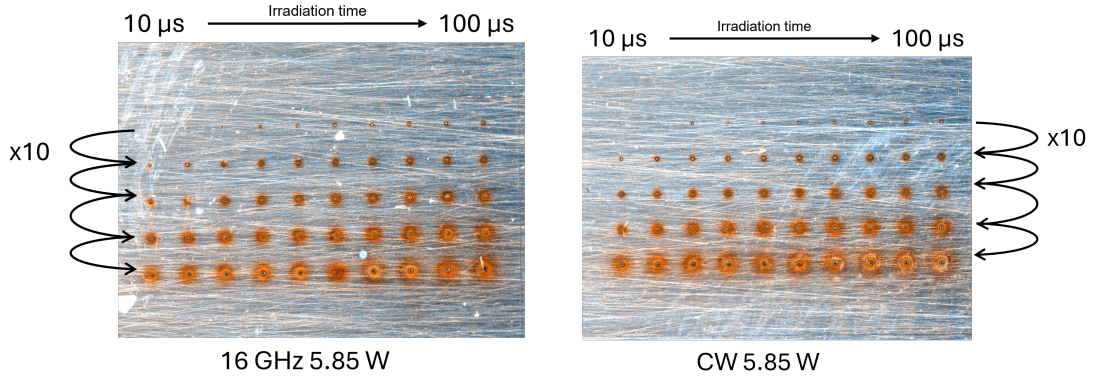

(a) 16 GHz 5.85 W (b) CW 5.85 W

Figure B.2: Binocular image of the hole drilling experiment on 316L with 16 GHz bursts (a) and in CW regime (b) for drilling times of 10 µs up to 1 s generated with the OURAL laser system.

generation experiments, it was observed that when an excessive amount of heat was deposited at the material surface, periodic wave-like structures were induced within the molten pool. These features were first identified and discussed in Section 3.1, and were subsequently observed again in the present experiment, although on a larger spatial scale. A representative image of the final surface exhibiting these so-called "thermal induced waves-like structures" is shown in Figure B.3.

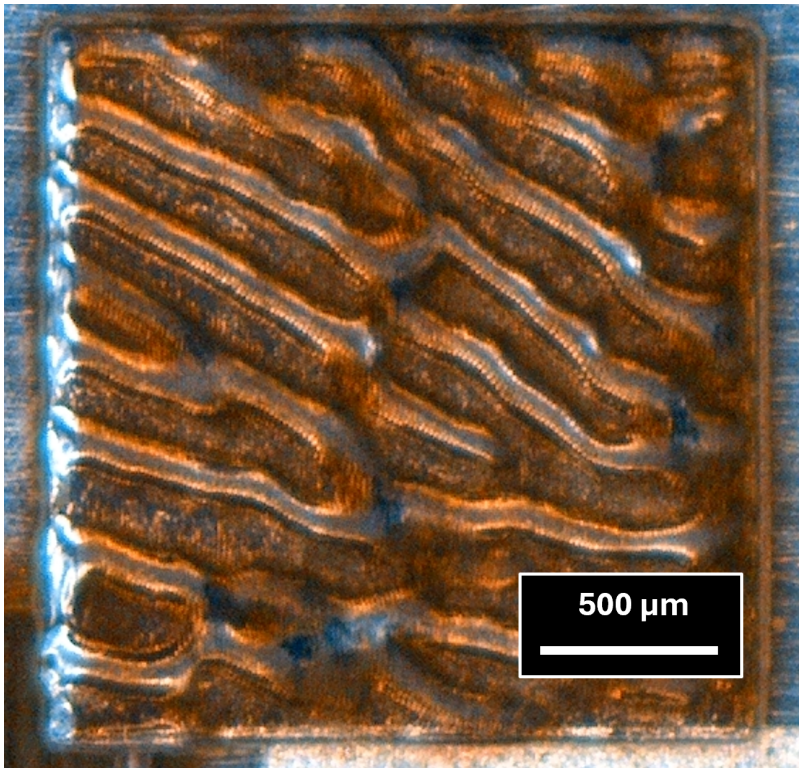

Figure B.3: Binocular microscope image of thermal wave-like surface structures generated using the 16 GHz OURAL laser system. The laser scanning direction is perpendicular to the observed surface modulation.

Appendix C

Vortex beam MHz-burst

In this appendix, the results obtained with a laser beam, spatially shaped using a vortex phase mask carrying an orbital angular momentum of $m = 1$, as explained in Section 1.4.2.3, are presented. The underlying physical mechanism has been detailed previously in Section 1.4.2.3. The objective of this section is to present the investigations of the laser-matter interaction for polishing applications based on visual analysis as it was carried out with the GHz-burst in Section 3.1.2.

It should be noted, however, that this beam-shaping configuration was implemented relatively late in the course of this work. Consequently, for the MHz-burst configuration the only shape investigated was the vortex.

The first step of the study focuses on the impact of a single burst on the sample surface. To this end, several beam spot sizes were investigated by translating the target along the optical axis using the Z-translation stage, thereby defocusing the beam at the surface. For each spot size, the burst energy was varied in steps of 8.5 µJ. In addition, for each parameter set, the number of pulses per burst (ppb) was investigated from 50 to 800 ppb.

The resulting surface modifications were characterized using an optical microscope equipped with a 20× objective. Representative results obtained in the MHz-burst configuration are presented in Fig. C.1.

By inspecting the first MHz-burst configuration (4 ppb) shown in Fig. C.1a, several characteristic features can be identified. For the smallest beam spot size (54 μm) a circular region is observed, without a distinct dark feature at its center in comparison to the results found with the GHz-burst. Instead, it seems that the interaction produces a hole with a strait floor and relatively low conical angle.

When increasing the beam spot size the central spike seems to appear but is only present for burst energies between 272 and 340 μJ. Below this threshold, the formation of LIPSS can be seen on the circular edge of the interaction and progressing toward the central region as the energy is decreased (see for 68 μJ). At a spot size of 100 μm, a slight "melt" is generated and the central region remains unaffected. For lower energies the same pattern as described previously occurs, the presence of LIPSS is observed and they slowly disappear as the energy is further decreased.

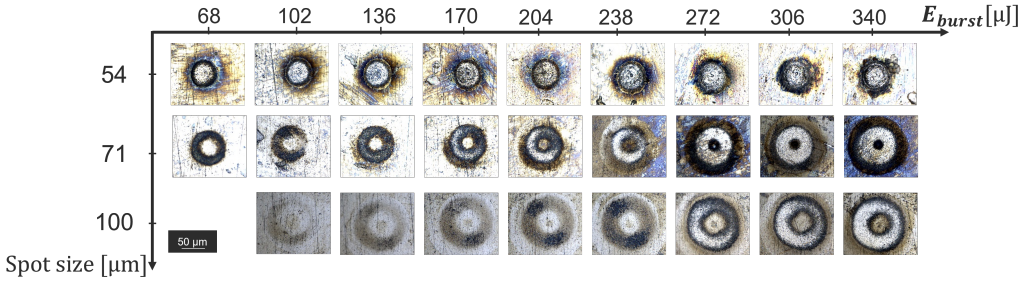

(a) 4 ppb

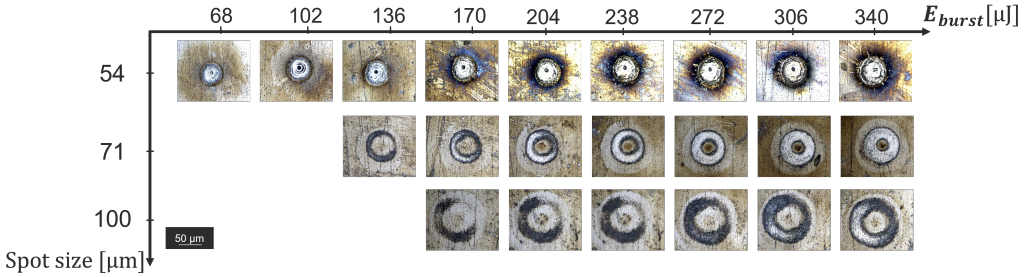

(b) 8 ppb

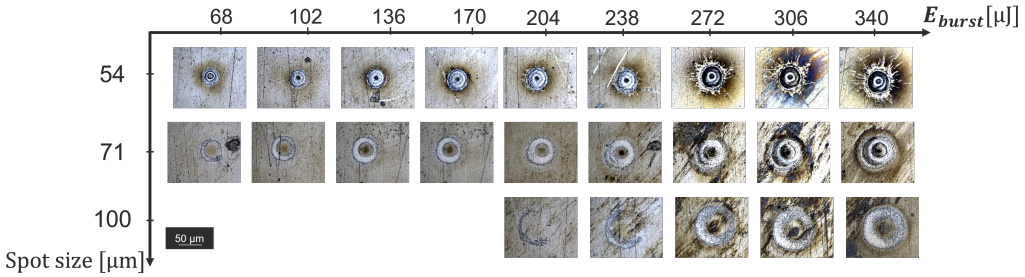

(c) 16 ppb

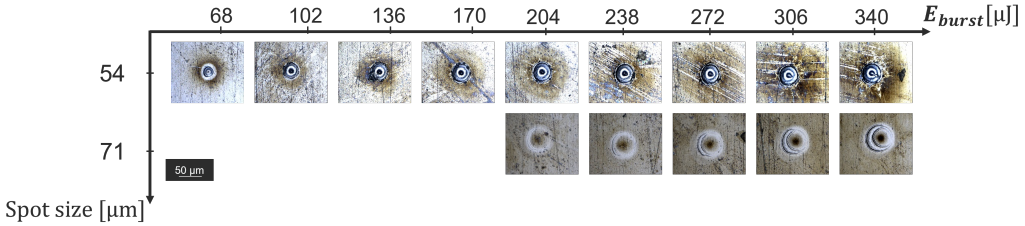

(d) 32 ppb

Figure C.1: Optical microscope images of vortex beam surface modifications with increasing number of pulses per burst, as a function of energy and spot size in MHz-burst mode with (a) 4 ppb,(b) 8 ppb,(c) 16 ppb,(d) 32 ppb.

Increasing the number of pulses per burst to 8 ppb (Fig. C.1b) leads to comparable trends. For the smallest spot size however, a molten pool with a central feature is observed. At a spot size of 71 μm, the central region remains unaffected. At lower burst energies, the molten region becomes increasingly inhomogeneous, which can be attributed to residual non-uniformities of the vortex phase mask used. For the largest spot size investigated (100 μm), the molten region nearly vanishes giving place to LIPSS for the majority of the studied energies.

This general trend persists as the number of pulses per burst is further increased

to 16 ppb and 32 ppb, as shown in Fig. C.1c and Fig. C.1d. At small beam spot sizes, excessive energy deposition leads to strong melting and protrusion. However, it can be noticed that in those two configurations the melted layer seems more reflective, indicating a better melting and higher surface tension. The outer radius of the molten region decreases with an increasing number of pulses per burst. For larger spot sizes, melting remains confined to the periphery, leaving the central region unaffected.

Overall, an increase in the number of pulses per burst alters the light-matter interaction at equivalent burst energy and leads to better melting of the surface.

Appendix D

Melted layer generation on Ta6V

In this appendix, the polishing/melted layer generation results obtained with a laser beam, gaussian and spatially shaped using a vortex phase mask carrying an orbital angular momentum of $m = 1$, as explained in Section 1.4.2.3, are presented. The underlying physical mechanism has been detailed previously in Section 1.4.2.3. The objective of this section is to investigate the laser-matter interaction for polishing applications based on visual analysis.

A preliminary study investigating the single burst interaction was performed and "optimal parameters" were identified but are not shown in this section. Based on those parameters an experiment of line scanning was performed. Different burst energies were investigated from 85 to 340 μJ and multiple spot-to-spot overlaps ranging from 45 % to 97 % were investigated. The resulting surface modifications for the gaussian and the vortex beams were characterized using an optical microscope equipped with a 20× objective. Representative results obtained in the GHz-burst configuration are presented in Figure D.1 and Figure D.2 for the gaussian and vortex beams, respectively.

Starting with the gaussian study, the spot size used was 91 μm, it can be noticed that for burst energies above 170 μJ a smoothed melted track is generated, as the spot-to-spot overlap increases the brightness of the observed track increases as well. However, exceeding a certain threshold in heat accumulation probably leads to an oxidation of the surface. The beginning of this process can be identified with the 91 % spot-to-spot overlap and 340 μJ burst energy, where a yellow line appears in the middle of the melted track. This feature is mostly due to the spatial beam distribution of the gaussian beam. Investigating the high overlap regime (97 %), one can observe different oxidation levels based on the energy per burst used, with blue and yellow at 170 μJ, grey and red at 238 μJ, and blue and purple at 340 μJ.

Overall optimal parameters for surface melting seem to be around 86 % in spot-to-spot overlap and with 238 μJ or 340 μJ burst energy.

Following with the vortex beam study, in this case the spot size used was 71 μm, it can be noticed that for a burst energy of 340 μJ an over-melting/ablation occurs, as the spot-to-spot overlap is increased the damage is getting worse. This difference with respect to the gaussian beam case is mostly explained by the reduction of the spot diameter leading to ablation instead of polishing. However, inspecting the lower energies, from 85 μJ to 238 μJ reveals a similar behavior as the one seen in the gaussian case. However, here again, exceeding a certain threshold in heat accumulation leads to an oxidation of the surface. The beginning of this process

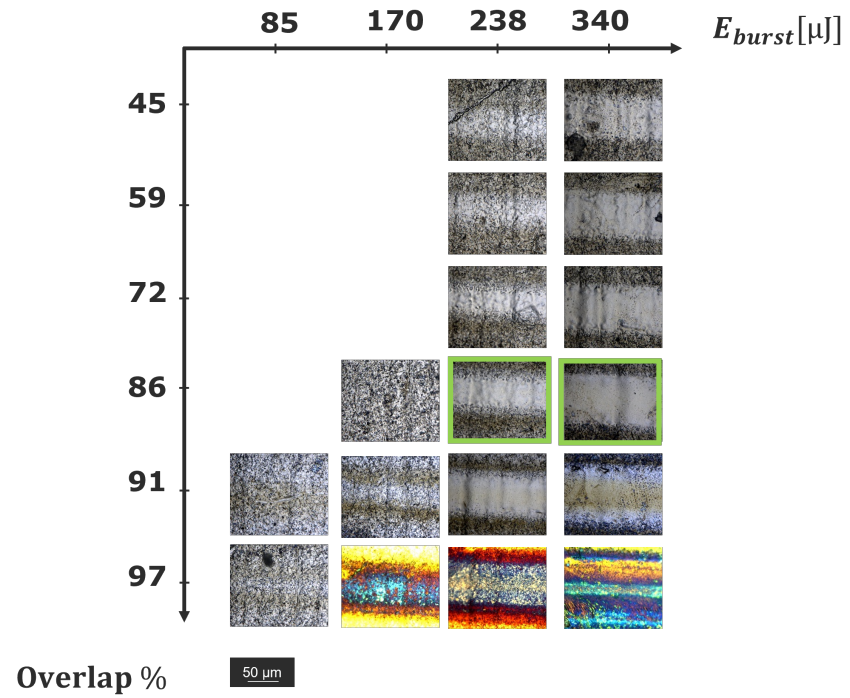

Figure D.1: Optical microscope images of spot-to-spot influence on surface quality for a gaussian beam, 800 ppb GHz-burst, for 4 burst energies, 85, 170, 238 and 340 μJ and a spot diameter of 91 μm.

can be identified with the 91 % spot-to-spot overlap with 170 and 238 μJ, where a yellow line appears in the melted track, but in opposition to the gaussian beam this oxidation line is more uniform over the transverse direction of the line, suggesting that the beam intensity and heat is more evenly distributed in the interaction zone. Investigating the high overlap regime (97 %), one can observe different oxidation levels based on the energy per burst used, with brown and yellow at 170 μJ, blue, orange at 238 μJ.

Overall optimal parameters for surface melting seem to be around 86 % in spot-to-spot overlap and with 85, 170 or 340 μJ burst energy.

With the good spot-to-spot overlap found, the influence of the line-to-line (L-2-L) overlap was investigated. Four configurations were considered: a negative overlap, a 25 % overlap, a 50 % and a 75 % overlap. Burst energies of 85 µJ, 170 µJ, and 238 µJ were tested for each configuration. The results are shown in Fig. D.3.

It can be directly observed that a negative line-to-line overlap (no overlap) produces surface morphologies matching those obtained for a single line. At 25 % line-to-line overlap a smooth surface seems to be generated for 85 µJ and 170 µJ, whereas a sign of "keyhole" can be identified for 238 µJ. Following with 50 % overlap, results are still reflective and smooth in appearance at 85 µJ and 170 µJ, but cracks at the surface start to be identified, probably due to a too high thermal load. While 238 µJ seems structured and presents signs of oxidation. Finally, at 75 %, the results reveal a significantly more oxidized and cracked surface over all the energies investigated. In those cases, the material appears to show relatively flat regions but presents a high degree of oxidation which further increases with higher burst energy. Additionally, cracks are more visible and more wide. These cracks may be determined by the recombination of the different species contained in this alloy, possibly

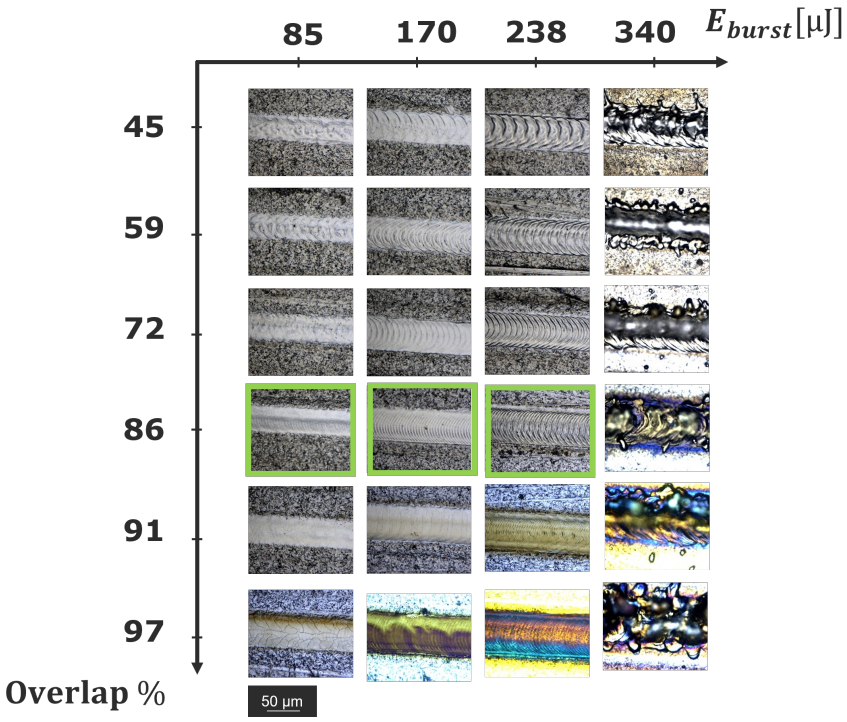

Figure D.2: Optical microscope images of spot-to-spot influence on surface quality for 800 ppb GHz burst with Vortex beam, for 4 burst energies, 85, 170, 238 and 340 μJ, and a spot diameter of 71 μm.

explaining the differences in "grain" size which appear to grow as the burst energy is increased.

These results show that the effect of burst energy, spot-to-spot overlap, and line-to-line overlap are strongly correlated and cannot be considered as independent processing parameters.

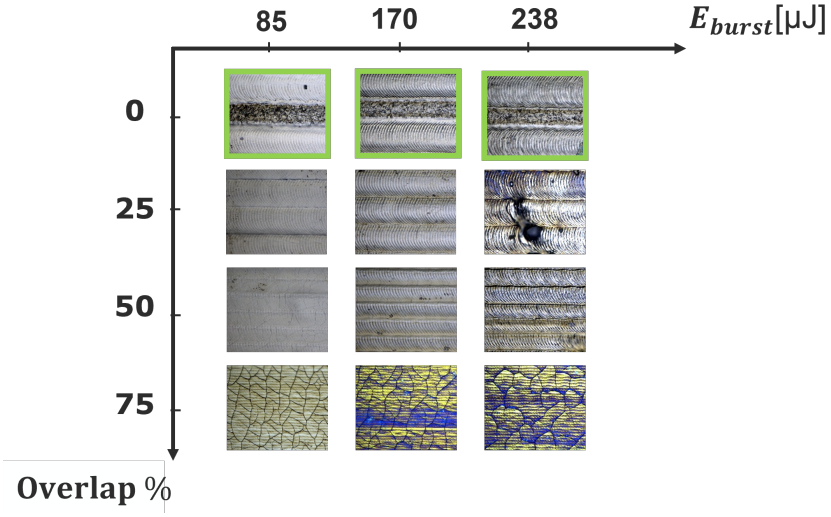

Figure D.3: Optical microscope images of line-to-line influence on surface quality for 800-ppb GHz-burst with vortex beam shaping, for 3 burst energies, 85, 170, and 238 μJ, and a spot diameter of 71 μm.

Appendix E

Reshaping with surface melting

In this last appendix, selected results obtained using a Gaussian laser beam on AL7075 are presented. Although the underlying physical mechanisms have not yet been fully investigated, the observations reveal a promising and intriguing behavior.

The initial objective was to reproduce the surface melting phenomena previously studied on 316L and Ti-6Al-4V (Ta6V), but this time on AL7075 and 2024 aluminum alloys. However, a completely different mechanism was observed. As illustrated in Figure E.1, a three-dimensional structure unexpectedly forms.



Figure E.1: Optical microscope images of reshaping through surface melting on AL7075, illustrated through a Shrek-like figure. 250 µJ, 2000 $m \cdot s^{-1}$, 10 000 passes, hatch of 12 µm.

One can distinguish the familiar facial shape of Shrek, the laser swept from right to left, leading to a strong migration of the matter towards the starting point. It can be seen on the various points of view given of the image that the different generated walls appear to have smooth external surfaces and get as high as 500 µm above the surface. Moreover, looking at this inside of the figure a strange texture of the material is present. A string/hair structure seems to be present and could not be agglomerated towards the wall even though their orientation hints on a migration towards it.